Numerical Algorithms for Vlasov-Poisson Equation and Applications to Coherent Electron Cooling

A Dissertation presented

by

Jun Ma

to

The Graduate School

in Partial Fulfillment of the

Requirements

for the Degree of

Doctor of Philosophy

in

Applied Mathematics and Statistics

(Computational Applied Mathematics)

Stony Brook University

May 2017

Stony Brook University

The Graduate School

Jun Ma

We, the dissertation committe for the above candidate for the Doctor of Philosophy degree, hereby recommend acceptance of this dissertation.

Roman Samulyak - Dissertation Advisor
Professor, Department of Applied Mathematics and Statistics
Scientist, Computational Science Initiative, Brookhaven National Laboratory

Vladimir N. Litvinenko - Dissertation Co-Advisor
Professor, Department of Physics and Astronomy
Senior Physicist, Collider Accelerator Department, Brookhaven National Laboratory

James Glimm - Chairperson of Defense
Distinguished Professor, Department of Applied Mathematics and Statistics

Matthew G. Reuter - Internal Committee Member
Assistant Professor, Department of Applied Mathematics and Statistics

Gang Wang - External Committee Member
Physicist, Collider Accelerator Department, Brookhaven National Laboratory

This dissertation is accepted by the Graduate School

Charles Taber
Dean of the Graduate School

Abstract of the Dissertation

Numerical Algorithms for Vlasov-Poisson Equation and Applications to Coherent Electron Cooling

by

Jun Ma

Doctor of Philosophy

in

Applied Mathematics and Statistics

(Computational Applied Mathematics)

Stony Brook University

2017

New algorithms for the particle-based numerical method, called AP-Cloud, for optimal solutions of Poisson-Vlasov equation have been developed and implemented in code SPACE, as well as a traditional particle-in-cell (PIC) electrostatic solver. While the traditional PIC method is based on a uniform Cartesian mesh, a linear charge deposition scheme, and Fast Fourier Transform solvers, the AP-Cloud method replaces the traditional PIC mesh with an adaptively chosen set of computational particles and is beneficial if the distribution of particles is non-uniform. The code SPACE is a parallel, relativistic, 3D electromagnetic PIC code developed for the simulations of relativistic particle beams, beam-plasma interactions, and plasma chemistry, and has been used in the simulation studies of coherent electron cooling experiments at the Brookhaven National Laboratory.

Coherent electron cooling is a novel technique for rapidly cooling high-energy, high-intensity hadron beams, and consists of three major components: a modulator, where each ion imprints a modulation signal on the electron beam, an amplifier where the modulation signals are amplified by orders, and a kicker where the electrons carrying the amplified signals interact with ions resulting in cooling of ion beam.

We have performed highly resolved numerical simulations to study the coherent electron cooling concept and support the relevant experiments. Modulator and kicker simulations are performed using code SPACE. Simulations of free electron laser, as the amplifier, are performed using the open source code GENESIS.

Numerical convergence and verification test problems for modulator simulations have been studied using electron beam with uniform spatial distribution, where analytic solutions of density and velocity modulations exist. A good agreement of theory and simulations has been obtained for the case of stationary and moving ions in uniform electron clouds with realistic distributions of thermal velocities.

Predictions of modulation process have been given for ions with reference and off-reference velocities and center and off-center locations in Gaussian electron beams with continuous focusing electric field and quadrupole magnetic field. Phase advance studies have been performed to explore the dynamics of electron beam in the transverse plane due to the quadrupole magnetic field, and to explain the behaviors of the transverse modulation signal in the modulator section.

The dynamics of the electron beam and the evolutions of the modulation signal in the coherent electron cooling process have been simulated by the combination use of code SPACE and GENESIS, using electron beam with Gaussian distribution and realistic profiles relevant to the Relativistic Heavy Ion Collider at the Brookhaven National Laboratory.

Dedication Page

To my wife and my parents.

Table of Contents

Contents

List of Figures

List of Tables

Acknowledgements

Pursing PhD is a wonderful journey in my life. I feel much grateful to many people who have instructed me and supported me in this trip.

First and foremost, I would like to express my deepest heartfelt gratitude to my advisor, Roman Samulyak, a respectable scholar and a responsible tutor, for his insightful comments, invaluable advice and constant help on my research and this thesis. He introduces me into the area of numerical simulations, and guides me in every stage of my research. Without his instruction, kindness and patience, I could not have completed my thesis. I admire his knowledge and personality.

I would also like to show my gratitude to my co-advisor, Vladimir N. Litvinenko, who lets me join the coherent electron cooling project, teaches me fundamentals of accelerator physics and offers me opportunities to continue my research.

My special thanks go to Gang Wang. He gives huge help in many aspects of my research, including understanding the physics mechanisms, building numerical models, designing algorithms, improving numerical settings and analysing simulation results.

I shall extend my thanks to my committee members, James Glimm and Matthew G. Reuter, for their helpful suggestions and comments on my thesis.

My thanks also go to Kwangmin Yu and Xingyu Wang, my colleagues at Stony Brook University, for their assistance in code development. I would like to thank Kwangmin Yu especially for his warm-heart encouragement and patient guide from the beginning of my PhD program.

I would like to thank Yichao Jing, my colleague from Collider Accelerator Department at Brookhaven National Laboratory, for his help in numerical simulations and useful comments.

I am grateful to Stony Brook University and Brookhaven National Laboratory. I have made many friends and learned a lot, and I really enjoyed my experience here.

I would like to express my sincere thanks to my dear wife, Rui Gong, for her patience. We met in Stony Brook University and we got married here. Being accompanied by her all these years, I never felt lonely. Her dedication and support have been the source of strength and encouragement for me.

Last but not least, I would like to show my most appreciation to my parents, my father, Rongrong Ma and my mother, Peifang Yu. They have taught me a lot since I was a child and they always tried their best to support me. In the first year I came to Stony Brook University as a master student without scholarship, they supported all my living expenses and tuition. There are no more words to express my gratitude to their unconditional love.

1 Introduction

1.1 Background Briefing

Effectively cooling ion-beams and hadron-beams at the energy of collision is of critical importance for assuring the productivity of present and future Nuclear Physics Colliders. The cooling of natural emittances contributes to longer, more efficient stores resuling in a significantly higher integrated luminosity. Coherent electron cooling (CEC) [1, 2, 3] promises to be a revolutionary technique outperforming competing techniques by orders of magnitude, and possibly the only technique capable of cooling intense proton beams at energies of 100 GeV and above. Using CEC at the Relativistic Heavy Ion Collider (RHIC) in the Brookhaven National Laboratory (BNL) promises up to a 10-fold increase in polarized proton luminosity in RHIC, and a 50-fold one in future polarized electron-ion collider eRHIC.

Being a novel concept, the CEC requires experimental demonstration, as well as numerical tools to predict the performance of the CEC process. To support the proof-of-principle CEC experiment, research institutes including the BNL, the Tech-X Corporation, Stony Brook University, the SLAC National Accelerator Laboratory (originally named Stanford Linear Accelerator Center), the Daresbury Laboratory (UK) and the Budker Institute of Nuclear Physics (BINP, Russia) have been involved in the collaboration.

The CEC system has been installed at BNL RHIC, and the proof-of-principle CEC experiment is in process.

In this work, we will present one of the numerical tools used for CEC experiment, the code SPACE [4]. The code has passed a set of verification tests and has given predictions of CEC process based on the realistic physical parameters of the CEC experiment.

1.2 Vlasov-Poisson Equation and Numerical Method

The time evolution of the probability density function of charged particles is described by the Boltzmann equation, introduced in [5] and given in equation (1),

$$\frac{\partial f}{\partial t} + \mathbf{v} \cdot \nabla f + \mathbf{F} \cdot \frac{\partial f}{\partial \mathbf{p}} = \left(\frac{\partial f}{\partial t} \right)_{coll} \tag{1}$$

where f is the probability density function depending on positions, momentum and time, $\mathbf{v}$ is the vector of velocities, $\mathbf{F}$ is the vector of instant forces on charged particles, $\mathbf{p}$ is the vector of momentum and the right hand side in equation (1) is the collision term.

Removing the collision term in equation (1), the collisionless Boltzmann equation is called Vlasov equation [6], and is given in equation (2).

$$\frac{\partial f}{\partial t} + \mathbf{v} \cdot \nabla f + \mathbf{F} \cdot \frac{\partial f}{\partial \mathbf{p}} = 0 \tag{2}$$

In the Vlasov-Maxwell system of equations, the force term $\mathbf{F}$ in equation (2) is the Lorentz force, given in equation (3),

$$\mathbf{F} = q(\mathbf{E} + \mathbf{v} \times \mathbf{B}) \tag{3}$$

where q is the electric charge of the particle, $\mathbf{v}$ is the velocity of the particle, $\mathbf{E}$ is the electric field and $\mathbf{B}$ is the magnetic field.

The electromagnetic field in equation (3) is solved using Maxwell's equations, given in equations (4) - (7),

$$\text{Faraday's law} \qquad \tfrac{\partial \mathbf{B}}{\partial t} = -\nabla \times \mathbf{E} \tag{4}$$

$$\text{Ampère's circuital law} \qquad \tfrac{\partial \mathbf{E}}{\partial t} = \tfrac{1}{\varepsilon_0 \mu_0} \nabla \times \mathbf{B} - \tfrac{1}{\varepsilon_0} \mathbf{J} \tag{5}$$

$$\text{Gauss's law} \qquad \nabla \cdot \mathbf{E} = \tfrac{\rho}{\varepsilon_0} \tag{6}$$

$$\text{No isolated magnetic charge} \qquad \nabla \cdot \mathbf{B} = 0 \tag{7}$$

where ε_0 is the vacuum permittivity, μ_0 is the vacuum permeability, $\mathbf{J}$ is the current density and ρ is the charge density.

In Vlasov-Poisson equation, with the approximation of zero-magnetic field for non-relativistic particles, the force term $\mathbf{F}$ in equation (2) is given in equation (8).

$$\mathbf{F} = q\mathbf{E} \tag{8}$$

where the electric field is obtained by taking the gradient of the electric potential, as is shown in equation (9),

$$\mathbf{E} = -\nabla \varphi \tag{9}$$

The electric potential φ can be solved using Poisson's equation, given in equation (10).

$$\Delta\varphi = -\frac{\rho}{\varepsilon_0} \tag{10}$$

The Vlasov-Poisson equation can be solved numerically using the traditional Particle-in-Cell (PIC) method and a new highly adaptive Particle-in-Cloud (AP-Cloud) method [7]. Both methods have been implemented in the code SPACE. The details of the numerical algorithms will be presented in section 2.

1.3 Coherent Electron Cooling

Cooling high-energy hadron beams is one of the major challenges in modern accelerator physics. Coherent electron cooling is a novel technique for rapidly cooling high-energy, high-intensity hadron beams. A general CEC system consists of three major components. The first section is a modulator, where each ion imprints a density wake on the electron distribution within designed co-propagation distance, typically one quarter of plasma oscillation period. The second section is a free electron laser (FEL), as an amplifier, where the density wakes are amplified by orders. The third section is a kicker, where the amplified wakes interacts with ions, resulting in dynamical friction for the ion that leads to cooling of ion beams. Figure 1 illustrates a general schematic of CEC. In advanced coherent electron cooling (ACEC), a three-pole wiggler is used as the amplifier, instead of the free electron laser.

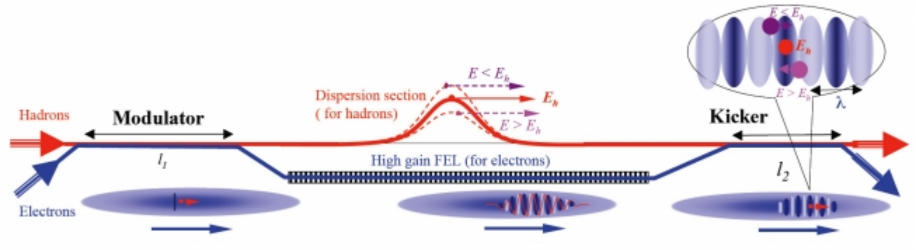

Figure 1: Schematic of coherent electron cooling concept.
* Figure is taken from [3].

Despite significant differences in their amplifiers, all proposed CEC systems share the same mechanism for the modulation process: Coulomb interactions between the ions and the surrounding cooling electrons. For ultra-relativistic beam energy, the relative modulation of the density of electrons due to their interaction with ions is orders of magnitudes smaller than unity and, consequently, it is viable to treat each ion individually and use superposition principal to obtain the net responses of electrons to all ions in the beam. Analytical solution of the electrons' response to a moving ion exists for a system consisting of electrons with uniform spatial distribution [8]. For a system with spatially non-uniform electrons, numerical approaches are employed either by solving the Vlasov equation [9] or by direct macro-particle simulations [10]. One of the difficulties in a macro-particle simulation relies on the fact that the signal due to the modulation is too weak compared to the shot noise resulting from the discreteness of macro-particles. In the approach adopted by G. Bell *et al.* [10], the difficulties are overcome by splitting the electrons into two groups, the background electrons and the δf electrons, and since only the δf electrons contain information about the modulation, the signal to noise ratio is significantly enhanced. In this work, we simulate the physical number of electrons via highly resolved simulations and follow a different approach to extract the modulation signal from the shot noise in a PIC simulation.

In this dissertation, we will firstly introduce the main numerical methods used for the simulations in chapter 2. Modulator simulation results will be presented in chapter 3, followed by the start-to-end simulation results of CEC process in chapter 4.

2 Numerical Algorithms for Vlasov-Poisson Equation

The code SPACE contains a module for solving equations in the electrostatic approximation. This code module was used in the present work as the modulation problem in co-propagating electron and ion beams is electrostatic in nature. The electrostatic module of SPACE employs two different approaches, the PIC method and the AP-Cloud method.

2.1 PIC Method

The traditional PIC method for the Poisson-Vlasov equation is based on a uniform Cartesian mesh, a linear charge deposition scheme, and FFT solvers. We firstly create a uniform Cartesian mesh for the computational domain, and mesh size is chosen appropriately according to the length scale of the particles' interactions. Particles' charges are deposited to the grid points of the mesh using linear interpolation, and charge density is calculated at grid points. Solution to the Poisson's equation (10) gives the electric potential. We apply numerical differentiation to the electric potential to obtain the electric field at the grid points, as is shown in equation (9). The PIC method for the Poisson-Vlasov equation implemented in code SPACE supports Dirichlet boundary condition, three-dimension open boundary condition, three-dimension periodic boundary condition and mixed boundary conditions (periodic in longitudinal and open in transverse).

PIC method with periodic boundary condition is very efficient because the discrete Laplace operator after discrete Fourier transform (DFT) is simply scalar multiplication, and the corresponding reverse operator is scalar division. So we can solve the electric potential after DFT very fast, and then use inverse discrete Fourier transform (IDFT) to get the desired electric potential.

Assume that we have the computational domain $\Omega = [0, L] \times [0, L] \times [0, L]$, and we discretize the domain uniformly using the mesh width $h = L/N$ for x, y, z directions, where N is the number of grids in each direction. Let l, m, n denote the index of grid points in x, y, z directions, respectively, and $\varphi_{l,m,n}$ denote the electric potential at the grid point (l,m,n) of the three-dimension computational domain. We have $0 \leq l, m, n \leq N$, and the periodic boundary condition gives equation (11).

$$
\begin{aligned}
\varphi_{0,m,n} &= \varphi_{N,m,n} \\
\varphi_{l,0,n} &= \varphi_{l,N,n} \\
\varphi_{l,m,0} &= \varphi_{l,m,N}
\end{aligned}
\tag{11}
$$

The discrete Fourier transform is defined in equation (12),

$$
\hat{\varphi}_{p,q,r} = \frac{1}{N^3} \sum_{l,m,n=0}^{N-1} e^{-i\frac{2\pi}{N}(pl+qm+rn)} \varphi_{l,m,n} \tag{12}
$$

where p, q, r are index of grid points in the three-dimension mesh after discrete Fourier transform. The corresponding inverse discrete Fourier transform is defined in equation (13).

$$
\varphi_{l,m,n} = \sum_{p,q,r=0}^{N-1} e^{i\frac{2\pi}{N}(pl+qm+rn)} \hat{\varphi}_{p,q,r} \tag{13}
$$

The discrete Laplace operator can be calculated in equation (14).

$$
\begin{aligned}
\Delta\varphi_{l,m,n} &= \frac{\varphi_{l+1,m,n} + \varphi_{l-1,m,n} - 2\varphi_{l,m,n}}{h^2} \\
&\quad + \frac{\varphi_{l,m+1,n} + \varphi_{l,m-1,n} - 2\varphi_{l,m,n}}{h^2} \\
&\quad + \frac{\varphi_{l,m,n+1} + \varphi_{l,m,n-1} - 2\varphi_{l,m,n}}{h^2} \\
&= \sum_{p,q,r=0}^{N-1} \left(\frac{e^{i\frac{2\pi}{N}p} + e^{-i\frac{2\pi}{N}p} - 2}{h^2} \right) e^{i\frac{2\pi}{N}(pl+qm+rn)} \hat{\varphi}_{p,q,r} \\
&\quad + \sum_{p,q,r=0}^{N-1} \left(\frac{e^{i\frac{2\pi}{N}q} + e^{-i\frac{2\pi}{N}q} - 2}{h^2} \right) e^{i\frac{2\pi}{N}(pl+qm+rn)} \hat{\varphi}_{p,q,r} \\
&\quad + \sum_{p,q,r=0}^{N-1} \left(\frac{e^{i\frac{2\pi}{N}r} + e^{-i\frac{2\pi}{N}r} - 2}{h^2} \right) e^{i\frac{2\pi}{N}(pl+qm+rn)} \hat{\varphi}_{p,q,r} \\
&= \sum_{p,q,r=0}^{N-1} \left(\frac{2\cos\left(\frac{2\pi p}{N}\right) + 2\cos\left(\frac{2\pi q}{N}\right) + 2\cos\left(\frac{2\pi r}{N}\right) - 6}{h^2} \right) e^{i\frac{2\pi}{N}(pl+qm+rn)} \hat{\varphi}_{p,q,r} \\
&= \sum_{p,q,r=0}^{N-1} \left(-\frac{4}{h^2} \right) \left(\sin^2\left(\frac{\pi p}{N}\right) + \sin^2\left(\frac{\pi q}{N}\right) + \sin^2\left(\frac{\pi r}{N}\right) \right) e^{i\frac{2\pi}{N}(pl+qm+rn)} \hat{\varphi}_{p,q,r}
\end{aligned}
\tag{14}
$$

In equation (14), we use the Euler's formula (15) and double-angle formula (16).

$$e^{i\theta} = \cos\theta + i\sin\theta \tag{15}$$

$$\cos 2\theta = 1 - 2\sin^2\theta \tag{16}$$

Comparing equations (13) and (14), we can see that the corresponding Laplace operator in the three-dimension space after DFT is simply a scalar multiplication to each grid point, given in equation (17).

$$\hat{\Delta} = \left(-\frac{4}{h^2}\right)\left(\sin^2\left(\frac{\pi p}{N}\right) + \sin^2\left(\frac{\pi q}{N}\right) + \sin^2\left(\frac{\pi r}{N}\right)\right) \tag{17}$$

If the mesh width is different in x, y, z directions, the Laplace operator after DFT can be obtained following the same derivation above, and is given in equation (18), where N_x, N_y, N_z denote grid numbers in each direction and h_x, h_y, h_z are the corresponding mesh widths.

$$\hat{\Delta} = -\frac{4}{h_x^2}\sin^2\left(\frac{\pi p}{N_x}\right) - \frac{4}{h_y^2}\sin^2\left(\frac{\pi q}{N_y}\right) - \frac{4}{h_z^2}\sin^2\left(\frac{\pi r}{N_z}\right) \tag{18}$$

We can solve the Poisson's equation (10) in the space after DFT. Firstly, take DFT of ρ to get $\hat{\rho}$. We know that the Laplace operator $\hat{\Delta}$ is scalar multiplication after DFT, so we can apply the reverse operator of $\hat{\Delta}$, which is scalar division, to $\hat{\rho}$, and get the $\hat{\varphi}$. Finally, applying IDFT to $\hat{\varphi}$ gives the desired solution φ. In code SPACE, we call the FFTW libraries to do the DFT and IDFT.

Solutions of Poisson's equation with open boundary condition is described in [11], and the PIC method in SPACE code follows the same routine. The main idea is that, to solve the Poisson's equation with open boundary condition, we need to double the computational domain size in each dimension, and make convolution of the change density distribution and the Green's function corresponding to the open boundary condition, in the enlarged domain, then the result gives the correct electric potential within the original computational domain. We improve the computing efficiency by using DFT. After DFT, the convolution operation becomes simply point-to-point multiplications of each corresponding grid point.

Solving Poisson's equation with mixed boundary conditions, typically periodic in longitudinal and open in transverse, is also implemented in code

SPACE. We make the periodic copies of the Green's function in longitudinal direction to get a new Green's function, and then follow the same routine as the solutions for open boundary condition, the resulting electric potential satisfies the mixed boundary condition, which is periodic in longitudinal and open in transverse.

To obtain the optimal accuracy using PIC method, we need to select the appropriate mesh size from the error analysis of PIC method. An uniform Cartesian mesh is used in traditional PIC method and the differential and integral operators are applied to the grid points. The discretization error is given in equation (19)

$$E_d = O\left(\rho(\mathbf{x})h^2\right) \tag{19}$$

where $\rho(\mathbf{x})$ is the charge density distribution in space and h is the mesh size.

The charge density is interpolated from charged particles to the grid points, and the particles' spatial distribution is generated randomly, which introduces the Monte Carlo noise to the right-hand-side of the Poisson's equation, i.e., the charge density distribution. The Monte Carlo noise is givein in equation (20)

$$E_m = O\left(\sqrt{\frac{\rho(\mathbf{x})}{nh^D}}\right) \tag{20}$$

where n is the number of computational particles and D is the number of dimensions in space.

The total error is minimized when the discretization error and the Monte Carlo noise are balanced with the optimal mesh size h given in equation (21)

$$h = O\left(\frac{1}{n\rho(\mathbf{x})}\right)^{\frac{1}{4+D}} \tag{21}$$

We can estimate the optimal mesh size using PIC method for uniformly distributed particles. But it is not possible to maintain the optimal mesh size for non-uniform systems using the traditional PIC method, as the charge density is not constant over the computational domain.

The AMR-PIC method (adaptive mesh refinement to particle-in-cell) [12] uses block-structured adaptive mesh refinement of a rectangular mesh to maintain the optimal mesh size for particles with non-uniform distributions. But AMR-PIC suffers from severe artificial forces, which is described in [12].

2.2 AP-Cloud Method

In addition to the traditional PIC solver, the code includes an implementation of the new highly adaptive Particle-in-Cloud method [7] that replaces the traditional PIC mesh with an adaptively chosen set of computational particles on an octree data structure and the weighted least squares method is used for differential and integral operators.

In AP-Cloud method, the discretization error using kth order generalized finite-difference (GFD) is given in equation (22), and the Monte Carlo noise is the same as that in PIC method, given ni equation (20).

$$E_d = O\left(\rho(\mathbf{x})h^{k-1}\right) \tag{22}$$

The discretization error and the Monte Carlo noise are balanced to minimize the total error in AP-Cloud method, with the optimal inter-particle distance, given in equation (23).

$$h = O\left(\frac{1}{n\rho(\mathbf{x})}\right)^{\frac{1}{2k+D-2}} \tag{23}$$

The AP-Cloud method maintains the optimal accuracy for non-uniform distributions of particles, and is free of the artifacts which is typical for AMR-PIC. In addition, the AP-Cloud method is especially beneficial if the distribution of particles is non-uniform and / or the computational domain is geometrically irregular or boundary conditions are of mixed types. We have compared results of PIC and AP-Cloud simulations of modulator-related problems. Both approaches have passed various verification tests. While PIC and AP-Cloud results were in good agreement, we found that the AP-Cloud methods produced higher quality results for Gaussian beams in computational domains with mixed boundary conditions which is periodic in longitudinal and open in the transverse directions.

2.3 Code SPACE

SPACE is a parallel, relativistic, 3D electromagnetic PIC code developed for the simulation of relativistic particle beams, beam-plasma interaction, and plasma chemistry. It also contains modules for solving equations in the electrostatic approximation.

The code has been used for the study of plasma dynamics in a dense gas filled RF cavities [13], designed for ionization cooling experiments, and

Table 1: Proton beam parameters for simulations of mitigation of beam-beam effect.

Beam energy	30 GeV
Normalized emittance	2e-6 m rad
Beta function	10 m
Number of protons per bunch	2e+11
Bunch duration	5 ns
Number of bunches	110
Bunch arrival interval	110 ns

the study of mitigation effect by beam-induced plasma [14]. We will give a brief introduction to the application to the study of mitigation effect by beam-induced plasma in this section.

Our goal is to demonstrate that plasma can effectively mitigate the beam-beam effect in circular colliders. The proton beam parameters we use are relevant to the RHIC at the BNL, and are shown in Table 1.

The process of plasma generation via ionization of neutral gas by proton beams is modelled by the Bethe-Bloch formula, which describes energy loss of an incident particle in matter by ionization. But the amount of energy absorbed by excitation processes is not precisely known in this case, we use an empirical formula and experimentally measured ionization cross-sections, given in equation (24), where dn_e/dt is the ionization rate, dN_p/dt is the inflow of protons in the elementary volume, L is the volume length, n_{gas}, n_e, n_i are number densities of neutral gas, plasma electrons, and plasma ions, respectively, and β_r is the recombination coefficient. The ionization cross section σ of energetic particles in molecular hydrogen was experimentally measured in [15].

$$\frac{dn_e}{dt} = \frac{dN_p}{dt}\sigma L n_{gas} - \beta_r n_e n_i \tag{24}$$

The recombination process of plasma is affected by the presence of neutral gas and the electric field of proton beam, and the recombination coefficient is an empirical coefficient [16, 17] shown in equation (25), where X is the ratio of electric field and hydrogen pressure, and c_1 and c_2 are empirical numerical coefficients. Measurements of plasma recombination in high-pressure hydrogen gas filled RF cavity at Fermilab [16, 17] are used to evaluate the recombination coefficient β_r in our simulations.

$$\beta_r = c_1 X^{-c_2} \tag{25}$$

Figure 2 shows the plasma generation process due to first five proton bunches. At this stage, plasma recombination process is negligible as the plasma density is relatively low. Long-time evolution of plasma density is shown in figure 3. As plasma density increases, recombination process becomes more important, and it balances the plasma generation process via ionization to reach a quasi-steady state. The plasma density at quasi-steady state is used in highly resolved three-dimension simulations of beam-plasma interaction.

In SPACE, we reproduce plasma at saturation regime and let proton beam travel through the plasma. We compare the transverse electric field of proton beam in vacuum and in plasma, and result is given in figure 4. The comparison clearly shows the reduction effect around the center, where plasma density is high. The explanation of the reduction of transverse electric field is the re-distribution of plasma electrons due to proton beam, given in figure 5. The proton beams attract plasma electrons and cause high density of plasma electrons in the center region, leading to the reduction of transverse electric field of proton beam.

The original SPACE code only outputs every single particles' six-dimension information (three-dimension in space and three-dimension in velocity), and data analysis studying the properties of the whole beam requires plenty of post processing. Diagnostic routines have been implemented in the code to provide more options of visualizing the particles beam, including one-dimension density distribution, one-dimension average velocity distribution with various averaging range and two dimension density distribution, within Cartesian coordinates or polar coordinates.

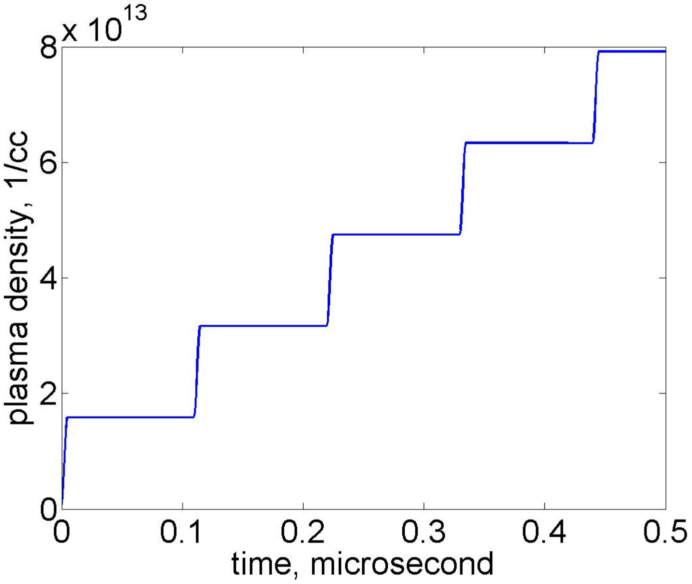

Figure 2: Plasma density evolution corresponding to first five bunches of proton beam.

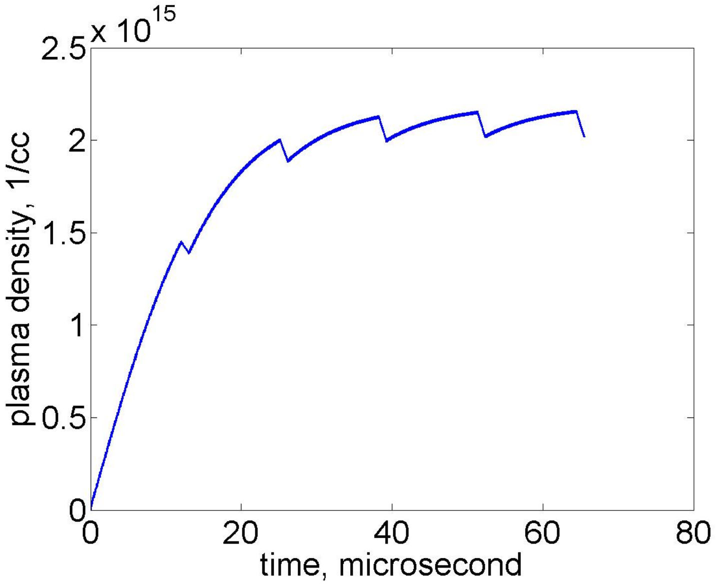

Figure 3: Evolution of plasma density created by proton ionization of neutral hydrogen.

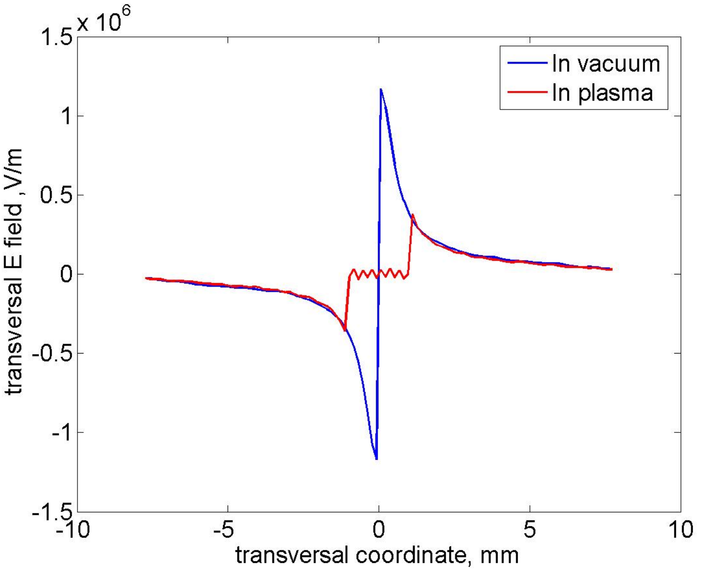

Figure 4: Comparison of electric field of proton beam in vacuum and in plasma.

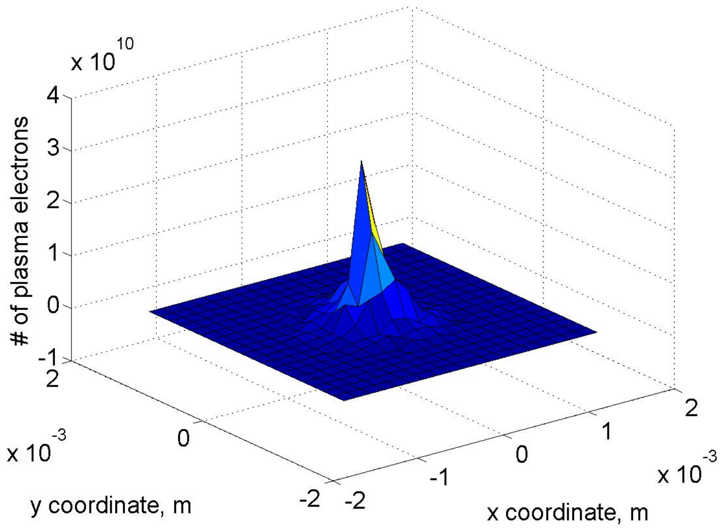

Figure 5: Re-distribution of plasma electrons due to proton beam.

3 Modulator Simulations of Coherent Electron Cooling

In this section, we will introduce the physical parameters, numerical algorithms, numerical convergence and verification tests and present the simulation results of modulator, the first section of coherent electron cooling.

3.1 Physical Parameters and Numerical Algorithms

Two species of particles are used in coherent electron cooling experiments, electron beam and ion beam. Table 2 lists main parameters of beams that are relevant to the Relativistic Heavy Ion Collider at Brookhaven National Laboratory.

Performing numerical simulations of modulator process in co-moving frame gains more advantages than in lab frame because of the relativistic velocity of the beams. In lab frame, such large velocity requires very large computational domain that occupies huge amount of memory, and we need to take into account the magnetic field by the beams as it is not negligible. And it has low efficiency using memory and computing source as beams occupy a relatively small space in the whole computational domain. With Lorentz transformation from lab frame to co-moving frame, beam's velocities are far less than light speed and we can reduce the computational domain's size to fit the beam size. Interactions between particles can be solved as an electrostatic problem as we can neglect magnetic field generated by moving charged particles at such low velocities. Instead of solving the full Maxwell's equations, we can calculate the electric potential from charge density distribution by solving Poisson's equation (10), and take gradient of the electric potential to get the electric field, as is shown in equation (9).

Reducing number of particles in numerical simulations is another way to improve computational efficiency. The two facts, that the ion-ion interactions are negligibly small on length scales relevant to the modulation process and that the relative density modulation of electrons due to ion is orders of magnitudes smaller than unity, allow us to use single ion, instead of the ion beam, in numerical simulations to get density modulation and velocity modulation. We can choose various locations and velocities for the single ion in numerical simulations, and use super position principle to get the overall density modulation and velocity modulation of electrons due to the whole

Table 2: Parameters of electron and ion beams.

Parameter	Electron beam	Ion beam, Au^{+79}
Beam energy	γ=42.9	γ=42.9
Peak current	100 A	
Bunch intensity	10 nC	1×10^9
Bunch length	10 ps (full)	2 ns (r.m.s.)
R.M.S. emittance	5 π mm mrad	2 π mm mrad
R.M.S. energy spread	1e-3	
Beta function at modulator	4 m	
Plasma frequency (lab frame)	1.5e+8 rad/s	
Transverse Debye length (lab frame)	3.4e-4 m	
Longitudinal Debye length (lab frame)	1.1e-6 m	

ion beam. Debye length describes the range of the ion's electrostatic effect. Now as we have single ion in simulations, we can use only those electrons that are within a few Debye lengths distances from ion instead of the whole electron beam, because electrons at further distances are merely affected by the ion and their contributions to modulation process are negligible.

Modulation process is affected by the temperature of electrons. In numerical simulations, we add random velocities to each electron to model the thermal velocities, and the distribution of the thermal velocities obey the "kappa-2" probability density function, as is shown in equation (26) [18], where β_x, β_y and β_z are characteristic velocity amplitudes in 3-dimensional Cartesian coordinates and $\vec{v}_0$ is the ion's velocity. In our simulations, the thermal velocity distribution parameters are chosen as $\beta_x = \beta_y = 2e + 6m/s$ and $\beta_z = 3e + 5m/s$ in the co-moving frame, which is consistent with experimental predictions.

$$f_0(\vec{v}) = \frac{n_0}{\pi^2 \beta_x \beta_y \beta_z} \left(1 + \frac{(v_x + v_{0x})^2}{\beta_x^2} + \frac{(v_y + v_{0y})^2}{\beta_y^2} + \frac{(v_z + v_{0z})^2}{\beta_z^2} \right)^{-2} \tag{26}$$

The reduction of equation (26) to 1D and 2D, respectively, are given in equation (27) and equation (28) [19].

$$f_0(v) = \frac{n_0}{\pi\beta} \left(1 + \frac{(v + v_0)^2}{\beta^2} \right)^{-1}, \tag{27}$$

$$f_0(\vec{v}) = \frac{n_0}{2\pi \beta_x \beta_y} \left(1 + \frac{(v_x + v_{0x})^2}{\beta_x^2} + \frac{(v_y + v_{0y})^2}{\beta_y^2} \right)^{-3/2} \tag{28}$$

Boundary conditions and external fields are selected in three sets of modulator simulations. For verification purpose and for comparison of numerical simulations with analytic solutions, we firstly assume uniform spatial distribution of electrons in a computational domain with periodic boundary conditions and without external fields, because the analytic solutions exist for a system consisting of electrons with uniform spatial distribution [8]. To study modulation processes relevant to conditions of real experiments, we use more realistic distribution for electron beam, which is Gaussian in transverse and in longitudinal directions rather than the assumption of uniform spatial distribution. As mentioned above, we select only the electrons within the range of a few Debye lengths from the single ion in numerical simulations. Electron beam's transverse sizes are comparable with Debye length, so that our simulations cover the whole beam in transverse. But electrons beam's longitudinal size is far larger than Debye length, and within a few Debye lengths the electron beam is approximately uniform in longitudinal. The part of electron beam used in our numerical simulations has Gaussian distribution in transverse and uniform distribution in longitudinal, so the boundary condition is set to be open in transverse and periodic in longitudinal. External fields are needed to maintain the electron beam, otherwise electrons will escape from the computational domain in transverse due to the expansion caused by space charge effect. We use an ideal continuous focusing field that can perfectly keep the Gaussian shape of the electron beam in transverse to study the modulation process with such distribution of electron beam. And then we use more realistic external fields, quadrupole magnetic field used in real experiments, to give prediction of electron beam dynamics in modulation process of coherent electron cooling.

One of the difficulties in modulator simulations is the strong shot noise, which reduces the signal-to-noise ratio, making the detection of the modulation process in density and velocity re-distribution very hard. We have tested two methods compressing the shot noise. One method improves the statistics by reducing the representing number of computational particles. The representing number determines how many real particles are represented by a computational particle, and its typical value is 1 (single electrons are resolved), which makes the shot noise four orders larger than signal. To reduce the shot noise, we decrease representing numbers to be 0.05, which is very computationally intensive, still gives two orders smaller signal compared with shot noise. Another method proved to be much more effective without causing significant increase of the computational cost. For each modulation problem, we perform two simulations with identical initial distributions of computational electrons. One simulation operates only with the electron beam while in the other simulation, the electron beam co-propagates with an ion. With the assumption that the Coulomb force from an ion only slightly changes the trajectories of the cooling electrons over the modulation process of coherent electron cooling, the influences of the ion can be obtained by taking the difference in the final electron distributions of the two simulations. This method effectively eliminates the shot noise and gives a clear redistribution of electrons due to interactions with single ion. Similar approach has been successfully applied to simulate the FEL amplification process in the presence of shot noise [20].

3.2 Numerical Convergence and Verification

In this section, we report results of numerical convergence and verification simulations using a single ion in the center of computational domain with surrounding electrons within the range of a few Debye lengths. Electron beam has uniform spatial distribution and satisfies the kappa-2 thermal velocity distribution. We use the same number of grid blocks per Debye length and periodic boundary conditions is used to model the infinite beam. This series of simulations demonstrated the numerical convergence and allowed us to select an optimal size of the PIC mesh and the number of particles for the remaining simulations described in this paper. Typical results of longitudinal density and velocity modulation, are shown in figure 6 and 7 respectively.

When using coarse mesh (5 grids per Debye length) and small (3×10^5) number of electron macro-particles (with each macro-particle representing 100 electrons, top left), the magnitudes of the density and velocity modulation are very close to the correct values, and the detailed spatial dependence (curve shape) is under-resolved and very noisy. The increase of the number of particles to 3×10^7 and using the same mesh (top right) greatly improves the smoothness of curves. Using fine mesh (20 grids per Debye length) and small (3×10^5) number of macro-particles (bottom left) induces largest noise due to bad statistics. Finally, the mesh refinement to 20 grids per Debye length and large (3×10^7) number of particles (bottom right) improve the resolution of gradients and reduces the overall simulation error of the density modulation. As the resolution of 20 grids per Debye length is still practical for computing in larger domains due to parallel scalability of our code, we used such a resolution and resolve real number of electrons in all simulations presented in this work. For data analysis and visualization, an additional smoothing technique is applied to reduce the noise.

Analytic solutions of density and velocity modulations exist for a system containing infinite electron beam with uniform spatial distribution. Theoretical values of density modulation is obtained in [19], and is given in equation (29):

$$\tilde{n}_1(x,t) = \frac{Z_i \omega_p}{\pi \beta} \int_0^t \frac{\psi \sin(\omega_p \psi) d\psi}{\psi^2 + \frac{(x+v_0\psi)^2}{\beta^2}}, \tag{29}$$

where $\tilde{n}_1(x,t)$ is the shielding response of the electrons to the ion, Z_i is the charge number of the ion ($Z_i = 79$ for a fully stripped gold ion), ω_p is plasma frequency, and β is the parameter in equation (27). In the co-propagation

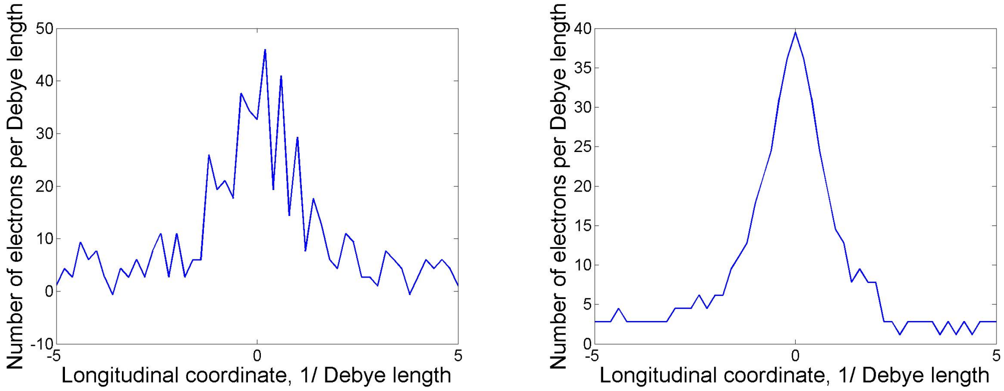

(a) 5 grids/λ_D, 3×10^5 particles (b) 5 grids/λ_D, 3×10^7 particles

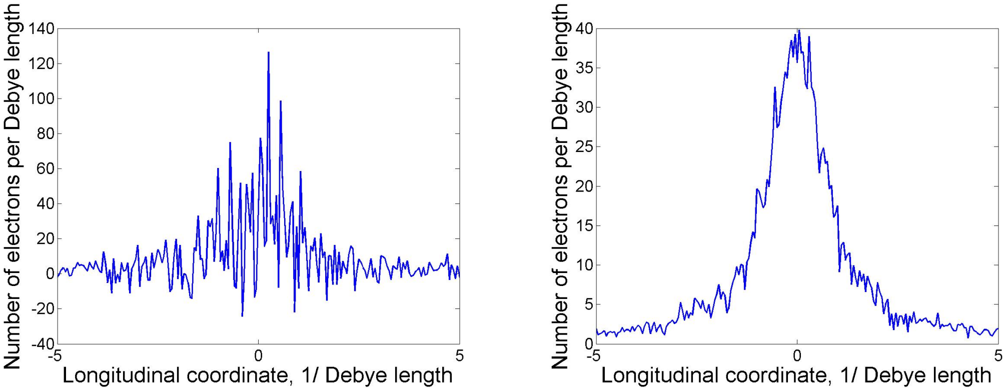

(c) 20 grids/λ_D, 3×10^5 particles (d) 20 grids/λ_D, 3×10^7 particles

Figure 6: Convergence study of longitudinal density modulation with mesh refinement and increase of particle number.

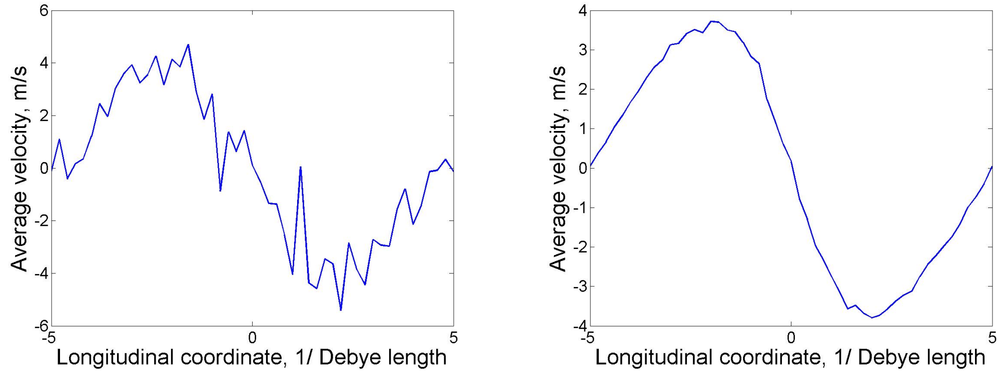

(a) 5 grids/λ_D, 3×10^5 particles (b) 5 grids/λ_D, 3×10^7 particles

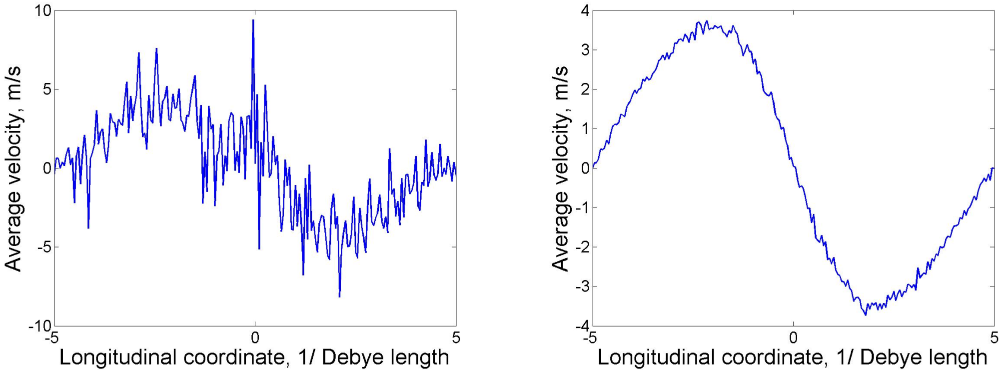

(c) 20 grids/λ_D, 3×10^5 particles (d) 20 grids/λ_D, 3×10^7 particles

Figure 7: Convergence study of longitudinal velocity modulation with mesh refinement and increase of particle number.

process, ion attracts surrounding electrons and causes the density growing of electrons near the ion's location. This process is affected by the temperature and the number density of the surrounding electrons. There is a limit of such modulation process. When the total charge of attracted electrons balances the ion's charge, the modulation process reaches a steady state. In the limiting case of $t \to \infty$, equation (29) gives the steady-state result in equation (30) [19].

$$\tilde{n}_1(x) = \frac{Z_i \omega_p}{2\beta} \exp\left(-\frac{\omega_p |x|}{\beta}\right), \tag{30}$$

Theoretical values of velocity modulation is derived from the analytic solution of energy modulation, which is obtained in [18] and is given in equation (31), and the expression of instantaneous current density $I_d(z,t)$ is given in equation (32) [18]:

$$\left\langle \frac{\delta E(z_l)}{E_0} \right\rangle = \frac{v_z}{c} = -\frac{1}{e n_0 \pi a^2 c} I_d\left(\gamma_0 z_l, \frac{L_{\text{mod}}}{\beta_0 \gamma_0 c}\right), \tag{31}$$

$$\begin{aligned} I_d(z,t) = \quad & -\frac{Z_i e \omega_p^2}{\pi} \int_0^t d\tau (z + v_{0,z}\tau) \left\{ \frac{a_z \sin(\omega_p \tau)}{[\bar{\beta}^2 \tau^2 + (z + v_{0,z}\tau)^2][1 + \bar{\beta}^2 \tau^2 + (z + v_{0,z}\tau)^2]/a^2} \right. \\ & \left. - \cos(\omega_p \tau) \left[\frac{\arctan(|z + v_{0,z}\tau| / ((\bar{\beta})\tau))}{|z + v_{0,z}\tau|} - \frac{\arctan\left(\sqrt{(z + v_{0,z}\tau)^2 + a^2} / (\bar{\beta}\tau)\right)}{\sqrt{(z + v_{0,z}\tau)^2 + a^2}} \right] \right\}, \end{aligned} \tag{32}$$

where z_l is the longitudinal coordinate in the lab frame, L_{mod} is the modulator length, a is the transverse RMS beam size, c is the speed of light, β_0 is the ratio of co-moving frame velocity to the speed of light, γ_0 is Lorentz factor, a_z is the Debye radius in the beam frame, and $v_{0,z}$ is the longitudinal velocity of ion in co-moving frame.

We compare our simulation results with analytic solutions using a stationary ion and a moving ion. A stationary ion moving with reference velocity is stationary in the co-moving frame, and the resulting longitudinal density and velocity modulation are given in figure 8, which shows a good agreement with theory.

In the next simulation, we use an ion moving with the velocity of $v_{0,z} = 1 \cdot \beta_z$ with respect to the electron cloud in the co-moving frame, and the com-

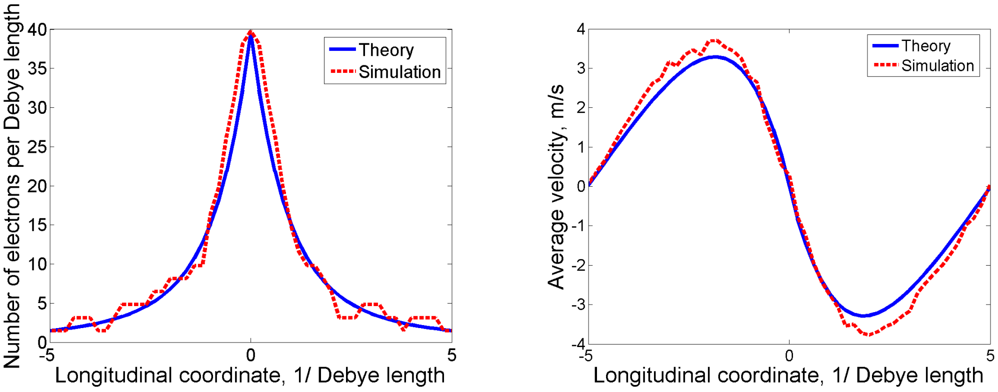

(a) Longitudinal density

(b) Longitudinal velocity

Figure 8: Comparison of theory and numerical simulations of density (a) and velocity (b) modulation by stationary ion with respect to uniform electron cloud.

parison with theory is shown in Figure 9. As before, simulations demonstrate a good agreement with the theory.

3.3 Modulator Simulations with Linear Focusing Field

In this section, we study the modulation processes for more realistic electron beams in continuous focusing fields.

The infinite electron beam with uniform spatial distribution used for the verification is not realistic in experiments, and a finite beam with Gaussian distribution in space is more relevant to the experiments of coherent electron cooling. As we are using single ion in numerical simulations, the computational domain size is a few Debye lengths in each direction, and only the electrons inside the computational domain are needed for numerical simulations. From the beam parameters in table 2, we calculate that the electron beam's transverse size is comparable with Debye length, and we can set the computational domain size relatively large to cover the whole profile of the electron beam in transverse directions. But the electron beam's longitudinal size is far larger than Debye length, so our computational domain can only contain a thin slice of electrons in longitudinal direction, compared with the whole electron beam. Within a few Debye lengths, we can assume a uniform distribution of electron beam in longitudinal directions. Accordingly, bound-

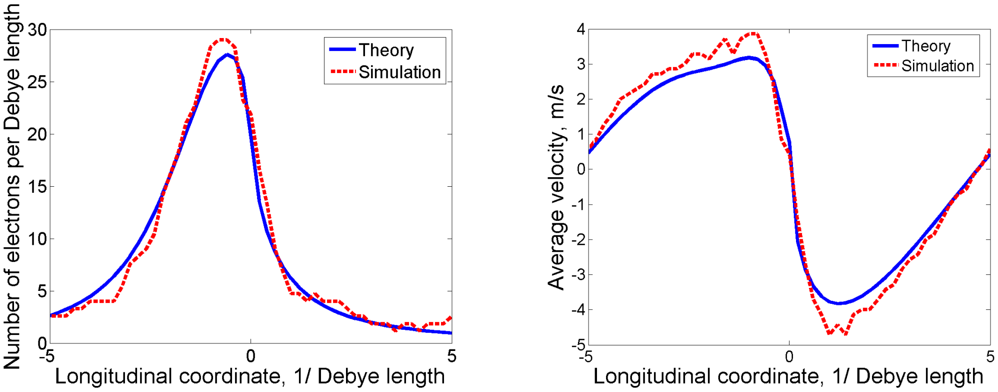

(a) Longitudinal density

(b) Longitudinal velocity

Figure 9: Comparison of theory and numerical simulations of density (a) and velocity (b) modulation by ion moving with β_z velocity with respect to uniform electron cloud.

ary conditions are set to be open in the transverse directions and periodic in the longitudinal direction.

Unlike the verification tests with uniform distributed electron beam filling the whole computational domain with periodic boundary conditions, now we have open boundary and Gaussian distribution of electron beam in transverse directions, and one difficulty is that electron beam expands and a large part of electrons escape the computational domain. There are two reasons for the expansion of the electron beam, one is the thermal velocity of electrons and the other is the space charge effect. External fields are required to compensate the expansion.

The linear focusing field in [19], given in equation (33), is used to prevent the beam expansion in the transverse direction due to thermal velocities.

$$\vec{E_0}(x) = \frac{m_e}{e}\frac{\sigma_v^2}{r_0^2}(x - x_0), \tag{33}$$

where x is the radial coordinate in transverse plane, x_0 and r_0 are the center and RMS values of x, and σ_v is the RMS velocity of the electron distribution.

Consider the expansion due to space charge effect, we need to calculate the electric field by the electron beam and apply the electric field with the same magnitude and opposite sign. Note that the electron beam used for numerical simulations has Gaussian distribution in transverse directions and uniform distribution in longitudinal direction, and the boundary is open in transverse and periodic in longitudinal, so the electric field due to space charge effect is zero in longitudinal direction and holds radial symmetry. Using Gauss's law, we can easily calculate the transverse electric field compensating space charge forces, which is given in equation (34).

$$\vec{E}_1(x) = \frac{q}{2\pi\varepsilon_0(x - x_0)} \left(1 - e^{-(x-x_0)^2/2r_0^2}\right) \tag{34}$$

where x is the radial coordinate in transverse plane, x_0 and r_0 are the center and RMS of x, and q is electron beam's line charge density.

Combination of equation (33) and equation (34) gives the focusing field keeping the electron beam from expansion due to thermal velocities and space charge effect. We perform test simulations to check the effect of such focusing fields. Figure 10 shows the electron beam's initial and final velocity distribution in modulation process, and it demonstrate that the focusing fields maintain the electron beam appropriately in velocity distribution. A relatively high oscillation in velocity distribution at the periphery of the beam has little effect on the modulation process, because that area is the very edge of the Gaussian distribution containing very few particles and those electrons are too far to be effected by the ion.

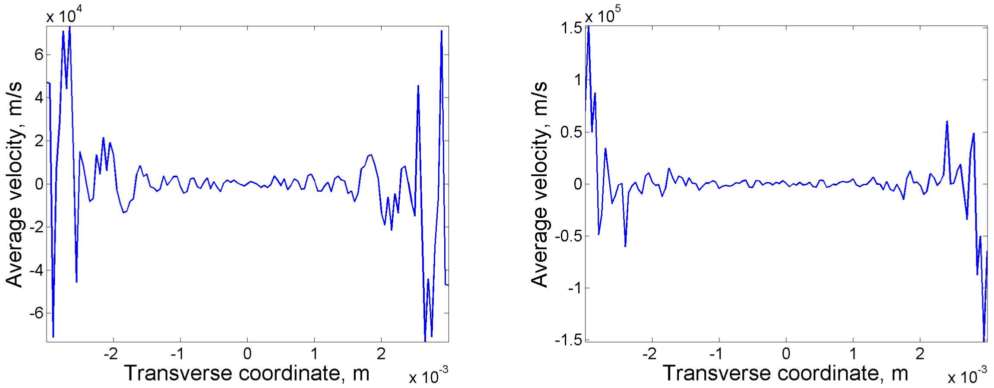

(a) Initial velocity

(b) Final velocity

Figure 10: Transverse velocities of electron beam in linear focusing field at initial (left) and at final (right).

Figure 11 gives the beta function change of the electron beam under the focusing fields. It shows that the focusing fields perfectly maintain the beam size during the modulation process.

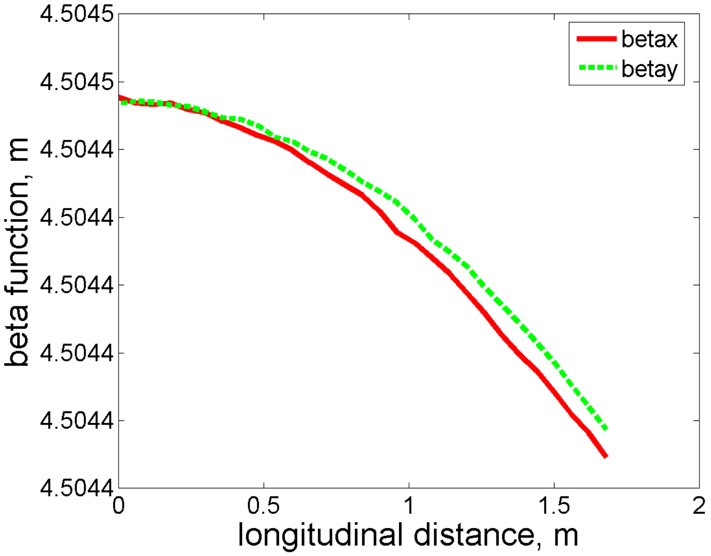

Figure 11: Beta function changes of electron beam in linear focusing field

We study the modulation process using single ion and surrounding electrons with Gaussian distribution in transverse and uniform distribution in longitudinal, under the ideal focusing fields.

We start with a stationary ion located at the center of the Gaussian electron beam, and simulation results of modulation process are presented in figures 12 - 15.

The length of modulator is 3m, which is the co-propagation distance of ion and electron beam in lab frame, and we study the density and velocity modulation in transverse and longitudinal during the process. Longitudinal density and velocity modulation contains important information of modulator, which are shown in figure 12. The longitudinal density modulation gradually builds up at surrounding region of ion and the velocity modulation also shows the attraction effect of the ion. Note that in previous verification tests, we use Debye length as the measurement of the domain size, because Debye length depends on the electron beam's density, and the uniform distributed electrons make the Debye length the same everywhere in the computational domain. Now we have electron beam with Gaussian distribution in transverse, the Debye length varies in different locations with different electrons density, so it is nature to measure domain size in meters in this case.

Figure 13 shows the transverse density and velocity modulation, which provide more information besides the longitudinal plots. Note that there are two directions in transverse plane, the horizontal direction (indicated as x direction here) and vertical direction (indicated as y direction here). In this set of simulations using linear focusing field, the system holds radial symmetry, and x and y directions are identical, and we typically choose x direction for visualization of transverse modulation.

Figure 14 is the density modulation viewed from the transverse plane at the final stage of modulator, and it shows the modulation process is symmetric in radial direction, as expected. Figure 15 is the density modulation from the plane containing the longitudinal direction and one transverse direction at the end of modulator. We do not expect symmetry in figure 15 as length scale is quite different in transverse and in longitudinal, because of the difference between the longitudinal Debye length and transverse Debye length.

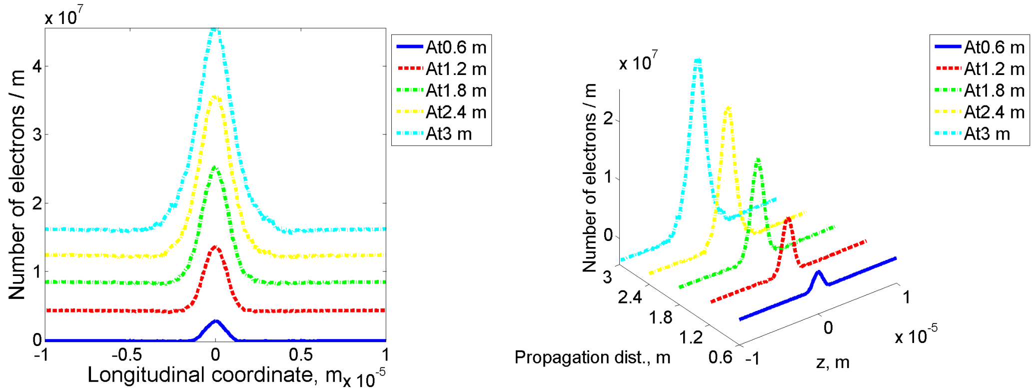

(a) Longitudinal density, 2D

(b) Longitudinal density, 3D

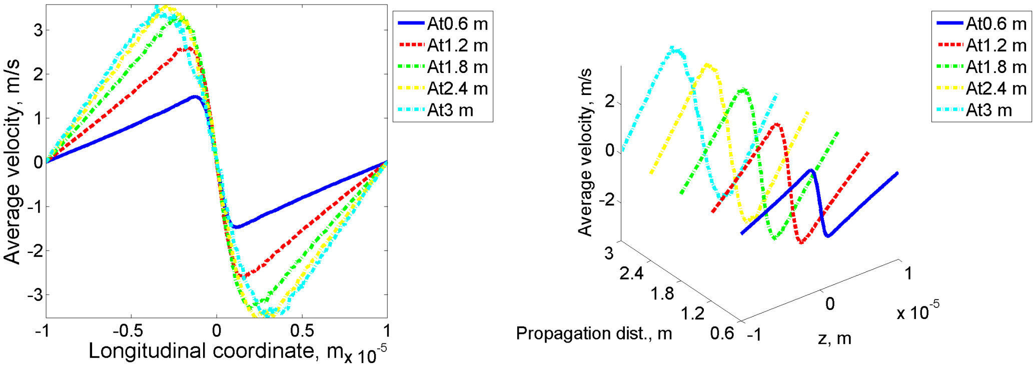

(c) Longitudinal velocity, 2D

(d) Longitudinal velocity, 3D

Figure 12: Longitudinal density and velocity modulation by reference energy ion in the center of the Gaussian electron beam in linear focusing field after 0.6m (blue, solid line), 1.2m (red, dash line), 1.8m (green, dash-dot line, 2.4m (yellow, dash-dot line) and 3m (cyan, dash-dot line)of co-propagation with electrons, curves in (a) are shifted to improve readability.

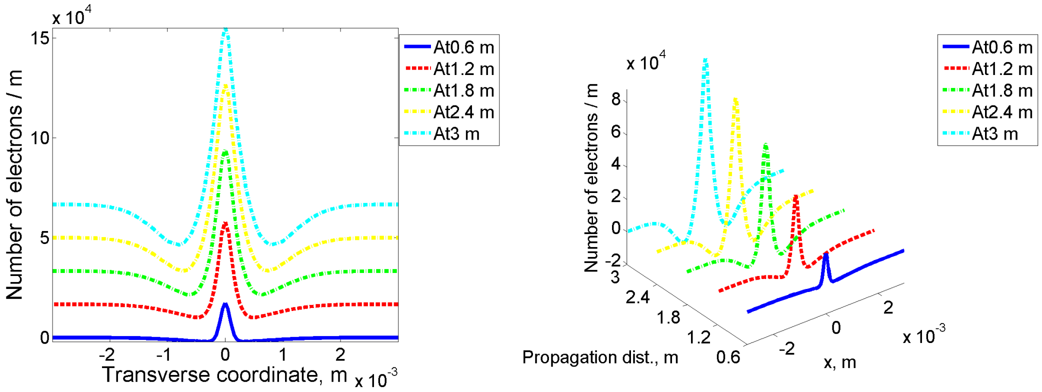

(a) Transverse density, 2D (b) Transverse density, 3D

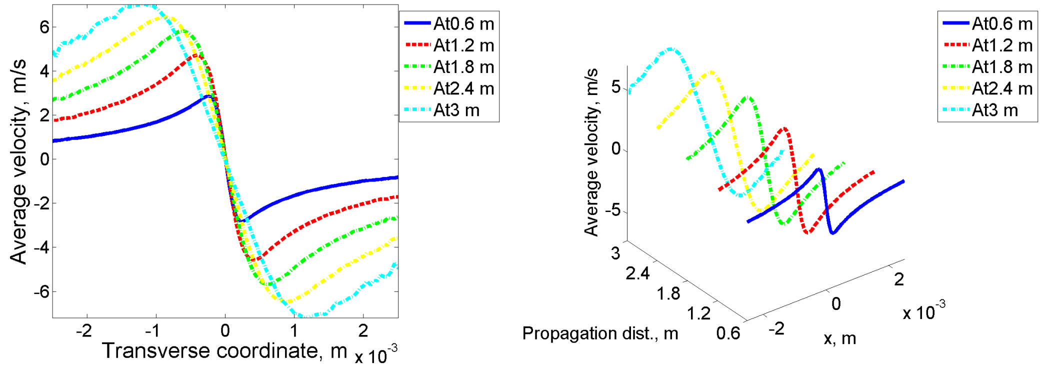

(c) Transverse velocity, 2D (d) Transverse velocity, 3D

Figure 13: Transverse density and velocity modulation by reference energy ion in the center of the Gaussian electron beam in linear focusing field after 0.6m (blue, solid line), 1.2m (red, dash line), 1.8m (green, dash-dot line, 2.4m (yellow, dash-dot line) and 3m (cyan, dash-dot line)of co-propagation with electrons, curves in (a) are shifted to improve readability.

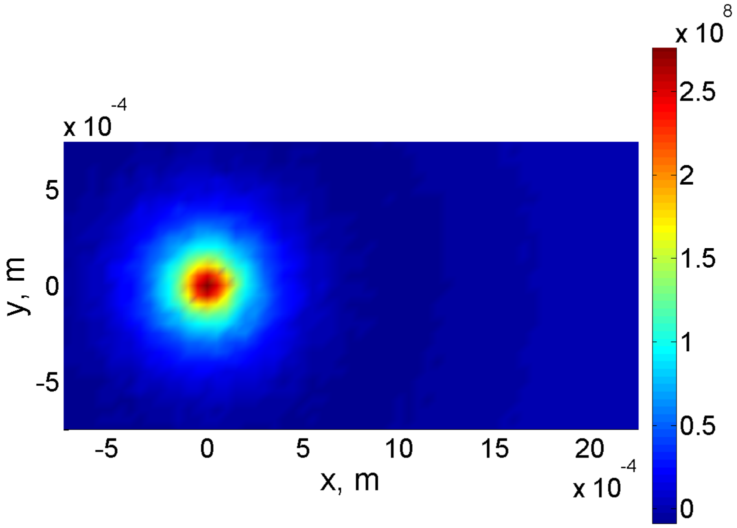

Figure 14: 2D (x and y) plot of density modulation, measured in numbers of electrons per square meters, by reference energy ion in the center of the Gaussian electron beam in linear focusing field

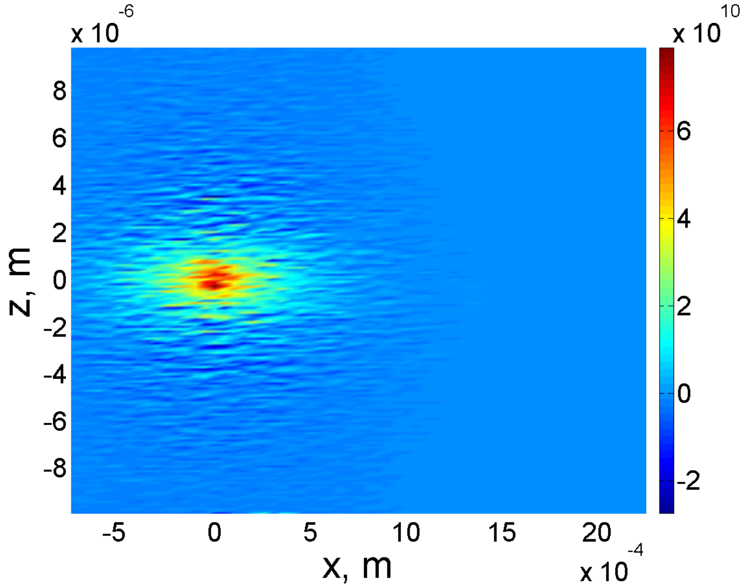

Figure 15: 2D (x and z) plot of density modulation, measured in numbers of electrons per square meters, by reference energy ion in the center of the Gaussian electron beam in linear focusing field

To obtain the results of modulation process due to the whole ion beam from the results of single ion simulations using super position principle, we need to repeat the single ion simulations using various locations and velocities for ion. In the next simulations, we study the effect of ion's locations on the modulation process, and the ion is stationary in the co-moving frame. As the electron beam in numerical simulations has uniform distribution in longitudinal, choosing different longitudinal locations for ion doesn't make difference, so we select different transverse locations for ion. The Gaussian electron beam is radial symmetric in transverse plane, and we typically choose various locations for ion along x direction. Typical ion locations used for numerical simulations are $0.5\sigma_x, 1.0\sigma_x, 1.5\sigma_x, 2.0\sigma_x$ off the center of the Gaussian electron beam along x direction, where σ_x is the RMS value of the Gaussian distribution of electron beam.

The simulations results of modulation process using a stationary ion 0.5σ off the center of the Gaussian electron beam are listed in figures 16 - 19.

Figure 16 shows that the longitudinal density and velocity modulation by a stationary ion 0.5σ off the center of the Gaussian electron beam are similar with the results using the stationary ion at the center of the Gaussian electron beam. At the ion's location, the electron beam's density is still high (approximately 88 percent of the peak density at center) to provide sufficient modulation, so we do not observe large difference between these two ion's locations.

Figure 17 shows that the transverse density modulation by a stationary ion 0.5σ off the center of the Gaussian electron beam drops a little, compared with the ion at the center. And we can observe that the transverse density modulation in no longer symmetric if the ion is off center of the electron beam. This non-symmetric modulation process is not clearly seen in the density modulation visualizations in figures 18 and 19, because the ion is still close to the center of the electron beam.

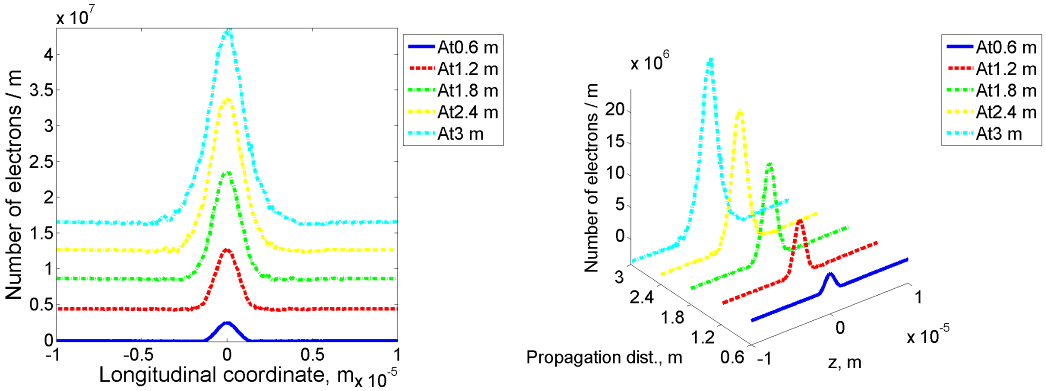

(a) Longitudinal density, 2D

(b) Longitudinal density, 3D

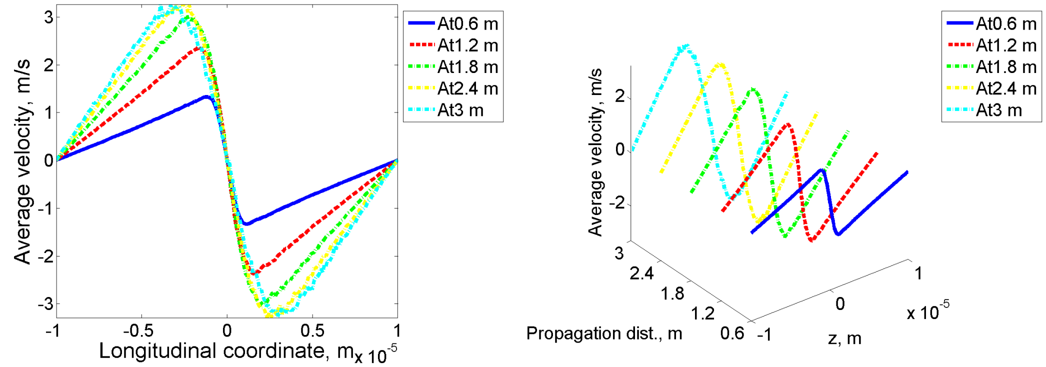

(c) Longitudinal velocity, 2D

(d) Longitudinal velocity, 3D

Figure 16: Longitudinal density and velocity modulation by reference energy ion 0.5σ off the center of the Gaussian electron beam in linear focusing field after 0.6m (blue, solid line), 1.2m (red, dash line), 1.8m (green, dash-dot line, 2.4m (yellow, dash-dot line) and 3m (cyan, dash-dot line)of co-propagation with electrons, curves in (a) are shifted to improve readability.

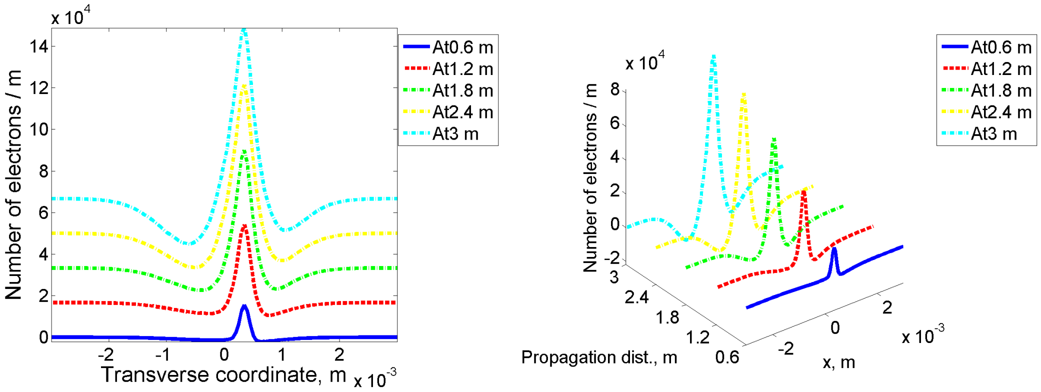

(a) Transverse density, 2D

(b) Transverse density, 3D

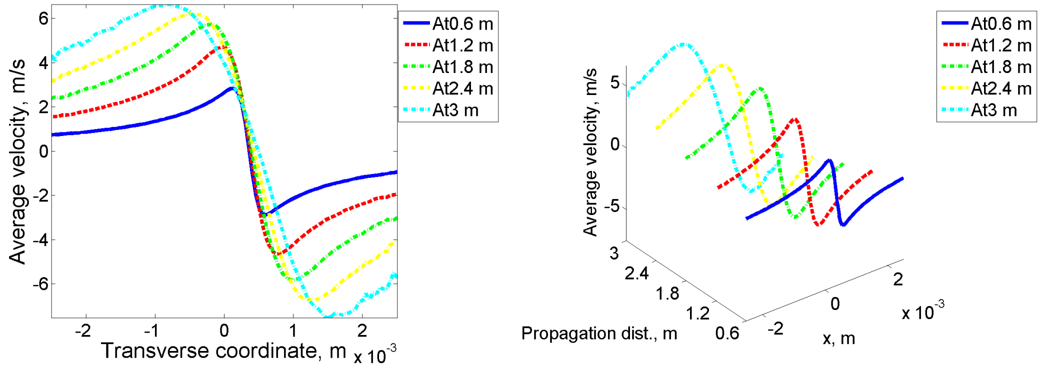

(c) Transverse velocity, 2D

(d) Transverse velocity, 3D

Figure 17: Transverse density and velocity modulation by reference energy ion 0.5σ off the center of the Gaussian electron beam in linear focusing field after 0.6m (blue, solid line), 1.2m (red, dash line), 1.8m (green, dash-dot line, 2.4m (yellow, dash-dot line) and 3m (cyan, dash-dot line)of co-propagation with electrons, curves in (a) are shifted to improve readability.

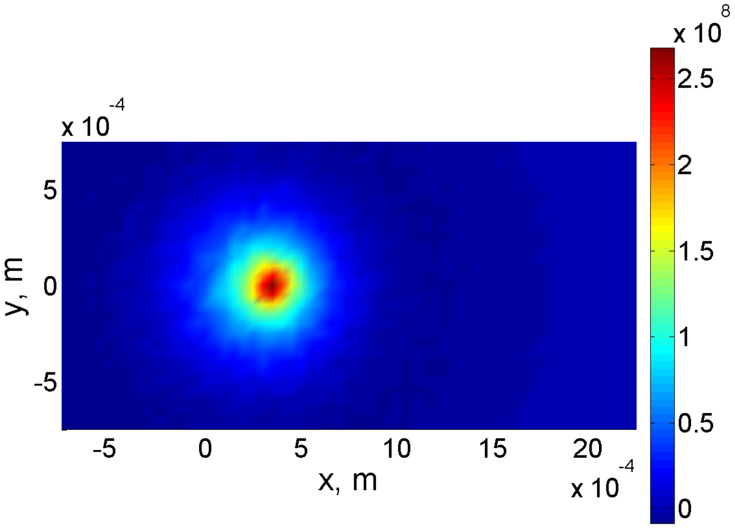

Figure 18: 2D (x and y) plot of density modulation, measured in numbers of electrons per square meters, by reference energy ion 0.5σ off the center of the Gaussian electron beam in linear focusing field

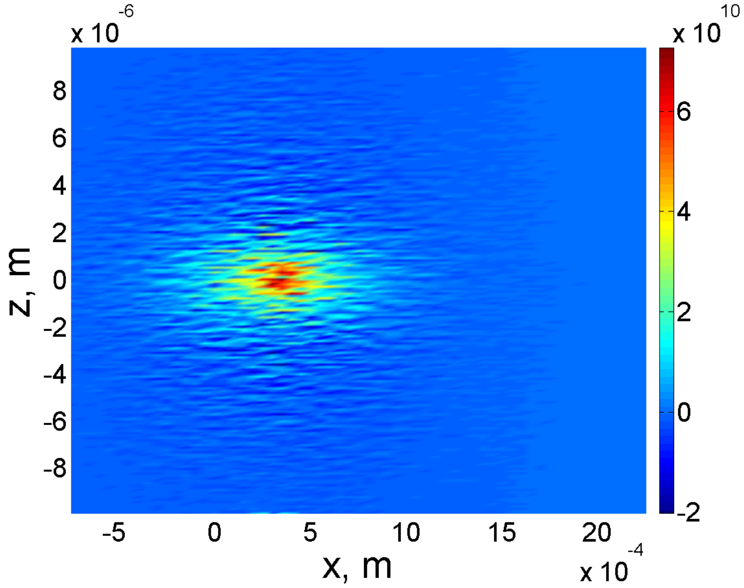

Figure 19: 2D (x and z) plot of density modulation, measured in numbers of electrons per square meters, by reference energy ion 0.5σ off the center of the Gaussian electron beam in linear focusing field

Figures 20 - 23 list the results of modulation process using a stationary ion 1σ off the center of the electron beam.

We observe obvious drop in longitudinal density and velocity modulation in figure 20, compared with using ion at center of electron beam. Modulation process depends on the density of electron beam. At the location 1σ off the center of electron beam, density of electron beam drops to approximately 60 percent of the peak density at the center, and causes the fall in modulation results. And from the figures 21 - 23, we notice that the non-symmetry in transverse direction is more clear when the ion's location moves towards the edge of the Gaussian electron beam.

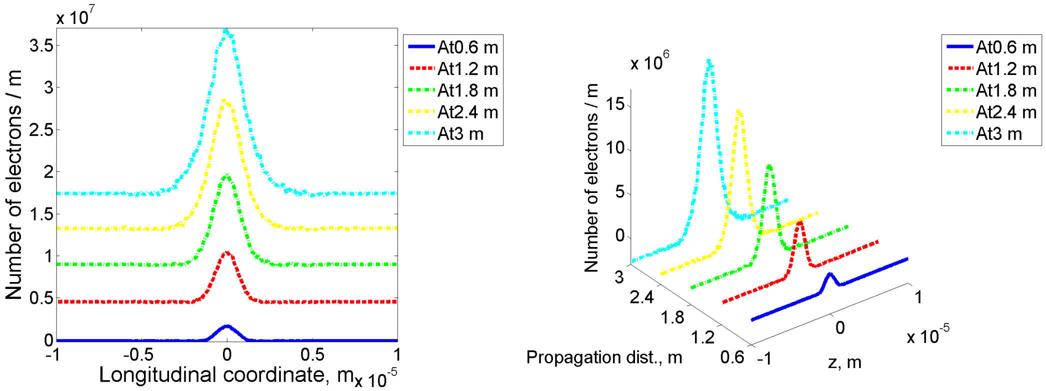

(a) Longitudinal density, 2D

(b) Longitudinal density, 3D

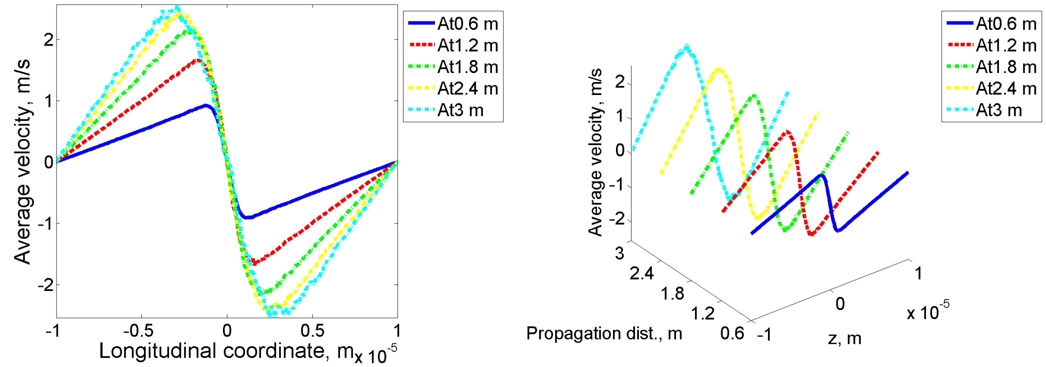

(c) Longitudinal velocity, 2D

(d) Longitudinal velocity, 3D

Figure 20: Longitudinal density and velocity modulation by reference energy ion 1σ off the center of the Gaussian electron beam in linear focusing field after 0.6m (blue, solid line), 1.2m (red, dash line), 1.8m (green, dash-dot line, 2.4m (yellow, dash-dot line) and 3m (cyan, dash-dot line)of co-propagation with electrons, curves in (a) are shifted to improve readability.

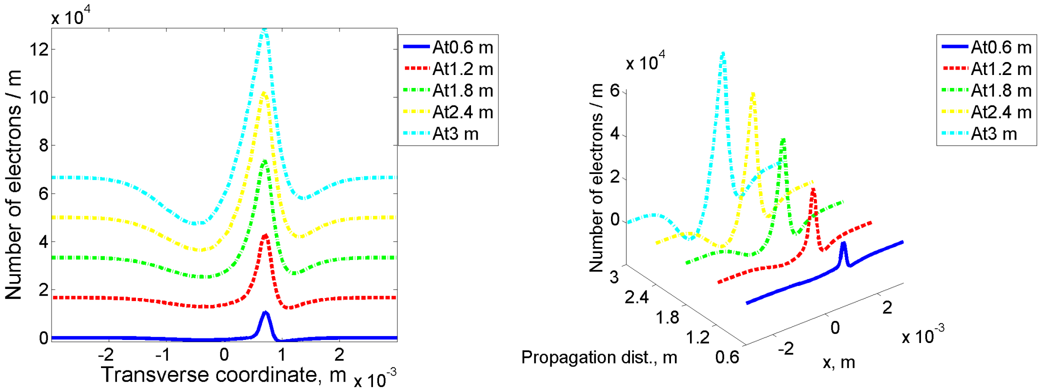

(a) Transverse density, 2D

(b) Transverse density, 3D

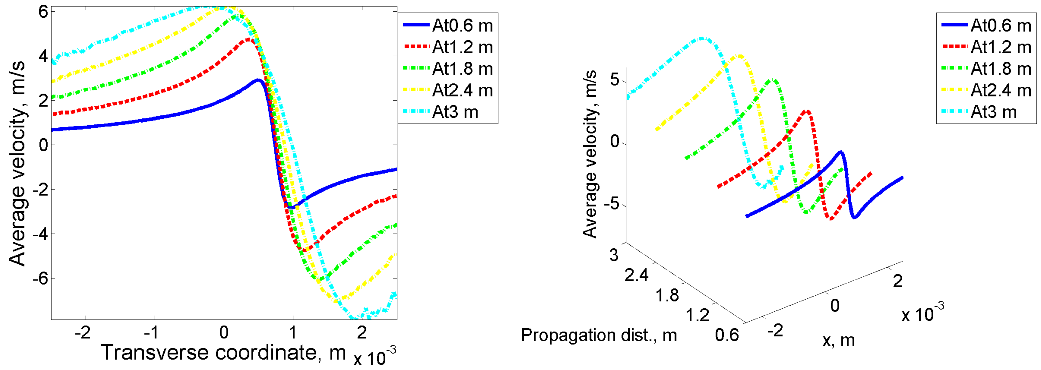

(c) Transverse velocity, 2D

(d) Transverse velocity, 3D

Figure 21: Transverse density and velocity modulation by reference energy ion 1σ off the center of the Gaussian electron beam in linear focusing field after 0.6m (blue, solid line), 1.2m (red, dash line), 1.8m (green, dash-dot line, 2.4m (yellow, dash-dot line) and 3m (cyan, dash-dot line)of co-propagation with electrons, curves in (a) are shifted to improve readability.

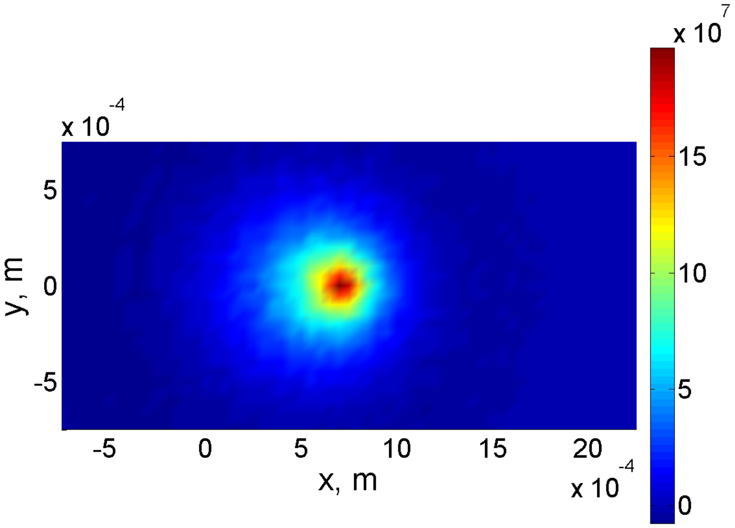

Figure 22: 2D (x and y) plot of density modulation, measured in numbers of electrons per square meters, by reference energy ion 1σ off the center of the Gaussian electron beam in linear focusing field

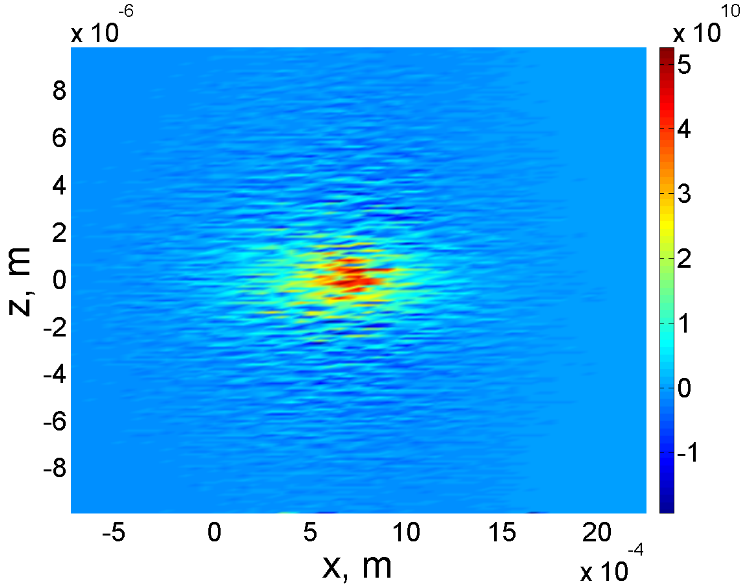

Figure 23: 2D (x and z) plot of density modulation, measured in numbers of electrons per square meters, by reference energy ion 1σ off the center of the Gaussian electron beam in linear focusing field

Figure 24 - 27 give results of modulation using stationary 1.5σ off the center of electron beam, where the electron's density is appoximately 30 percent of the peak density at the center, so the modulation drops more.

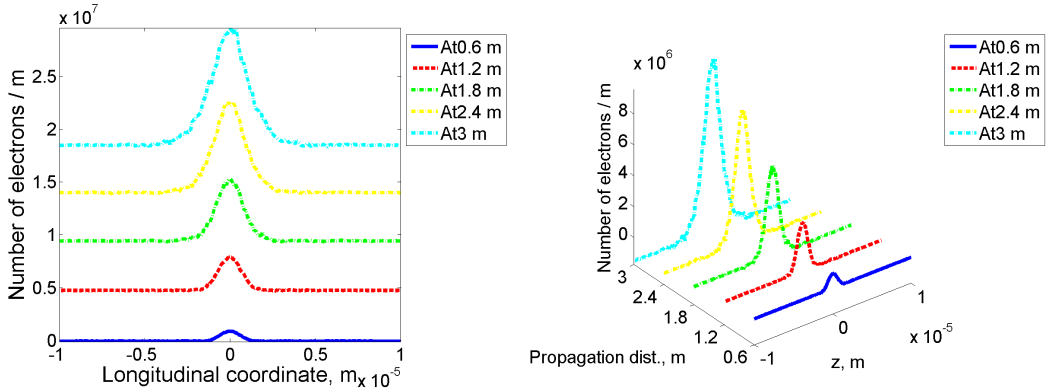

(a) Longitudinal density, 2D (b) Longitudinal density, 3D

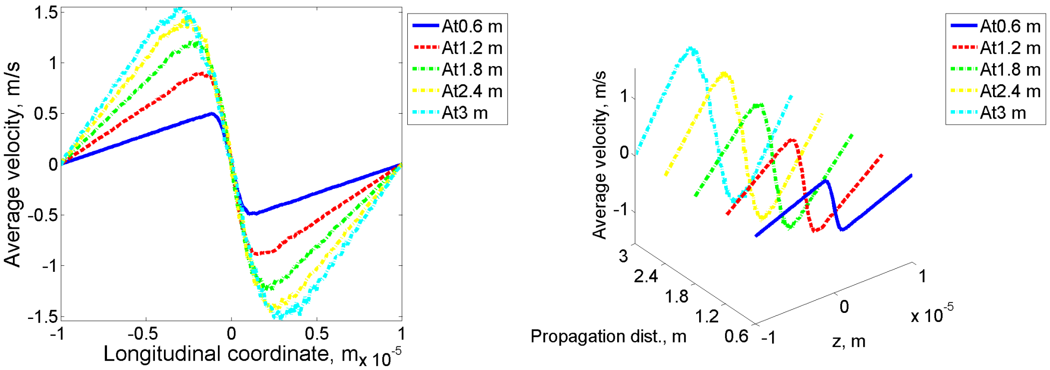

(c) Longitudinal velocity, 2D (d) Longitudinal velocity, 3D

Figure 24: Longitudinal density and velocity modulation by reference energy ion 1.5σ off the center of the Gaussian electron beam in linear focusing field after 0.6m (blue, solid line), 1.2m (red, dash line), 1.8m (green, dash-dot line, 2.4m (yellow, dash-dot line) and 3m (cyan, dash-dot line)of co-propagation with electrons, curves in (a) are shifted to improve readability.

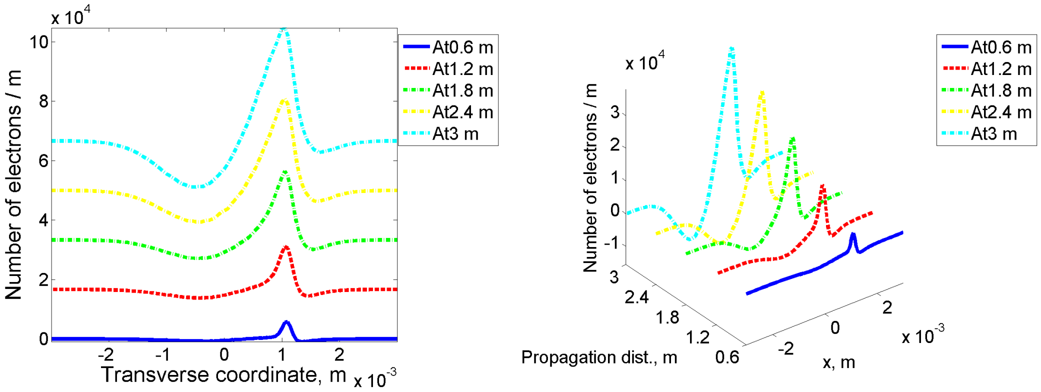

(a) Transverse density, 2D

(b) Transverse density, 3D

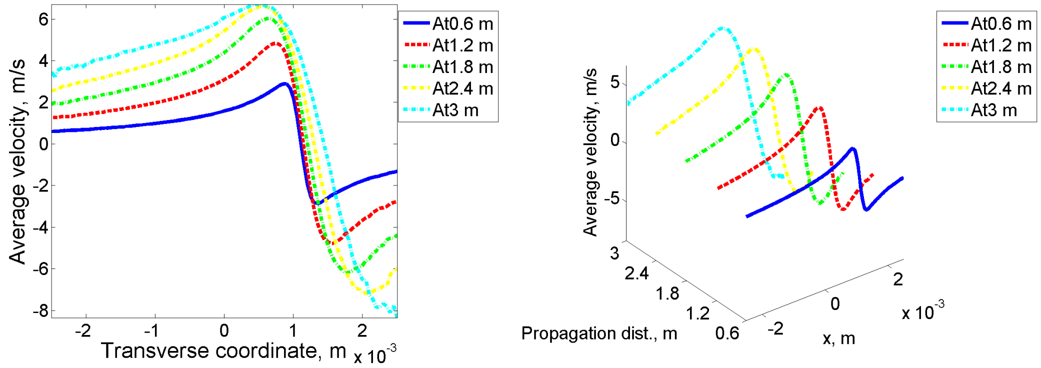

(c) Transverse velocity, 2D

(d) Transverse velocity, 3D

Figure 25: Transverse density and velocity modulation by reference energy ion 1.5σ off the center of the Gaussian electron beam in linear focusing field after 0.6m (blue, solid line), 1.2m (red, dash line), 1.8m (green, dash-dot line, 2.4m (yellow, dash-dot line) and 3m (cyan, dash-dot line)of co-propagation with electrons, curves in (a) are shifted to improve readability.

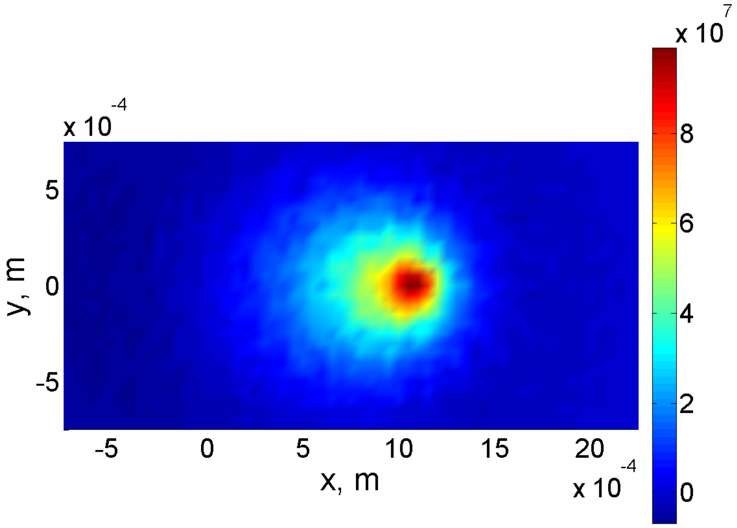

Figure 26: 2D (x and y) plot of density modulation, measured in numbers of electrons per square meters, by reference energy ion 1.5σ off the center of the Gaussian electron beam in linear focusing field

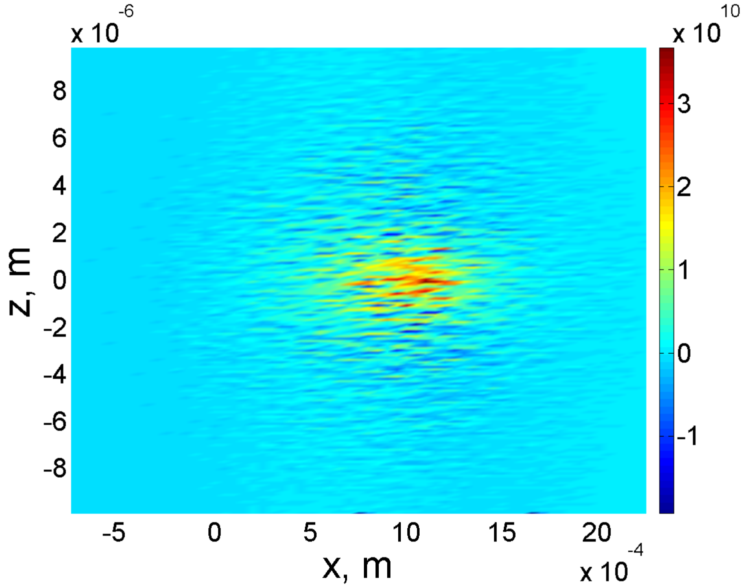

Figure 27: 2D (x and z) plot of density modulation, measured in numbers of electrons per square meters, by reference energy ion 1.5σ off the center of the Gaussian electron beam in linear focusing field

Finally we put the ion 2σ away from the center of the electron beam, where the electrons' density is only 13 percent of the peak density at the center, and the simulations results are given in figures 28 - 31. Modulation becomes very weak because the density of electrons is too low at ion's location to provide sufficient modulation, at this temperature level. The non-symmetry is obviously seen in figure 30. Figure 31 contains more noise because of insufficient number of computational particles for electrons.

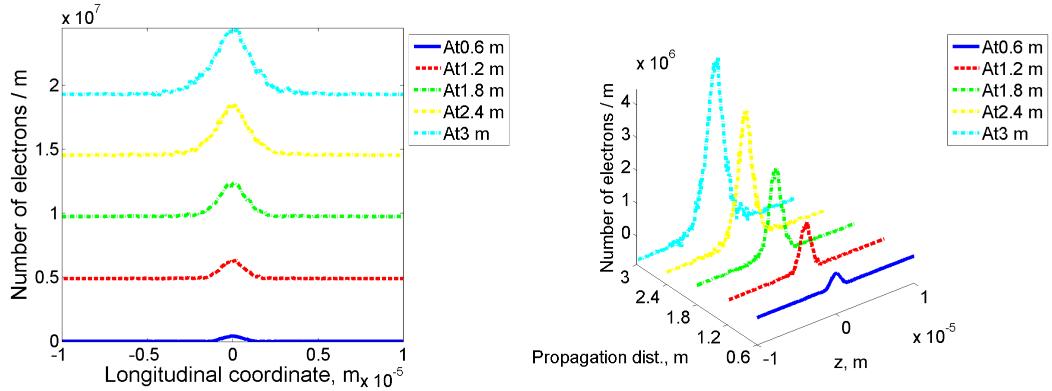

(a) Longitudinal density, 2D (b) Longitudinal density, 3D

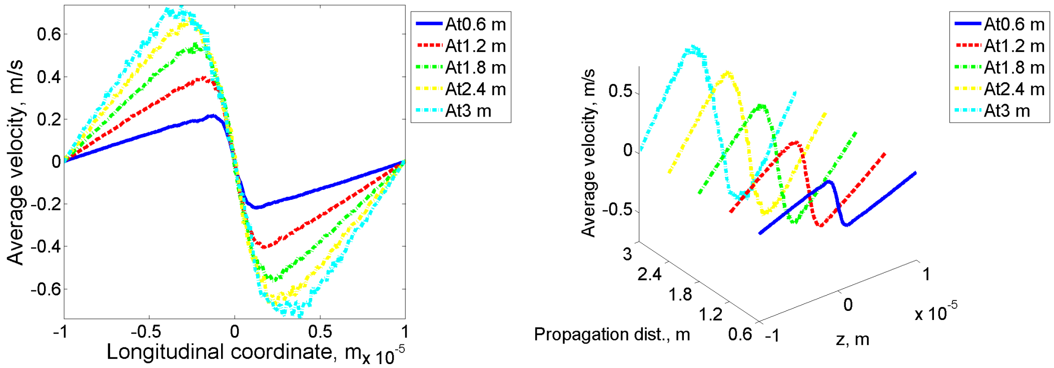

(c) Longitudinal velocity, 2D (d) Longitudinal velocity, 3D

Figure 28: Longitudinal density and velocity modulation by reference energy ion 2σ off the center of the Gaussian electron beam in linear focusing field after 0.6m (blue, solid line), 1.2m (red, dash line), 1.8m (green, dash-dot line, 2.4m (yellow, dash-dot line) and 3m (cyan, dash-dot line)of co-propagation with electrons, curves in (a) are shifted to improve readability.

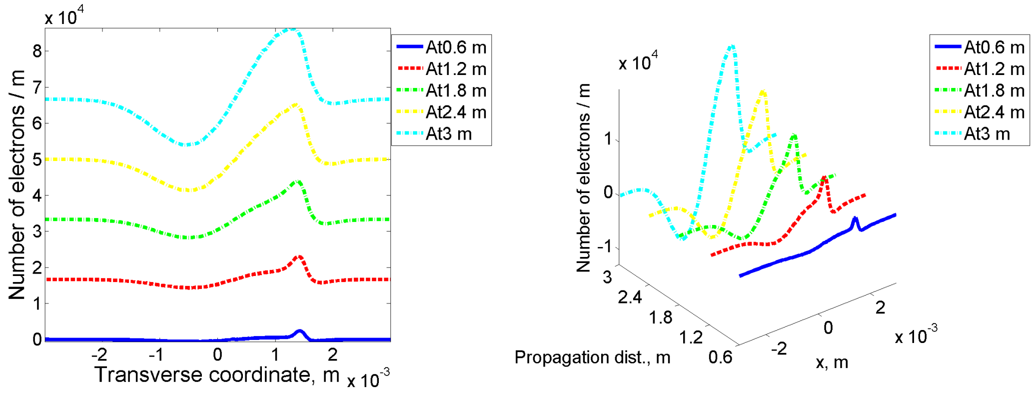

(a) Transverse density, 2D

(b) Transverse density, 3D

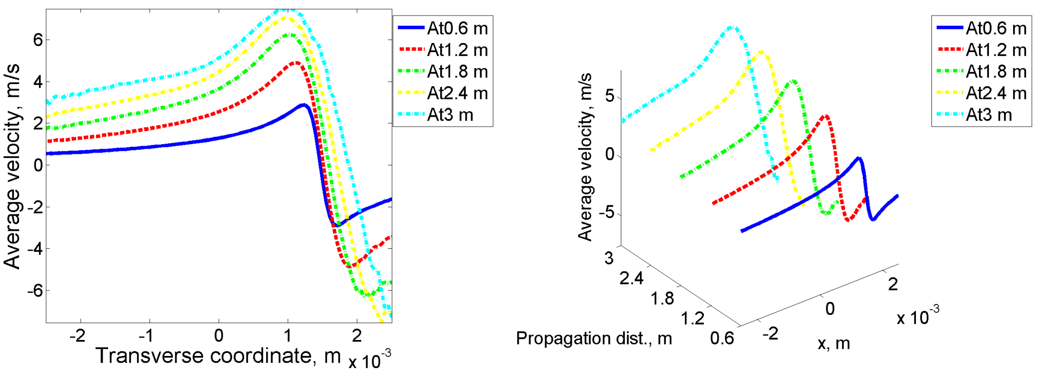

(c) Transverse velocity, 2D

(d) Transverse velocity, 3D

Figure 29: Transverse density and velocity modulation by reference energy ion 2σ off the center of the Gaussian electron beam in linear focusing field after 0.6m (blue, solid line), 1.2m (red, dash line), 1.8m (green, dash-dot line, 2.4m (yellow, dash-dot line) and 3m (cyan, dash-dot line)of co-propagation with electrons, curves in (a) are shifted to improve readability.

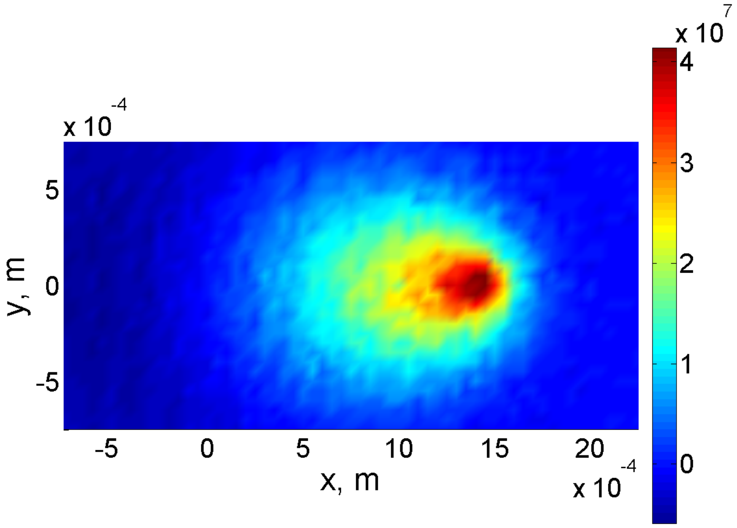

Figure 30: 2D (x and y) plot of density modulation, measured in numbers of electrons per square meters, by reference energy ion 2σ off the center of the Gaussian electron beam in linear focusing field

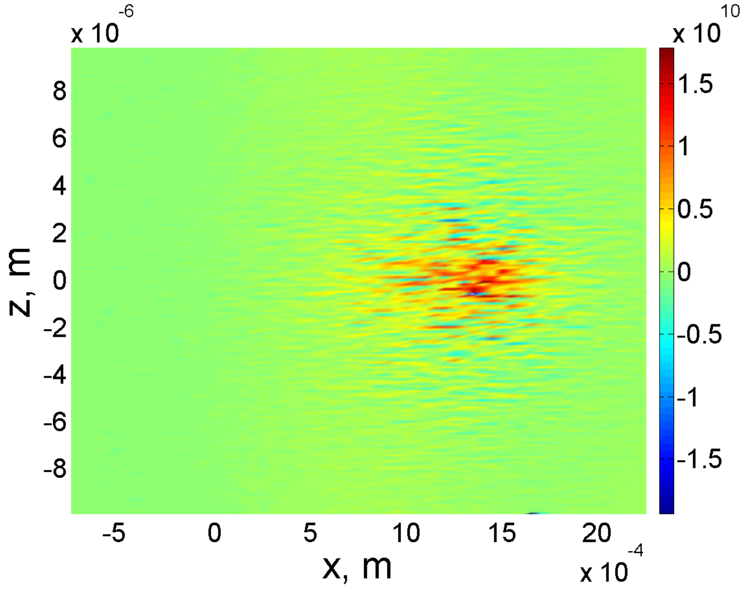

Figure 31: 2D (x and z) plot of density modulation, measured in numbers of electrons per square meters, by reference energy ion 2σ off the center of the Gaussian electron beam in linear focusing field

We collect modulation results at the final stage of modulator using a stationary ion at various transverse locations, and present the comparisons in figure 32. When the ion's location moves towards the edge of the Gaussian electron beam, density modulation drops along with the drop of the electron beam's density.

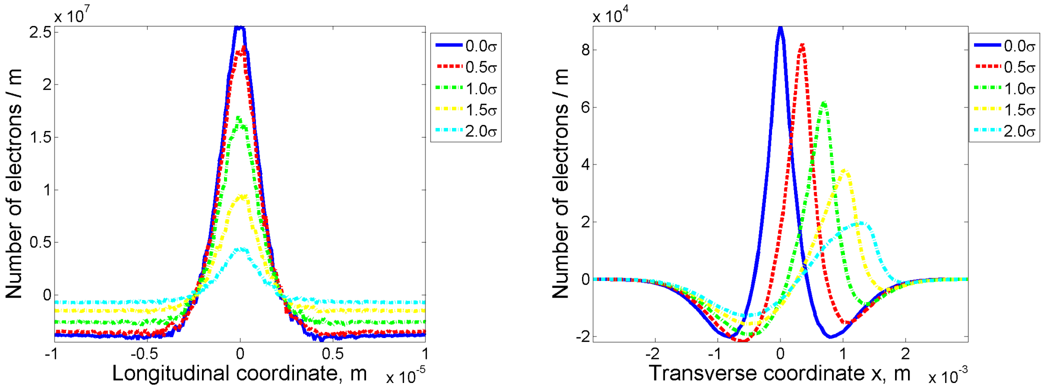

(a) Longitudinal density (b) Transverse density

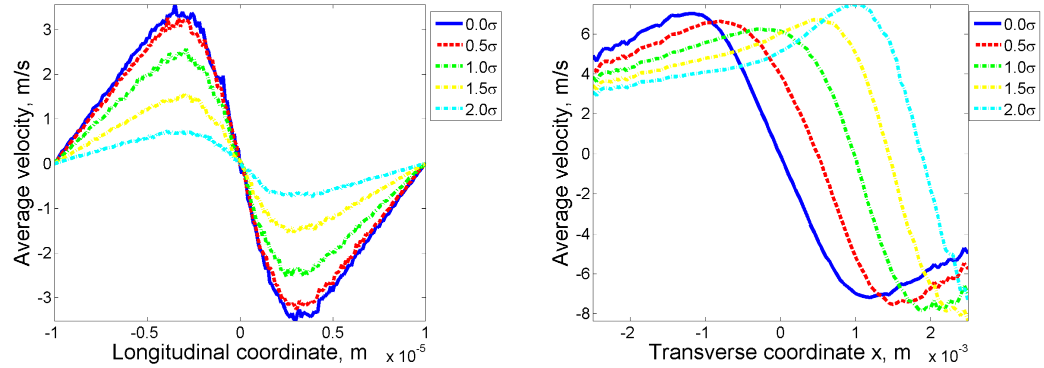

(c) Longitudinal velocity (d) Transverse velocity

Figure 32: Density and velocity modulation by reference energy ion with various distances off the center of the Gaussian electron beam in linear focusing field after 3m of co-propagation with electrons.

In next simulations, we study the dependence of modulation process on ion's velocity. We repeat the modulator simulations using a moving ion with velocity of $v_{0,z} = 1 \cdot \beta_z$ with respect to the electron cloud in the co-moving frame. β_z is the characteristic velocity amplitudes in longitudinal direction for kappa-2 thermal velocity distribution of electron beam, see equation (26). In numerical simulations, the co-moving frame is set to have the same velocity with the ion, so the ion is actually still stationary in the co-moving frame, but the whole electron beam gains a moving velocity towards the opposite direction.

We start with the the moving ion located at the center of the electron beam initially, and the results are shown in figures 33 - 36.

The results of longitudinal density and velocity modulation clearly reflect the effect of the ion's moving velocity, as the modulation signal is moving left in the modulator section.

The transverse density and velocity modulation are still symmetric because the ion's moving velocity is along longitudinal direction and the ion is located at the center of the electron beam, so is the figure 35. And figure 36 shows the non-symmetry as longitudinal direction is included.

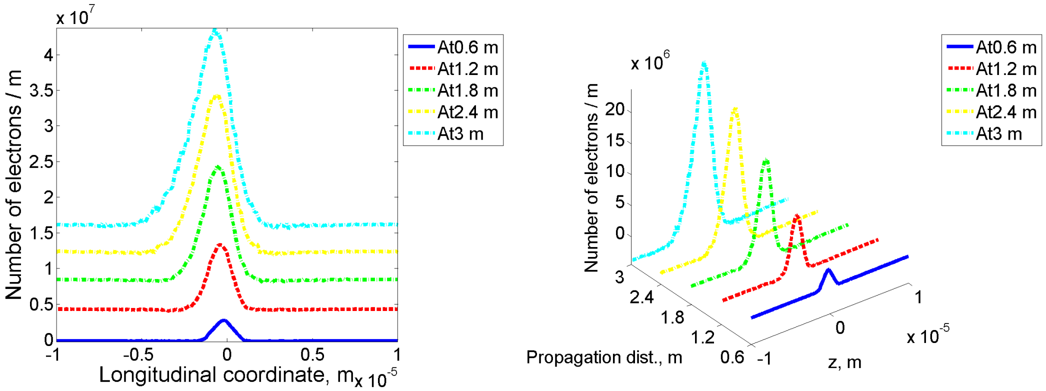

(a) Longitudinal density, 2D

(b) Longitudinal density, 3D

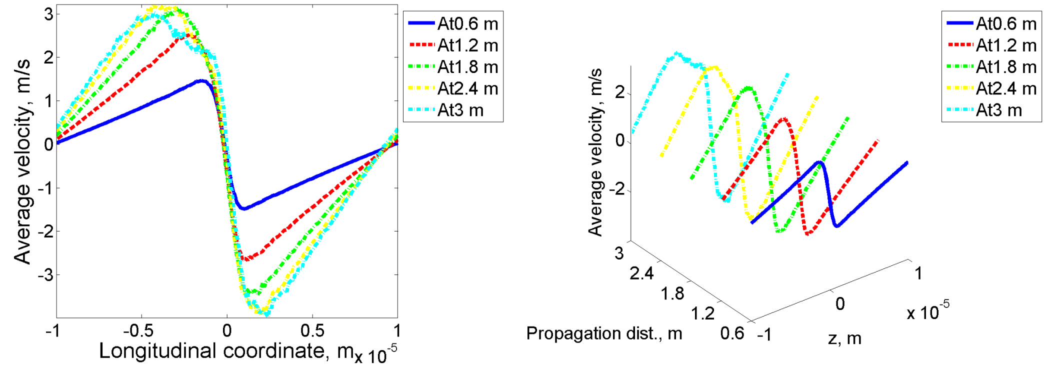

(c) Longitudinal velocity, 2D

(d) Longitudinal velocity, 3D

Figure 33: Longitudinal density and velocity modulation by moving ion in the center of the Gaussian electron beam in linear focusing field after 0.6m (blue, solid line), 1.2m (red, dash line), 1.8m (green, dash-dot line, 2.4m (yellow, dash-dot line) and 3m (cyan, dash-dot line)of co-propagation with electrons, curves in (a) are shifted to improve readability.

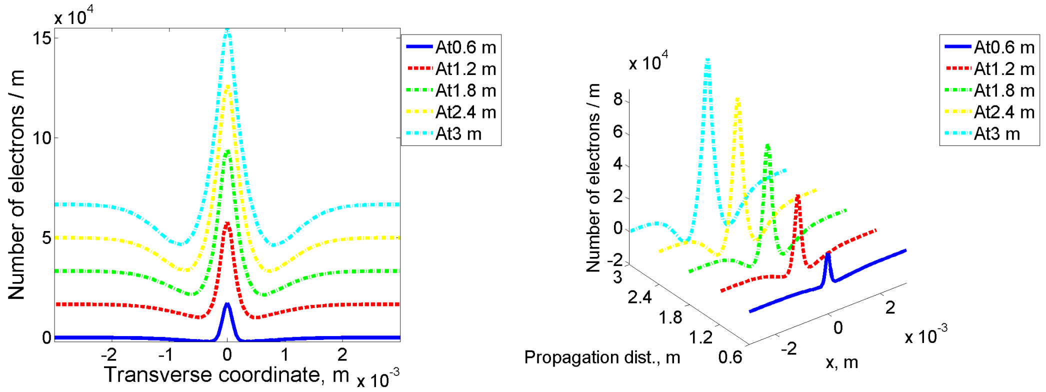

(a) Transverse density, 2D (b) Transverse density, 3D

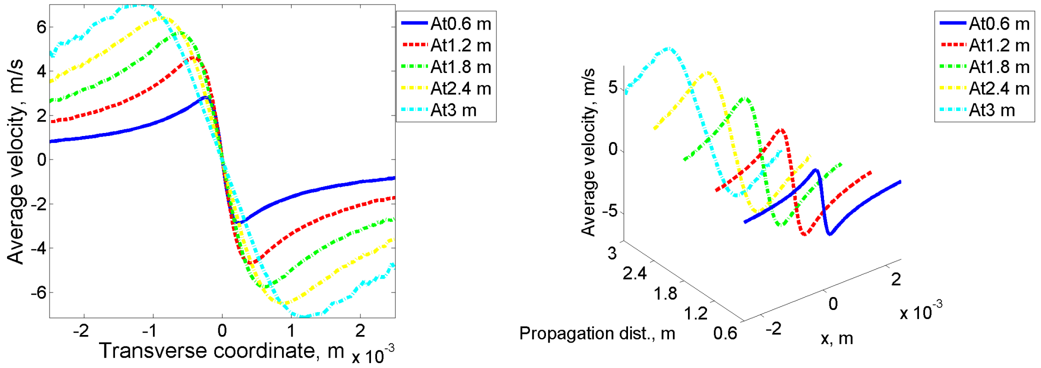

(c) Transverse velocity, 2D (d) Transverse velocity, 3D

Figure 34: Transverse density and velocity modulation by moving ion in the center of the Gaussian electron beam in linear focusing field after 0.6m (blue, solid line), 1.2m (red, dash line), 1.8m (green, dash-dot line, 2.4m (yellow, dash-dot line) and 3m (cyan, dash-dot line)of co-propagation with electrons, curves in (a) are shifted to improve readability.

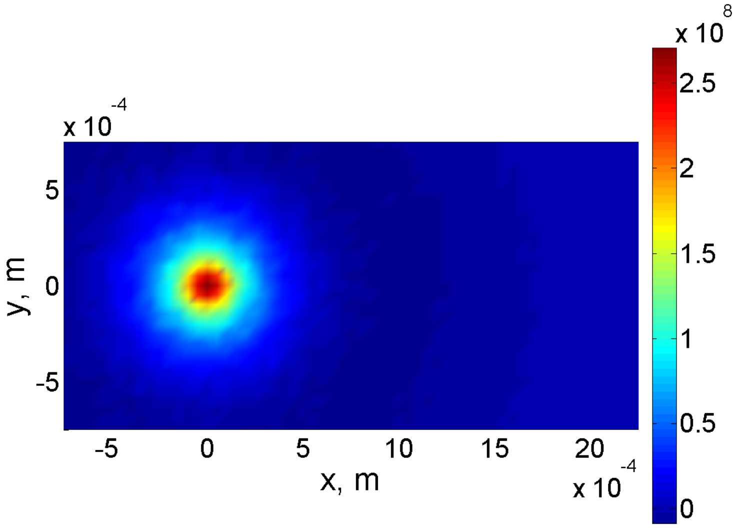

Figure 35: 2D (x and y) plot of density modulation, measured in numbers of electrons per square meters, by moving ion in the center of the Gaussian electron beam in linear focusing field

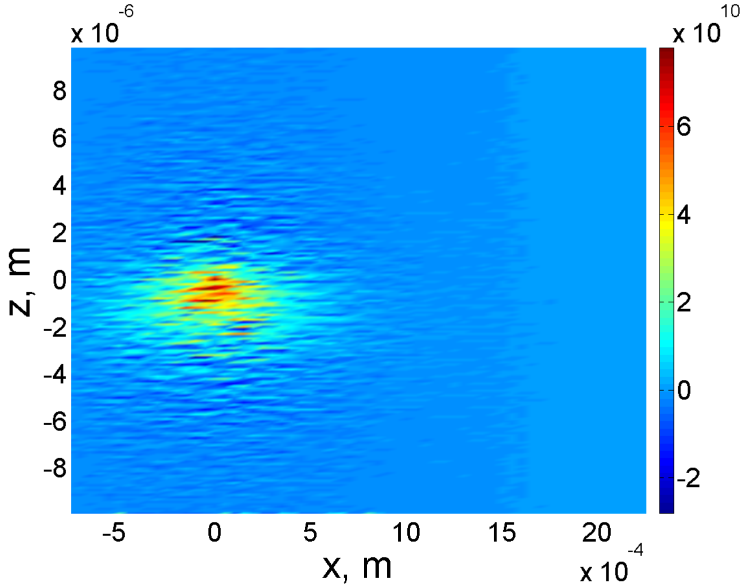

Figure 36: 2D (x and z) plot of density modulation, measured in numbers of electrons per square meters, by moving ion in the center of the Gaussian electron beam in linear focusing field

We want to study the combined effects from moving ion and off center locations on the modulation process. Similar with the simulations using stationary ion, we put the moving ion at the locations $0.5\sigma_x, 1.0\sigma_x, 1.5\sigma_x.2.0\sigma_x$ off the center of the Gaussian electron beam along x direction, where σ_x is the RMS value of the Gaussian distribution of electron beam.

Figures 37 - 40 are the modulation results using a moving ion 0.5σ off the center of the electron beam.

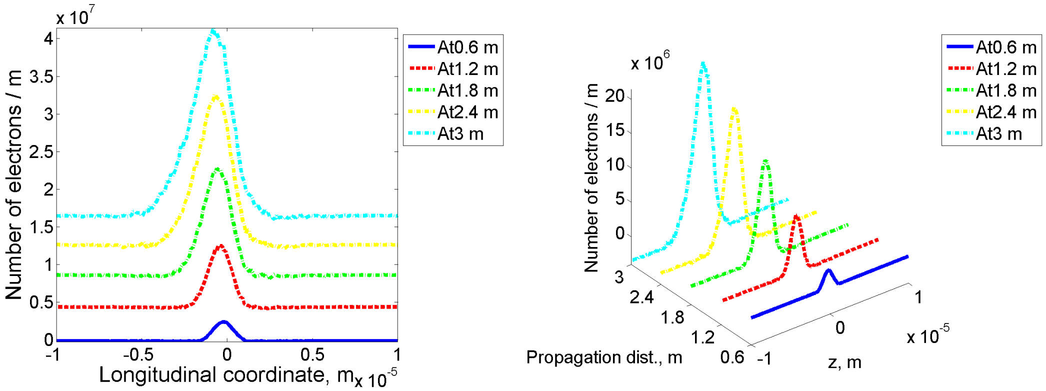

(a) Longitudinal density, 2D

(b) Longitudinal density, 3D

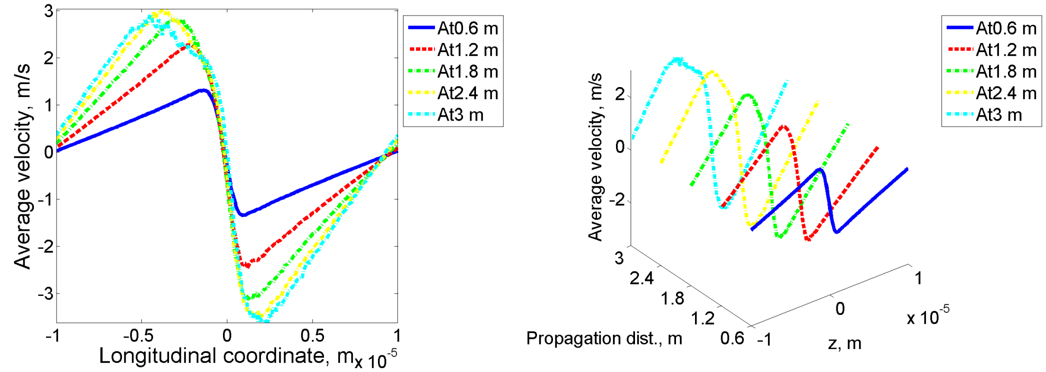

(c) Longitudinal velocity, 2D

(d) Longitudinal velocity, 3D

Figure 37: Longitudinal density and velocity modulation by moving ion 0.5σ off the center of the Gaussian electron beam in linear focusing field after 0.6m (blue, solid line), 1.2m (red, dash line), 1.8m (green, dash-dot line, 2.4m (yellow, dash-dot line) and 3m (cyan, dash-dot line)of co-propagation with electrons, curves in (a) are shifted to improve readability.

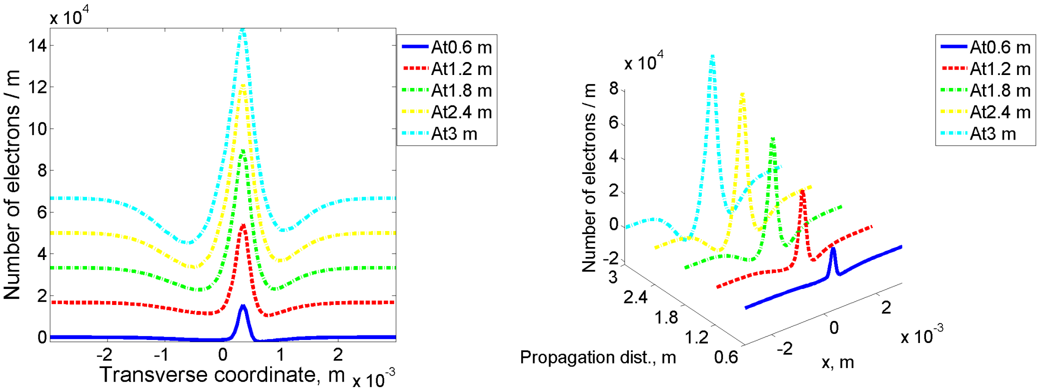

(a) Transverse density, 2D

(b) Transverse density, 3D

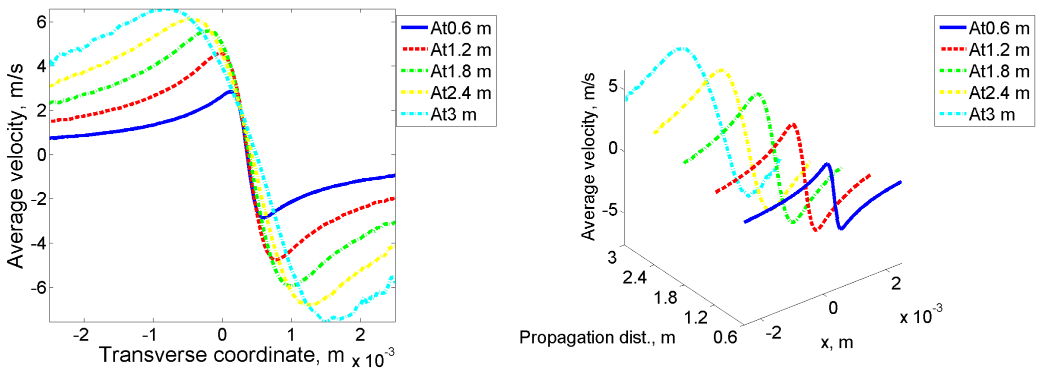

(c) Transverse velocity, 2D

(d) Transverse velocity, 3D

Figure 38: Transverse density and velocity modulation by moving ion 0.5σ off the center of the Gaussian electron beam in linear focusing field after 0.6m (blue, solid line), 1.2m (red, dash line), 1.8m (green, dash-dot line, 2.4m (yellow, dash-dot line) and 3m (cyan, dash-dot line)of co-propagation with electrons, curves in (a) are shifted to improve readability.

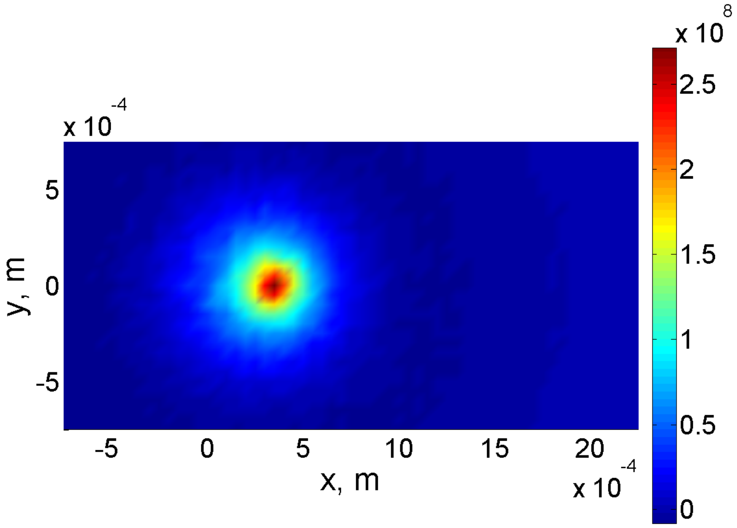

Figure 39: 2D (x and y) plot of density modulation, measured in numbers of electrons per square meters, by moving ion 0.5σ off the center of the Gaussian electron beam in linear focusing field

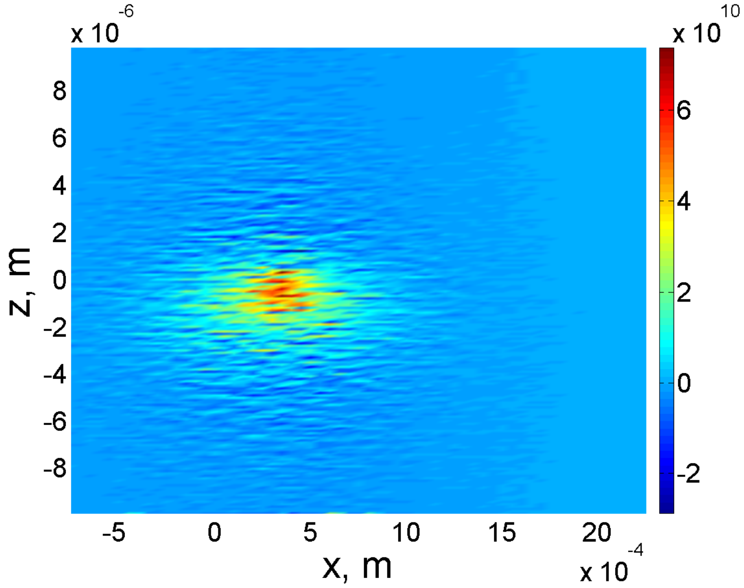

Figure 40: 2D (x and z) plot of density modulation, measured in numbers of electrons per square meters, by moving ion 0.5σ off the center of the Gaussian electron beam in linear focusing field

Figures 41 - 44 give the simulation results using a moving ion 1σ off the center of the electron beam. We can clearly observe the effect from moving velocity in longitudinal modulation plots, and effect from the off center location in transverse location, and both cause the drop in density modulation, and figure 44 shows the combined effects.

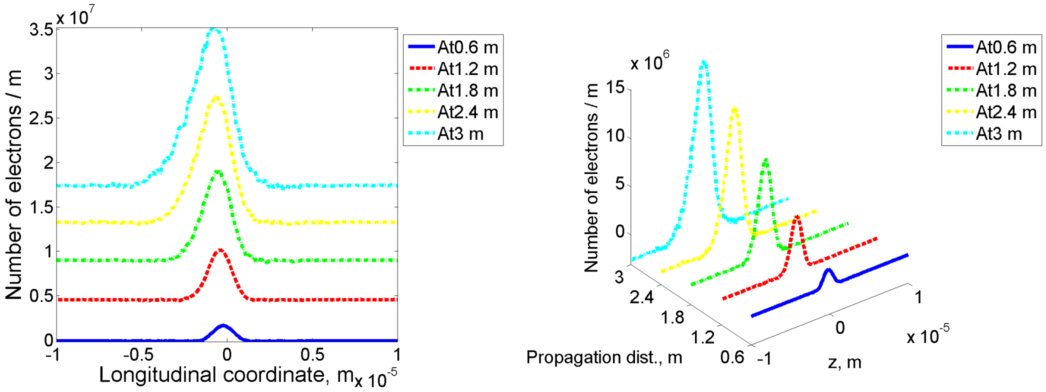

(a) Longitudinal density, 2D

(b) Longitudinal density, 3D

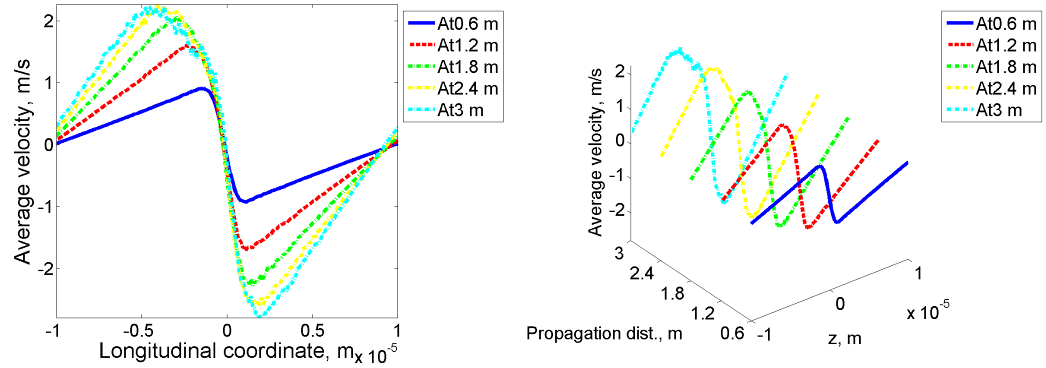

(c) Longitudinal velocity, 2D

(d) Longitudinal velocity, 3D

Figure 41: Longitudinal density and velocity modulation by moving ion 1σ off the center of the Gaussian electron beam in linear focusing field after 0.6m (blue, solid line), 1.2m (red, dash line), 1.8m (green, dash-dot line, 2.4m (yellow, dash-dot line) and 3m (cyan, dash-dot line)of co-propagation with electrons, curves in (a) are shifted to improve readability.

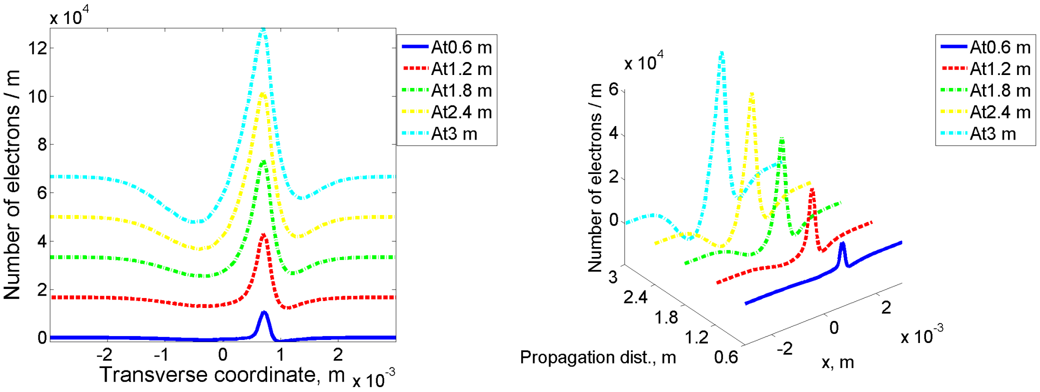

(a) Transverse density, 2D (b) Transverse density, 3D

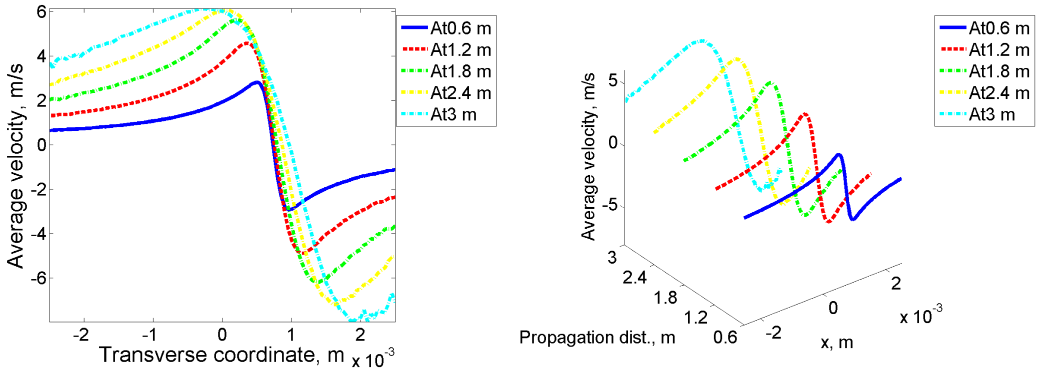

(c) Transverse velocity, 2D (d) Transverse velocity, 3D

Figure 42: Transverse density and velocity modulation by moving ion 1σ off the center of the Gaussian electron beam in linear focusing field after 0.6m (blue, solid line), 1.2m (red, dash line), 1.8m (green, dash-dot line, 2.4m (yellow, dash-dot line) and 3m (cyan, dash-dot line)of co-propagation with electrons, curves in (a) are shifted to improve readability.

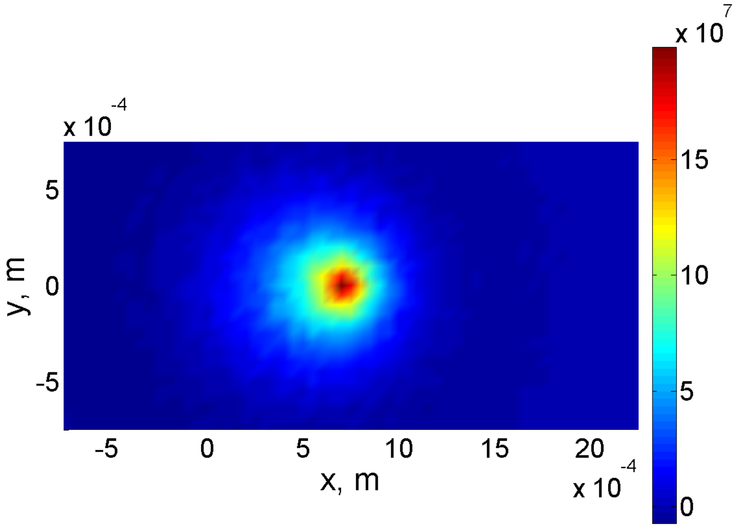

Figure 43: 2D (x and y) plot of density modulation, measured in numbers of electrons per square meters, by moving ion 1σ off the center of the Gaussian electron beam in linear focusing field

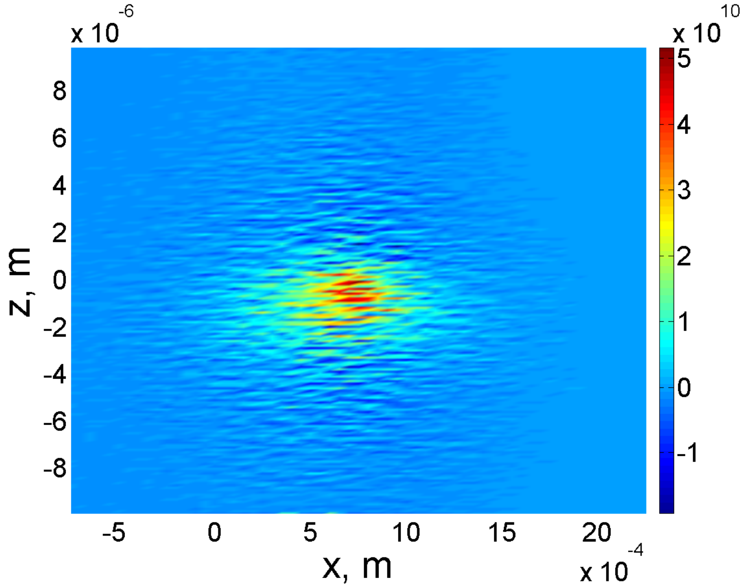

Figure 44: 2D (x and z) plot of density modulation, measured in numbers of electrons per square meters, by moving ion 1σ off the center of the Gaussian electron beam in linear focusing field

Following figures 45 - 48 are results using moving ion 1.5σ off the center of the electron beam.

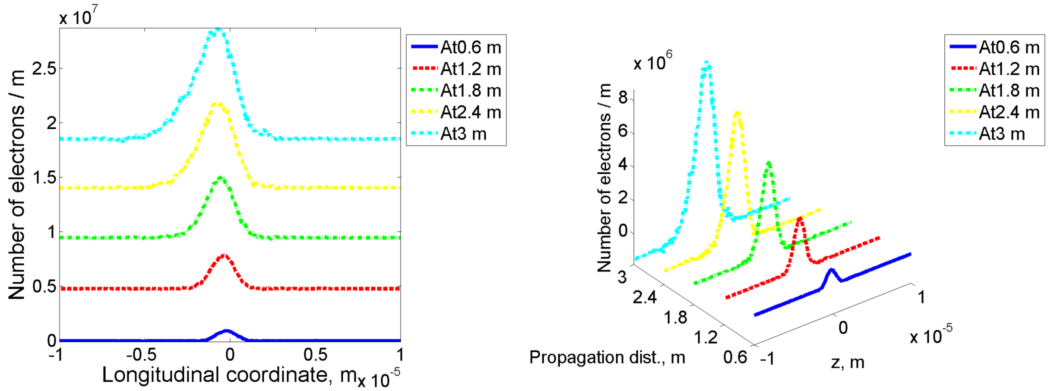

(a) Longitudinal density, 2D

(b) Longitudinal density, 3D

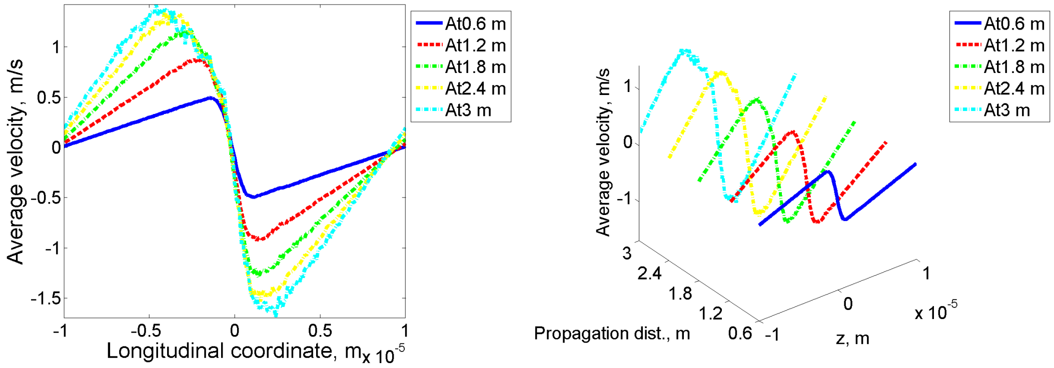

(c) Longitudinal velocity, 2D

(d) Longitudinal velocity, 3D

Figure 45: Longitudinal density and velocity modulation by moving ion 1.5σ off the center of the Gaussian electron beam in linear focusing field after 0.6m (blue, solid line), 1.2m (red, dash line), 1.8m (green, dash-dot line, 2.4m (yellow, dash-dot line) and 3m (cyan, dash-dot line)of co-propagation with electrons, curves in (a) are shifted to improve readability.

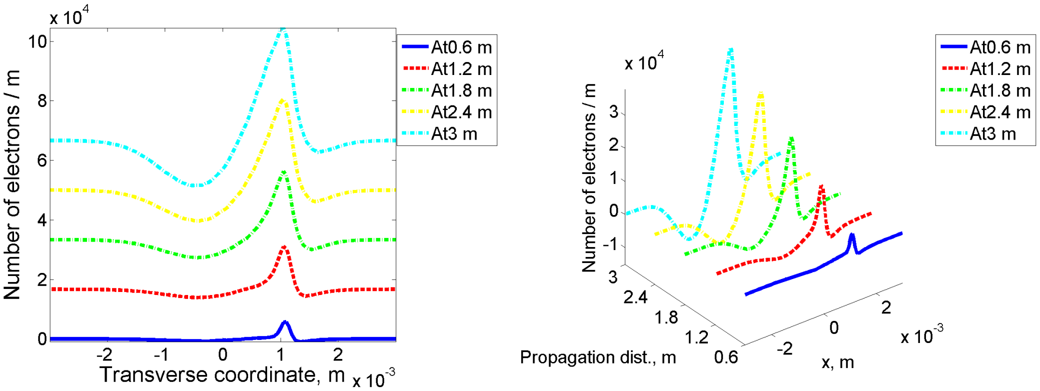

(a) Transverse density, 2D (b) Transverse density, 3D

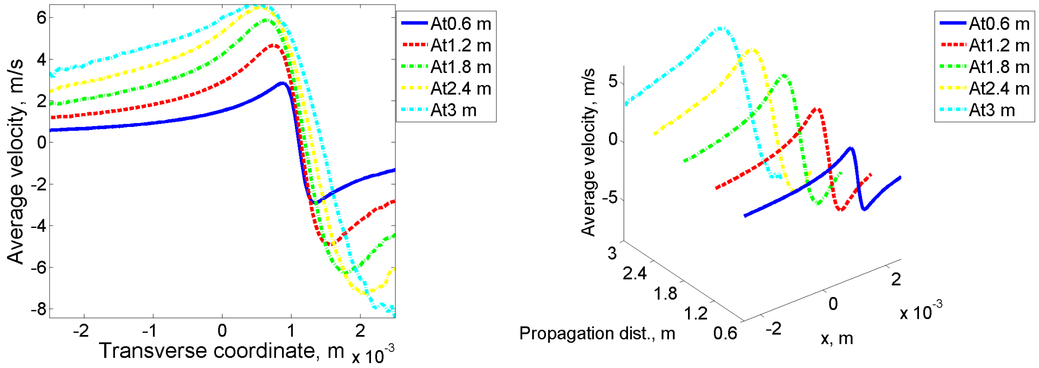

(c) Transverse velocity, 2D (d) Transverse velocity, 3D

Figure 46: Transverse density and velocity modulation by moving ion 1.5σ off the center of the Gaussian electron beam in linear focusing field after 0.6m (blue, solid line), 1.2m (red, dash line), 1.8m (green, dash-dot line, 2.4m (yellow, dash-dot line) and 3m (cyan, dash-dot line)of co-propagation with electrons, curves in (a) are shifted to improve readability.

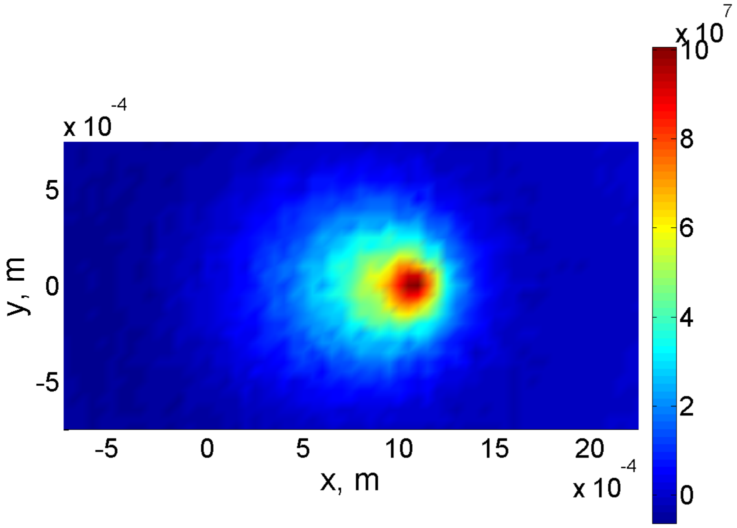

Figure 47: 2D (x and y) plot of density modulation, measured in numbers of electrons per square meters, by moving ion 1.5σ off the center of the Gaussian electron beam in linear focusing field

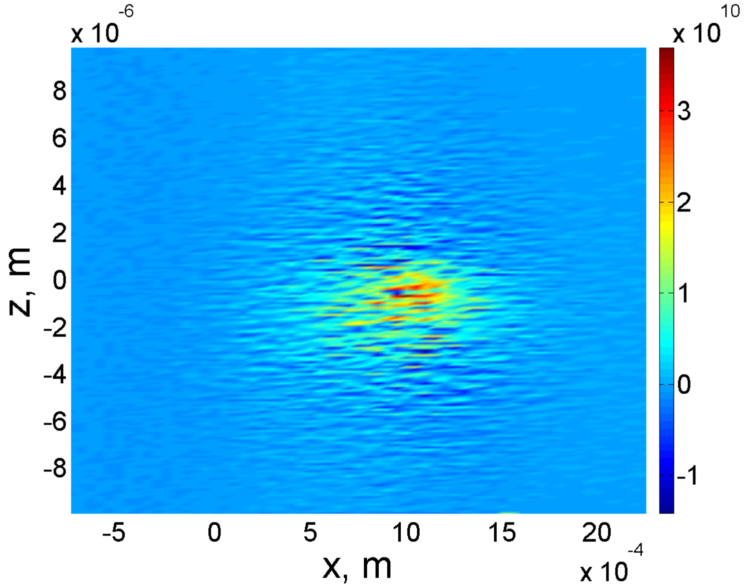

Figure 48: 2D (x and z) plot of density modulation, measured in numbers of electrons per square meters, by moving ion 1.5σ off the center of the Gaussian electron beam in linear focusing field

Finally, we put the moving ion 2σ away from the center of the electron beam. This setting gives very weak modulation signal.

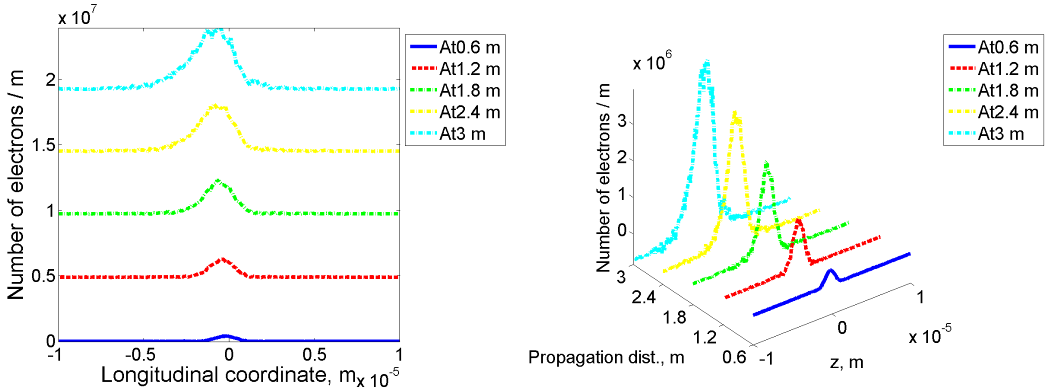

(a) Longitudinal density, 2D

(b) Longitudinal density, 3D

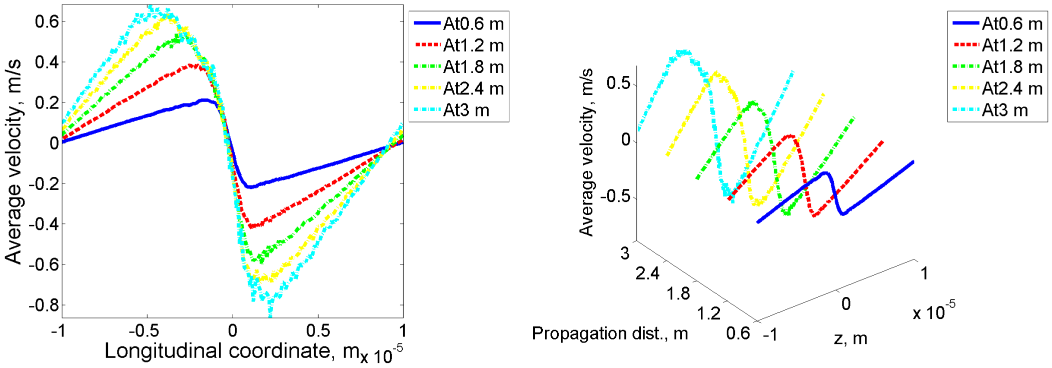

(c) Longitudinal velocity, 2D

(d) Longitudinal velocity, 3D

Figure 49: Longitudinal density and velocity modulation by moving ion 2σ off the center of the Gaussian electron beam in linear focusing field after 0.6m (blue, solid line), 1.2m (red, dash line), 1.8m (green, dash-dot line, 2.4m (yellow, dash-dot line) and 3m (cyan, dash-dot line)of co-propagation with electrons, curves in (a) are shifted to improve readability.

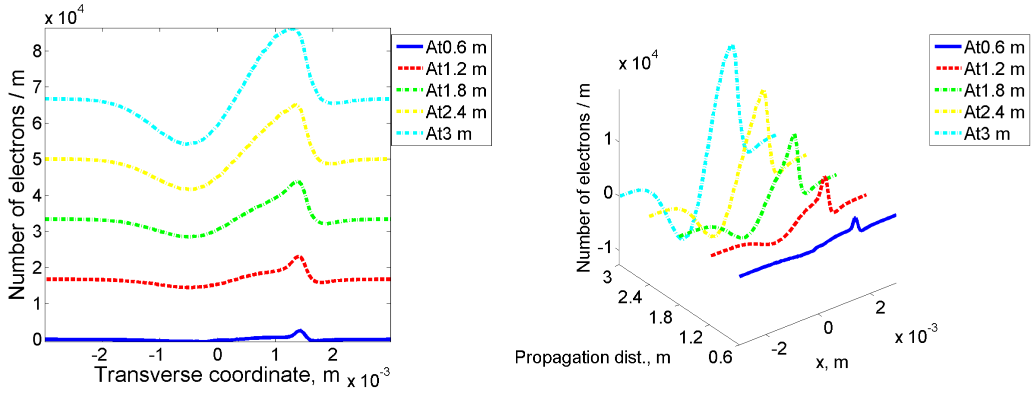

(a) Transverse density, 2D

(b) Transverse density, 3D

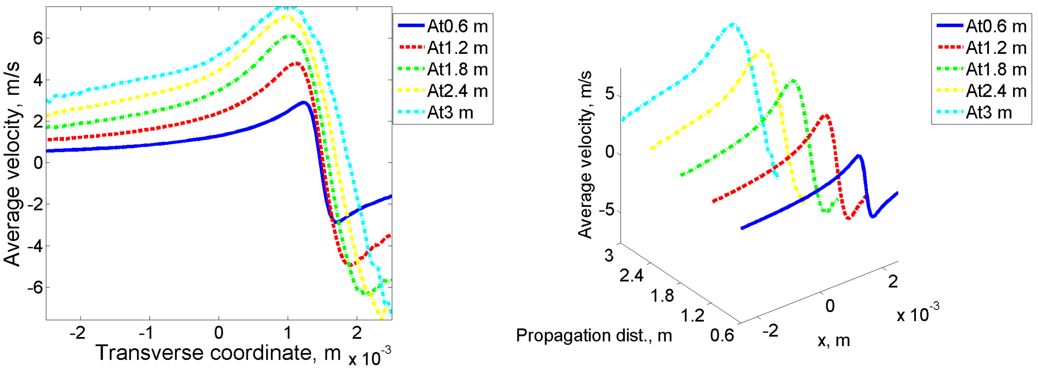

(c) Transverse velocity, 2D

(d) Transverse velocity, 3D

Figure 50: Transverse density and velocity modulation by moving ion 2σ off the center of the Gaussian electron beam in linear focusing field after 0.6m (blue, solid line), 1.2m (red, dash line), 1.8m (green, dash-dot line, 2.4m (yellow, dash-dot line) and 3m (cyan, dash-dot line)of co-propagation with electrons, curves in (a) are shifted to improve readability.

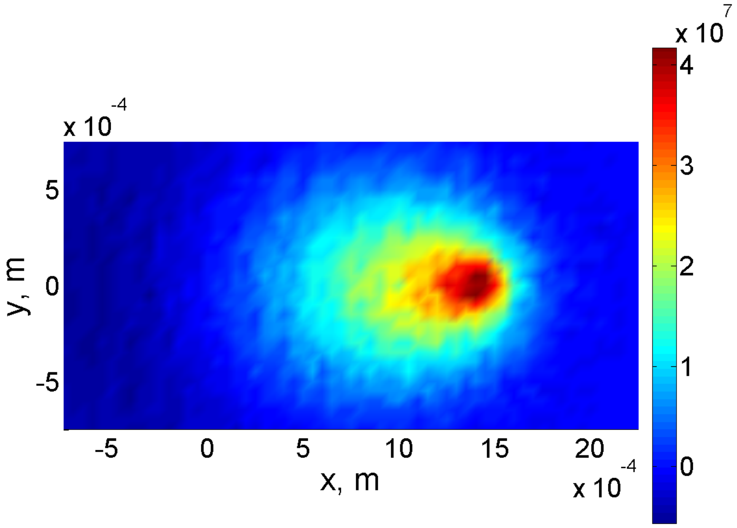

Figure 51: 2D (x and y) plot of density modulation, measured in numbers of electrons per square meters, by moving ion 2σ off the center of the Gaussian electron beam in linear focusing field

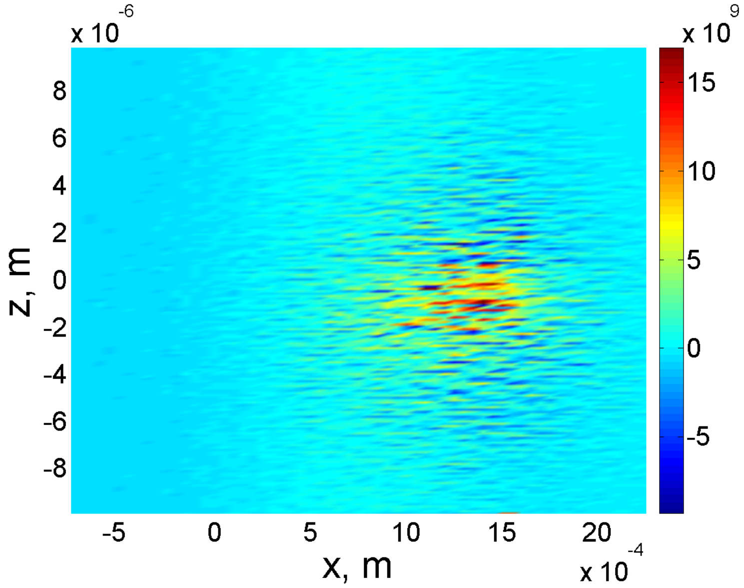

Figure 52: 2D (x and z) plot of density modulation, measured in numbers of electrons per square meters, by moving ion 2σ off the center of the Gaussian electron beam in linear focusing field

Similar with simulations using stationary ion, we collect results of the final density and velocity distribution of electron beam using moving ion at different locations, and present them in figure 53. The transverse density and velocity modulation are similar with using stationary ion, the further the ion, the lower the modulation signal. And in longitudinal density and velocity modulation, besides the similar trend, we also observe the moving of the modulation signal due to the moving velocity of ion.

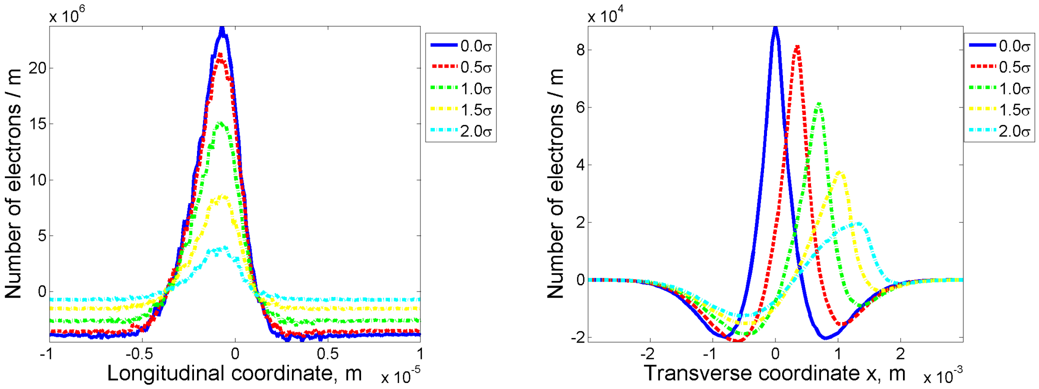

(a) Longitudinal density (b) Transverse density

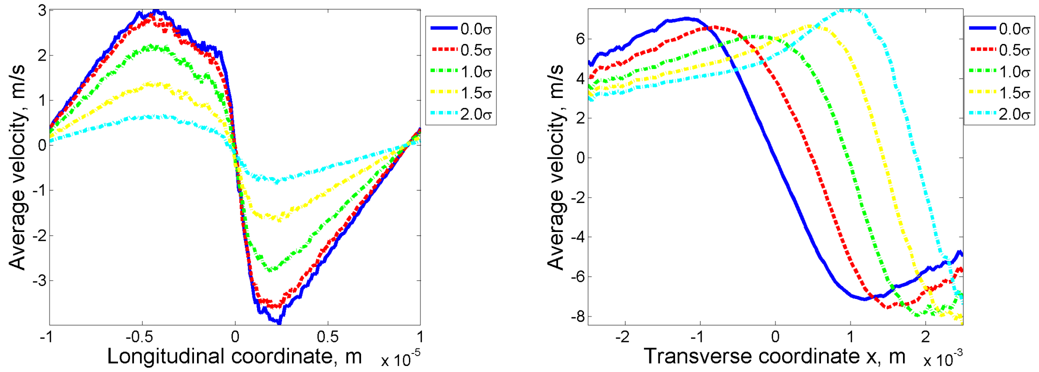

(c) Longitudinal velocity (d) Transverse velocity

Figure 53: Density and velocity modulation by moving ion with various distances off the center of the Gaussian electron beam in linear focusing field after 3m of co-propagation with electrons.

Figure 54 gives comparison between stationary and moving ion, both at the center of electron beam. The density modulation due to a moving ion, shown in figure 54, holds the non-symmetry, with a sharp gradient in the direction of the ion velocity and a long tail in the opposite direction. The longitudinal velocity modulations using a stationary ion and a moving ion give consistent results. However, the total number of electrons in the longitudinal density modulation due to the moving ion is the same as the modulation using a stationary ion. A possible reason is that, the ion moves in longitudinal direction with respect to the electron beam and the electrons are uniformly distributed in longitudinal, so the density of background electrons is the same for the stationary ion and the moving ion during the modulator section, and therefore gives the same number of modulated electrons.

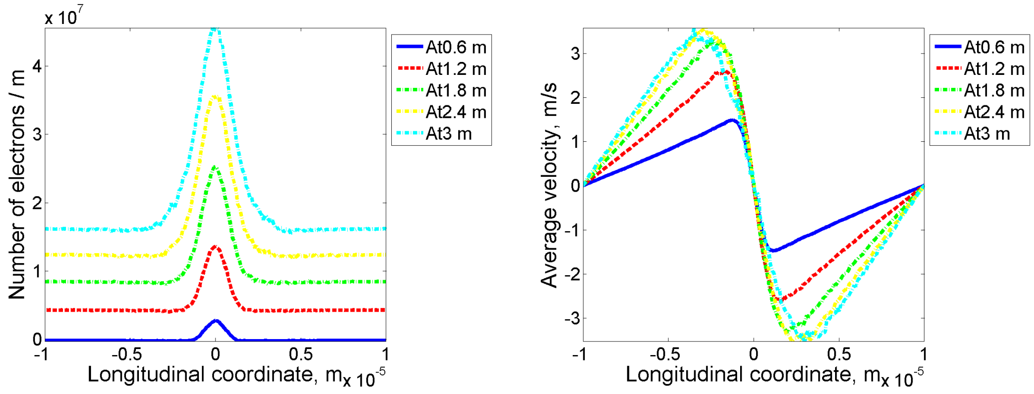

(a) Longitudinal density, stationary ion (b) Longitudinal velocity, stationary ion

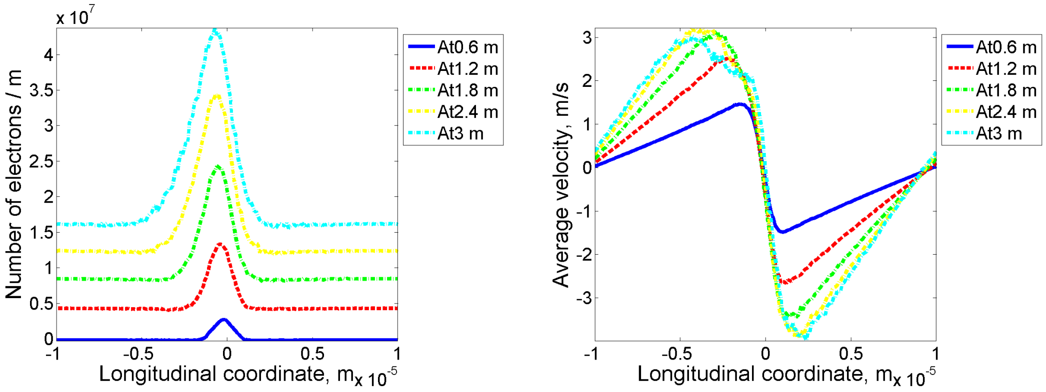

(c) Longitudinal density, moving ion (d) Longitudinal velocity, moving ion

Figure 54: Longitudinal density and velocity modulation by reference energy ion and moving ion in the center of the Gaussian electron beam in linear focusing field, curves in (a) and (c) are shifted to improve readability.

3.4 Modulator Simulations with Quadrupole Field

In this section, we present simulation results of the modulation processes for ions in Gaussian electron beams with a quadrupole magnetic field. The linear focusing field used in previous section is designed to ideally maintain the electron beam, but creating such electric field is hard in real experiments. In the coherent electron cooling experiments, magnetic field generated by a set of quadrupoles is used to keep the electron beam's transverse size.

The quadrupole magnetic field with hard edge is given in equation (35), which assumes only transverse magnetic fields, so there is discontinuities in longitudinal direction and the magnetic field is not Maxwell compatible.

$$\begin{aligned} B_y = &\quad K \cdot x \\ B_x = &\quad K \cdot y \end{aligned} \tag{35}$$

We also have used the quadrupole magnetic field with fringe in longitudinal direction, which is Maxwell compatible. The analytic expressions for quadrupole magnetic fields with fringe are studied in [21], and we use the fringe fields expressed in equations (36) and (37), where L is the longitudinal effective length of the quadrupole and b_1 is relevant to the quadrupole's transverse size which is approximately π/b_1. Our simulations demonstrate that the effect of the fringe field on the modulation process is negligibly small, and therefore we use the hard-edge quadrupole field to reduce the computation cost.

$$\begin{aligned} B_x = &\quad -\frac{G}{b_1} \cdot \left(B_{\mathrm{fr,x}}(b_1 x, b_1 y, b_1(z - \frac{1}{2}L)) + B_{\mathrm{fr,x}}(b_1 x, b_1 y, b_1(-z - \frac{1}{2}L)) \right) \\ B_y = &\quad -\frac{G}{b_1} \cdot \left(B_{\mathrm{fr,y}}(b_1 x, b_1 y, b_1(z - \frac{1}{2}L)) + B_{\mathrm{fr,y}}(b_1 x, b_1 y, b_1(-z - \frac{1}{2}L)) \right) \\ B_z = &\quad -\frac{G}{b_1} \cdot \left(B_{\mathrm{fr,z}}(b_1 x, b_1 y, b_1(z - \frac{1}{2}L)) - B_{\mathrm{fr,z}}(b_1 x, b_1 y, b_1(-z - \frac{1}{2}L)) \right) \end{aligned} \tag{36}$$

$$
\begin{aligned}
B_{\mathrm{fr,x}}(x,y,z) = &\ \frac{1}{4}\left(-y - 2\arctan\left(-\frac{\sin(y)}{e^{-z}+\cos(y)}\right) + \frac{y\sinh(z)}{\cos(x)+\cosh(z)}\right) \\
B_{\mathrm{fr,y}}(x,y,z) = &\ \frac{1}{4}\left(-x - 2\arctan\left(-\frac{\sin(x)}{e^{-z}+\cos(x)}\right) + \frac{x\sinh(z)}{\cos(y)+\cosh(z)}\right) \\
B_{\mathrm{fr,z}}(x,y,z) = &\ \frac{1}{4}\left(\frac{y\sin(x)}{\cos(x)+\cosh(z)} + \frac{x\sin(y)}{\cos(y)+\cosh(z)}\right)
\end{aligned}
\tag{37}
$$

Setup of the quadrupole focusing field is relevant to the experiments in RHIC at BNL. We let the electron beam propagate through the quadrupole fields in modulator of coherent electron cooling, and track the beta functions of the beam to study the effect from the quadrupoles on the electron beam. Figure 55 shows the changes of beta functions, which is relevant to the transverse beam size, due to the quadrupole field. We use results from code MAD-X as benchmark, where space charge effect is ignored. Simulation 1 is performed with code SPACE, and uses the electron beam with space charge effect turned off to make fair comparison with MAD-X, and gives good agreement. Simulations 2 with code SPACE turns on the space charge effect, and differs from MAD-X, as space charge effect is included. Our results also demonstrate that the effect of the fringe magnetic field on the modulation process is negligibly small, so we use the quadrupole magnetic fields with hard edge in our simulations as it saves more floating point operations. We use this quadrupole field and include space charge effect for following modulator simulations.

To study the modulation process under the quadrupole magnetic fields, we start with a stationary ion located at the center of the Gaussian electron beam, and the result are presented in figures 56 - 58. In previous simulations results using linear focusing fields, we choose horizontal direction x to present modulation process in transverse directions, as the system holds radial symmetry in transverse plane. The quadrupole magnetic fields are no longer radially symmetric in the transverse plane, so we present the transverse modulation process in horizontal direction x and vertical direction y to better understand the simulations results.

In figure 56, the longitudinal density and velocity modulations are similar as the previous simulations using linear focusing fields, and are gradually built over time, but there is non-symmetry in the longitudinal velocity modulation if we take a close look. The reason is that, the quadrupole magnetic fields change each electron's transverse velocity without changing its total en-

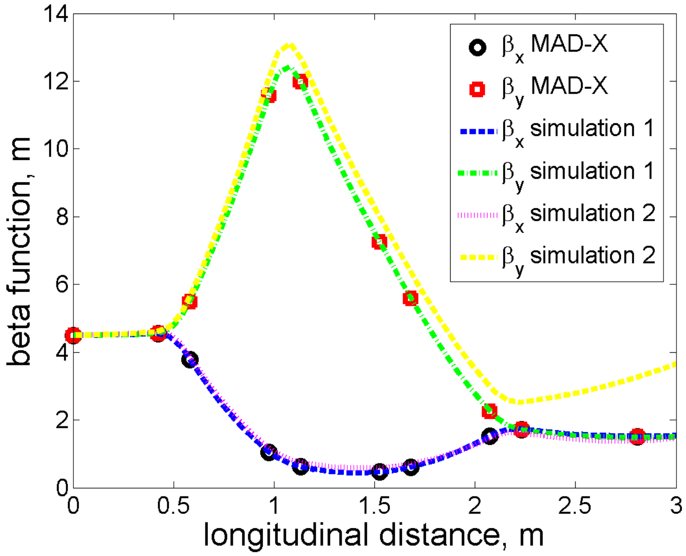

Figure 55: Comparison of MAD-X and code SPACE of transverse beta function changes in quadrupole field

ergy, so the electron beam's longitudinal velocity is also affected during the modulation process, which is similar as using a moving ion. But note that, the longitudinal velocity difference between the electron beam and the ion is constant in previous moving ion simulations under linear focusing fields, and is changing under the quadrupole magnetic fields.

In figure 57, the transverse modulation in x direction is quite different from the simulations using linear focusing fields. The transverse density modulation does not grow over time, but increases and decreases during the modulation process. The transverse velocity modulation does not always show the attraction effect from ion, but has reverse slopes at several locations. The reason for these behaviors in transverse modulations process is the quadrupole magnetic fields. The quadrupole fields could cause the phase advance of the electron beam in the transverse phase space and nonlinearity in the space charge effect of the electron beam, especially at the locations where the electron beam's transverse size is extremely small. The beta function in x direction is very small during the modulation process, as is shown in figure 55. With such small transverse beam size, quadrupole magnetic fields have very strong effects on the electron beam's distribution in transverse phase

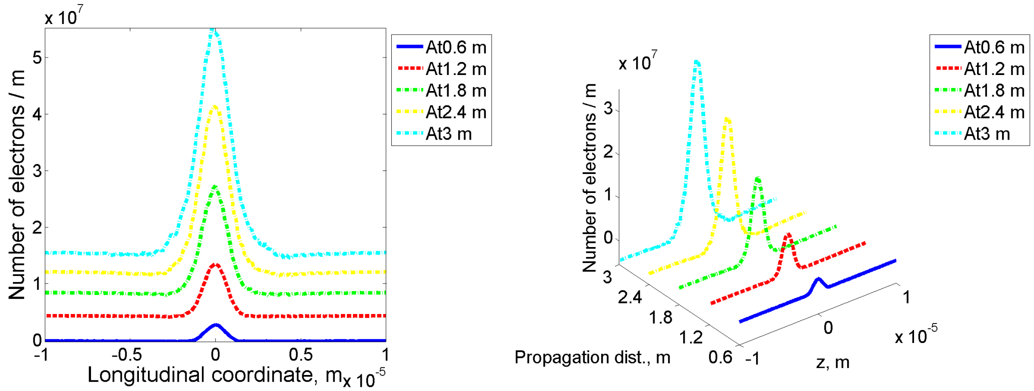

(a) Longitudinal density, 2D

(b) Longitudinal density, 3D

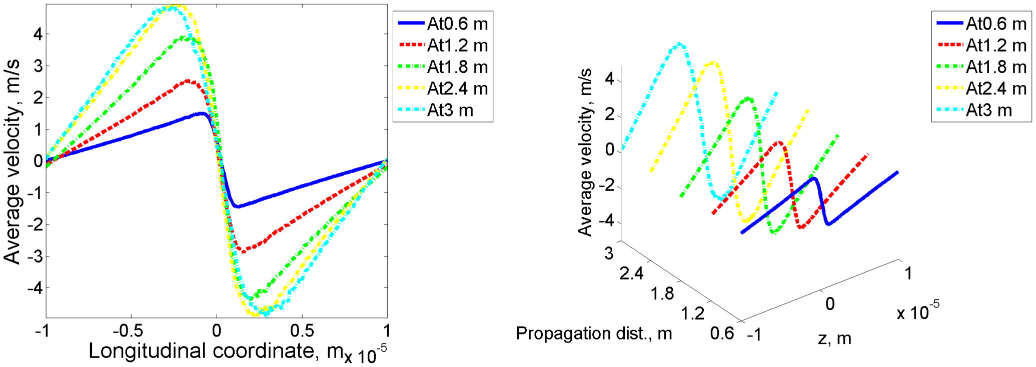

(c) Longitudinal velocity, 2D

(d) Longitudinal velocity, 3D

Figure 56: Longitudinal density and velocity modulation by reference energy ion in the center of the Gaussian electron beam in quadrupole focusing field after 0.6m (blue, solid line), 1.2m (red, dash line), 1.8m (green, dash-dot line, 2.4m (yellow, dash-dot line) and 3m (cyan, dash-dot line)of co-propagation with electrons, curves in (a) are shifted to improve readability.

space. The modulation process in y, shown in figure 58 also supports this explanation. At initial stages of modulator, beta function in y is increasing, so the quadrupole fields do not affect the modulation process in y direction that strong. At late stage, beta function in y keeps decreasing, as is shown in figure 55, we can observe the effects from the quadrupole magnetic fields, the drop in transverse density modulation and the reverse slope in transverse velocity modulation.

We will continue presenting the simulation results of modulation process using quadrupole magnetic fields in this section, and a more detailed study of phase advance due to the quadrupole fields is presented in the next section.

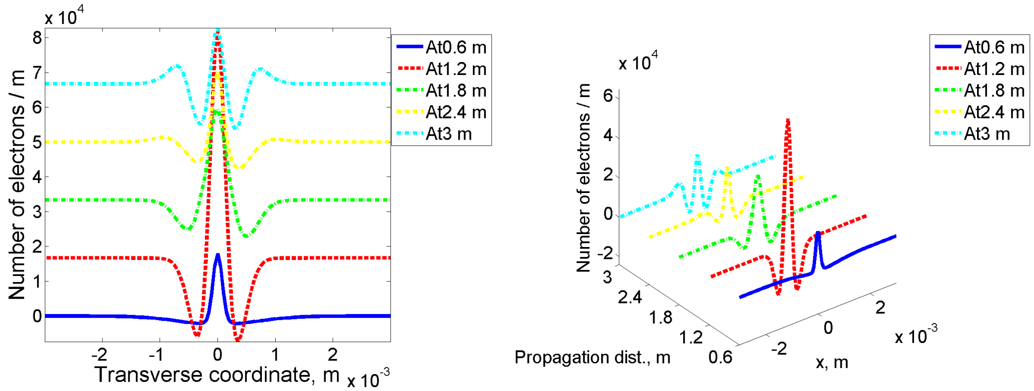

(a) Transverse (x) density, 2D

(b) Transverse (x) density, 3D

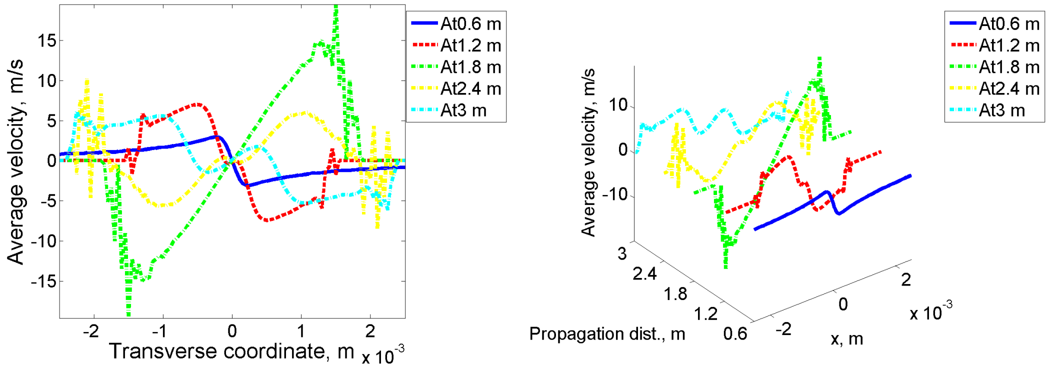

(c) Transverse (x) velocity, 2D

(d) Transverse (x) velocity, 3D

Figure 57: Transverse (x) density and velocity modulation by reference energy ion in the center of the Gaussian electron beam in quadrupole focusing field after 0.6m (blue, solid line), 1.2m (red, dash line), 1.8m (green, dash-dot line, 2.4m (yellow, dash-dot line) and 3m (cyan, dash-dot line)of co-propagation with electrons, curves in (a) are shifted to improve readability.

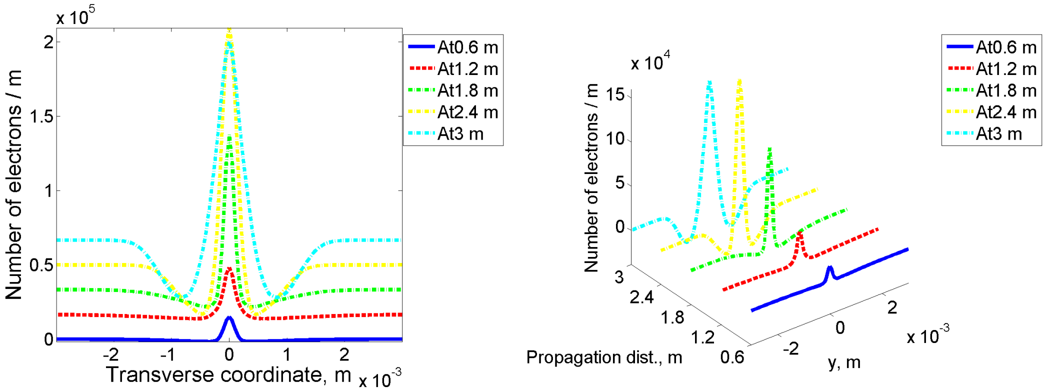

(a) Transverse (y) density, 2D

(b) Transverse (y) density, 3D

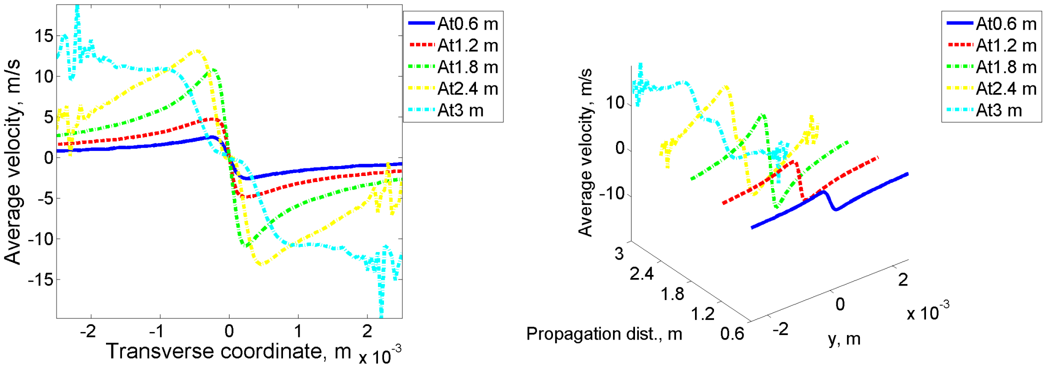

(c) Transverse (y) velocity, 2D

(d) Transverse (y) velocity, 3D

Figure 58: Transverse (y) density and velocity modulation by reference energy ion in the center of the Gaussian electron beam in quadrupole focusing field after 0.6m (blue, solid line), 1.2m (red, dash line), 1.8m (green, dash-dot line, 2.4m (yellow, dash-dot line) and 3m (cyan, dash-dot line)of co-propagation with electrons, curves in (a) are shifted to improve readability.

Similar with the simulations using linear focusing fields, we study the modulation process with various positions for stationary ion, and typical ion locations are $0.0\sigma_x, 0.5\sigma_x, 1.0\sigma_x, 1.5\sigma_x, 2.0\sigma_x$ off the center of the Gaussian electron beam. The system with quadrupole focusing field does not hold radial symmetry, and each direction for off-center locations gives different modulation results. In this study, we choose two typical directions, the horizontal x and the vertical y, and the off center locations of ion could be along x and y.

Figures 59 - 70 list the simulations results of modulation process using a stationary ion at various off-center locations along x direction in the quadrupole focusing field.

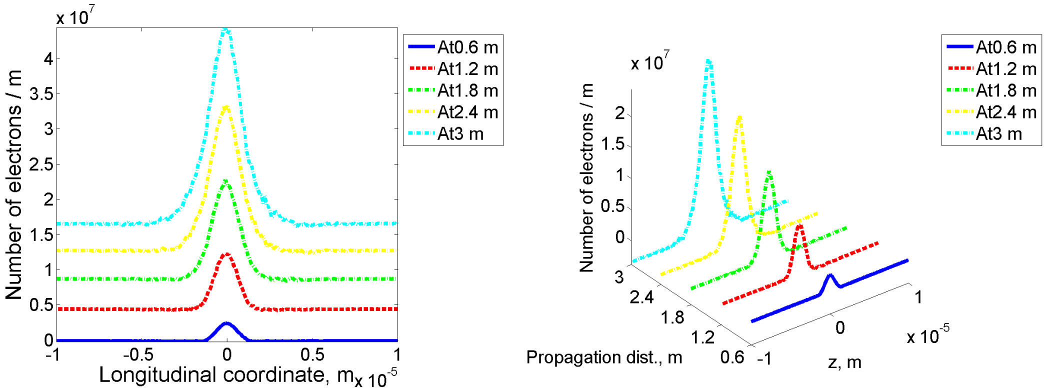

(a) Longitudinal density, 2D

(b) Longitudinal density, 3D

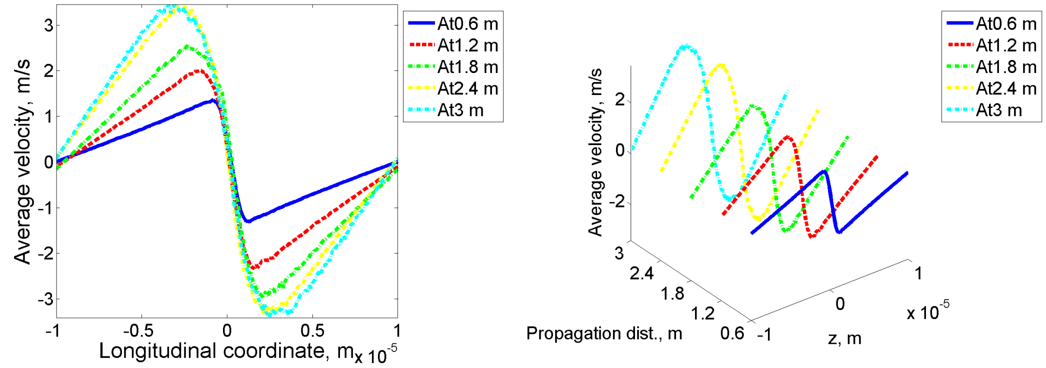

(c) Longitudinal velocity, 2D

(d) Longitudinal velocity, 3D

Figure 59: Longitudinal density and velocity modulation by reference energy ion 0.5σ off the center of the Gaussian electron beam along x in quadrupole focusing field after 0.6m (blue, solid line), 1.2m (red, dash line), 1.8m (green, dash-dot line, 2.4m (yellow, dash-dot line) and 3m (cyan, dash-dot line)of co-propagation with electrons, curves in (a) are shifted to improve readability.

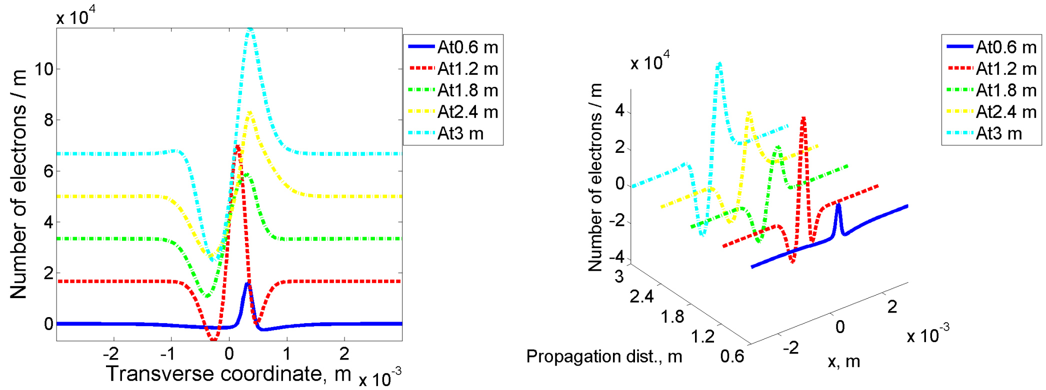

(a) Transverse (x) density, 2D (b) Transverse (x) density, 3D

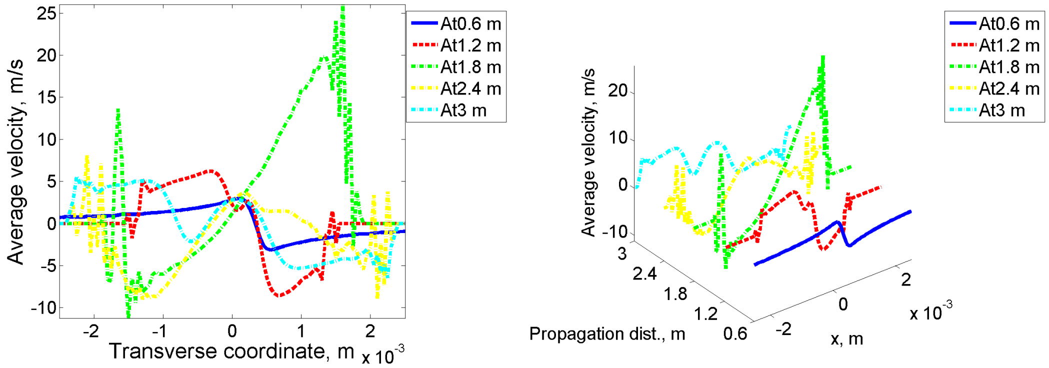

(c) Transverse (x) velocity, 2D (d) Transverse (x) velocity, 3D

Figure 60: Transverse (x) density and velocity modulation by reference energy ion 0.5σ off the center of the Gaussian electron beam along x in quadrupole focusing field after 0.6m (blue, solid line), 1.2m (red, dash line), 1.8m (green, dash-dot line, 2.4m (yellow, dash-dot line) and 3m (cyan, dash-dot line)of co-propagation with electrons, curves in (a) are shifted to improve readability.

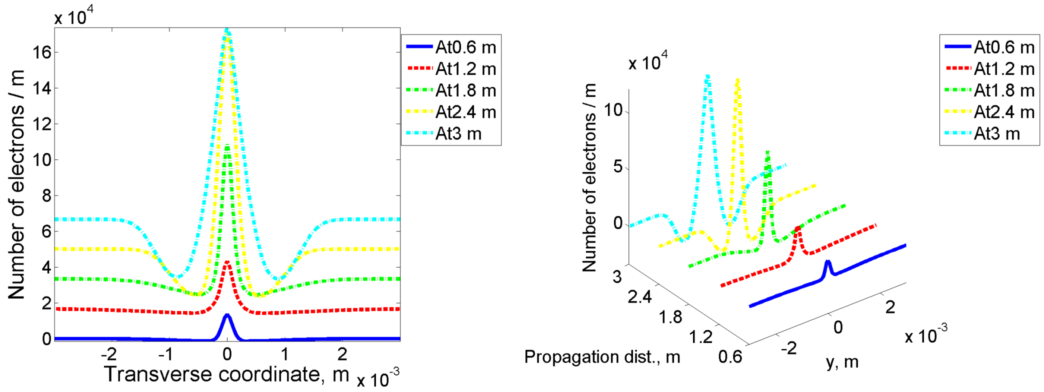

(a) Transverse (y) density, 2D (b) Transverse (y) density, 3D

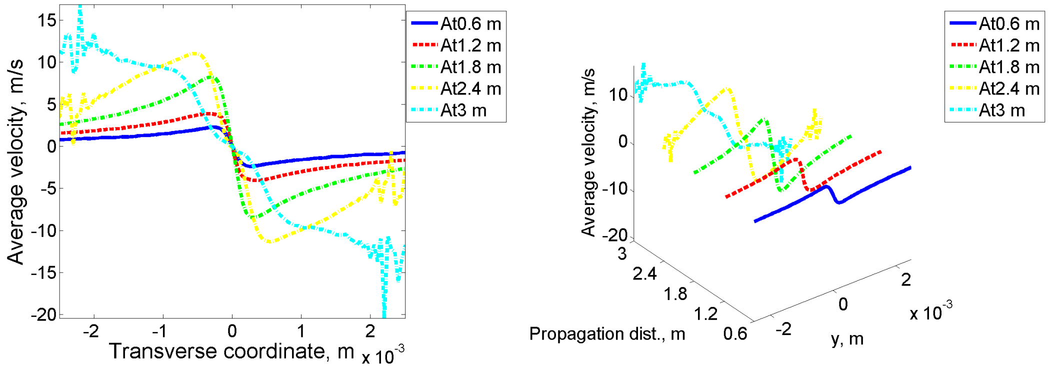

(c) Transverse (y) velocity, 2D (d) Transverse (y) velocity, 3D

Figure 61: Transverse (y) density and velocity modulation by reference energy ion 0.5σ off the center of the Gaussian electron beam along x in quadrupole focusing field after 0.6m (blue, solid line), 1.2m (red, dash line), 1.8m (green, dash-dot line, 2.4m (yellow, dash-dot line) and 3m (cyan, dash-dot line)of co-propagation with electrons, curves in (a) are shifted to improve readability.

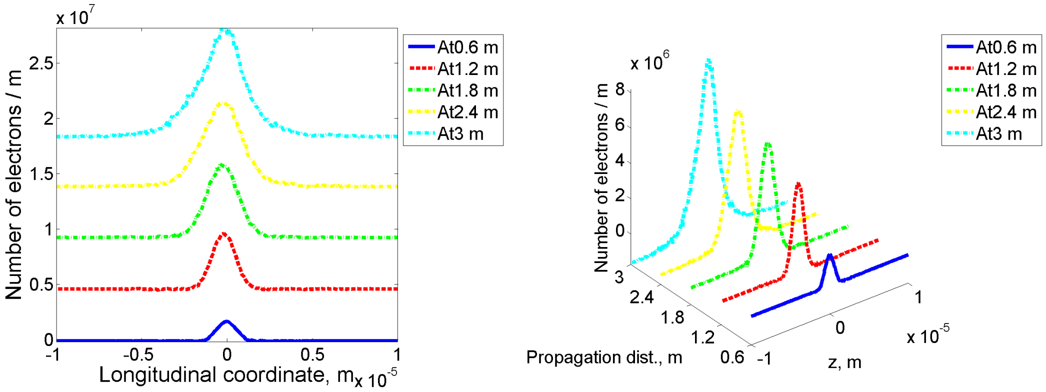

(a) Longitudinal density, 2D (b) Longitudinal density, 3D

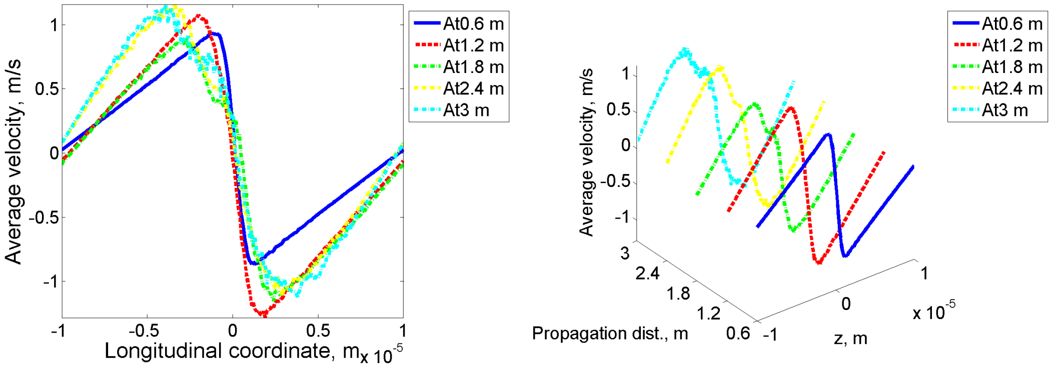

(c) Longitudinal velocity, 2D (d) Longitudinal velocity, 3D

Figure 62: Longitudinal density and velocity modulation by reference energy ion 1σ off the center of the Gaussian electron beam along x in quadrupole focusing field after 0.6m (blue, solid line), 1.2m (red, dash line), 1.8m (green, dash-dot line, 2.4m (yellow, dash-dot line) and 3m (cyan, dash-dot line)of co-propagation with electrons, curves in (a) are shifted to improve readability.

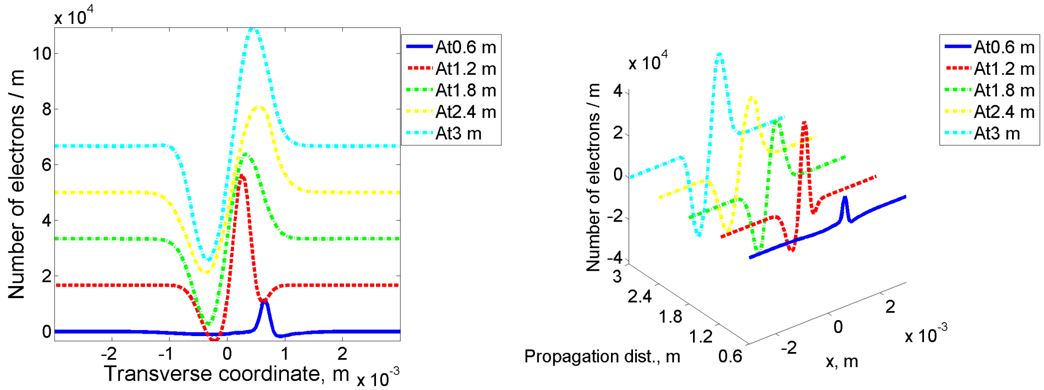

(a) Transverse (x) density, 2D (b) Transverse (x) density, 3D

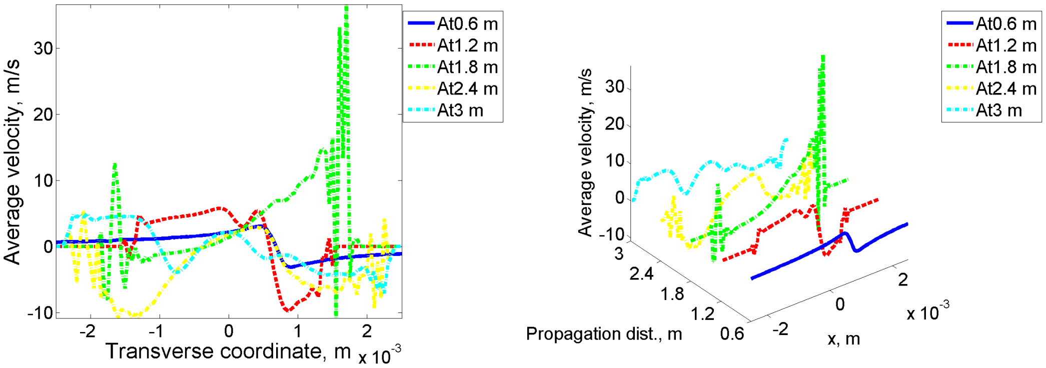

(c) Transverse (x) velocity, 2D (d) Transverse (x) velocity, 3D

Figure 63: Transverse (x) density and velocity modulation by reference energy ion 1σ off the center of the Gaussian electron beam along x in quadrupole focusing field after 0.6m (blue, solid line), 1.2m (red, dash line), 1.8m (green, dash-dot line, 2.4m (yellow, dash-dot line) and 3m (cyan, dash-dot line)of co-propagation with electrons, curves in (a) are shifted to improve readability.

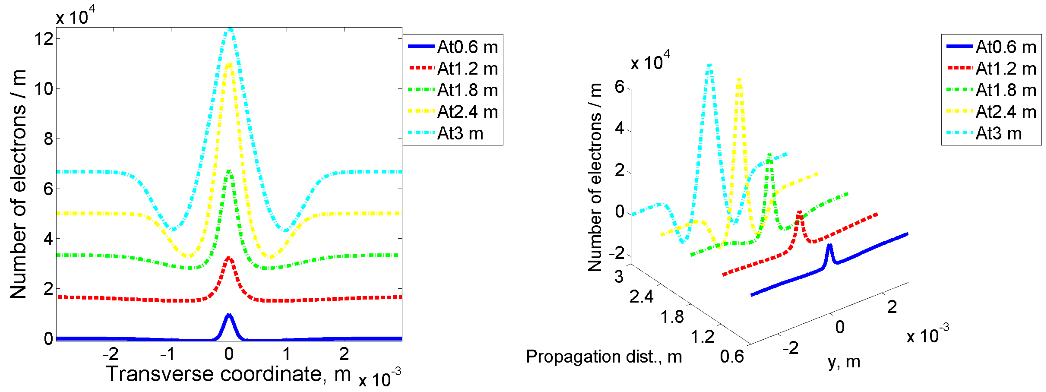

(a) Transverse (y) density, 2D

(b) Transverse (y) density, 3D

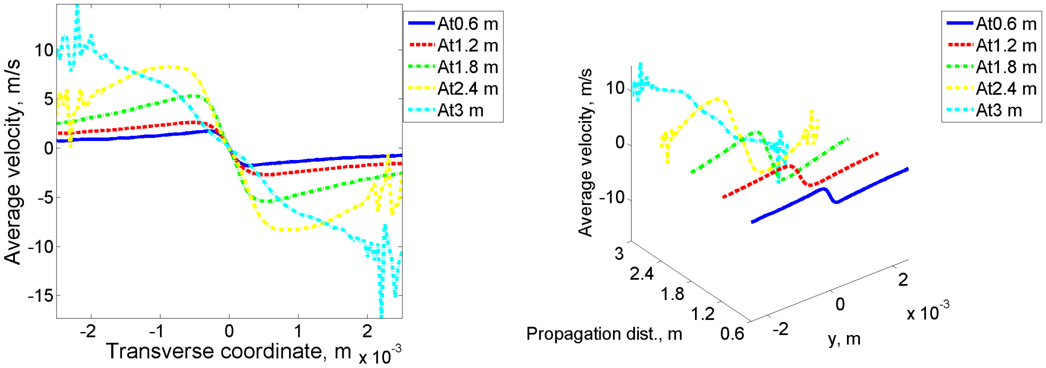

(c) Transverse (y) velocity, 2D

(d) Transverse (y) velocity, 3D

Figure 64: Transverse (y) density and velocity modulation by reference energy ion 1σ off the center of the Gaussian electron beam along x in quadrupole focusing field after 0.6m (blue, solid line), 1.2m (red, dash line), 1.8m (green, dash-dot line, 2.4m (yellow, dash-dot line) and 3m (cyan, dash-dot line)of co-propagation with electrons, curves in (a) are shifted to improve readability.

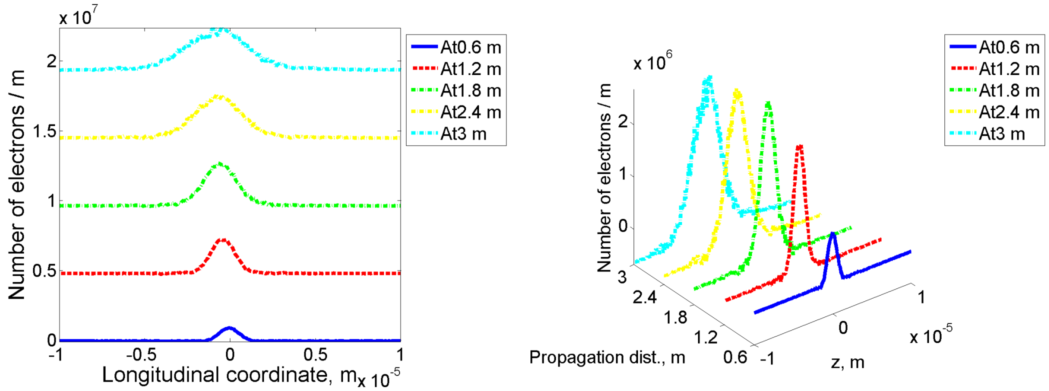

(a) Longitudinal density, 2D (b) Longitudinal density, 3D

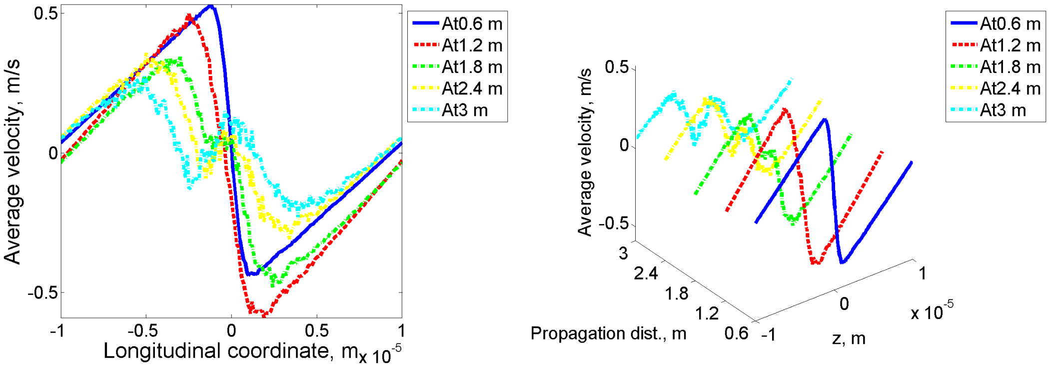

(c) Longitudinal velocity, 2D (d) Longitudinal velocity, 3D

Figure 65: Longitudinal density and velocity modulation by reference energy ion 1.5σ off the center of the Gaussian electron beam along x in quadrupole focusing field after 0.6m (blue, solid line), 1.2m (red, dash line), 1.8m (green, dash-dot line, 2.4m (yellow, dash-dot line) and 3m (cyan, dash-dot line)of co-propagation with electrons, curves in (a) are shifted to improve readability.

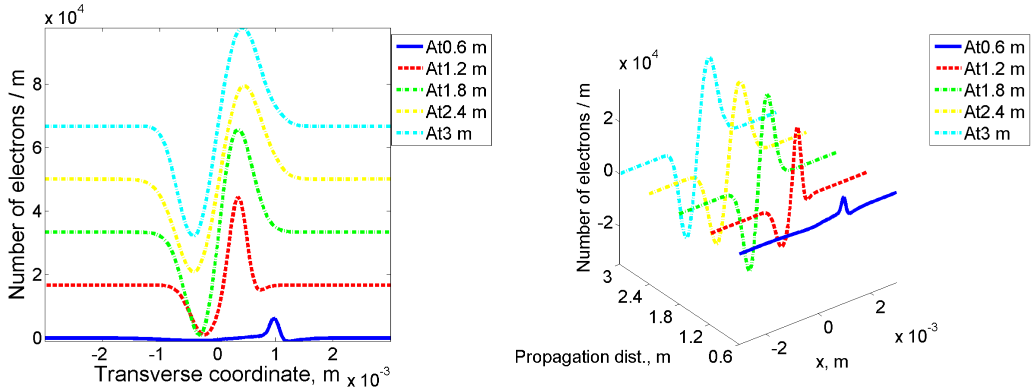

(a) Transverse (x) density, 2D (b) Transverse (x) density, 3D

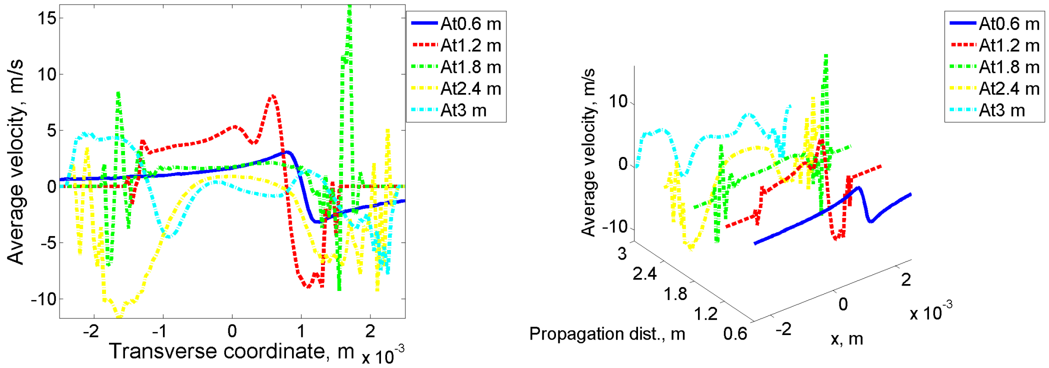

(c) Transverse (x) velocity, 2D (d) Transverse (x) velocity, 3D

Figure 66: Transverse (x) density and velocity modulation by reference energy ion 1.5σ off the center of the Gaussian electron beam along x in quadrupole focusing field after 0.6m (blue, solid line), 1.2m (red, dash line), 1.8m (green, dash-dot line, 2.4m (yellow, dash-dot line) and 3m (cyan, dash-dot line)of co-propagation with electrons, curves in (a) are shifted to improve readability.

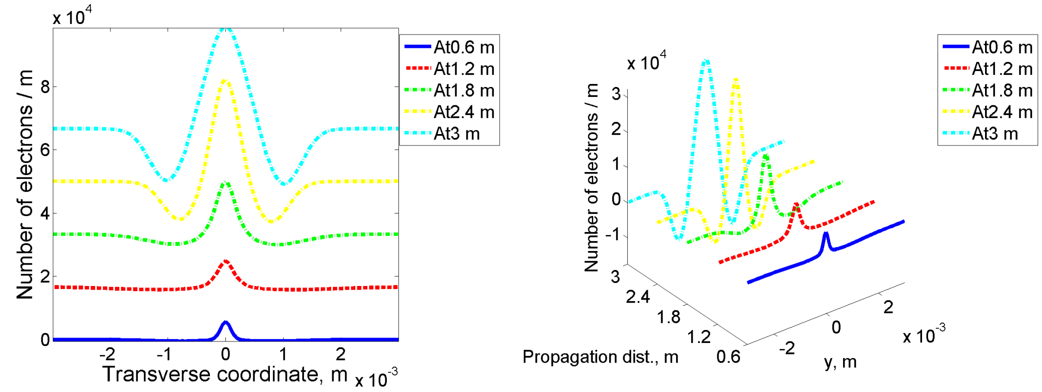

(a) Transverse (y) density, 2D (b) Transverse (y) density, 3D

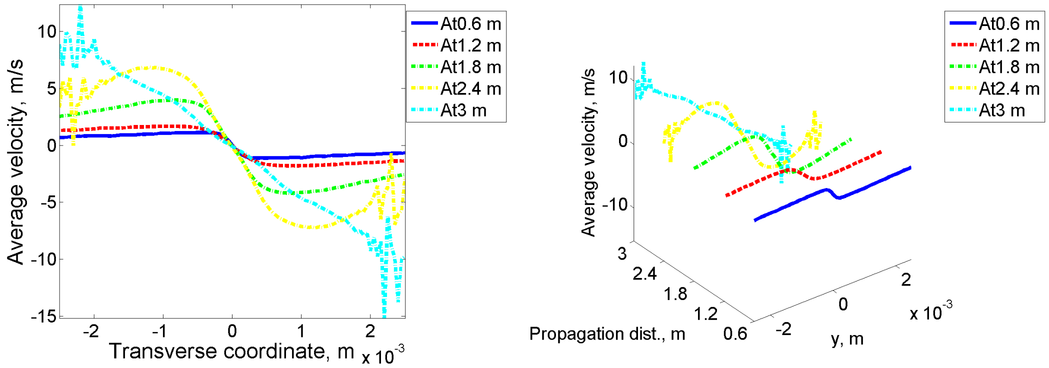

(c) Transverse (y) velocity, 2D (d) Transverse (y) velocity, 3D

Figure 67: Transverse (y) density and velocity modulation by reference energy ion 1.5σ off the center of the Gaussian electron beam along x in quadrupole focusing field after 0.6m (blue, solid line), 1.2m (red, dash line), 1.8m (green, dash-dot line, 2.4m (yellow, dash-dot line) and 3m (cyan, dash-dot line)of co-propagation with electrons, curves in (a) are shifted to improve readability.

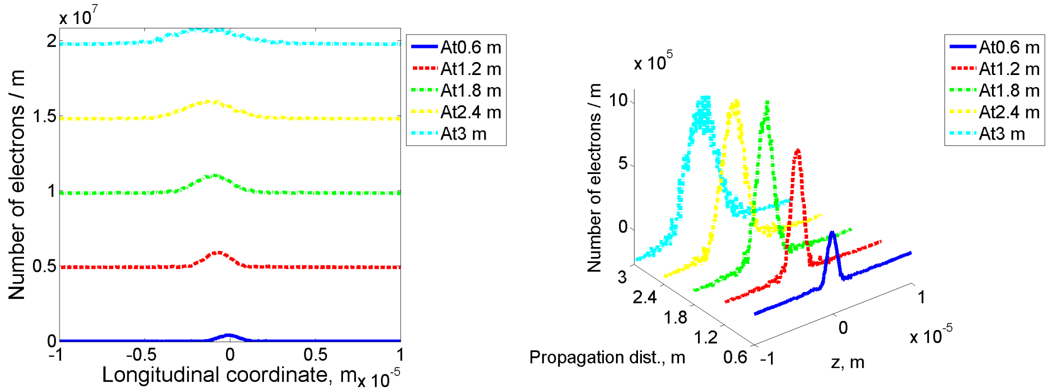

(a) Longitudinal density, 2D (b) Longitudinal density, 3D

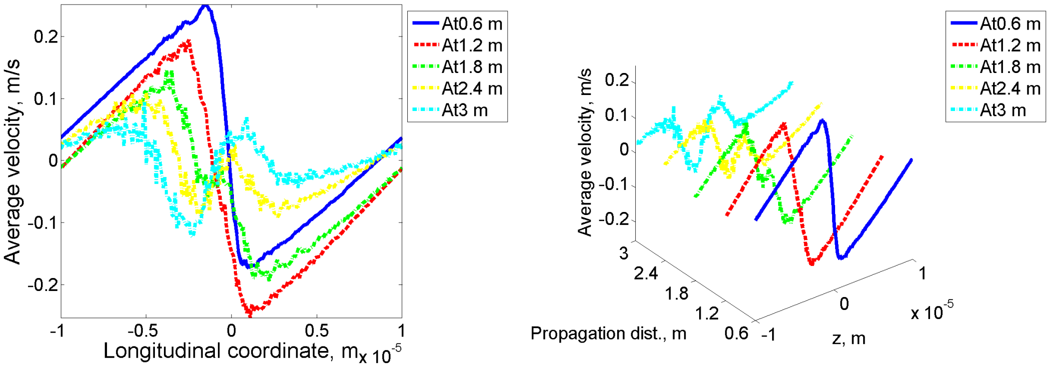

(c) Longitudinal velocity, 2D (d) Longitudinal velocity, 3D

Figure 68: Longitudinal density and velocity modulation by reference energy ion 2σ off the center of the Gaussian electron beam along x in quadrupole focusing field after 0.6m (blue, solid line), 1.2m (red, dash line), 1.8m (green, dash-dot line, 2.4m (yellow, dash-dot line) and 3m (cyan, dash-dot line)of co-propagation with electrons, curves in (a) are shifted to improve readability.

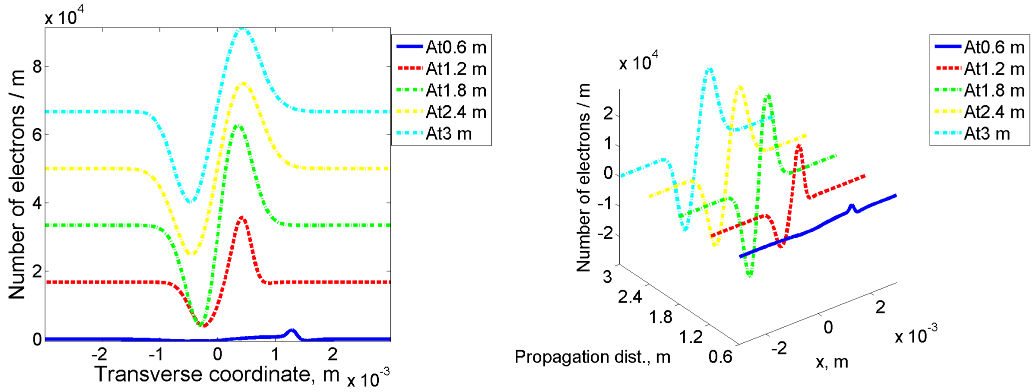

(a) Transverse (x) density, 2D (b) Transverse (x) density, 3D

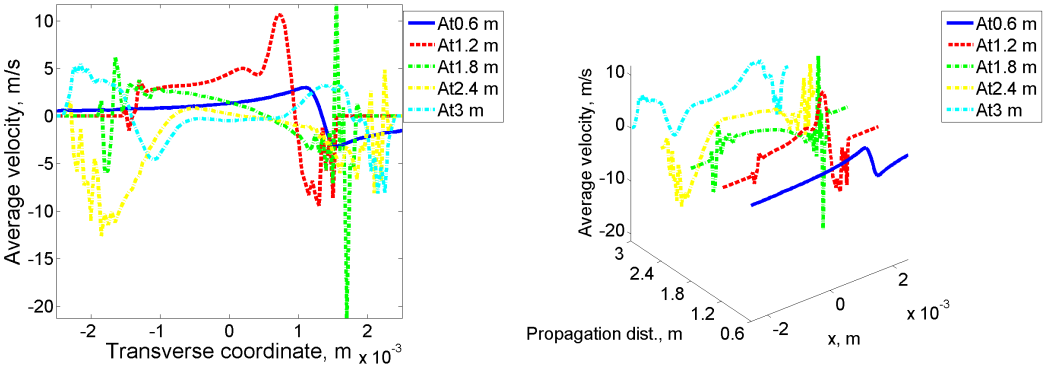

(c) Transverse (x) velocity, 2D (d) Transverse (x) velocity, 3D

Figure 69: Transverse (x) density and velocity modulation by reference energy ion 2σ off the center of the Gaussian electron beam along x in quadrupole focusing field after 0.6m (blue, solid line), 1.2m (red, dash line), 1.8m (green, dash-dot line, 2.4m (yellow, dash-dot line) and 3m (cyan, dash-dot line)of co-propagation with electrons, curves in (a) are shifted to improve readability.

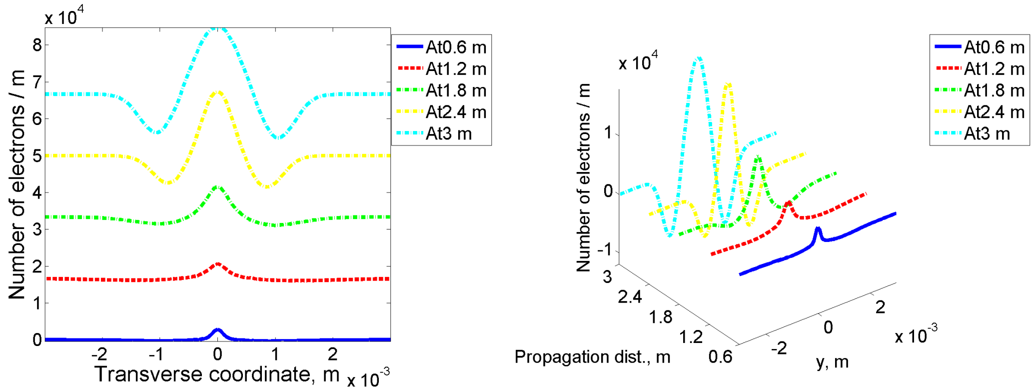

(a) Transverse (y) density, 2D

(b) Transverse (y) density, 3D

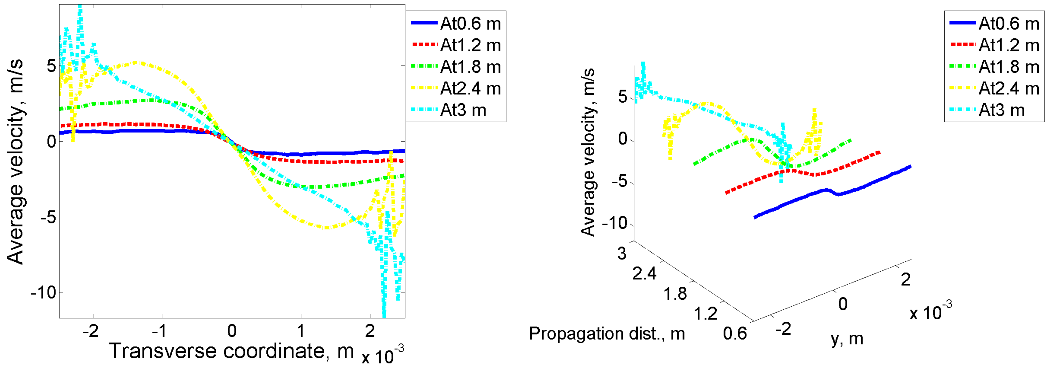

(c) Transverse (y) velocity, 2D

(d) Transverse (y) velocity, 3D

Figure 70: Transverse (y) density and velocity modulation by reference energy ion 2σ off the center of the Gaussian electron beam along x in quadrupole focusing field after 0.6m (blue, solid line), 1.2m (red, dash line), 1.8m (green, dash-dot line, 2.4m (yellow, dash-dot line) and 3m (cyan, dash-dot line)of co-propagation with electrons, curves in (a) are shifted to improve readability.

We also collect simulation results of the final density and velocity distribution of electron beam using stationary ion at different locations along x direction under the quadrupole focusing field, and present them in figure 71 and 72. The longitudinal modulation results in figure 71 show that, when ion moves towards the edge of the electron beam, the density modulation drops. The asymmetry in the modulation plots is due to the quadrupole fields changing the transverse and longitudinal velocities of the electron beam. The further the ion's location, the stronger effects from the quadrupole magnetic fields on the surrounding electrons of the ion's location. The transverse density and velocity modulations in x and y directions are combination effects from the ion's attraction and the quadrupole magnetic fields.

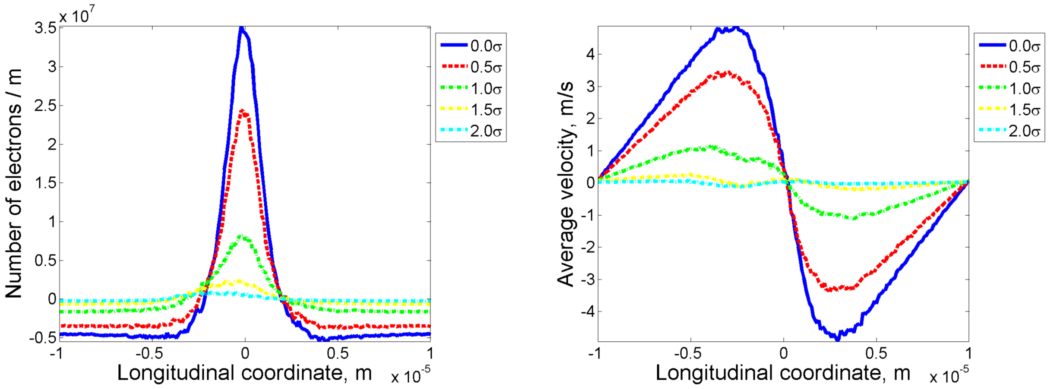

(a) Longitudinal density (b) Longitudinal velocity

Figure 71: Longitudinal density and velocity modulation by reference energy ion with various distances off the center of the Gaussian electron beam along x in quadrupole focusing field after 3m of co-propagation with electrons.

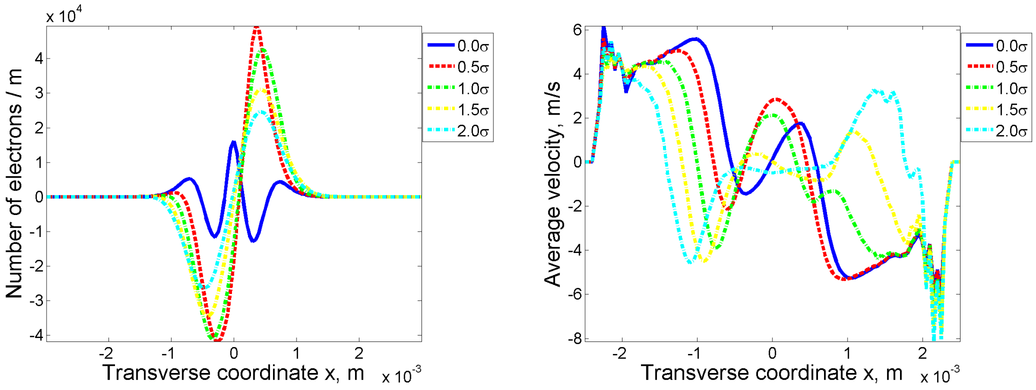

(a) Transverse (x) density (b) Transverse (x) velocity

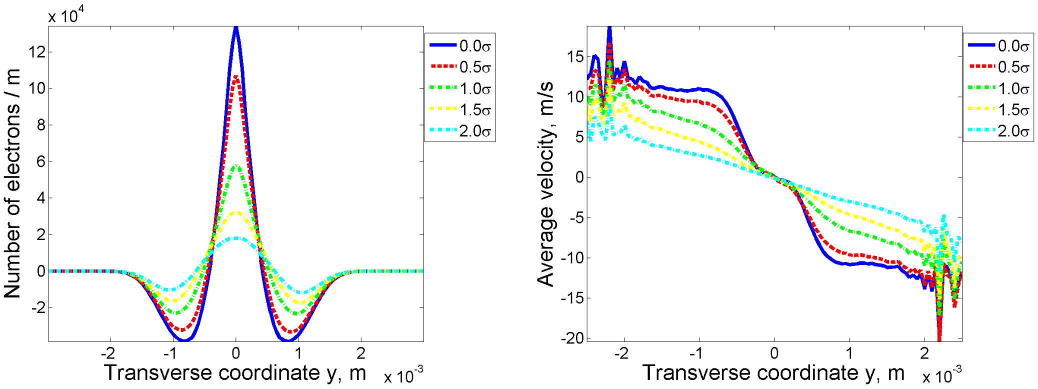

(c) Transverse (y) density (d) Transverse (y) velocity

Figure 72: Transverse density and velocity modulation by reference energy ion with various distances off the center of the Gaussian electron beam along x in quadrupole focusing field after 3m of co-propagation with electrons.

Figures 73 - 84 give the modulation results using a stationary ion at various off-center locations along y direction in the quadrupole focusing field. And the comparisons of final density and velocity distributions are presented in figures 85 and 86, with various off-center locations along y direction for ion.

The effects from quadrupole magnetic fields are not so strong in this set of simulations, compared with the simulations using off-center locations along x direction. One reason is that, the transverse beam size of electron beam in x direction is extremely small during the modulation process, and the quadrupole fields may cause strong nonlinearity of space charge effect, and resulting in some reverse slopes in the modulation plots. Another reason is that, we put the ion some distance away from the center of the electron beam in the measurement of the initial electron beam size. In the modulator, the transverse beam size of electron beam is compressed so much that the ion is getting relatively even further from the center of the electron beam, where there are few electrons, which causes large oscillations.

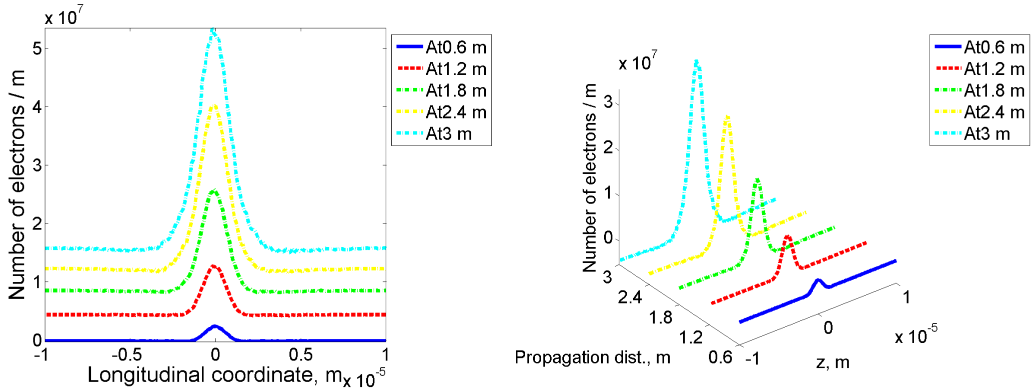

(a) Longitudinal density, 2D (b) Longitudinal density, 3D

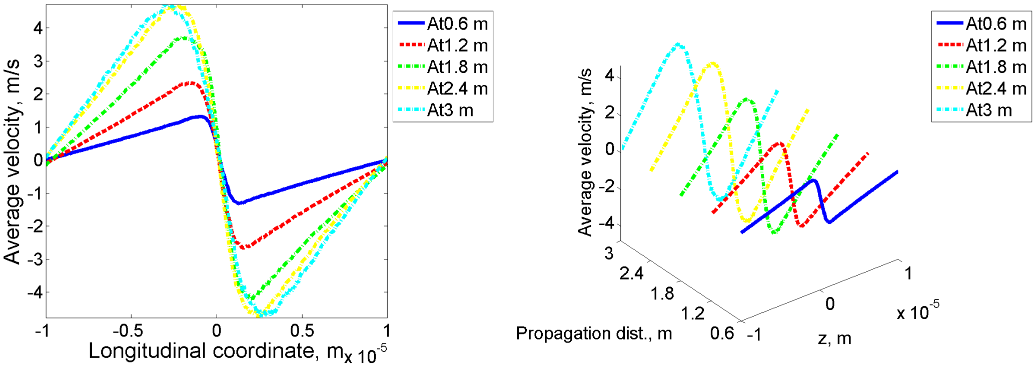

(c) Longitudinal velocity, 2D (d) Longitudinal velocity, 3D

Figure 73: Longitudinal density and velocity modulation by reference energy ion 0.5σ off the center of the Gaussian electron beam along y in quadrupole focusing field after 0.6m (blue, solid line), 1.2m (red, dash line), 1.8m (green, dash-dot line, 2.4m (yellow, dash-dot line) and 3m (cyan, dash-dot line)of co-propagation with electrons, curves in (a) are shifted to improve readability.

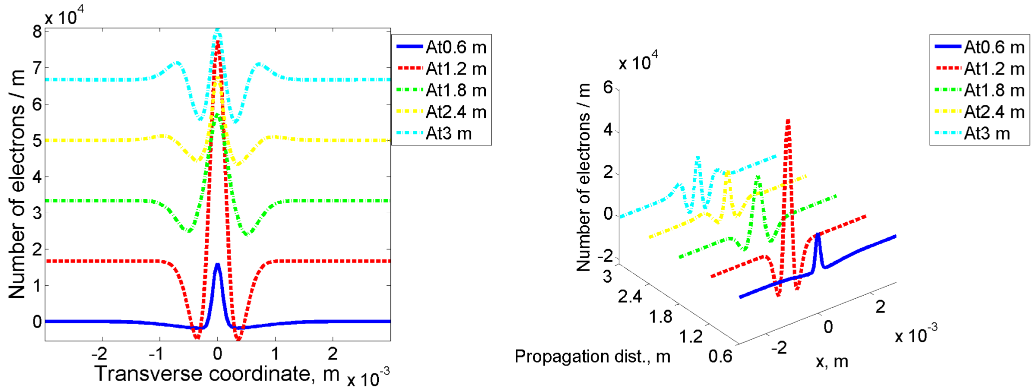

(a) Transverse (x) density, 2D (b) Transverse (x) density, 3D

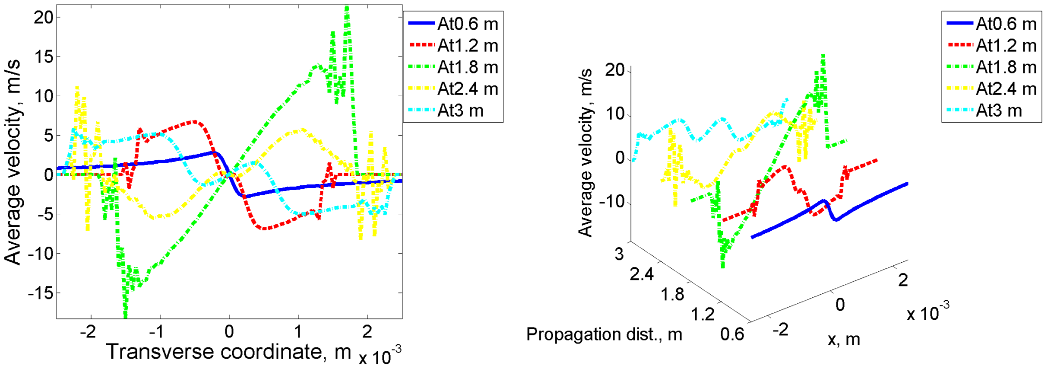

(c) Transverse (x) velocity, 2D (d) Transverse (x) velocity, 3D

Figure 74: Transverse (x) density and velocity modulation by reference energy ion 0.5σ off the center of the Gaussian electron beam along y in quadrupole focusing field after 0.6m (blue, solid line), 1.2m (red, dash line), 1.8m (green, dash-dot line, 2.4m (yellow, dash-dot line) and 3m (cyan, dash-dot line)of co-propagation with electrons, curves in (a) are shifted to improve readability.

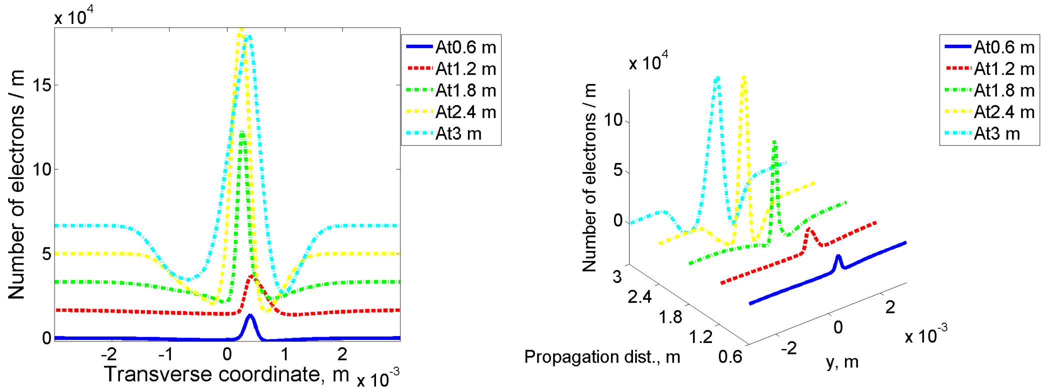

(a) Transverse (y) density, 2D

(b) Transverse (y) density, 3D

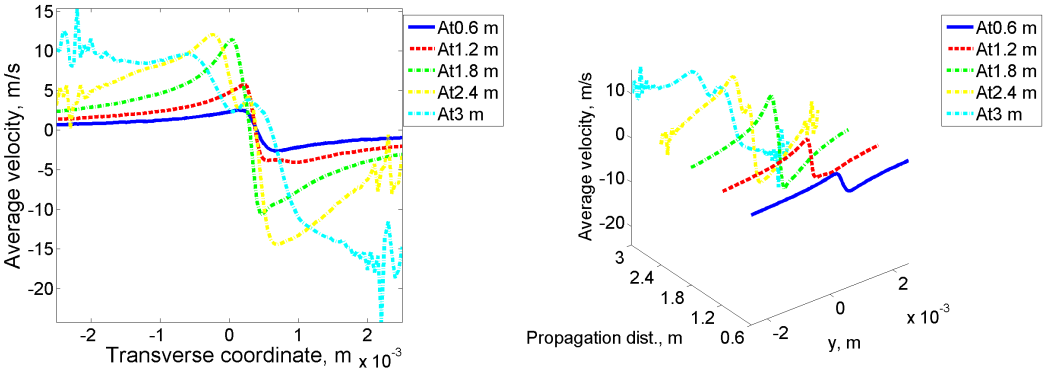

(c) Transverse (y) velocity, 2D

(d) Transverse (y) velocity, 3D

Figure 75: Transverse (y) density and velocity modulation by reference energy ion 0.5σ off the center of the Gaussian electron beam along y in quadrupole focusing field after 0.6m (blue, solid line), 1.2m (red, dash line), 1.8m (green, dash-dot line, 2.4m (yellow, dash-dot line) and 3m (cyan, dash-dot line)of co-propagation with electrons, curves in (a) are shifted to improve readability.

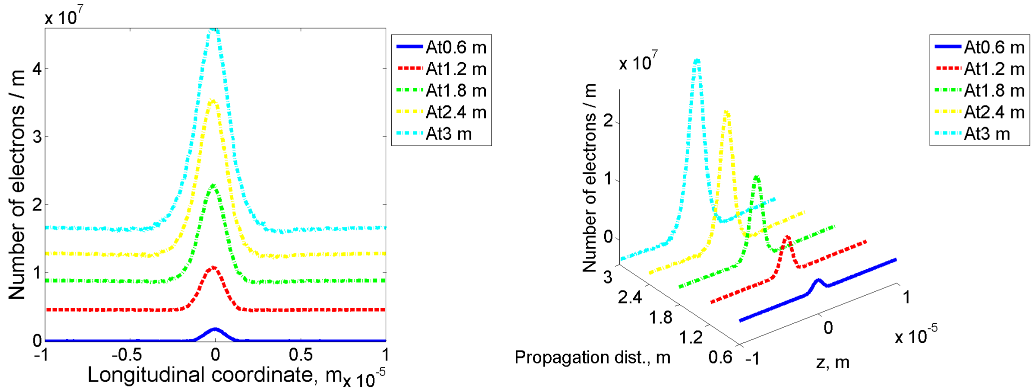

(a) Longitudinal density, 2D

(b) Longitudinal density, 3D

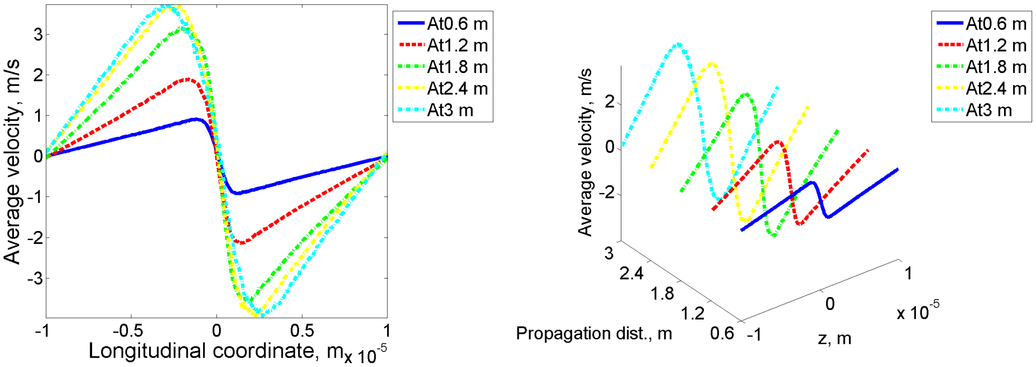

(c) Longitudinal velocity, 2D

(d) Longitudinal velocity, 3D

Figure 76: Longitudinal density and velocity modulation by reference energy ion 1σ off the center of the Gaussian electron beam along y in quadrupole focusing field after 0.6m (blue, solid line), 1.2m (red, dash line), 1.8m (green, dash-dot line, 2.4m (yellow, dash-dot line) and 3m (cyan, dash-dot line)of co-propagation with electrons, curves in (a) are shifted to improve readability.

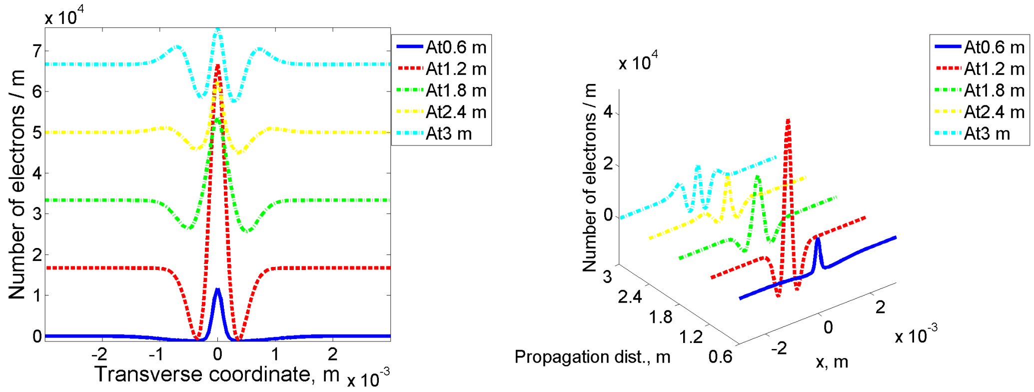

(a) Transverse (x) density, 2D (b) Transverse (x) density, 3D

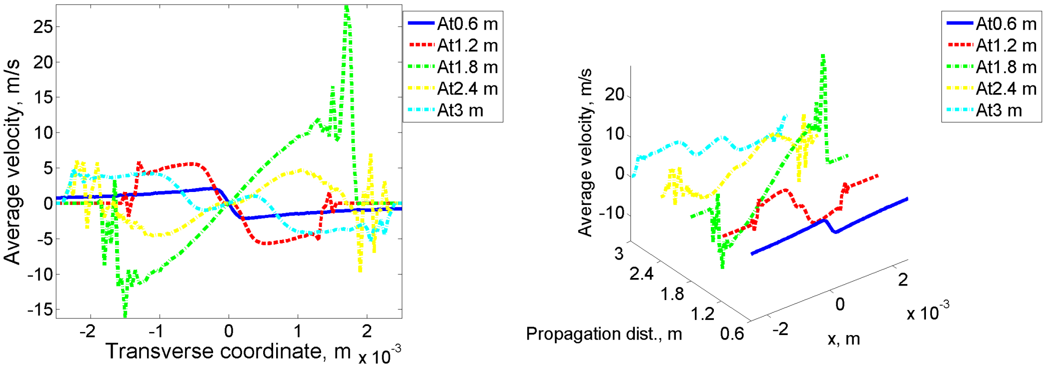

(c) Transverse (x) velocity, 2D (d) Transverse (x) velocity, 3D

Figure 77: Transverse (x) density and velocity modulation by reference energy ion 1σ off the center of the Gaussian electron beam along y in quadrupole focusing field after 0.6m (blue, solid line), 1.2m (red, dash line), 1.8m (green, dash-dot line, 2.4m (yellow, dash-dot line) and 3m (cyan, dash-dot line)of co-propagation with electrons, curves in (a) are shifted to improve readability.

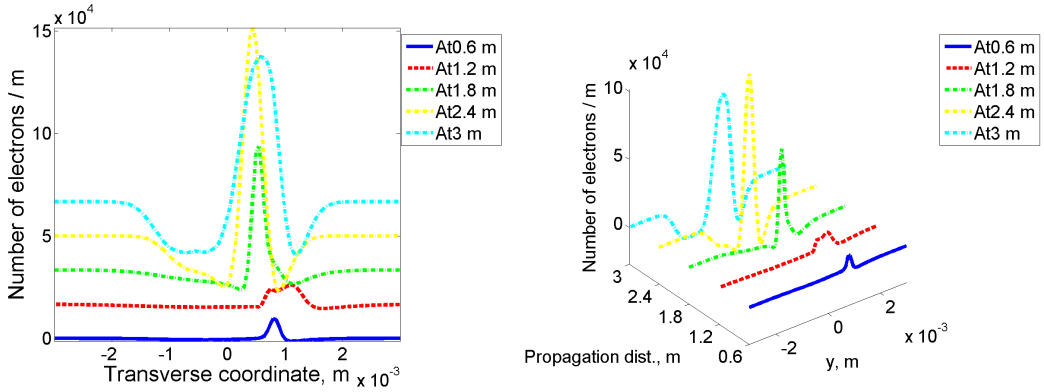

(a) Transverse (y) density, 2D (b) Transverse (y) density, 3D

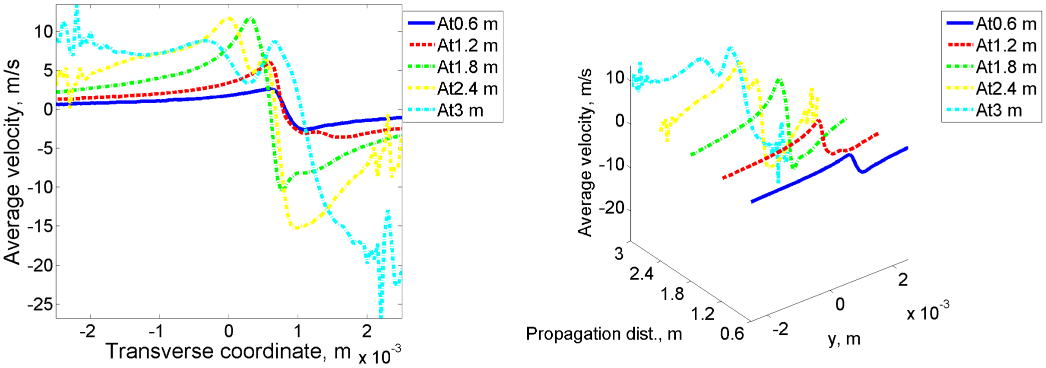

(c) Transverse (y) velocity, 2D (d) Transverse (y) velocity, 3D

Figure 78: Transverse (y) density and velocity modulation by reference energy ion 1σ off the center of the Gaussian electron beam along y in quadrupole focusing field after 0.6m (blue, solid line), 1.2m (red, dash line), 1.8m (green, dash-dot line, 2.4m (yellow, dash-dot line) and 3m (cyan, dash-dot line)of co-propagation with electrons, curves in (a) are shifted to improve readability.

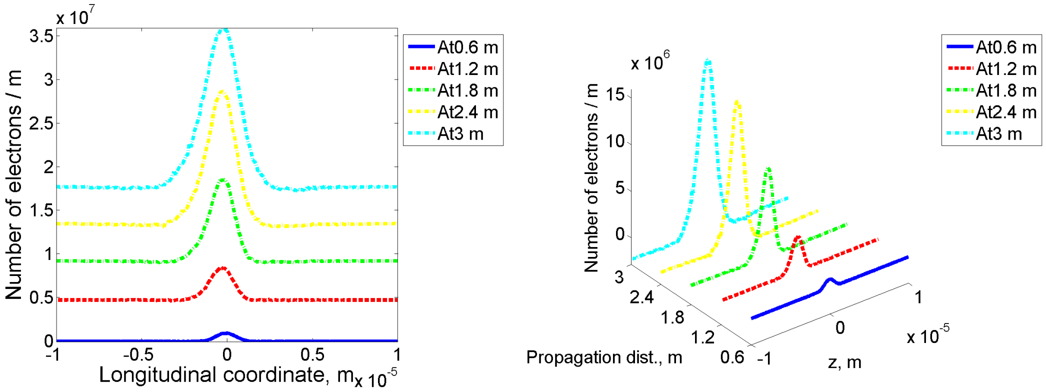

(a) Longitudinal density, 2D

(b) Longitudinal density, 3D

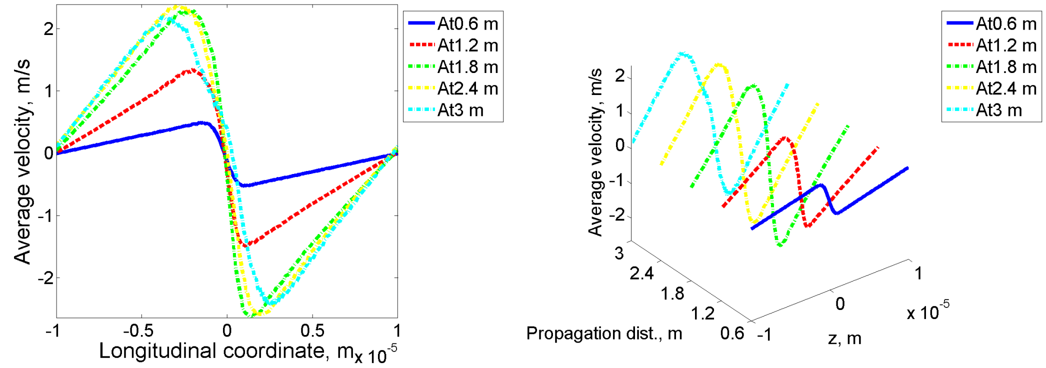

(c) Longitudinal velocity, 2D

(d) Longitudinal velocity, 3D

Figure 79: Longitudinal density and velocity modulation by reference energy ion 1.5σ off the center of the Gaussian electron beam along y in quadrupole focusing field after 0.6m (blue, solid line), 1.2m (red, dash line), 1.8m (green, dash-dot line, 2.4m (yellow, dash-dot line) and 3m (cyan, dash-dot line)of co-propagation with electrons, curves in (a) are shifted to improve readability.

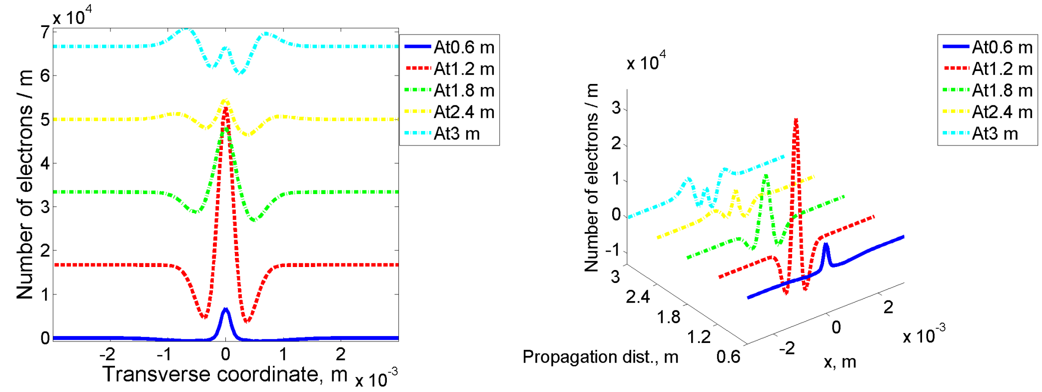

(a) Transverse (x) density, 2D

(b) Transverse (x) density, 3D

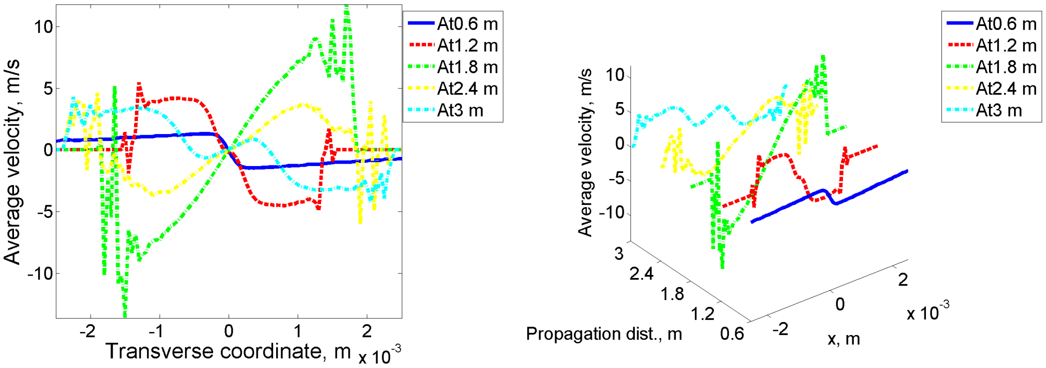

(c) Transverse (x) velocity, 2D

(d) Transverse (x) velocity, 3D

Figure 80: Transverse (x) density and velocity modulation by reference energy ion 1.5σ off the center of the Gaussian electron beam along y in quadrupole focusing field after 0.6m (blue, solid line), 1.2m (red, dash line), 1.8m (green, dash-dot line, 2.4m (yellow, dash-dot line) and 3m (cyan, dash-dot line)of co-propagation with electrons, curves in (a) are shifted to improve readability.

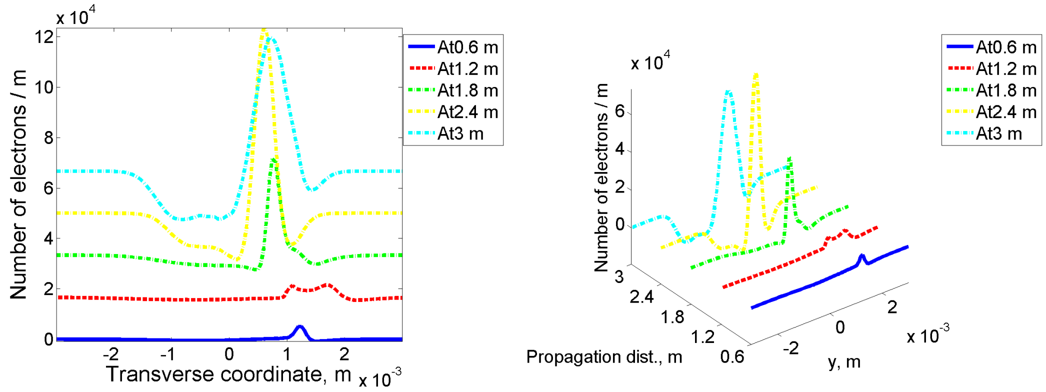

(a) Transverse (y) density, 2D

(b) Transverse (y) density, 3D

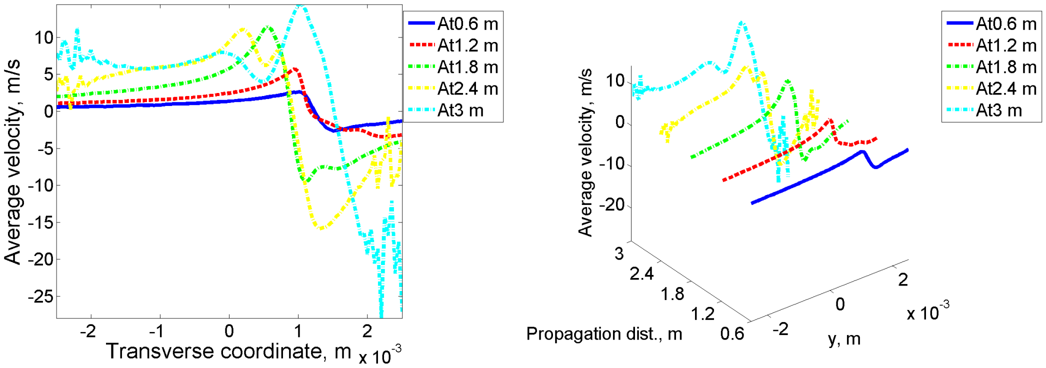

(c) Transverse (y) velocity, 2D

(d) Transverse (y) velocity, 3D

Figure 81: Transverse (y) density and velocity modulation by reference energy ion 1.5σ off the center of the Gaussian electron beam along y in quadrupole focusing field after 0.6m (blue, solid line), 1.2m (red, dash line), 1.8m (green, dash-dot line, 2.4m (yellow, dash-dot line) and 3m (cyan, dash-dot line)of co-propagation with electrons, curves in (a) are shifted to improve readability.

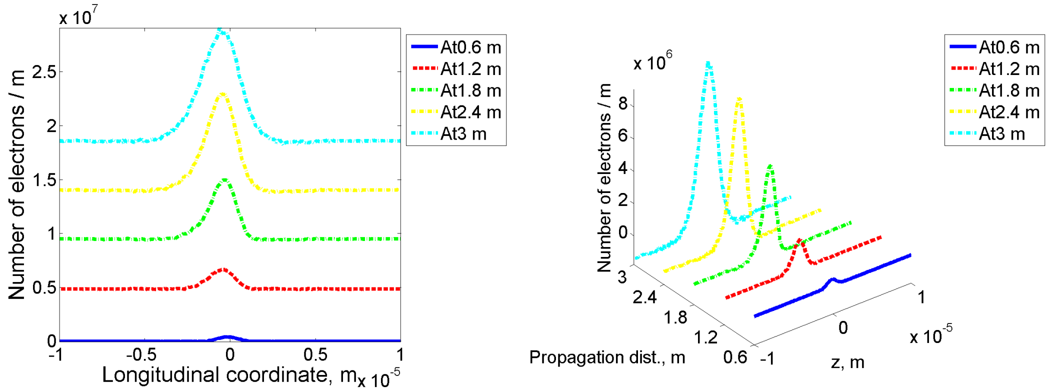

(a) Longitudinal density, 2D (b) Longitudinal density, 3D

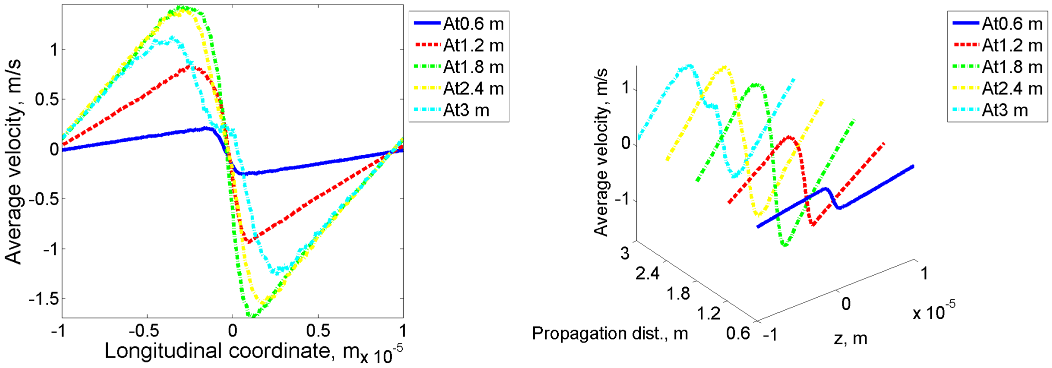

(c) Longitudinal velocity, 2D (d) Longitudinal velocity, 3D

Figure 82: Longitudinal density and velocity modulation by reference energy ion 2σ off the center of the Gaussian electron beam along y in quadrupole focusing field after 0.6m (blue, solid line), 1.2m (red, dash line), 1.8m (green, dash-dot line, 2.4m (yellow, dash-dot line) and 3m (cyan, dash-dot line)of co-propagation with electrons, curves in (a) are shifted to improve readability.

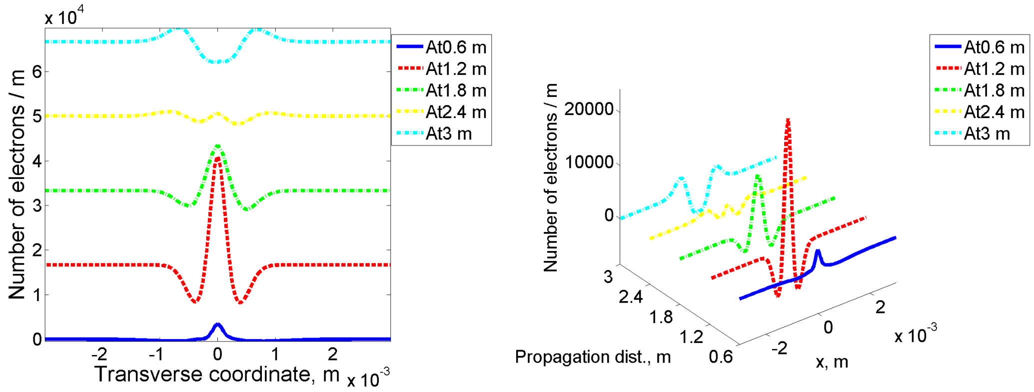

(a) Transverse (x) density, 2D (b) Transverse (x) density, 3D

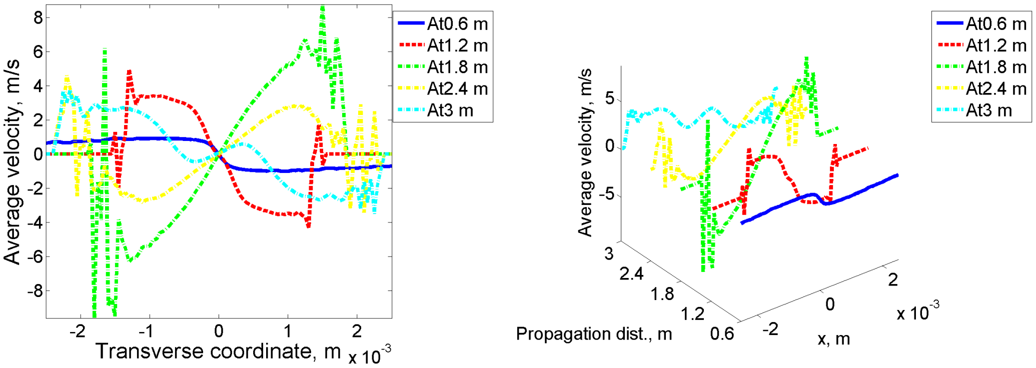

(c) Transverse (x) velocity, 2D (d) Transverse (x) velocity, 3D

Figure 83: Transverse (x) density and velocity modulation by reference energy ion 2σ off the center of the Gaussian electron beam along y in quadrupole focusing field after 0.6m (blue, solid line), 1.2m (red, dash line), 1.8m (green, dash-dot line, 2.4m (yellow, dash-dot line) and 3m (cyan, dash-dot line)of co-propagation with electrons, curves in (a) are shifted to improve readability.

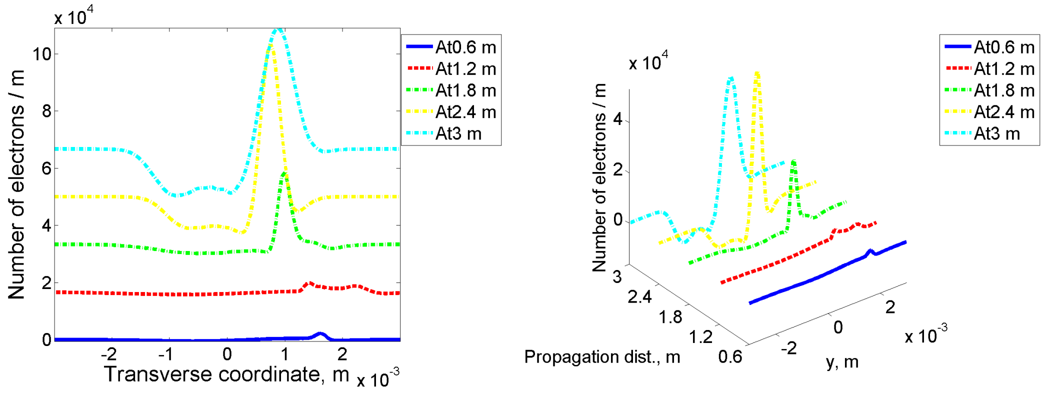

(a) Transverse (y) density, 2D (b) Transverse (y) density, 3D

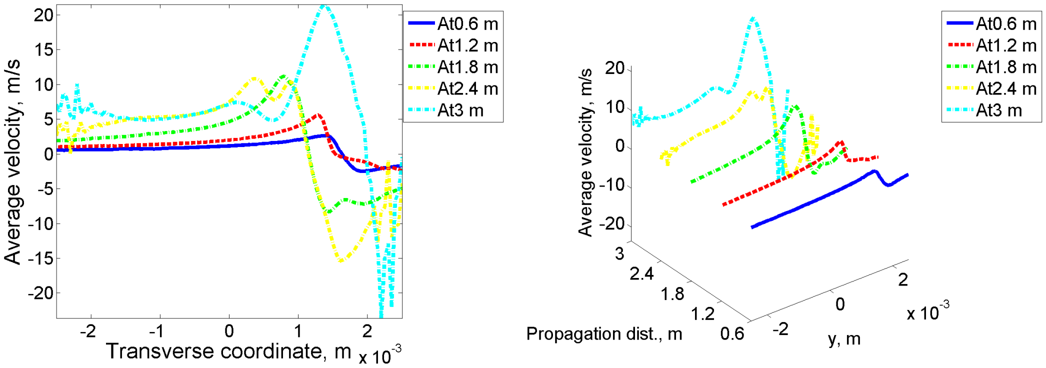

(c) Transverse (y) velocity, 2D (d) Transverse (y) velocity, 3D

Figure 84: Transverse (y) density and velocity modulation by reference energy ion 2σ off the center of the Gaussian electron beam along y in quadrupole focusing field after 0.6m (blue, solid line), 1.2m (red, dash line), 1.8m (green, dash-dot line, 2.4m (yellow, dash-dot line) and 3m (cyan, dash-dot line)of co-propagation with electrons, curves in (a) are shifted to improve readability.

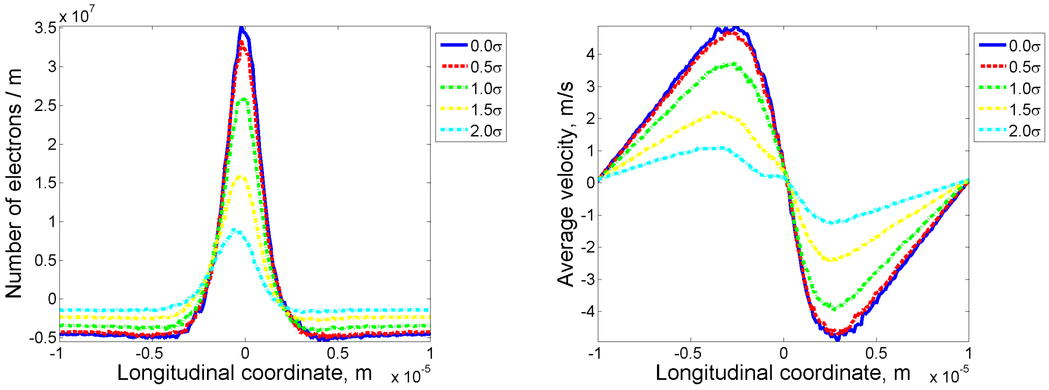

(a) Longitudinal density (b) Longitudinal velocity

Figure 85: Longitudinal density and velocity modulation by reference energy ion with various distances off the center of the Gaussian electron beam along y in quadrupole focusing field after 3m of co-propagation with electrons.

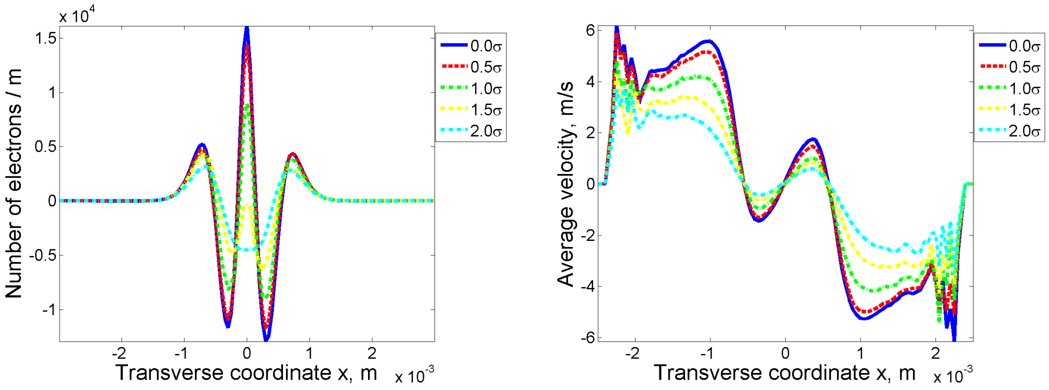

(a) Transverse (x) density (b) Transverse (x) velocity

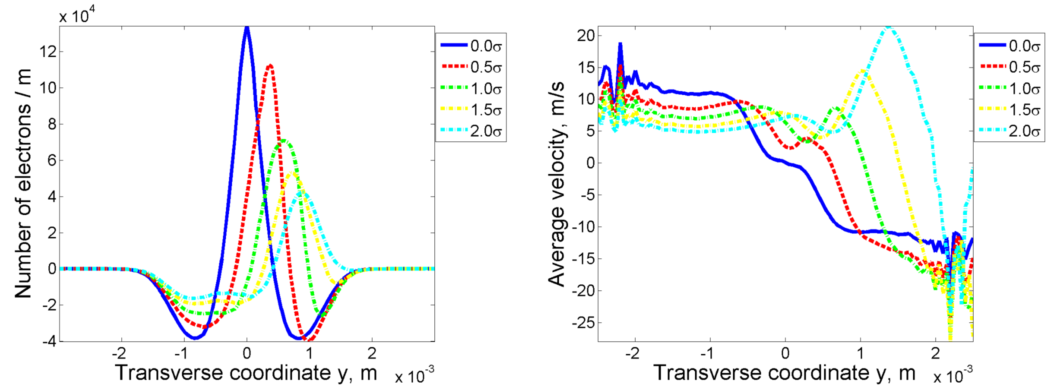

(c) Transverse (y) density (d) Transverse (y) velocity

Figure 86: Transverse density and velocity modulation by reference energy ion with various distances off the center of the Gaussian electron beam along y in quadrupole focusing field after 3m of co-propagation with electrons.

In the next simulations, we want to study the effects from the ion's velocities on the modulation process. We start with an ion at the center of the electron beam with velocity $v_{0,z} = 1 \cdot \beta_z$ with respect to the electron cloud in the co-moving frame. Again, β_z is the characteristic velocity amplitudes in longitudinal direction for kappa-2 thermal velocity distribution of electron beam. The results are shown in figures 87 - 89.

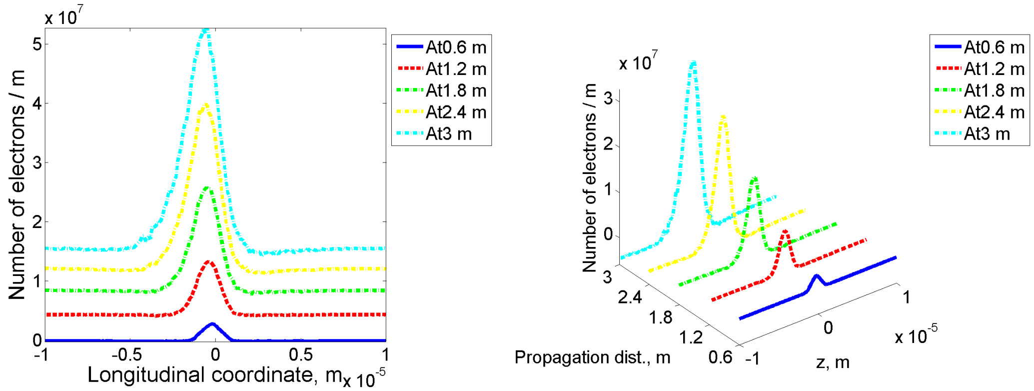

(a) Longitudinal density, 2D

(b) Longitudinal density, 3D

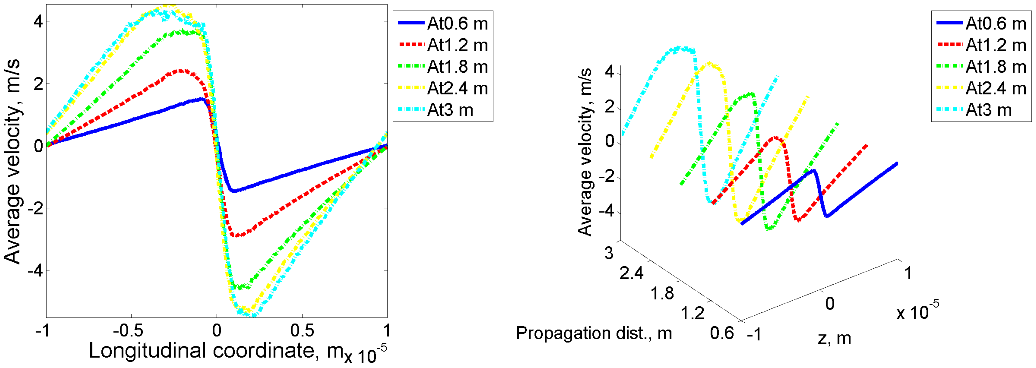

(c) Longitudinal velocity, 2D

(d) Longitudinal velocity, 3D

Figure 87: Longitudinal density and velocity modulation by moving ion in the center of the Gaussian electron beam in quadrupole focusing field after 0.6m (blue, solid line), 1.2m (red, dash line), 1.8m (green, dash-dot line, 2.4m (yellow, dash-dot line) and 3m (cyan, dash-dot line)of co-propagation with electrons, curves in (a) are shifted to improve readability.

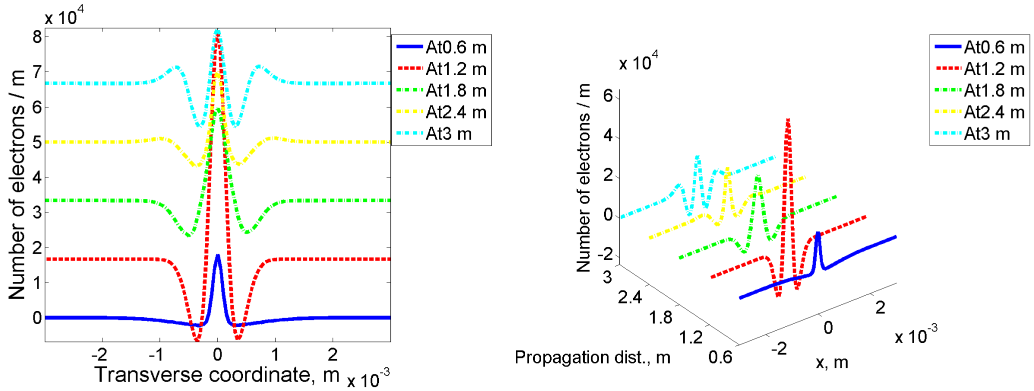

(a) Transverse (x) density, 2D

(b) Transverse (x) density, 3D

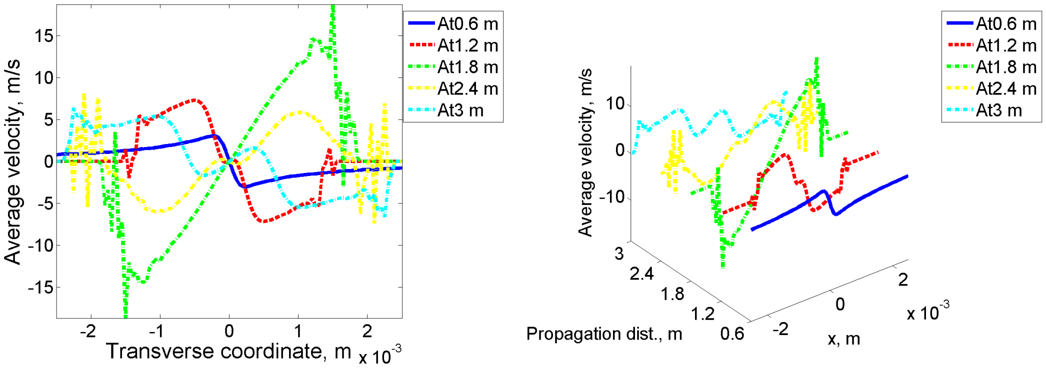

(c) Transverse (x) velocity, 2D

(d) Transverse (x) velocity, 3D

Figure 88: Transverse (x) density and velocity modulation by moving ion in the center of the Gaussian electron beam in quadrupole focusing field after 0.6m (blue, solid line), 1.2m (red, dash line), 1.8m (green, dash-dot line, 2.4m (yellow, dash-dot line) and 3m (cyan, dash-dot line)of co-propagation with electrons, curves in (a) are shifted to improve readability.

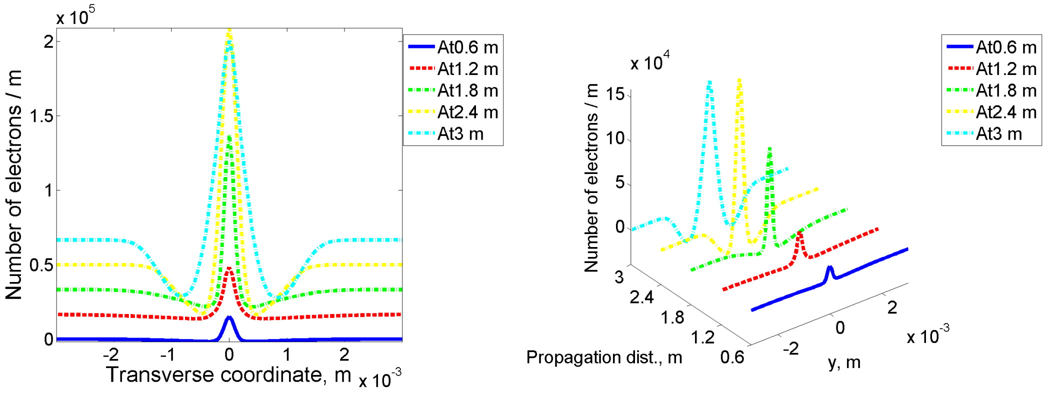

(a) Transverse (y) density, 2D

(b) Transverse (y) density, 3D

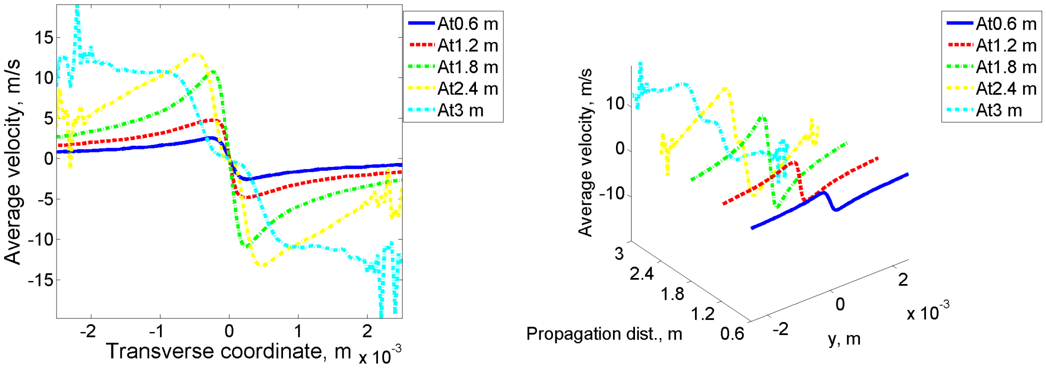

(c) Transverse (y) velocity, 2D

(d) Transverse (y) velocity, 3D

Figure 89: Transverse (y) density and velocity modulation by moving ion in the center of the Gaussian electron beam in quadrupole focusing field after 0.6m (blue, solid line), 1.2m (red, dash line), 1.8m (green, dash-dot line, 2.4m (yellow, dash-dot line) and 3m (cyan, dash-dot line)of co-propagation with electrons, curves in (a) are shifted to improve readability.

We compare the modulation results by a stationary ion and a moving ion, both at the center of electron beam, and the comparison is given in figure 90. Similar with the simulations under linear focusing fields, lower density and velocity modulations are observed using a moving ion than using a stationary ion.

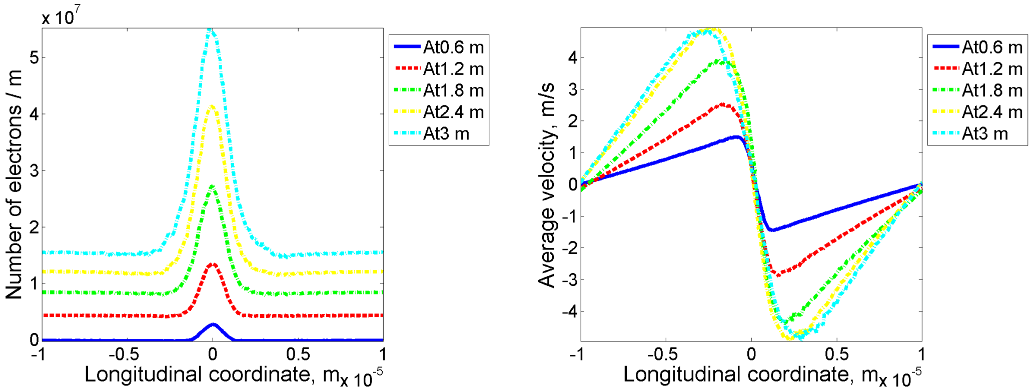

(a) Longitudinal density, stationary ion (b) Longitudinal velocity, stationary ion

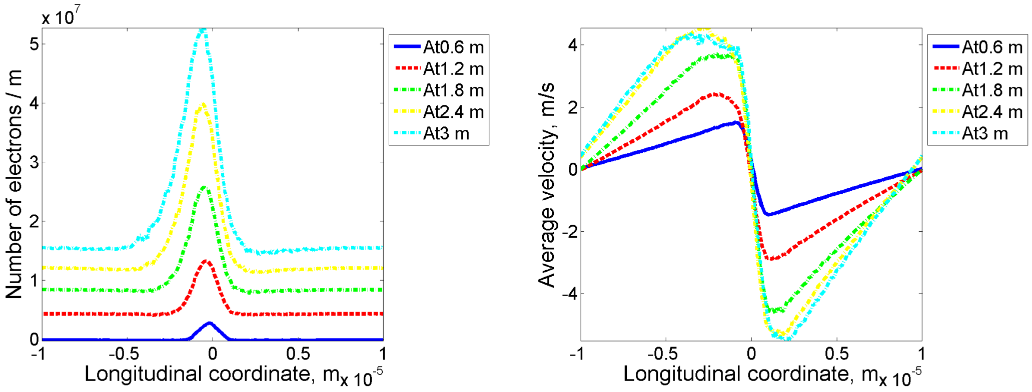

(c) Longitudinal density, moving ion (d) Longitudinal velocity, moving ion

Figure 90: Longitudinal density and velocity modulation by reference energy ion and moving ion in the center of the Gaussian electron beam in quadrupole focusing field, curves in (a) and (c) are shifted to improve readability.

In following simulations, we study the modulation process using a moving ion at various off-center locations along x direction and y direction. Figure 91 - 102 are the results using a moving ion at different off-center locations along x direction, and the comparisons of final distributions are presented in figures 103 and 104. And the results of off-center locations along y direction for ion are given in figures 105 - 116, and comparisons of final distributions with various off-center locations along y direction are shown in figures 117 - 118.

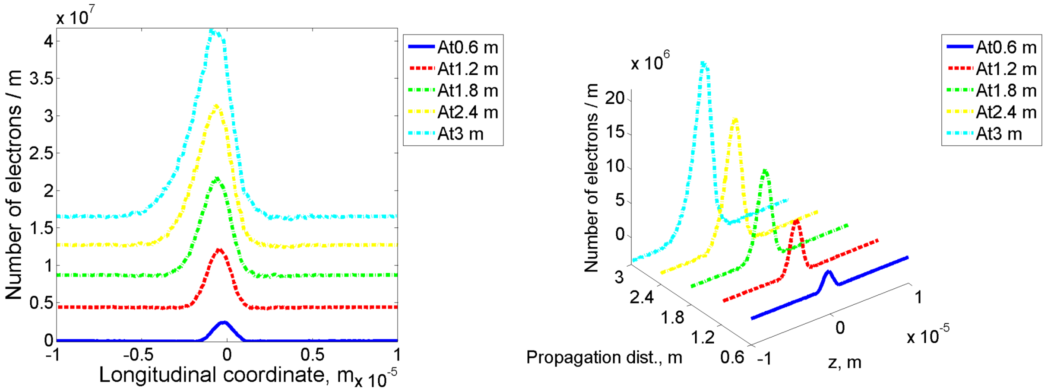

(a) Longitudinal density, 2D

(b) Longitudinal density, 3D

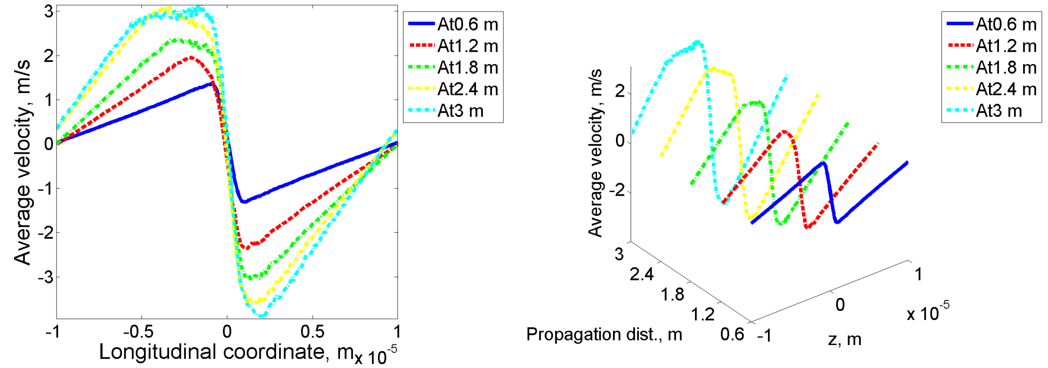

(c) Longitudinal velocity, 2D

(d) Longitudinal velocity, 3D

Figure 91: Longitudinal density and velocity modulation by moving ion 0.5σ off the center of the Gaussian electron beam along x in quadrupole focusing field after 0.6m (blue, solid line), 1.2m (red, dash line), 1.8m (green, dash-dot line, 2.4m (yellow, dash-dot line) and 3m (cyan, dash-dot line)of co-propagation with electrons, curves in (a) are shifted to improve readability.

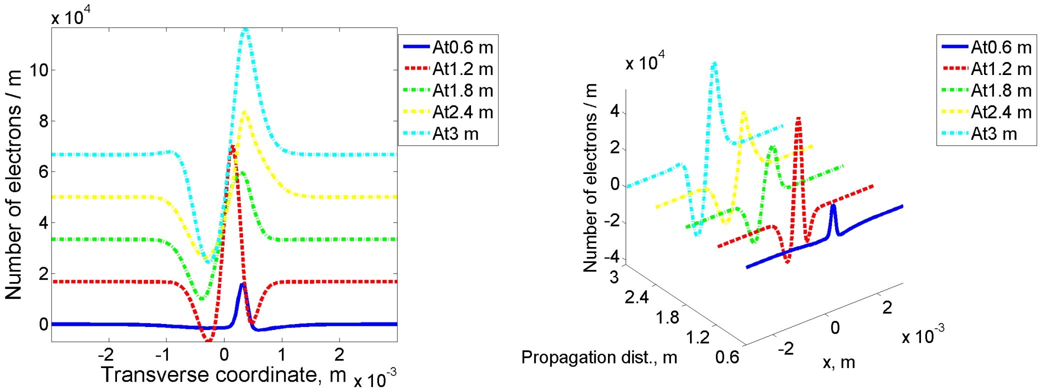

(a) Transverse (x) density, 2D

(b) Transverse (x) density, 3D

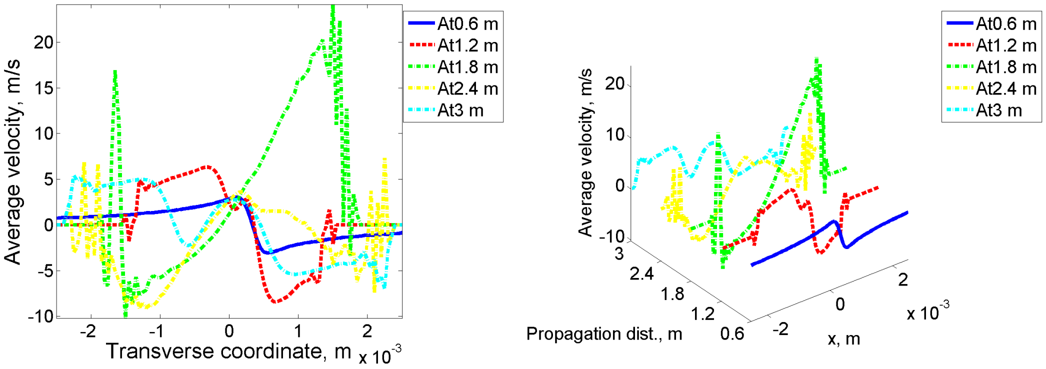

(c) Transverse (x) velocity, 2D

(d) Transverse (x) velocity, 3D

Figure 92: Transverse (x) density and velocity modulation by moving ion 0.5σ off the center of the Gaussian electron beam along x in quadrupole focusing field after 0.6m (blue, solid line), 1.2m (red, dash line), 1.8m (green, dash-dot line, 2.4m (yellow, dash-dot line) and 3m (cyan, dash-dot line)of co-propagation with electrons, curves in (a) are shifted to improve readability.

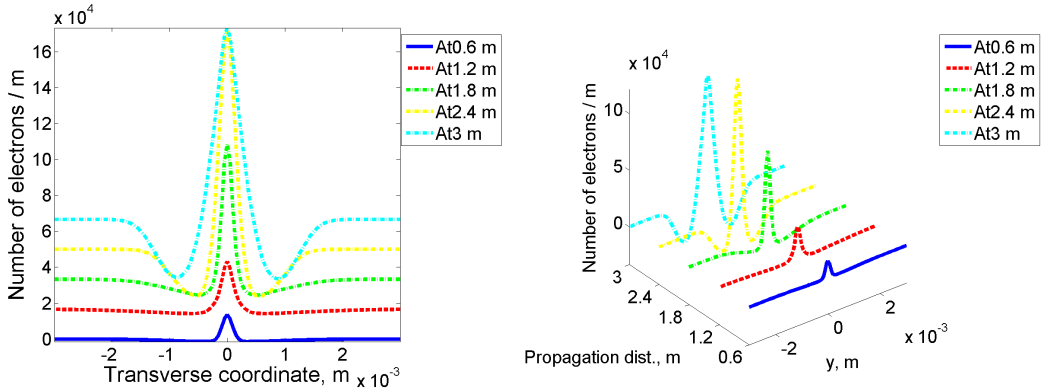

(a) Transverse (y) density, 2D

(b) Transverse (y) density, 3D

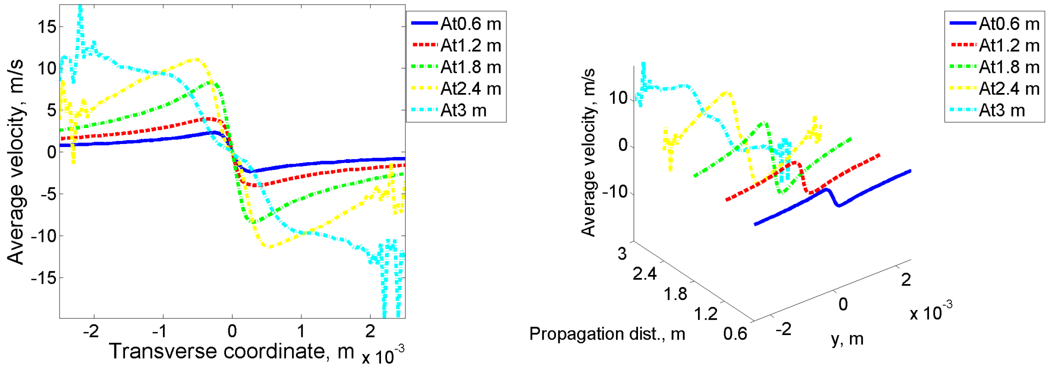

(c) Transverse (y) velocity, 2D

(d) Transverse (y) velocity, 3D

Figure 93: Transverse (y) density and velocity modulation by moving ion 0.5σ off the center of the Gaussian electron beam along x in quadrupole focusing field after 0.6m (blue, solid line), 1.2m (red, dash line), 1.8m (green, dash-dot line, 2.4m (yellow, dash-dot line) and 3m (cyan, dash-dot line)of co-propagation with electrons, curves in (a) are shifted to improve readability.

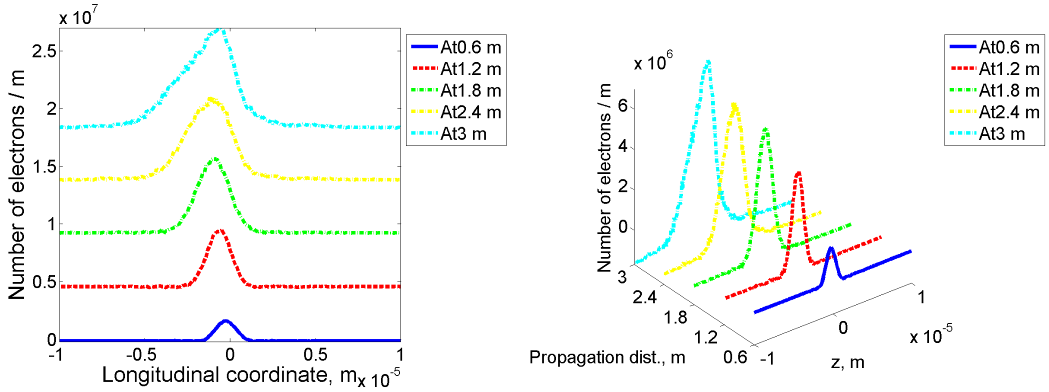

(a) Longitudinal density, 2D

(b) Longitudinal density, 3D

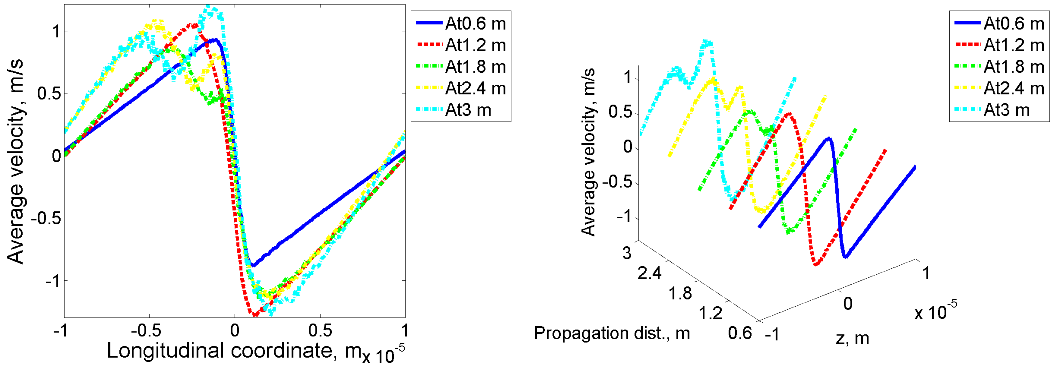

(c) Longitudinal velocity, 2D

(d) Longitudinal velocity, 3D

Figure 94: Longitudinal density and velocity modulation by moving ion 1σ off the center of the Gaussian electron beam along x in quadrupole focusing field after 0.6m (blue, solid line), 1.2m (red, dash line), 1.8m (green, dash-dot line, 2.4m (yellow, dash-dot line) and 3m (cyan, dash-dot line)of co-propagation with electrons, curves in (a) are shifted to improve readability.

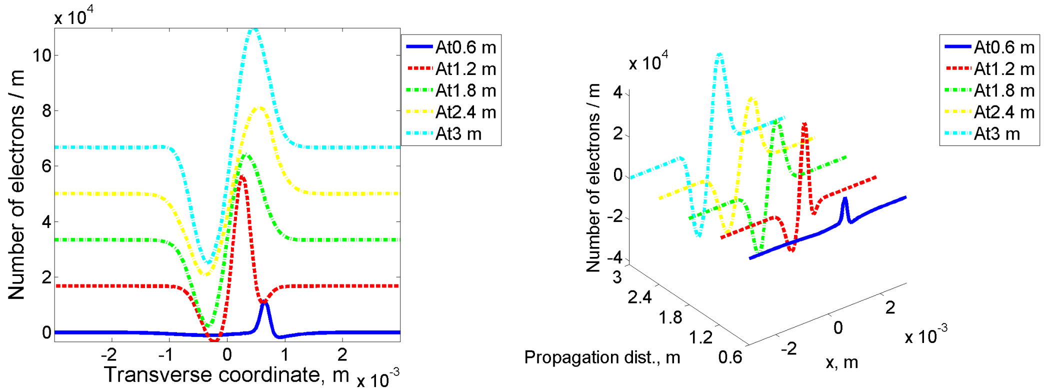

(a) Transverse (x) density, 2D (b) Transverse (x) density, 3D

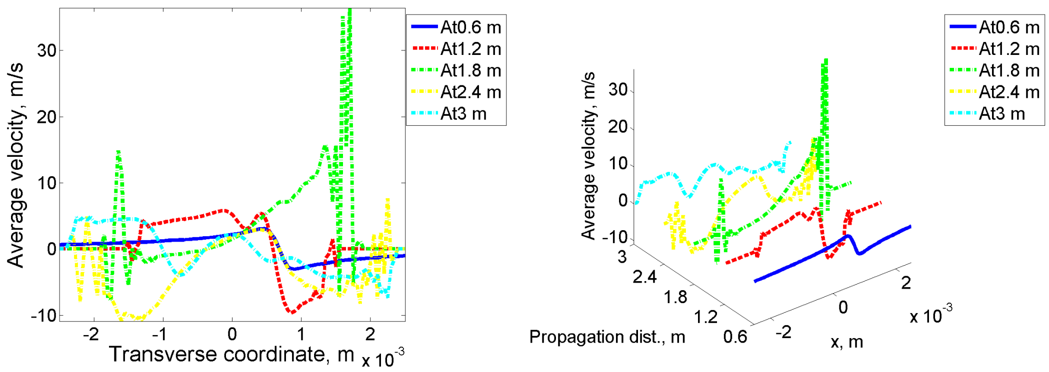

(c) Transverse (x) velocity, 2D (d) Transverse (x) velocity, 3D

Figure 95: Transverse (x) density and velocity modulation by moving ion 1σ off the center of the Gaussian electron beam along x in quadrupole focusing field after 0.6m (blue, solid line), 1.2m (red, dash line), 1.8m (green, dash-dot line, 2.4m (yellow, dash-dot line) and 3m (cyan, dash-dot line)of co-propagation with electrons, curves in (a) are shifted to improve readability.

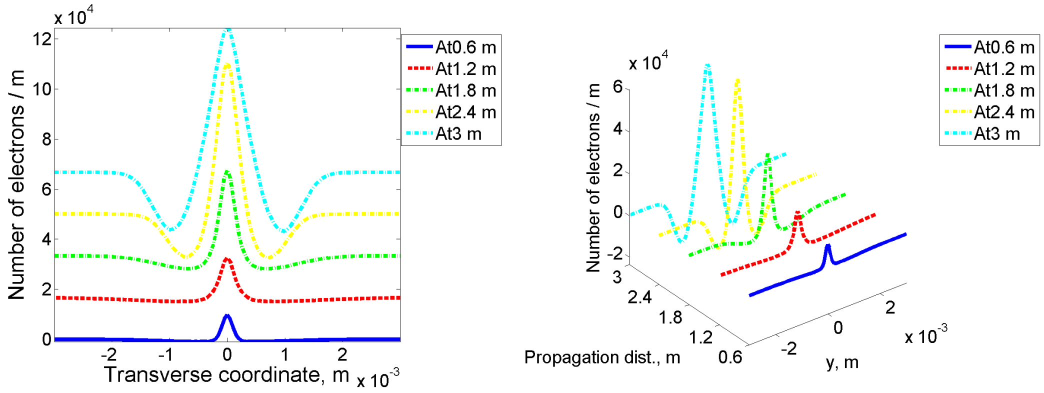

(a) Transverse (y) density, 2D (b) Transverse (y) density, 3D

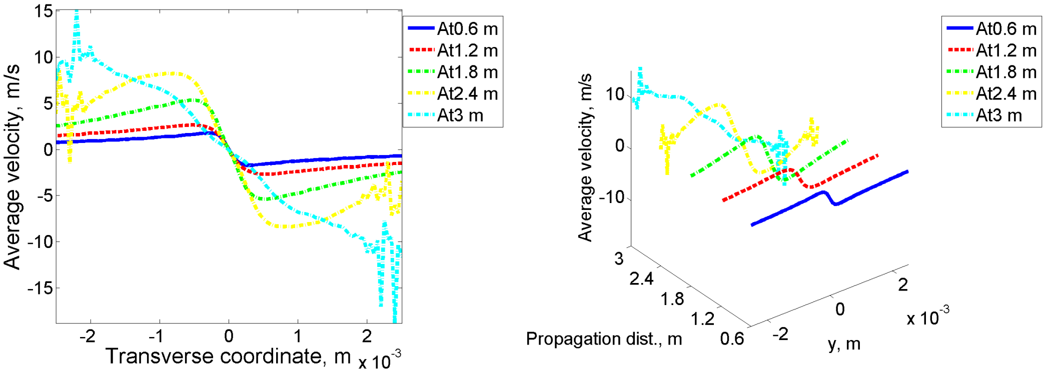

(c) Transverse (y) velocity, 2D (d) Transverse (y) velocity, 3D

Figure 96: Transverse (y) density and velocity modulation by moving ion 1σ off the center of the Gaussian electron beam along x in quadrupole focusing field after 0.6m (blue, solid line), 1.2m (red, dash line), 1.8m (green, dash-dot line, 2.4m (yellow, dash-dot line) and 3m (cyan, dash-dot line)of co-propagation with electrons, curves in (a) are shifted to improve readability.

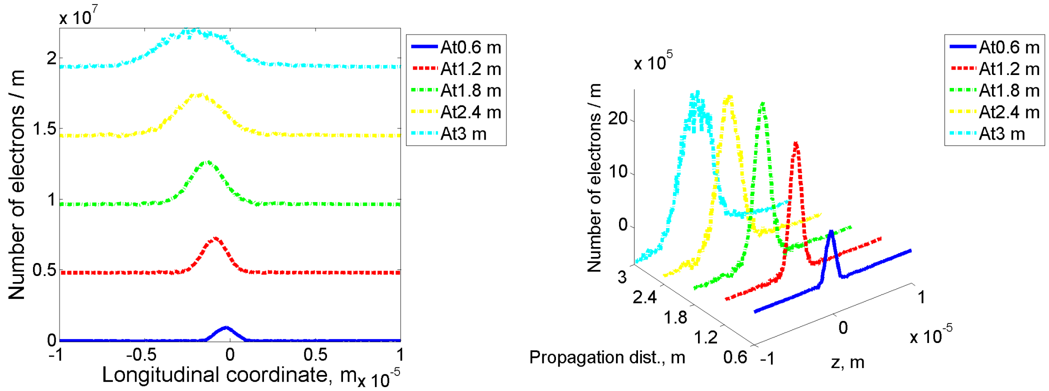

(a) Longitudinal density, 2D

(b) Longitudinal density, 3D

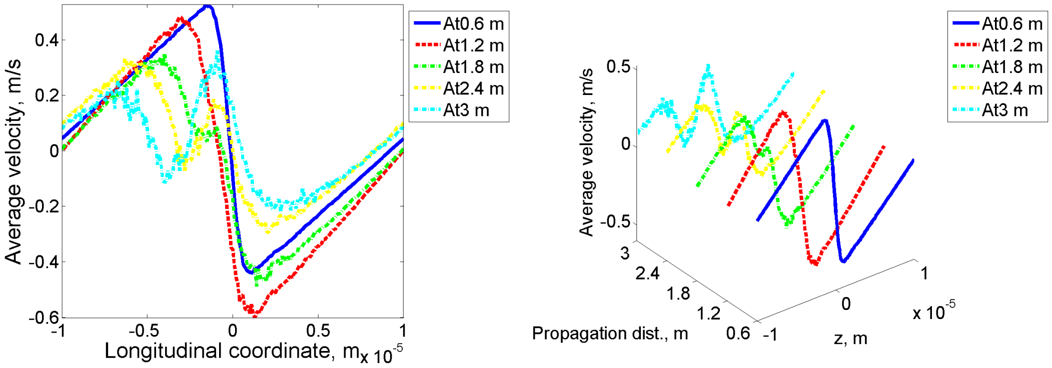

(c) Longitudinal velocity, 2D

(d) Longitudinal velocity, 3D

Figure 97: Longitudinal density and velocity modulation by moving ion 1.5σ off the center of the Gaussian electron beam along x in quadrupole focusing field after 0.6m (blue, solid line), 1.2m (red, dash line), 1.8m (green, dash-dot line, 2.4m (yellow, dash-dot line) and 3m (cyan, dash-dot line)of co-propagation with electrons, curves in (a) are shifted to improve readability.

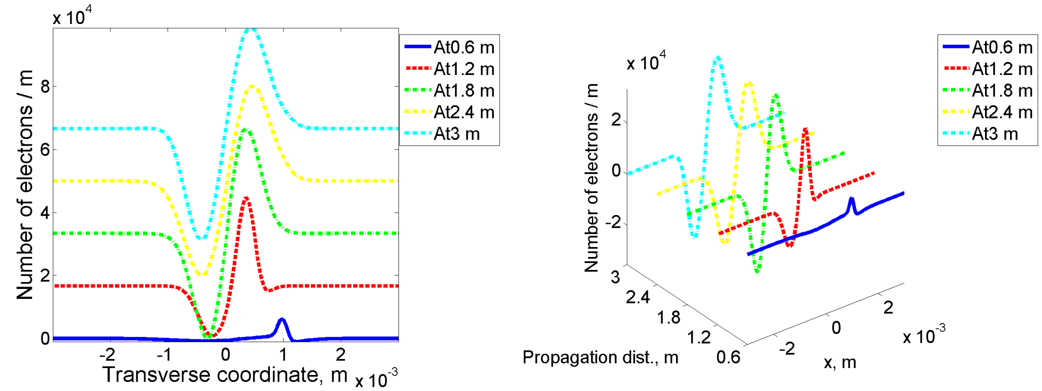

(a) Transverse (x) density, 2D

(b) Transverse (x) density, 3D

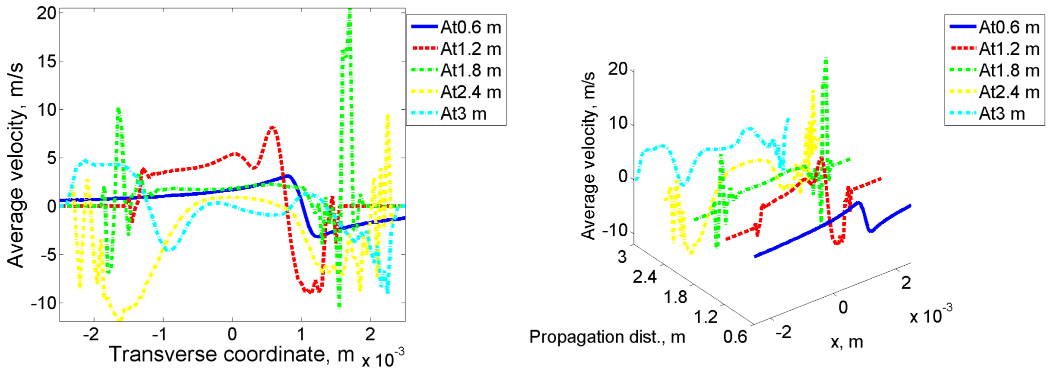

(c) Transverse (x) velocity, 2D

(d) Transverse (x) velocity, 3D

Figure 98: Transverse (x) density and velocity modulation by moving ion 1.5σ off the center of the Gaussian electron beam along x in quadrupole focusing field after 0.6m (blue, solid line), 1.2m (red, dash line), 1.8m (green, dash-dot line, 2.4m (yellow, dash-dot line) and 3m (cyan, dash-dot line)of co-propagation with electrons, curves in (a) are shifted to improve readability.

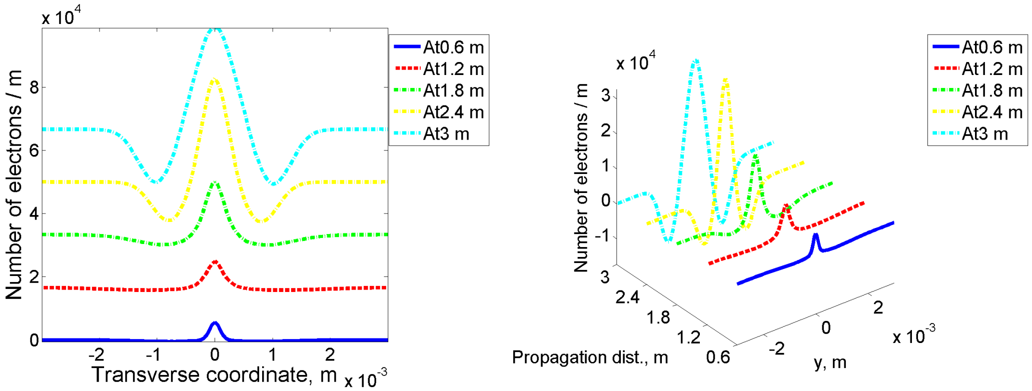

(a) Transverse (y) density, 2D

(b) Transverse (y) density, 3D

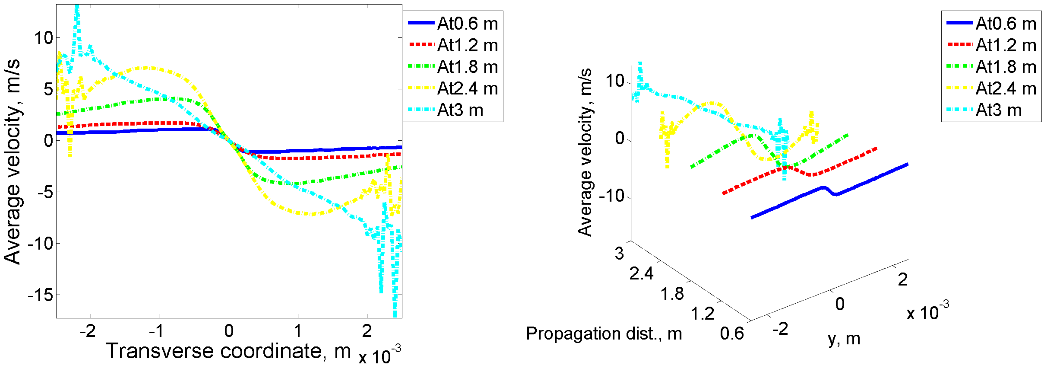

(c) Transverse (y) velocity, 2D

(d) Transverse (y) velocity, 3D

Figure 99: Transverse (y) density and velocity modulation by moving ion 1.5σ off the center of the Gaussian electron beam along x in quadrupole focusing field after 0.6m (blue, solid line), 1.2m (red, dash line), 1.8m (green, dash-dot line, 2.4m (yellow, dash-dot line) and 3m (cyan, dash-dot line)of co-propagation with electrons, curves in (a) are shifted to improve readability.

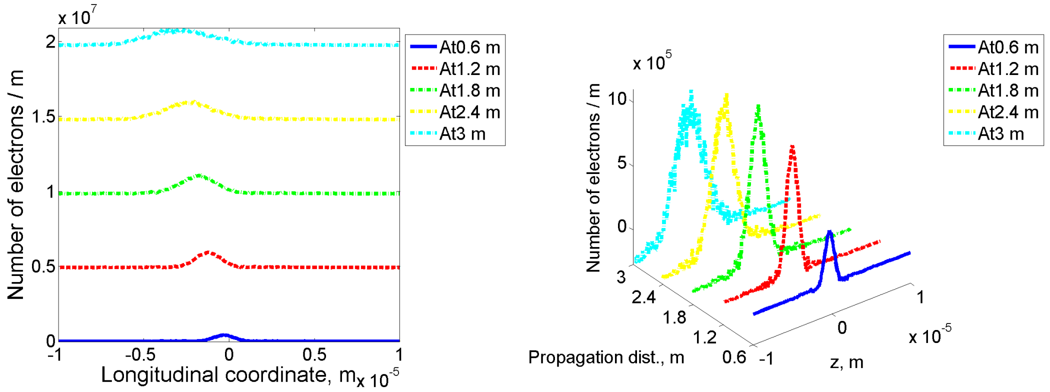

(a) Longitudinal density, 2D

(b) Longitudinal density, 3D

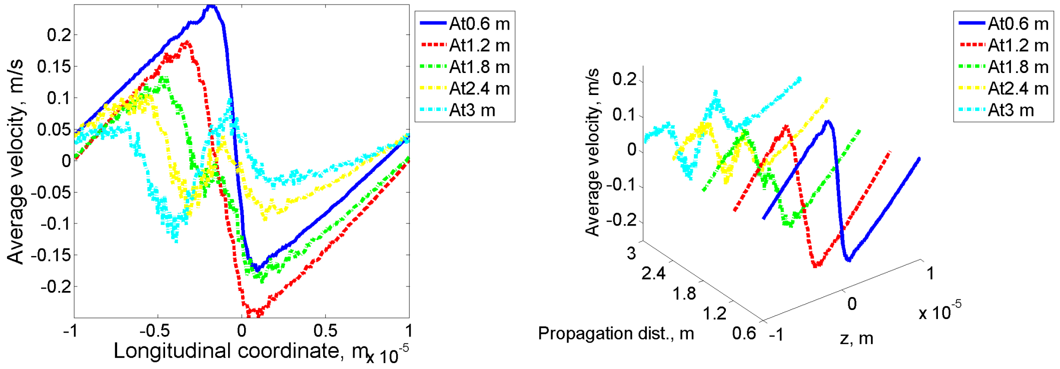

(c) Longitudinal velocity, 2D

(d) Longitudinal velocity, 3D

Figure 100: Longitudinal density and velocity modulation by moving ion 2σ off the center of the Gaussian electron beam along x in quadrupole focusing field after 0.6m (blue, solid line), 1.2m (red, dash line), 1.8m (green, dash-dot line, 2.4m (yellow, dash-dot line) and 3m (cyan, dash-dot line)of co-propagation with electrons, curves in (a) are shifted to improve readability.

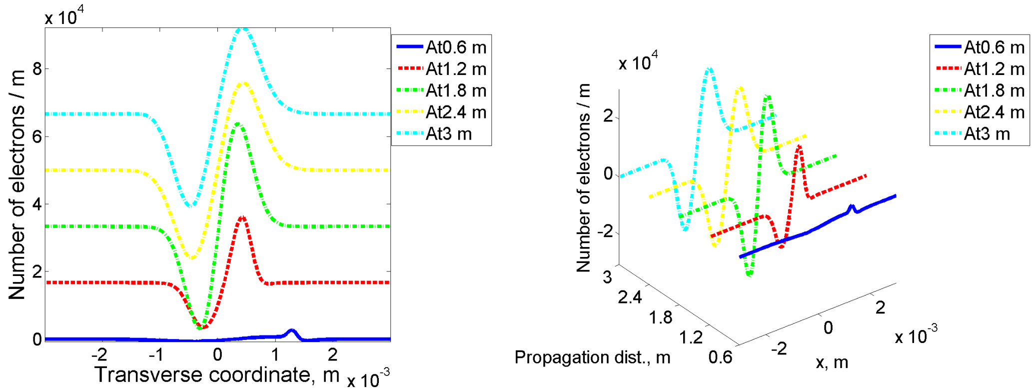

(a) Transverse (x) density, 2D

(b) Transverse (x) density, 3D

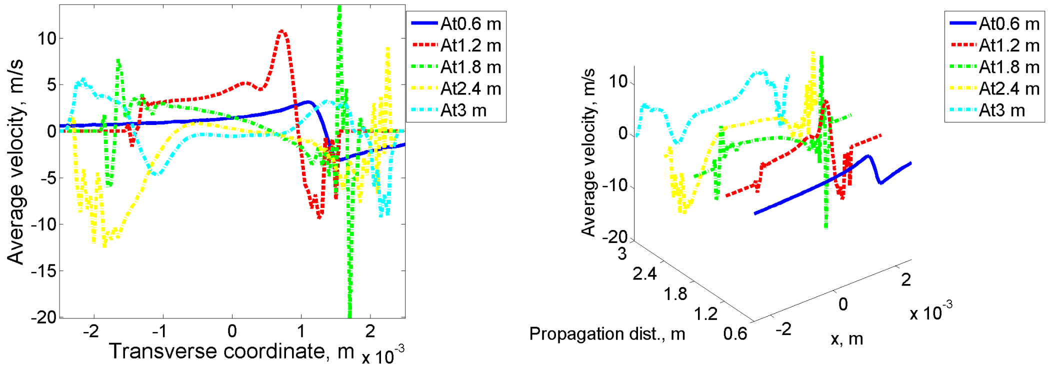

(c) Transverse (x) velocity, 2D

(d) Transverse (x) velocity, 3D

Figure 101: Transverse (x) density and velocity modulation by moving ion 2σ off the center of the Gaussian electron beam along x in quadrupole focusing field after 0.6m (blue, solid line), 1.2m (red, dash line), 1.8m (green, dash-dot line, 2.4m (yellow, dash-dot line) and 3m (cyan, dash-dot line)of co-propagation with electrons, curves in (a) are shifted to improve readability.

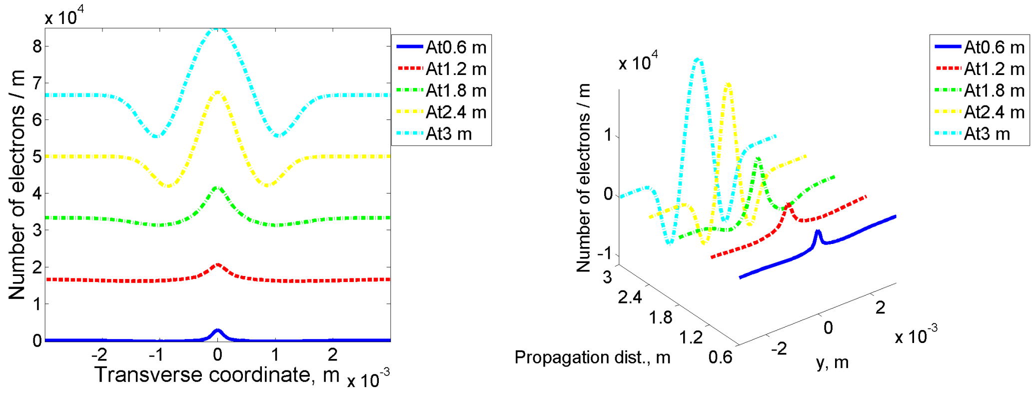

(a) Transverse (y) density, 2D (b) Transverse (y) density, 3D

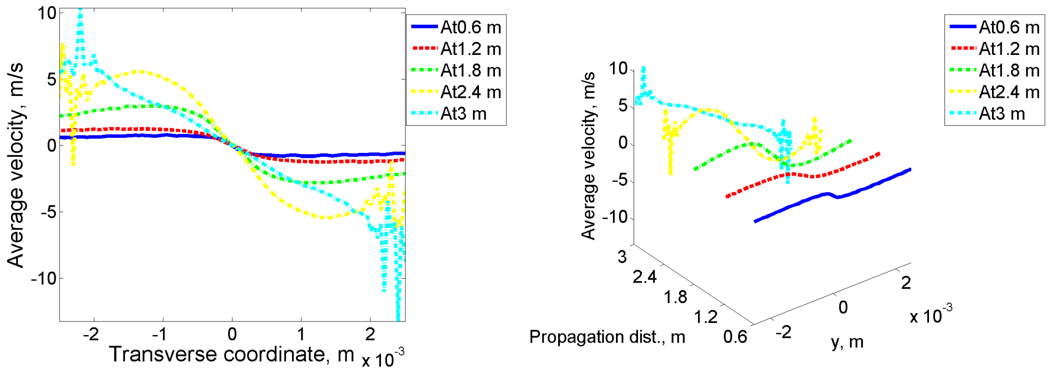

(c) Transverse (y) velocity, 2D (d) Transverse (y) velocity, 3D

Figure 102: Transverse (y) density and velocity modulation by moving ion 2σ off the center of the Gaussian electron beam along x in quadrupole focusing field after 0.6m (blue, solid line), 1.2m (red, dash line), 1.8m (green, dash-dot line, 2.4m (yellow, dash-dot line) and 3m (cyan, dash-dot line)of co-propagation with electrons, curves in (a) are shifted to improve readability.

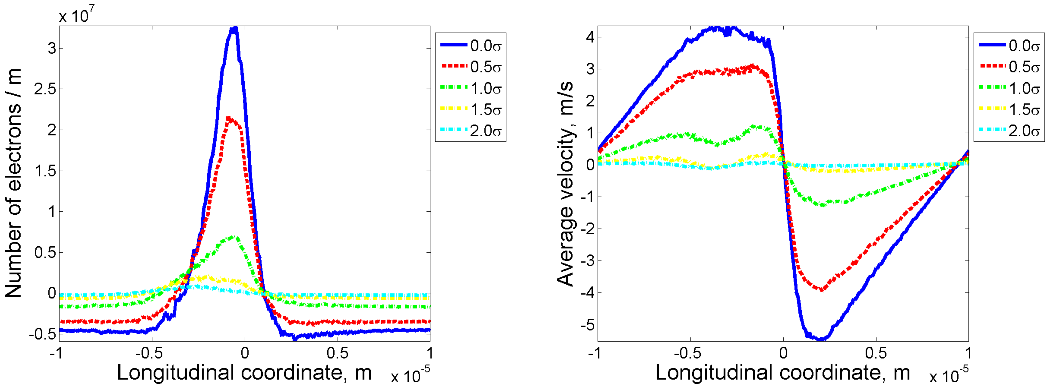

(a) Longitudinal density

(b) Longitudinal velocity

Figure 103: Longitudinal density and velocity modulation by moving ion with various distances off the center of the Gaussian electron beam along x in quadrupole focusing field after 3m of co-propagation with electrons.

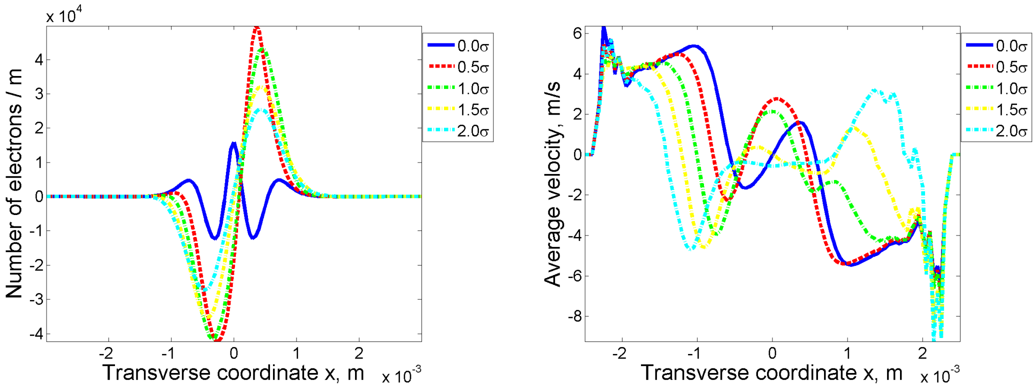

(a) Transverse (x) density (b) Transverse (x) velocity

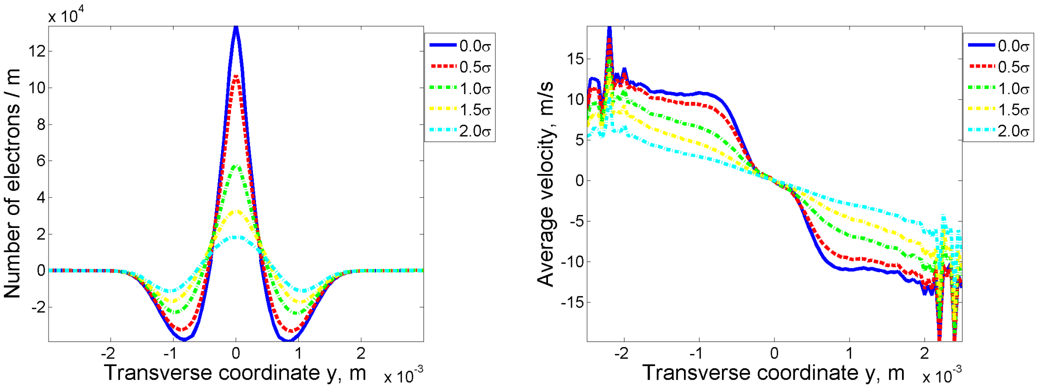

(c) Transverse (y) density (d) Transverse (y) velocity

Figure 104: Transverse density and velocity modulation by moving ion with various distances off the center of the Gaussian electron beam along x in quadrupole focusing field after 3m of co-propagation with electrons.

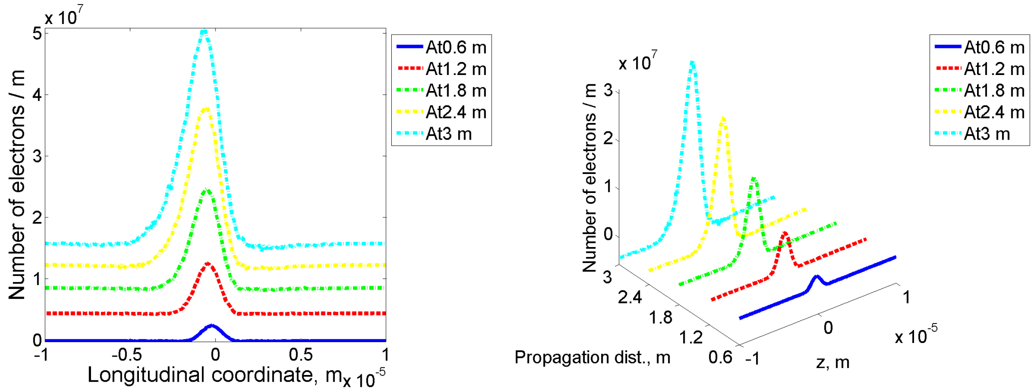

(a) Longitudinal density, 2D (b) Longitudinal density, 3D

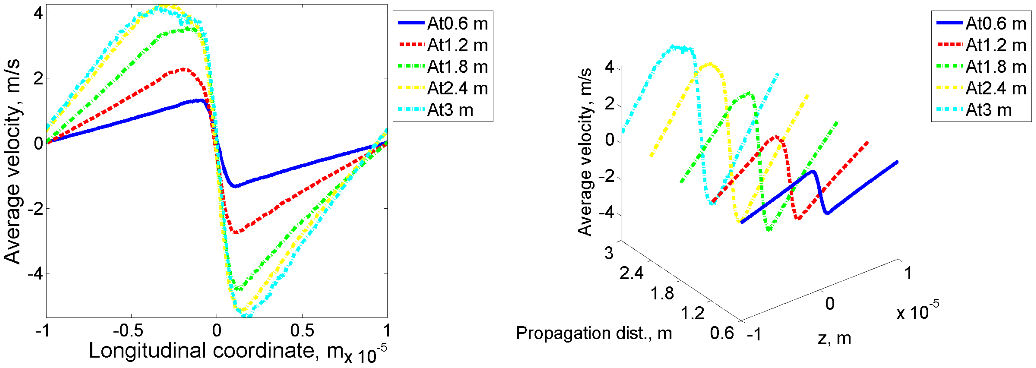

(c) Longitudinal velocity, 2D (d) Longitudinal velocity, 3D

Figure 105: Longitudinal density and velocity modulation by moving ion 0.5σ off the center of the Gaussian electron beam along y in quadrupole focusing field after 0.6m (blue, solid line), 1.2m (red, dash line), 1.8m (green, dash-dot line, 2.4m (yellow, dash-dot line) and 3m (cyan, dash-dot line)of co-propagation with electrons, curves in (a) are shifted to improve readability.

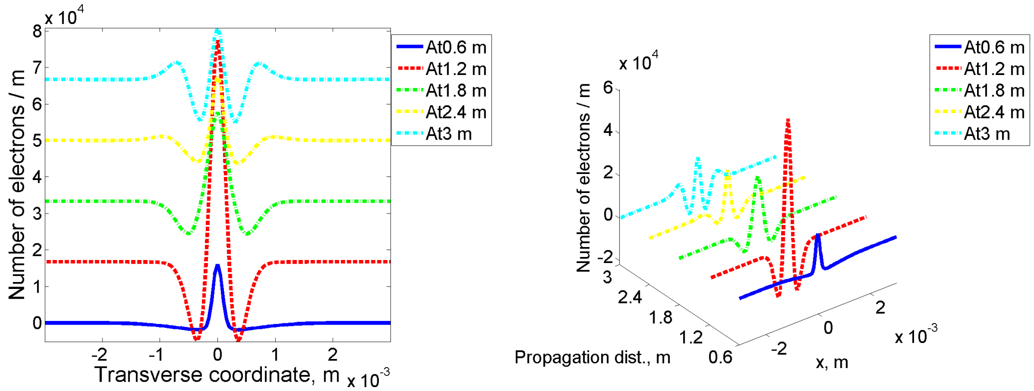

(a) Transverse (x) density, 2D (b) Transverse (x) density, 3D

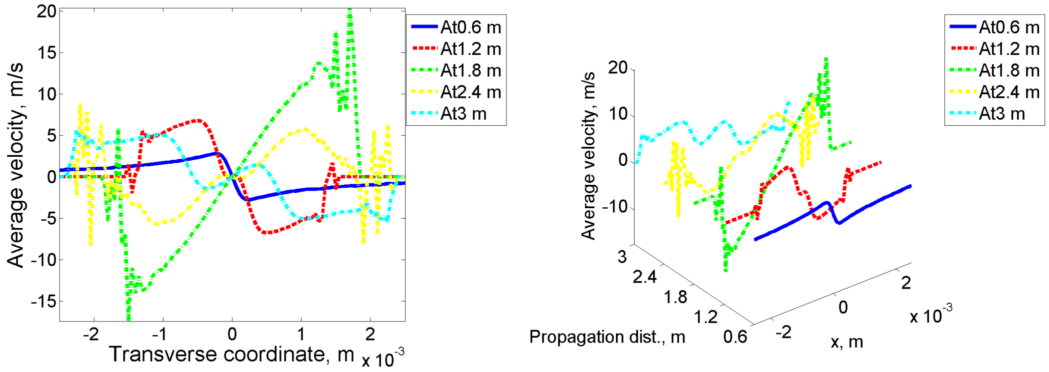

(c) Transverse (x) velocity, 2D (d) Transverse (x) velocity, 3D

Figure 106: Transverse (x) density and velocity modulation by moving ion 0.5σ off the center of the Gaussian electron beam along y in quadrupole focusing field after 0.6m (blue, solid line), 1.2m (red, dash line), 1.8m (green, dash-dot line, 2.4m (yellow, dash-dot line) and 3m (cyan, dash-dot line)of co-propagation with electrons, curves in (a) are shifted to improve readability.

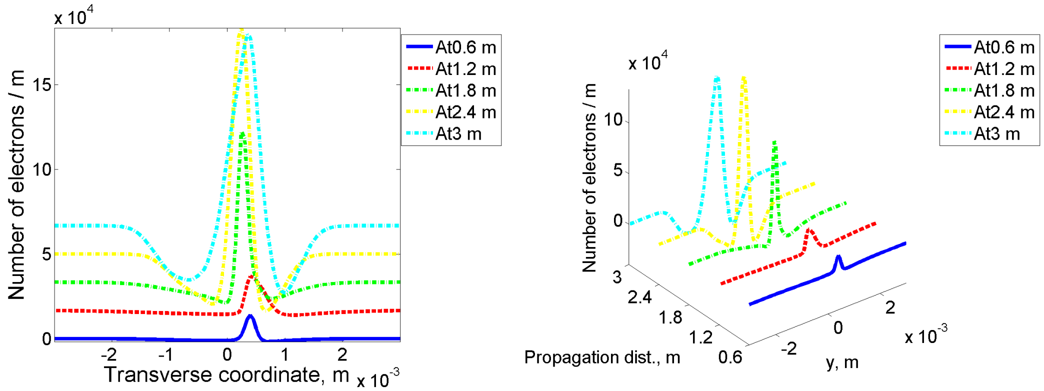

(a) Transverse (y) density, 2D (b) Transverse (y) density, 3D

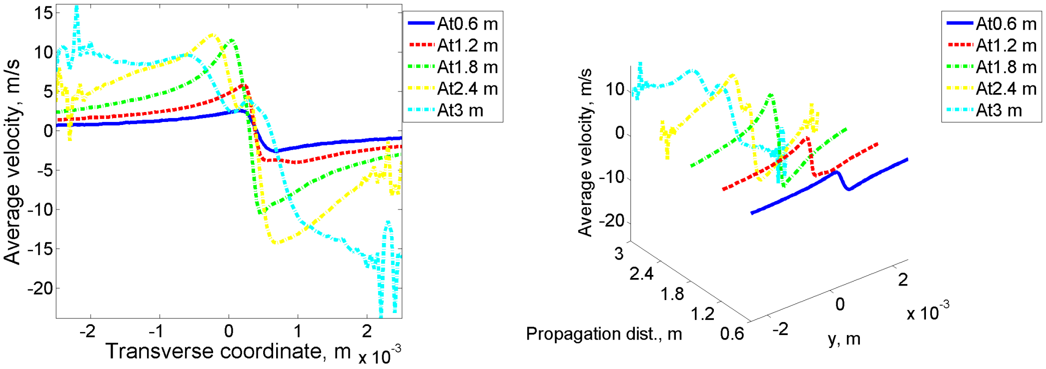

(c) Transverse (y) velocity, 2D (d) Transverse (y) velocity, 3D

Figure 107: Transverse (y) density and velocity modulation by moving ion 0.5σ off the center of the Gaussian electron beam along y in quadrupole focusing field after 0.6m (blue, solid line), 1.2m (red, dash line), 1.8m (green, dash-dot line, 2.4m (yellow, dash-dot line) and 3m (cyan, dash-dot line)of co-propagation with electrons, curves in (a) are shifted to improve readability.

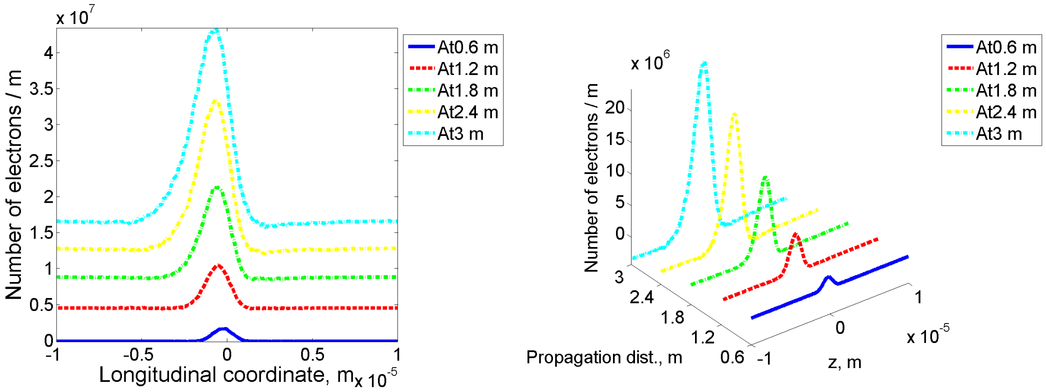

(a) Longitudinal density, 2D (b) Longitudinal density, 3D

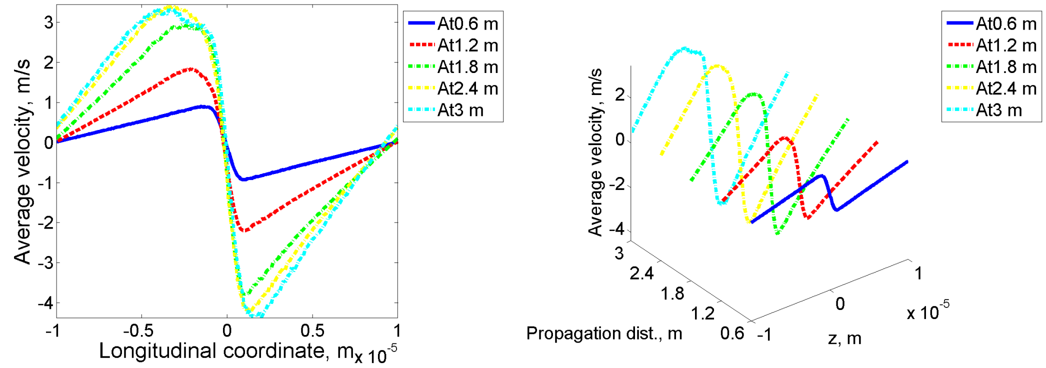

(c) Longitudinal velocity, 2D (d) Longitudinal velocity, 3D

Figure 108: Longitudinal density and velocity modulation by moving ion 1σ off the center of the Gaussian electron beam along y in quadrupole focusing field after 0.6m (blue, solid line), 1.2m (red, dash line), 1.8m (green, dash-dot line, 2.4m (yellow, dash-dot line) and 3m (cyan, dash-dot line)of co-propagation with electrons, curves in (a) are shifted to improve readability.

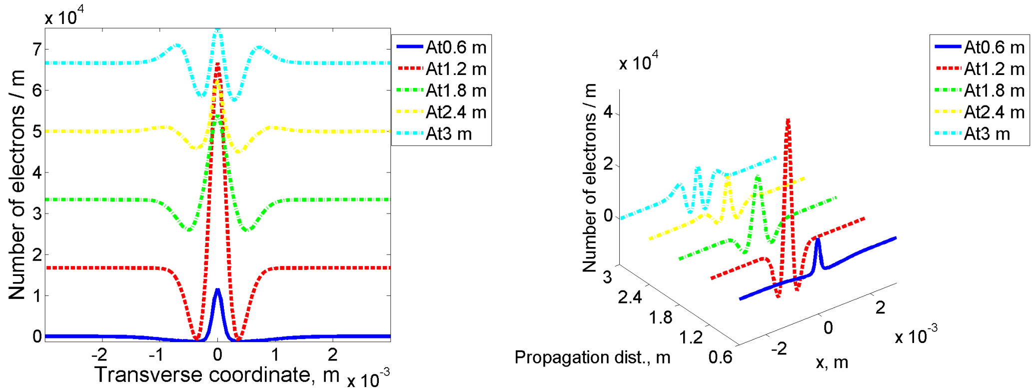

(a) Transverse (x) density, 2D (b) Transverse (x) density, 3D

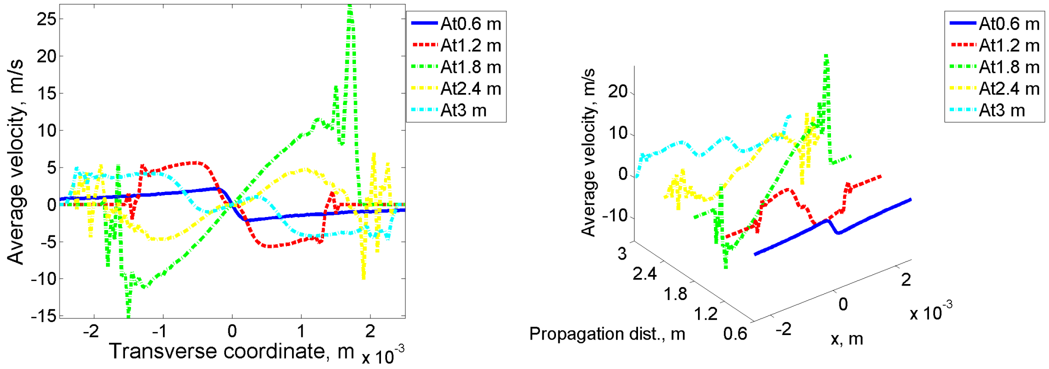

(c) Transverse (x) velocity, 2D (d) Transverse (x) velocity, 3D

Figure 109: Transverse (x) density and velocity modulation by moving ion 1σ off the center of the Gaussian electron beam along y in quadrupole focusing field after 0.6m (blue, solid line), 1.2m (red, dash line), 1.8m (green, dash-dot line, 2.4m (yellow, dash-dot line) and 3m (cyan, dash-dot line)of co-propagation with electrons, curves in (a) are shifted to improve readability.

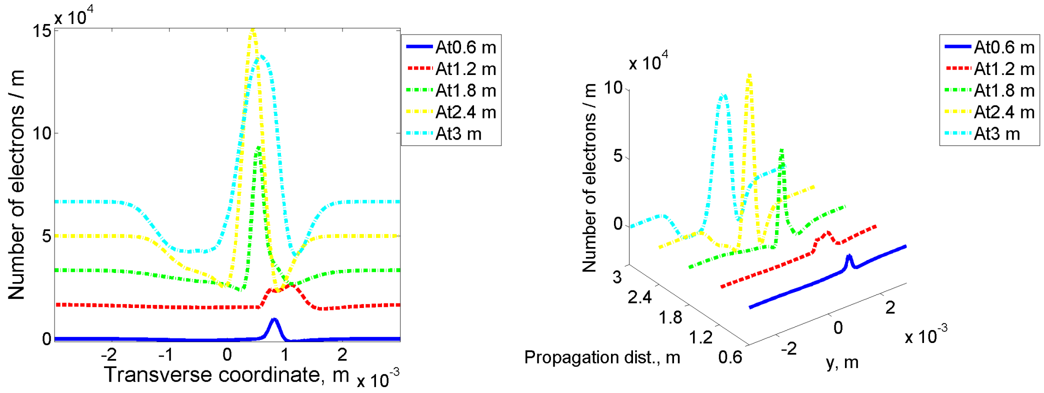

(a) Transverse (y) density, 2D (b) Transverse (y) density, 3D

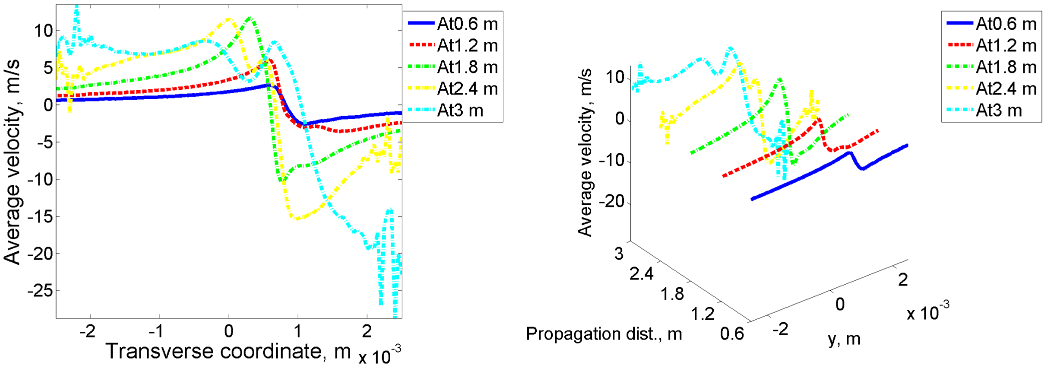

(c) Transverse (y) velocity, 2D (d) Transverse (y) velocity, 3D

Figure 110: Transverse (y) density and velocity modulation by moving ion 1σ off the center of the Gaussian electron beam along y in quadrupole focusing field after 0.6m (blue, solid line), 1.2m (red, dash line), 1.8m (green, dash-dot line, 2.4m (yellow, dash-dot line) and 3m (cyan, dash-dot line)of co-propagation with electrons, curves in (a) are shifted to improve readability.

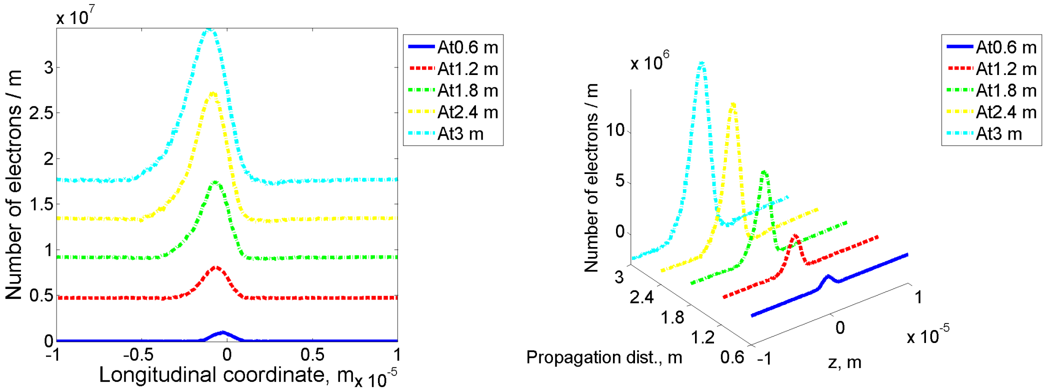

(a) Longitudinal density, 2D (b) Longitudinal density, 3D

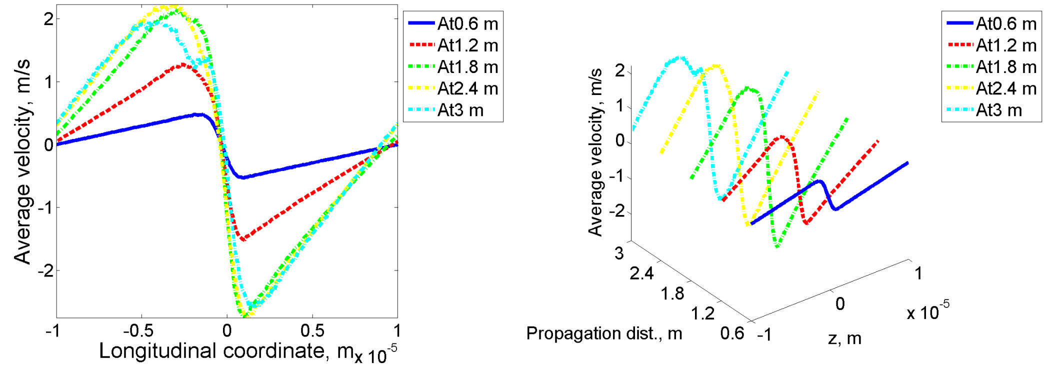

(c) Longitudinal velocity, 2D (d) Longitudinal velocity, 3D

Figure 111: Longitudinal density and velocity modulation by moving ion 1.5σ off the center of the Gaussian electron beam along y in quadrupole focusing field after 0.6m (blue, solid line), 1.2m (red, dash line), 1.8m (green, dash-dot line, 2.4m (yellow, dash-dot line) and 3m (cyan, dash-dot line)of co-propagation with electrons, curves in (a) are shifted to improve readability.

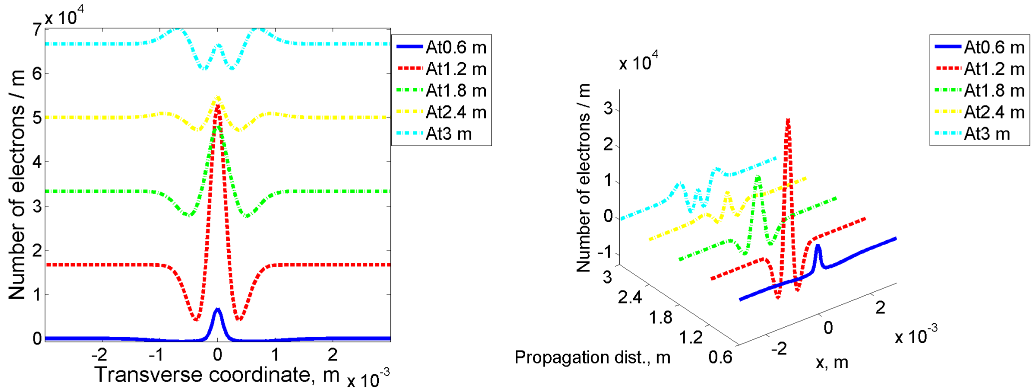

(a) Transverse (x) density, 2D

(b) Transverse (x) density, 3D

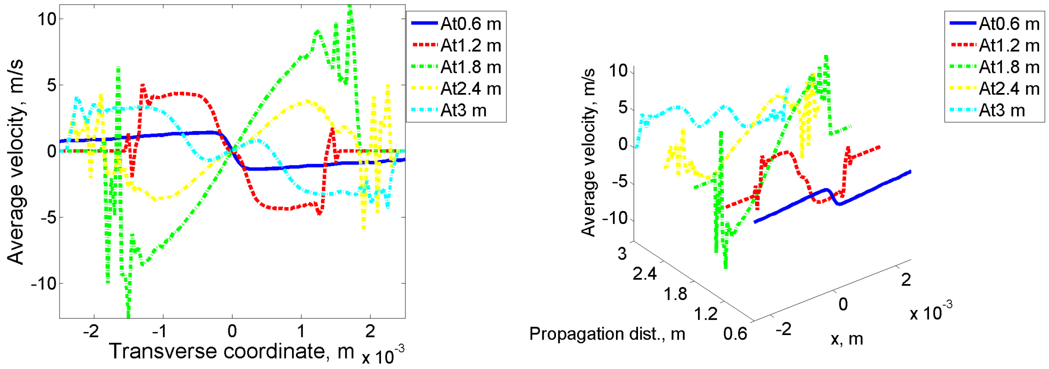

(c) Transverse (x) velocity, 2D

(d) Transverse (x) velocity, 3D

Figure 112: Transverse (x) density and velocity modulation by moving ion 1.5σ off the center of the Gaussian electron beam along y in quadrupole focusing field after 0.6m (blue, solid line), 1.2m (red, dash line), 1.8m (green, dash-dot line, 2.4m (yellow, dash-dot line) and 3m (cyan, dash-dot line)of co-propagation with electrons, curves in (a) are shifted to improve readability.

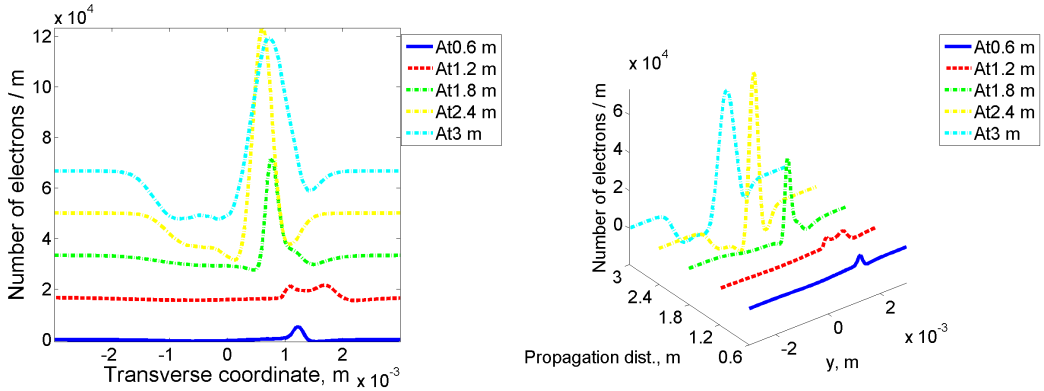

(a) Transverse (y) density, 2D

(b) Transverse (y) density, 3D

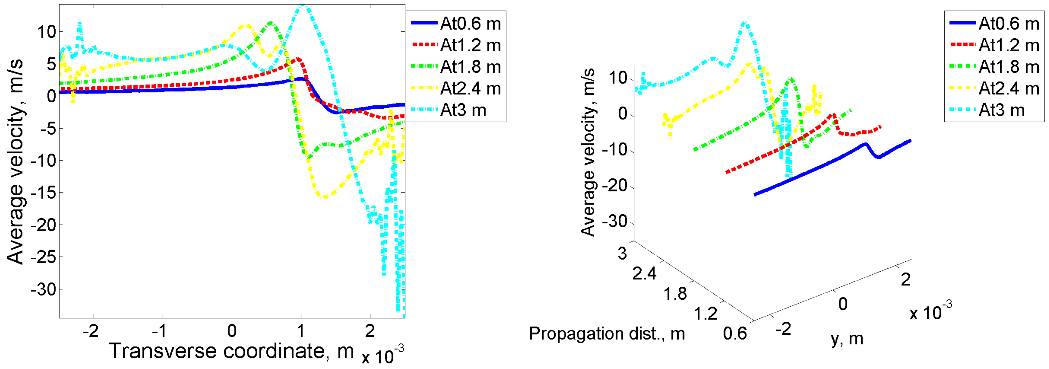

(c) Transverse (y) velocity, 2D

(d) Transverse (y) velocity, 3D

Figure 113: Transverse (y) density and velocity modulation by moving ion 1.5σ off the center of the Gaussian electron beam along y in quadrupole focusing field after 0.6m (blue, solid line), 1.2m (red, dash line), 1.8m (green, dash-dot line, 2.4m (yellow, dash-dot line) and 3m (cyan, dash-dot line)of co-propagation with electrons, curves in (a) are shifted to improve readability.

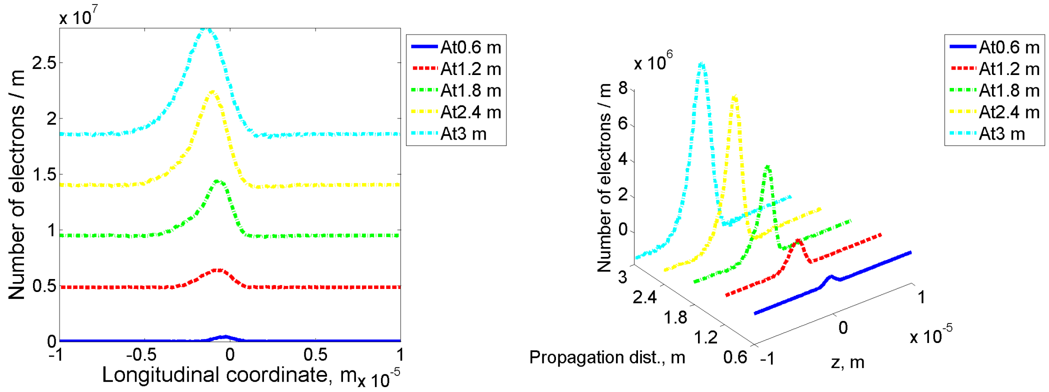

(a) Longitudinal density, 2D

(b) Longitudinal density, 3D

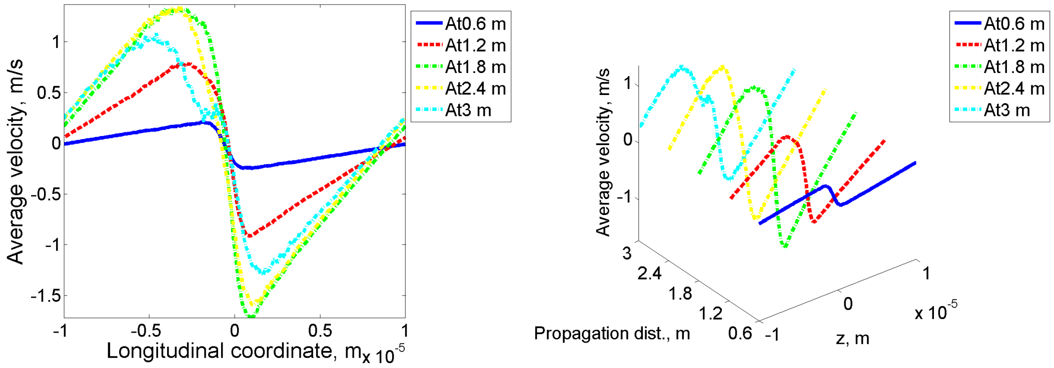

(c) Longitudinal velocity, 2D

(d) Longitudinal velocity, 3D

Figure 114: Longitudinal density and velocity modulation by moving ion 2σ off the center of the Gaussian electron beam along y in quadrupole focusing field after 0.6m (blue, solid line), 1.2m (red, dash line), 1.8m (green, dash-dot line, 2.4m (yellow, dash-dot line) and 3m (cyan, dash-dot line)of co-propagation with electrons, curves in (a) are shifted to improve readability.

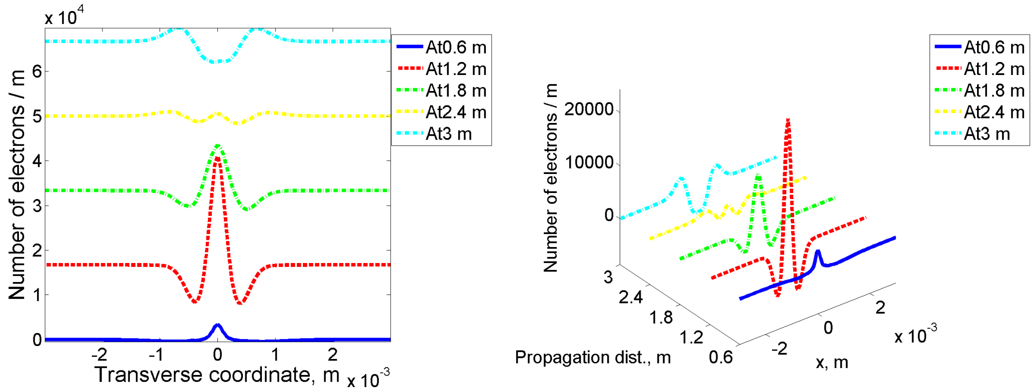

(a) Transverse (x) density, 2D (b) Transverse (x) density, 3D

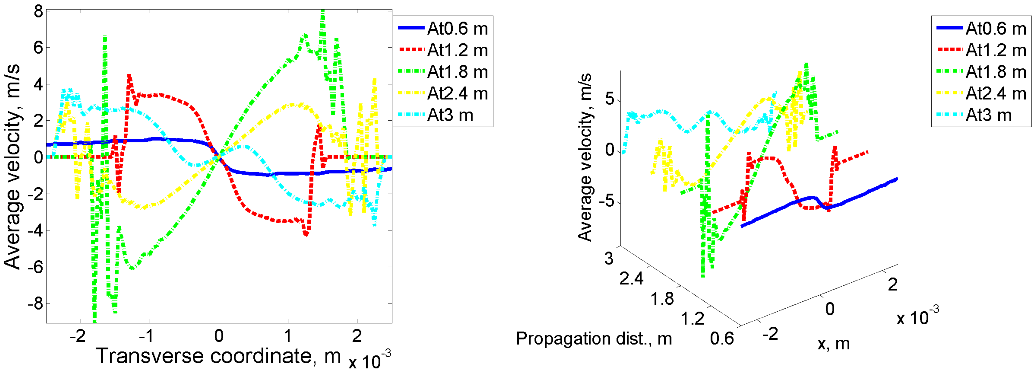

(c) Transverse (x) velocity, 2D (d) Transverse (x) velocity, 3D

Figure 115: Transverse (x) density and velocity modulation by moving ion 2σ off the center of the Gaussian electron beam along y in quadrupole focusing field after 0.6m (blue, solid line), 1.2m (red, dash line), 1.8m (green, dash-dot line, 2.4m (yellow, dash-dot line) and 3m (cyan, dash-dot line)of co-propagation with electrons, curves in (a) are shifted to improve readability.

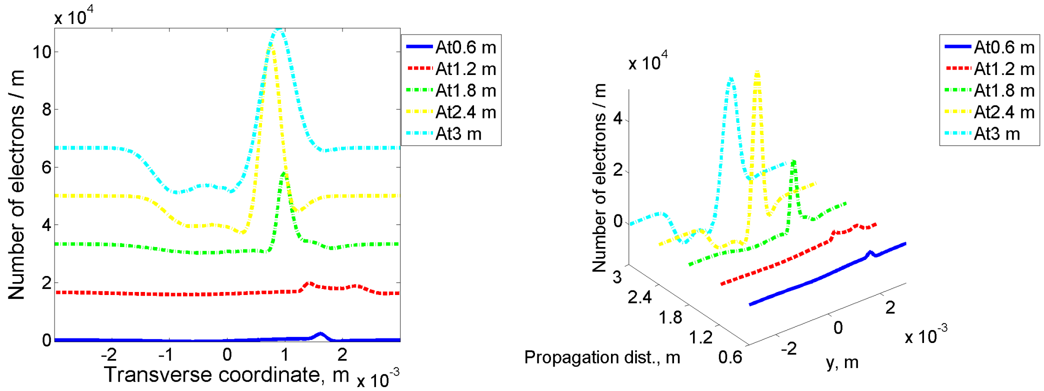

(a) Transverse (y) density, 2D (b) Transverse (y) density, 3D

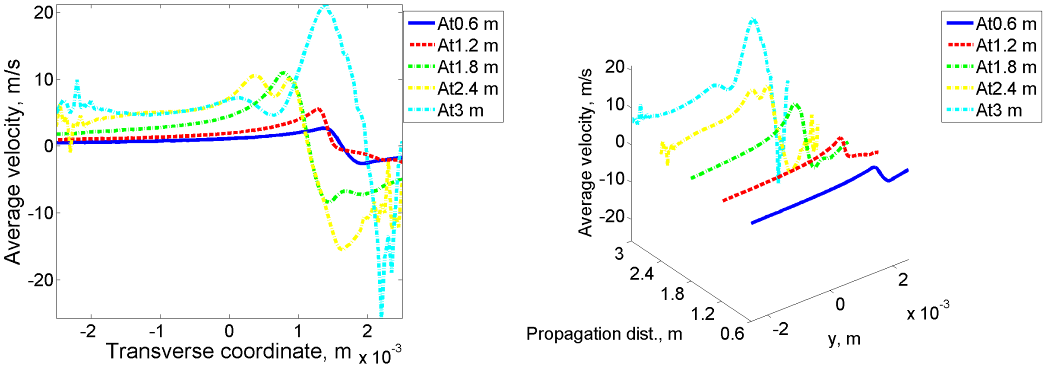

(c) Transverse (y) velocity, 2D (d) Transverse (y) velocity, 3D

Figure 116: Transverse (y) density and velocity modulation by moving ion 2σ off the center of the Gaussian electron beam along y in quadrupole focusing field after 0.6m (blue, solid line), 1.2m (red, dash line), 1.8m (green, dash-dot line, 2.4m (yellow, dash-dot line) and 3m (cyan, dash-dot line)of co-propagation with electrons, curves in (a) are shifted to improve readability.

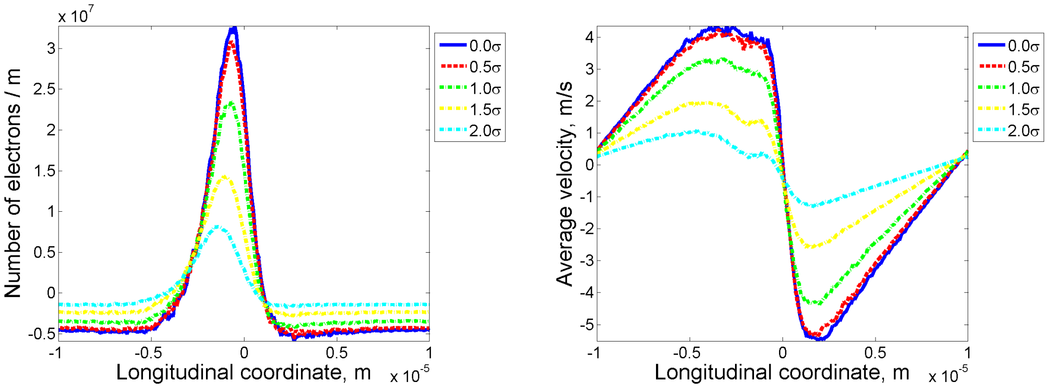

(a) Longitudinal density (b) Longitudinal velocity

Figure 117: Longitudinal density and velocity modulation by moving ion with various distances off the center of the Gaussian electron beam along y in quadrupole focusing field after 3m of co-propagation with electrons.

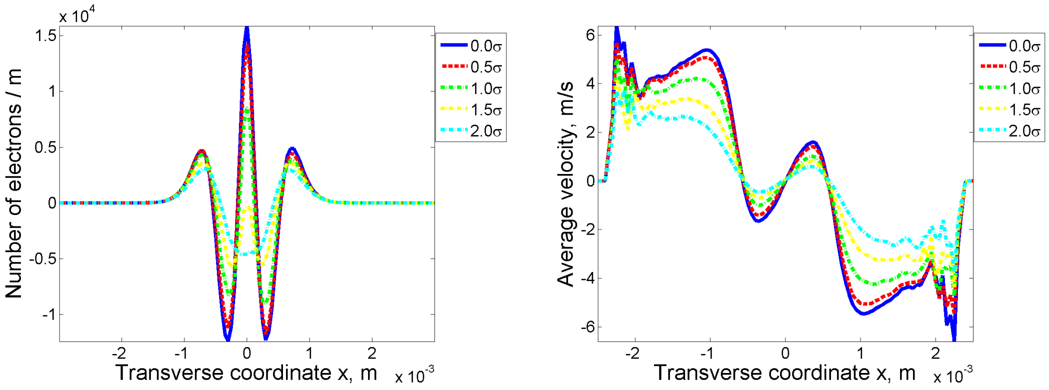

(a) Transverse (x) density (b) Transverse (x) velocity

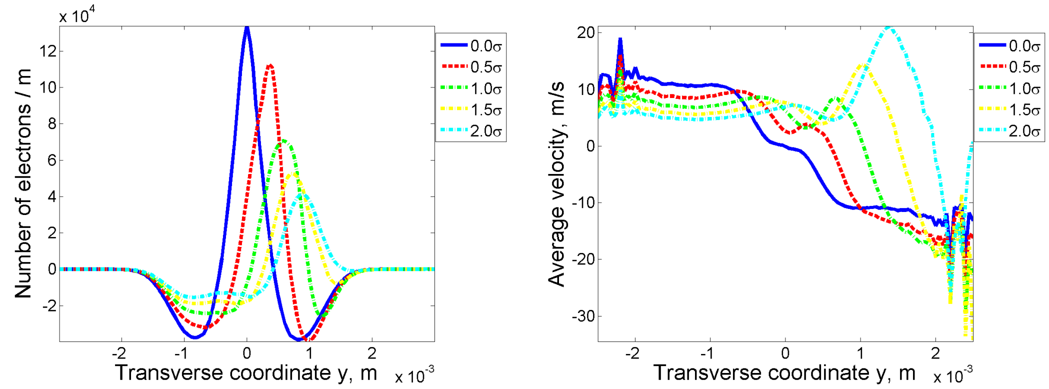

(c) Transverse (y) density (d) Transverse (y) velocity

Figure 118: Transverse density and velocity modulation by moving ion with various distances off the center of the Gaussian electron beam along y in quadrupole focusing field after 3m of co-propagation with electrons.

The simulation results in this section give predictions for the experiments of modulator section in coherent electron cooling, as we use realistic distribution for electron beam and appropriate boundary conditions, and the settings for quadrupole magnetic fields in simulations are relevant to the real experiments.

3.5 Phase Advance in Quadrupole Field

In the modulator simulations using quadupoles focusing fields, the modulation signal due to the ion is orders smaller, compared with the random motion of the electron beam and the effect from the quadrupole magnetic fields. In order to extract the modulation signal, we always run two simulations with identical initial electron distribution, one without ion and one with ion, and we take difference of the density and velocity distribution between these two simulations to get the modulation signal. This subtraction could eliminate the noise from randomness and the global motion of the electron beam due to the quadrupole fields, but some large motion of background still affects the resulting signals even after the subtraction, which are shown in the modulation results using quadrupole fields in last section. The force for background's motion is the space charge effect, and kick from quadrupole may introduce nonlinearity to the space charge effect. To confirm that the reverse slopes in transverse velocity modulations are due to the quadrupole focusing fields, we make the following comparison between the simulation with quadrupoles and without any quadrupole (pure space charge effect).

Figure 119 shows the comparison of transverse beam size of the electron beam between two simulations. In one simulation, there is no quadrupole focusing field and the electron beam expands due to the space charge effect. In another simulation, the quadrupole magnetic fields change the electron beam's transverse size during the modulation process. Figure 120 shows that the modulation process without any quadrupole focusing fields is similar with the simulations using linear focusing fields that the velocity modulation gradually builds up. But the quadrupole fields affect not only the background electron beam but also modulation signal, and is responsible for the reverse slopes in the velocity modulation results.

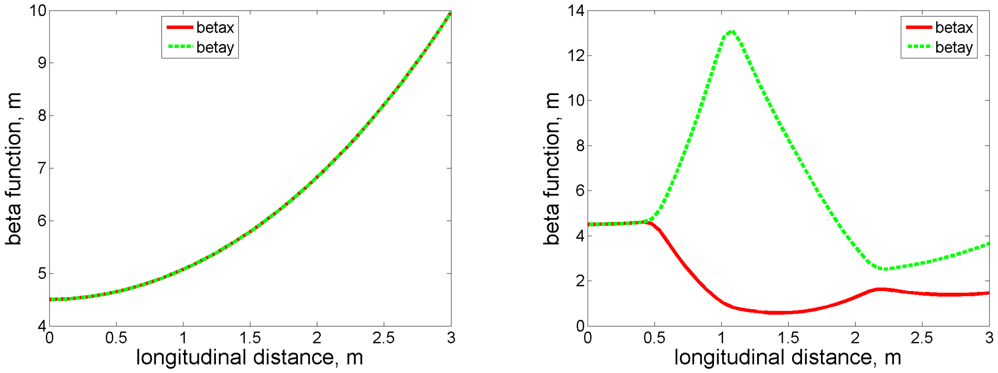

(a) Space charge only (b) Space charge with quadrupoles

Figure 119: Comparison of beta function changes between with and without quadrupoles.

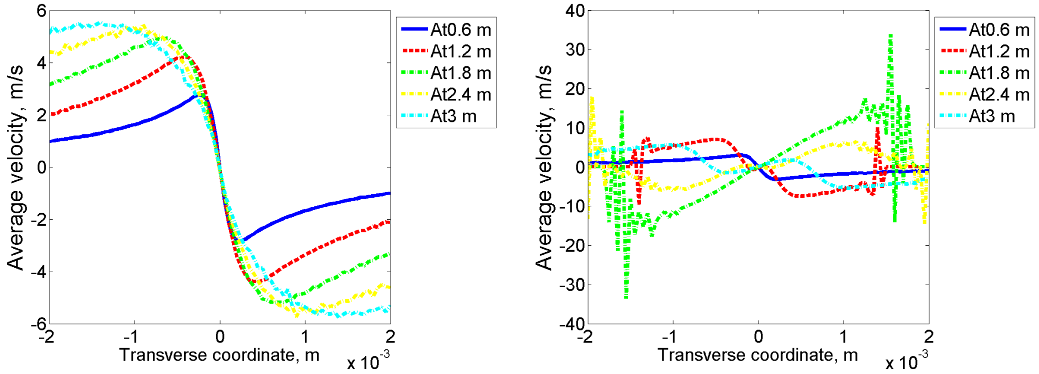

(a) Space charge only (b) Space charge with quadrupoles

Figure 120: Comparison of transverse velocity modulation changes between with and without quadrupoles.

In order to study the details of electron beam dynamics under the quadrupole focusing fields, we track the motion of a line of particles. These particles are evenly distributed along the x direction, with zero initial velocity in the comoving frame, and they form a horizontal line in phase space, and we track the dynamics of this line of particles in the phase space under the quadrupole focusing fields. This line of particles with zero initial velocity can represent the dynamics of the background electron beam without attractions from the ion. We also add initial velocity kick to the line of particles to model the modulation due to the ion, for the studies of effects from quadrupole magnetic fields on the dynamics of the modulation signal. But the real velocity modulation by the single ion is orders smaller than the effects from the quadrupole fields, so we increase the modulation signal by orders to clearly view the dynamics of the modulation signal qualitatively. Here we choose the phase space consisting of x and x', as the quadrupole fields have stronger effects in x direction rather than y direction.

We start our phase studies using the transfer matrix derived from the Hill's equation. In accelerator physics, the transverse motions of beams at different locations along the designed longitudinal trajectory can be estimated by the Hill's equation, given in equation (38),

$$\begin{aligned} x''(s) + K_x(s)x(s) = & \ 0 \\ y''(s) + K_y(s)y(s) = & \ 0 \end{aligned} \tag{38}$$

where x is the transverse coordinate in horizontal direction, y is the transverse coordinate in vertical direction, s is the longitudinal location in the designed orbit in accelerators, parameters $K_x(s)$ and $K_y(s)$ depend on the components along the longitudinal orbit. Note that, equation (38) is the first order calculation of the transverse motions for the particles with reference energy and designed momentum. As we consider the phase space consisting of x and x', we only need to solve the equation (39), which is the Hill's equation in horizontal direction.

$$x''(s) + K_x(s)x(s) = 0 \tag{39}$$

Given initial conditions, the solution to equation (39) can be written in the form (40),

$$\begin{pmatrix} x(s) \\ x'(s) \end{pmatrix} = M(s, s_0) \begin{pmatrix} x(s_0) \\ x'(s_0) \end{pmatrix} \tag{40}$$

where $x(s_0)$ and $x'(s_0)$ are initial location and velocity, and $M(s, s_0)$ is the transfer matrix depending on the parameter $K_x(s)$ in equation (39). Specific values of $K_x(s)$ for focusing quadrupole, de-focusing quadupole and drift space are given in (41), where K is related with the the strength of the quadrupole.

$$K_x(s) = \begin{cases} K(K > 0), & \text{focusing quadrupole} \\ 0, & \text{drift space} \\ K(K < 0), & \text{de-focusing quadrupole} \end{cases} \tag{41}$$

Using the values in equation (41), the transfer matrix $M(s, s_0)$ can be explicitly solved, given in equation (42), where $l = s - s_0$ is the longitudinal propagating distance.

$$M(s, s_0) = \begin{cases} \begin{pmatrix} \cos\sqrt{K}l & \frac{1}{\sqrt{K}}\sin\sqrt{K}l \\ -\sqrt{K}\sin\sqrt{K}l & \cos\sqrt{K}l \end{pmatrix}, & \text{focusing quadrupole} \\ \begin{pmatrix} 1 & l \\ 0 & 1 \end{pmatrix}, & \text{drift space} \\ \begin{pmatrix} \cosh\sqrt{|K|}l & \frac{1}{\sqrt{|K|}}\sinh\sqrt{|K|}l \\ \sqrt{|K|}\sinh\sqrt{|K|}l & \cosh\sqrt{|K|}l \end{pmatrix}, & \text{de-focusing quadrupole} \end{cases} \tag{42}$$

Under the thin-lens approximation for quadrupoles, given in equation (43),

$$\lim_{l \to 0} |K| l = \frac{1}{f} \tag{43}$$

The transfer matrix can be approximated as in equation (44).

$$M(s, s_0) \to \begin{cases} \begin{pmatrix} 1 & 0 \\ -1/f & 1 \end{pmatrix}, & \text{focusing quadrupole} \\ \begin{pmatrix} 1 & l \\ 0 & 1 \end{pmatrix}, & \text{drift space} \\ \begin{pmatrix} 1 & 0 \\ 1/f & 1 \end{pmatrix}, & \text{de-focusing quadrupole} \end{cases} \tag{44}$$

Using the approximations of transfer matrix given in equation (44), we track the transverse motions of the line of particles in transverse phase space along x direction. Resulting dynamics of the transverse phase advance of the lines of particles with and without initial velocity modulation are presented in figure 121.

Four quadrupole magnets are installed in the modulator section of coherent electron cooling experiments, and we calculate the distributions of the line of particles in the transverse phase space after each quadrupole, as well as at the entrance and exit of the modulator section. The lines of particles without initial velocity kick represent the background electron beam in our modulator simulations, and are shown in black dot lines in figure 121. The quadrupole magnetic fields give strong velocity kick to the line of particles, especially at the locations far from the center, and cause the rotation of the line of particles in the phase space, and eventually reverse this line in x direction at late stages of modulator. The modulation signal, shown in blue circles in figure 121, also rotates in the phase space due to the quadrupole magnetic fields. The rotation speed is different for the lines of particles with and without initial velocity modulation, within the same quadrupole magnetic fields. The rotations of electrons in the phase space and the different rotation speeds of background electrons and modulated electrons are the reasons for the reverse slopes in transverse velocity modulations in previous simulations results of modulation process using quadrupole focusing fields. In previous modulator simulations, as shot noise and quadrupole fields' effects are orders larger than the modulation signal due to a single ion, we always take difference between two simulations, one with ion and one without ion, to extract the modulation signal from the shot noise and motions due to quadrupole magnetic fields. If the background electron beam is reversed in the transverse phase space, the modulation signal on top of the background is also reversed. In addition, the background and the signal rotates in different speeds in the phase space, which makes the process more complicate. We can see that, both the reverse slopes in transverse velocity modulation in figure 57 and the reverse of the background in x direction in figure 121 happen at the locations where the transverse beam size is compressed by the quadrupole fields, and nonlinearity in space charge effect due to the quadrupole fields become very strong when the beam size is extremely small.

We also perform the simulations of similar phase advance studies using code SPACE, and the results are given in figure 122.

In figure 122, the dynamics of the lines of particles in the transverse plane are consistent with figure 121 which are obtained using transfer matrix derived from Hill's equation. The discrepancy in the distributions of par-

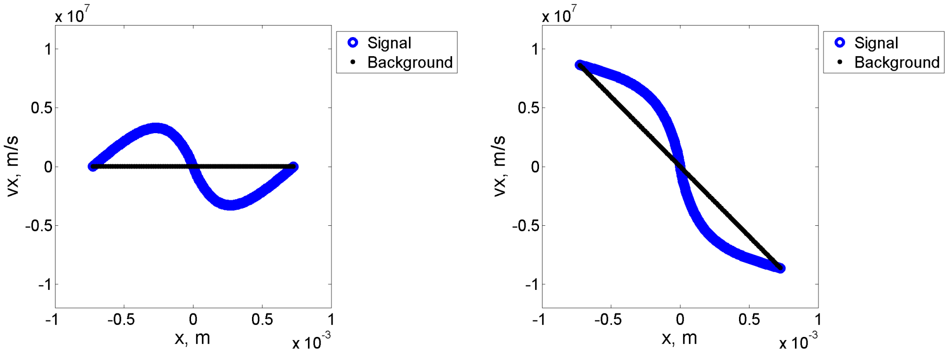

(a) At entrance of modulator (b) After quadrupole 1

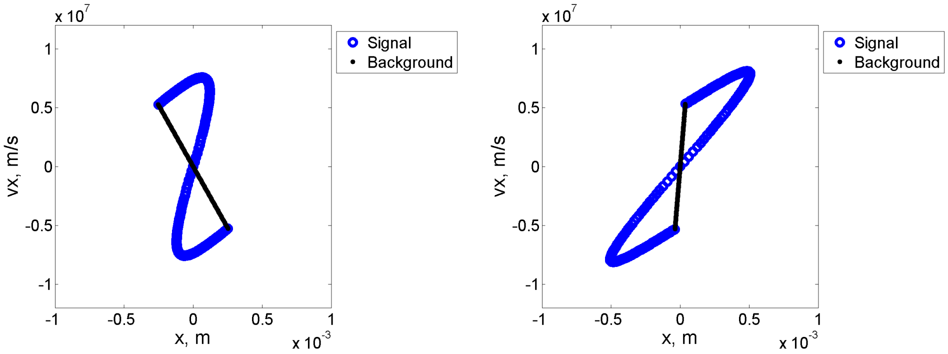

(c) After quadrupole 2 (d) After quadrupole 3

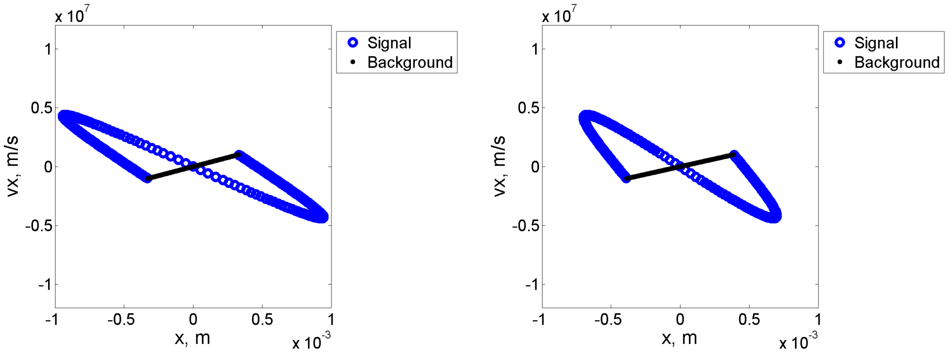

(e) After quadrupole 4 (f) At exit of modulator

Figure 121: Phase advance of a line of particles with / without initial velocity kick, using transfer matrix, under the quadrupole focusing field, at various propagating distances in modulator.

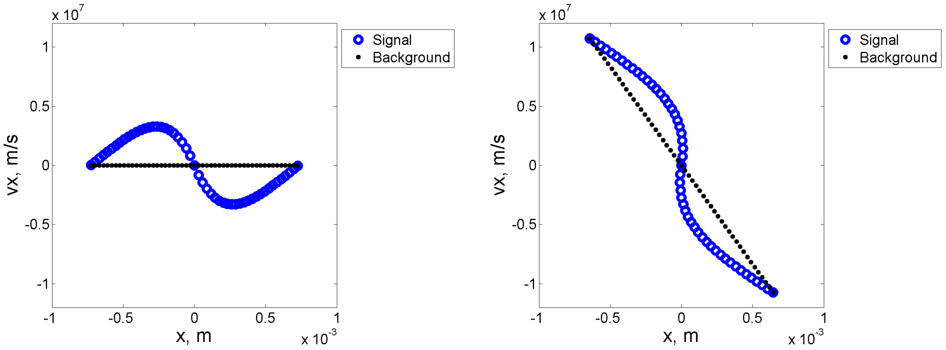

(a) At entrance of modulator

(b) After quadrupole 1

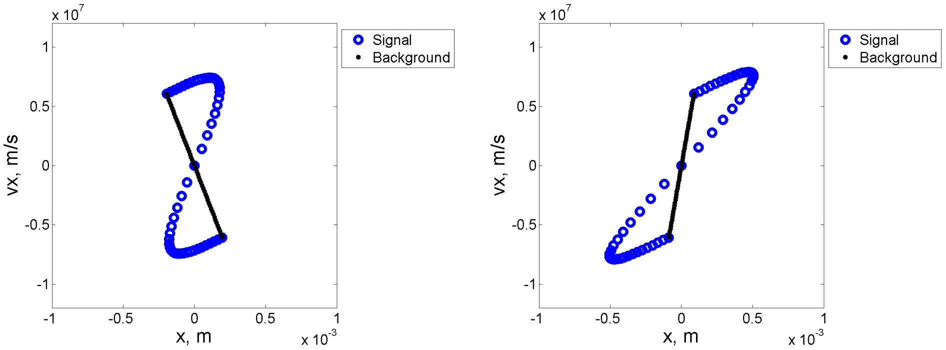

(c) After quadrupole 2

(d) After quadrupole 3

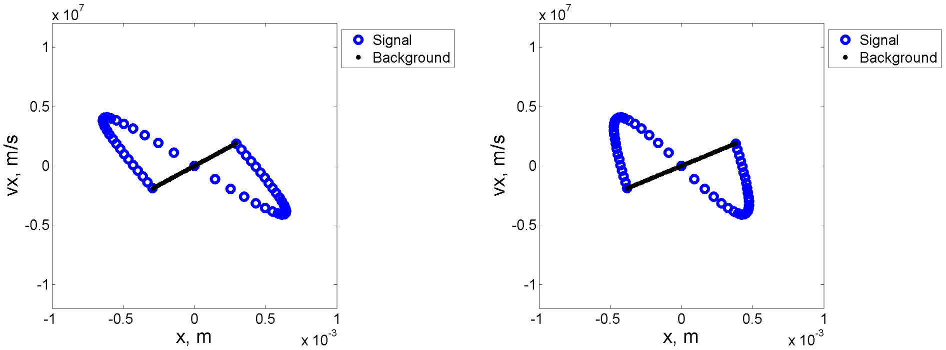

(e) After quadrupole 4

(f) At exit of modulator

Figure 122: Phase advance of a line of particles with / without initial velocity kick, using SPACE code, under the quadrupole focusing field, at various propagating distances in modulator.

ticles in transverse phase space between using transfer matrix and SPACE code is due to the different assumptions of quadrupoles for these two methods. The method using transfer matrix uses the thin-lens approximation for quadrupole magnetic fields, which assumes that the longitudinal size of the quadrupoles is extremely small and the corresponding magnetic fields only give an instant velocity kick to the particles at the points where the quadrupoles are located. The method using SPACE code sets regular longitudinal size for all of the four quadrupoles in modulator section, and the length of quadrupoles are relevant to the coherent electron cooling experiments, so this method gives more realistic results which are close to the experiments.

The results in figure 122 consider a line of particles propagating through the modulator section under the quadrupole magnetic fields. As there are a few particles used for the phase advance studies, the space charge effect is negligibly small. In following phase advance studies, we want to study the influence of the space charge effect on the phase advance. The lines of particles are embedded into the whole electron beam and we repeat the simulations of phase advance studies in SPACE code. The resulting dynamics of the lines of particles are given in figure 123.

We can visualize the influence of the space charge effect from the whole electron beam by comparing figures 122 and 123. As expected, the space charge effect slows down the phase advance and the rotation speed of the lines of particles in the transverse phase space. The background line of particles (shown in black dots) without whole electron beam has already reversed after quadrupole 3 in figure 122d, and the same line of particles embedded in the electron beam is not reversed after quadrupole 3 in figure 123d. The space charge effect also changes the shape of the background line of particles because it causes expansion of the particles in transverse directions, so the background line of particles is no longer a straight line but with some curves, and these curves are also affected by the quadrupole magnetic fields. The modulation signal is also affected by the space charge effect.

The phase advance studies clearly show the effects from the quadrupole magnetic fields on the motions of electron beam in the transverse phase space, and we track a specific line of particles instead of calculating global quantities averaged over whole electron beam. The quadrupole magnetic fields could dramatically rotates the electron beam in phase space and even reverse it, and this is the reason for the reverse slopes in the transverse velocity modulations in the previous section.

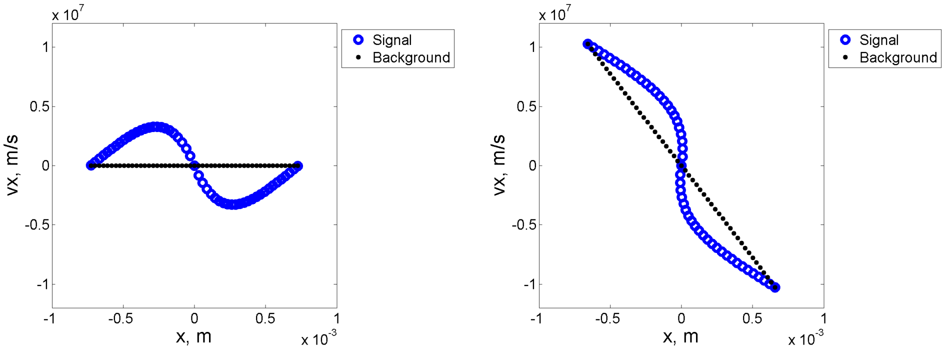

(a) At entrance of modulator (b) After quadrupole 1

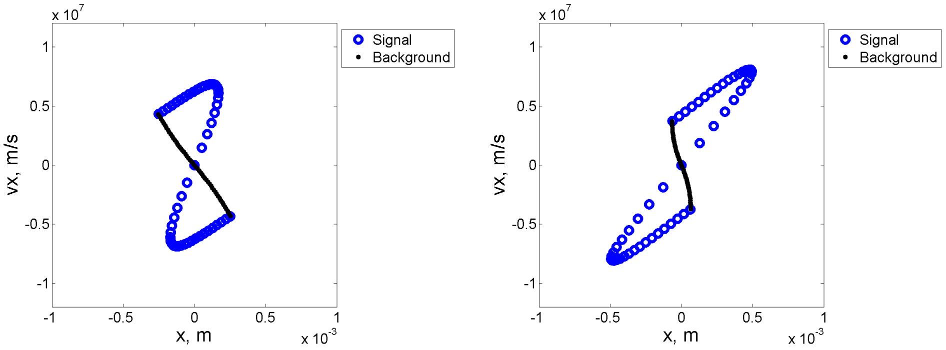

(c) After quadrupole 2 (d) After quadrupole 3

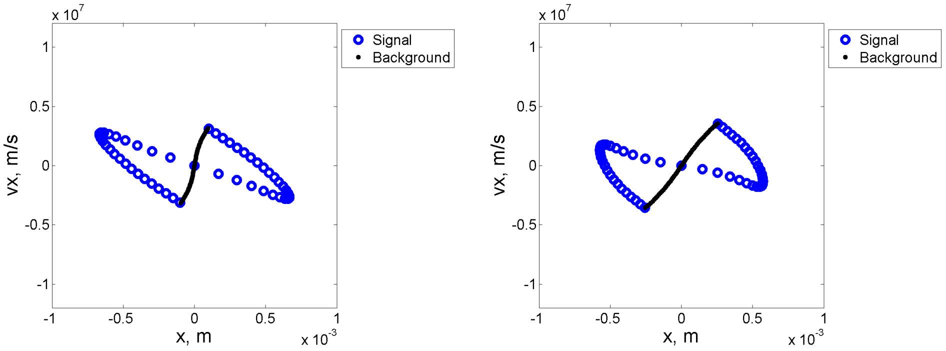

(e) After quadrupole 4 (f) At exit of modulator

Figure 123: Phase advance of a line of particles with / without initial velocity kick, using SPACE code, under the quadrupole focusing field, at various propagating distances in modulator, taking into account the space charge effect from the whole electron beam.

4 Start-to-end Simulations of Coherent Electron Cooling

In this section, we present the simulations results for the start-to-end process of coherent electron cooling.

The results of the modulation simulations from previous sections are used as the input of the amplifier, the second section of coherent electron cooling. The goal of the amplifier is to increase the modulation signal by orders, compared with the origin modulation signal from the modulator. In current experiments, the free electron laser (FEL) device is used as the amplifier.

We use the code GENESIS [22] to perform FEL simulations. We do not use code SPACE for the FEL simulations because the computational domain size increases by orders and the number of real electrons grows proportionally. In FEL simulations, the optical wavelength is an important parameter determining the longitudinal size of the computational domain. Calculated using the settings relevant to the coherent electron cooling experiments, the optical wavelength is 1.357e-5 m. FEL simulations usually requires a computational domain with the longitudinal size a few hundred times of the optical wavelength, and we typically use 400 times of optical wavelength as the longitudinal domain size of FEL simulations for coherent electron cooling. The computational domain used in the modulator simulations covers only a few optical wavelengths in longitudinal, and using 400 times of optical wavelength as the longitudinal domain size in code SPACE means that we have to increase the domain size by orders of magnitude, and the number of electrons is also increased proportionally. As code SPACE resolves the interactions between particles and electromagnetic fields in longitudinal and transverse directions within local regions, the computing time using code SPACE becomes extremely long, even with the parallel compatibility of the code. GENESIS does not resolve the local interactions between particles, but focuses on the bunching of the electron beam with the length scale of optical wavelength. So using GENESIS saves running time for our numerical simulations, without losing too much information of the electron beam. The main information, which are important for coherent electron cooling, are the longitudinal density and velocity modulation in the electron beam. And GENESIS mainly solve the beam dynamics in longitudinal direction for FEL simulations.

4.1 Software for FEL Simulations

GENESIS [22] is designed to perform high gain FEL simulations. In GENESIS simulations, the computational domain is divided into a few hundred slices in longitudinal direction, and the length of each slice is the optical wavelength, which is an important parameter for FEL devices. To measure the gain during the FEL process, we need to calculate the bunching factor, given in equation (45),

$$b_m = \frac{\sum_{i_p=1}^{n_p} e^{im\theta_{i_p}}}{n_p} \tag{45}$$

where b_m is the bunching factor of a slice for the m-th harmonic, n_p is the number of computational particles within the slice, i_p is the index for the computational particles, i is the imaginary unit, m is the harmonic number and θ_{i_p} is the phase of the computational particle in the slice.

Bunching factor b_m is calculated for one slice by averaging the phases of all computational particles within that slice, and is commonly used for harmonic number $m = 1$. The magnitude of the bunching factor describes how strong the electrons are bunched within the slice. The bunching factor could be increased by orders thought an FEL process, unless the saturation is reached. Saturation happens when the electrons are bunched too much resulting in overshooting, and the bunching factor can not increase and may even drop.

GENESIS allows simulations using macro computational particles, with each computational particle representing many real particles. One difficulty in using macro computational particles in GENESIS is the shot noise in bunching factor. Assume that, in one slice, the number of computational particles is n_p and the number of real particles is N, and n_p is always less than N. The correct shot noise should be proportional to $1/\sqrt{N}$. But if we generate computational particles randomly, the shot noise would be proportional to $1/\sqrt{n_p}$, which is larger than the correct shot noise. If we let the electrons containing larger shot noise through the FEL process, the system may reach the saturation much faster than the real physics process. So we need to control the shot noise in the bunching factor.

GENESIS controls the shot noise in two steps. Firstly, generate the phases of electrons manually to make the noise in bunching factor is exactly 0, which is called quiet start. Then add shot noise with correct scale to each electron's phase to make the resulting noise in bunching factor in the correct scale, which is proportional to $1/\sqrt{N}$. The algorithm for loading the correct shot noise is described in [23].

In the following calculations, we will describe and verify the methods used in GENESIS in quiet start process and adding perturbations for correct shot noise in bunching factors.

In the first step, quiet start, one slice is divided into several bins, and let n_{bin} denote the number of bins. Number of computational particles in each bin is n_p/n_{bin}, and we call it number of beamlet, $n_{beamlet} = n_p/n_{bin}$. We start with filling the first bin randomly, and then add mirror particles in remaining bins using equation (46).

$$\theta_{i_p+i\cdot n_{beamlet}} = \theta_{i_p} + i \cdot \frac{2\pi}{n_{bin}}, 1 \leq i < n_{bin}, 1 \leq i_p \leq n_{beamlet} \tag{46}$$

We can consider θ as a 2D array $\theta_{j,k}$, where j specifies the bin, and k specifies the beamlet, $0 \leq j < n_{bin}$, $1 \leq k \leq n_{beamlet}$. Equation (46) can be written as (47).

$$\theta_{j,k} = \theta_{0,k} + j \cdot \frac{2\pi}{n_{bin}}, 1 \leq j < n_{bin}, 1 \leq k \leq n_{beamlet} \tag{47}$$

Before checking the bunching factor, we want to introduce some useful summation formula. Assume z is a complex number $z = \cos\theta + i\sin\theta$, we have equation (48), where n is an integer.

$$z^n = \cos n\theta + i \sin n\theta \tag{48}$$

If $z \neq 1$, we have the summation (49).

$$\sum_{i=1}^{n} z^n = \frac{z(z^n - 1)}{z - 1} \tag{49}$$

If $z = 1$, the summation is simply (50).

$$\sum_{i=1}^{n} z^n = n \tag{50}$$

In addition, if we compare the real part and image part on left hand side and right hand side of equation 49, we have (51). Equation 51 is valid when $\theta \neq 2k\pi$, where k is an integer.

$$\begin{aligned}\sum_{i=1}^{n}\sin n\theta = &\quad \frac{-\cos(n+1/2)\theta+\cos\theta/2}{2\sin(\theta/2)}\\ \sum_{i=1}^{n}\cos n\theta = &\quad \frac{\sin(n+1/2)\theta-\sin\theta/2}{2\sin(\theta/2)}\end{aligned}\tag{51}$$

Now we calculate the bunching factor with for the m-th harmonic in equation (52).

$$\begin{aligned}b_m &= \frac{1}{n_p}\sum_{i_p=1}^{n_p} e^{im\theta_{i_p}}\\ &= \frac{1}{n_p}\sum_{k=1}^{n_{beamlet}}\sum_{j=1}^{n_{bin}} e^{im\theta_{j,k}}\\ &= \frac{1}{n_p}\sum_{k=1}^{n_{beamlet}}\sum_{j=1}^{n_{bin}} e^{im\left(\theta_{0,k}+(j-1)\cdot\frac{2\pi}{n_{bin}}\right)}\\ &= \frac{1}{n_p}\sum_{k=1}^{n_{beamlet}} e^{im\theta_{0,k}}\sum_{j=1}^{n_{bin}} e^{im(j-1)\frac{2\pi}{n_{bin}}}\end{aligned}\tag{52}$$

When $m < n_{bin}$, we have $\frac{2\pi m}{n_{bin}} < 2\pi$, and equation (49) is applicable in calculating the bunching factor in (53).

$$\begin{aligned}b_m &= \frac{1}{n_p}\sum_{k=1}^{n_{beamlet}} e^{im\theta_{0,k}}\sum_{j=1}^{n_{bin}} e^{im(j-1)\frac{2\pi}{n_{bin}}}\\ &= \frac{1}{n_p}\sum_{k=1}^{n_{beamlet}} e^{im\theta_{0,k}}\frac{e^{i2\pi m/n_{bin}}\left(e^{in_{bin}\cdot 2\pi m/n_{bin}}-1\right)}{e^{i2\pi m/n_{bin}}-1}\\ &= \frac{1}{n_p}\sum_{k=1}^{n_{beamlet}} e^{im\theta_{0,k}}\frac{e^{i2\pi m/n_{bin}}\left(e^{i2\pi m}-1\right)}{e^{i2\pi m/n_{bin}}-1}\\ &= \frac{1}{n_p}\sum_{k=1}^{n_{beamlet}} e^{im\theta_{0,k}}\cdot 0\\ &= 0\end{aligned}\tag{53}$$

When $m = n_{bin}$, we have $\frac{2\pi m}{n_{bin}} = 2\pi$, and the bunching factor is calculated in equation (54), which depends on $\theta_{0,k}$.

$$\begin{aligned} b_m &= \frac{1}{n_p} \sum_{k=1}^{n_{beamlet}} e^{im\theta_{0,k}} \sum_{j=1}^{n_{bin}} e^{im(j-1)\frac{2\pi}{n_{bin}}} \\ &= \frac{1}{n_p} \sum_{k=1}^{n_{beamlet}} e^{in_{bin}\theta_{0,k}} \cdot n_{bin} \\ &= \frac{n_{bin}}{n_p} \sum_{k=1}^{n_{beamlet}} e^{in_{bin}\theta_{0,k}} \end{aligned} \tag{54}$$

For a given harmonic number m, we can use $n_{bin} > m$ to create the phases of electrons following the equation (47), and make the resulting bunching factor b_m exactly zero. This step is the quiet start.

The second step is to add perturbations $\delta\theta_{j,k}$ to make the resulting bunching factor proportional to $1/\sqrt{N}$. We use the $\delta\theta_{j,k}$ given in [23], and is shown in equation (55),

$$\delta\theta_{j,k} = \sum_{m=1}^{m=M} a_{m,k} \cos m\theta_{j,k} + b_{m,k} \sin m\theta_{j,k} \tag{55}$$

where m is the harmonic number, M should satisfy $M < n_{bin}/2$ (the reason will be discussed later), $a_{m,k}$ and $b_{m,k}$ follow 1D normal distribution centered at zero with rms σ_m which obeys (56),

$$\sigma_m^2 = \frac{2}{m^2 N_b} \tag{56}$$

where $N_b = N/n_{beamlet}$, is the number of real particles per beamlet.

For a given harmonic m and a given beamlet k, the average of $\cos m\theta_{j,k}$ is calculated in (57).

$$
\begin{aligned}
< \cos m\theta >_k &= \frac{1}{n_{bin}}\sum_{j=1}^{n_{bin}}\cos\Big(m(\theta_{j,k}+\delta\theta_{j,k})\Big) \\
&= \frac{1}{n_{bin}}\sum_{j=1}^{n_{bin}}\Big(\cos m\theta_{j,k}\cos m\delta\theta_{j,k}-\sin m\theta_{j,k}\sin m\delta\theta_{j,k}\Big), \quad m\delta\theta_{j,k} << 1 \\
&\approx \frac{1}{n_{bin}}\sum_{j=1}^{n_{bin}}\Big(\cos m\theta_{j,k}-m\delta\theta_{j,k}\sin m\theta_{j,k}\Big), \quad m < n_{bin} \\
&= -\frac{1}{n_{bin}}\sum_{j=1}^{n_{bin}} m\delta\theta_{j,k}\sin m\theta_{j,k} \\
&= -\frac{1}{n_{bin}}\sum_{j=1}^{n_{bin}} m\Big(\sum_{l=1}^{l=M} a_{l,k}\cos l\theta_{j,k}+b_{l,k}\sin l\theta_{j,k}\Big)\sin m\theta_{j,k} \\
&= -\frac{1}{n_{bin}}\sum_{j=1}^{n_{bin}} mb_{m,k}\sin^2 m\theta_{j,k} \\
&= -\frac{1}{n_{bin}}\sum_{j=1}^{n_{bin}} mb_{m,k}\frac{1-\cos 2m\theta_{j,k}}{2} \\
&= -\frac{mb_{m,k}}{2}+\frac{mb_{m,k}}{2n_{bin}}\sum_{j=1}^{n_{bin}}\cos 2m\theta_{j,k} \qquad (57)
\end{aligned}
$$

The term $\sum_{j=1}^{n_{bin}}\cos 2m\theta_{j,k}$ in equation (57) is calculated in (58).

$$
\begin{aligned}
\sum_{j=1}^{n_{bin}}\cos 2m\theta_{j,k} &= \sum_{j=1}^{n_{bin}}\cos 2m\left(\theta_{0,k}+(j-1)\cdot\frac{2\pi}{n_{bin}}\right) \qquad (58) \\
&= \sum_{j=1}^{n_{bin}}\cos 2m\theta_{0,k}\cos 2m(j-1)\cdot\frac{2\pi}{n_{bin}}-\sin 2m\theta_{0,k}\sin 2m(j-1)\cdot\frac{2\pi}{n_{bin}} \\
&= \cos 2m\theta_{0,k}\sum_{j=1}^{n_{bin}}\cos 2m(j-1)\cdot\frac{2\pi}{n_{bin}}-\sin 2m\theta_{0,k}\sum_{j=1}^{n_{bin}}\sin 2m(j-1)\cdot\frac{2\pi}{n_{bin}}
\end{aligned}
$$

If $m < \frac{n_{bin}}{2}$, we have $2m\cdot\frac{2\pi}{n_{bin}} < 2\pi$, and equation (51) is applicable to have (59).

$$\begin{aligned}
\sum_{j=1}^{n_{bin}} \cos 2m\theta_{j,k} &= \cos 2m\theta_{0,k} \sum_{j=1}^{n_{bin}} \cos 2m(j-1)\cdot\frac{2\pi}{n_{bin}} - \sin 2m\theta_{0,k} \sum_{j=1}^{n_{bin}} \sin 2m(j-1)\cdot\frac{2\pi}{n_{bin}} \\
&= \cos 2m\theta_{0,k} \sum_{j=1}^{n_{bin}} \cos 2mj\cdot\frac{2\pi}{n_{bin}} - \sin 2m\theta_{0,k} \sum_{j=1}^{n_{bin}} \sin 2mj\cdot\frac{2\pi}{n_{bin}} \\
&= \cos 2m\theta_{0,k} \frac{\sin(n_{bin}+\frac{1}{2})\frac{4m\pi}{n_{bin}} - \sin\frac{2m\pi}{n_{bin}}}{2\sin\frac{4m\pi}{n_{bin}}} \\
&\quad - \sin 2m\theta_{0,k} \frac{-\cos(n_{bin}+\frac{1}{2})\frac{4m\pi}{n_{bin}} + \cos\frac{2m\pi}{n_{bin}}}{2\sin\frac{4m\pi}{n_{bin}}} \\
&= \cos 2m\theta_{0,k} \frac{\sin\frac{2m\pi}{n_{bin}} - \sin\frac{2m\pi}{n_{bin}}}{2\sin\frac{4m\pi}{n_{bin}}} \\
&\quad - \sin 2m\theta_{0,k} \frac{-\cos\frac{2m\pi}{n_{bin}} + \cos\frac{2m\pi}{n_{bin}}}{2\sin\frac{4m\pi}{n_{bin}}} \\
&= 0 \qquad (59)
\end{aligned}$$

And therefore we have(60).

$$\begin{aligned}
<\cos m\theta>_k &= -\frac{mb_{m,k}}{2} + \frac{mb_{m,k}}{2n_{bin}} \sum_{j=1}^{n_{bin}} \cos 2m\theta_{j,k} \\
&= -\frac{mb_{m,k}}{2} \qquad (60)
\end{aligned}$$

If $m = \frac{n_{bin}}{2}$, we have $2m\cdot\frac{2\pi}{n_{bin}} = 2\pi$, we can obtain (61).

$$\begin{aligned}
\sum_{j=1}^{n_{bin}} \cos 2m\theta_{j,k} &= \cos 2m\theta_{0,k} \sum_{j=1}^{n_{bin}} \cos 2m(j-1)\cdot\frac{2\pi}{n_{bin}} - \sin 2m\theta_{0,k} \sum_{j=1}^{n_{bin}} \sin 2m(j-1)\cdot\frac{2\pi}{n_{bin}} \\
&= n_{bin} \cos 2m\theta_{0,k} \qquad (61)
\end{aligned}$$

Therefore we have (62).

$$
\begin{aligned}
< \cos m\theta >_k &= -\frac{mb_{m,k}}{2} + \frac{mb_{m,k}}{2n_{bin}} \sum_{j=1}^{n_{bin}} \cos 2m\theta_{j,k} \\
&= -\frac{mb_{m,k}}{2} + \frac{mb_{m,k}}{2n_{bin}} \cdot n_{bin} \cos 2m\theta_{0,k} \\
&= -\frac{mb_{m,k}}{2}(1 - \cos 2m\theta_{0,k}) \qquad (62)
\end{aligned}
$$

From the quiet start section, we know that $\theta_{0,k}$ is uniformly distributed on $(0, \frac{2\pi}{n_{bin}})$, so we can calculate the mean value of $\cos 2m\theta_{0,k}$ in (63).

$$
\begin{aligned}
< \cos 2m\theta_{0,k} > &= \frac{1}{\frac{2\pi}{n_{bin}}} \int_{\theta=0}^{\theta=\frac{2\pi}{n_{bin}}} \cos 2m\theta d\theta \\
&= \frac{1}{\frac{2\pi}{n_{bin}}} \frac{1}{2m} \sin 2m\theta \Big|_{\theta=0}^{\theta=\frac{2\pi}{n_{bin}}} \\
&= \frac{n_{bin}}{4m\pi} \sin \frac{4m\pi}{n_{bin}}, \quad m = \frac{n_{bin}}{2} \\
&= \frac{1}{2\pi} \sin 2\pi \\
&= 0 \qquad (63)
\end{aligned}
$$

Equations (62) and (63) show that $< \cos m\theta >_k$ depends on $\theta_{0,k}$, and with mean value $-\frac{mb_{m,k}}{2}$ when $m = \frac{n_{bin}}{2}$.

Similarly, we can calculate the average of $\sin m\theta_{j,k}$ in (64).

$$
\begin{aligned}
<\sin m\theta>_k &= \frac{1}{n_{bin}} \sum_{j=1}^{n_{bin}} \sin\Big(m(\theta_{j,k} + \delta\theta_{j,k})\Big) \\
&= \frac{1}{n_{bin}} \sum_{j=1}^{n_{bin}} \Big(\sin m\theta_{j,k} \cos m\delta\theta_{j,k} + \cos m\theta_{j,k} \sin m\delta\theta_{j,k}\Big), \quad m\delta\theta_{j,k} << 1 \\
&\approx \frac{1}{n_{bin}} \sum_{j=1}^{n_{bin}} \Big(\sin m\theta_{j,k} + m\delta\theta_{j,k} \cos m\theta_{j,k}\Big), \quad m < n_{bin} \\
&= \frac{1}{n_{bin}} \sum_{j=1}^{n_{bin}} m\delta\theta_{j,k} \cos m\theta_{j,k} \\
&= \frac{1}{n_{bin}} \sum_{j=1}^{n_{bin}} m\Big(\sum_{l=1}^{l=M} a_{l,k} \cos l\theta_{j,k} + b_{l,k} \sin l\theta_{j,k}\Big) \cos m\theta_{j,k} \\
&= \frac{1}{n_{bin}} \sum_{j=1}^{n_{bin}} m a_{m,k} \cos^2 m\theta_{j,k} \\
&= \frac{1}{n_{bin}} \sum_{j=1}^{n_{bin}} m a_{m,k} \frac{1 + \cos 2m\theta_{j,k}}{2} \\
&= \frac{m a_{m,k}}{2} + \frac{m a_{m,k}}{2n_{bin}} \sum_{j=1}^{n_{bin}} \cos 2m\theta_{j,k} \qquad (64)
\end{aligned}
$$

If $m < \frac{n_{bin}}{2}$, we have (65).

$$
<\sin m\theta>_k = \frac{m a_{m,k}}{2} \qquad (65)
$$

If $m = \frac{n_{bin}}{2}$, we have (66).

$$
\begin{aligned}
<\sin m\theta>_k &= \frac{m a_{m,k}}{2} + \frac{m a_{m,k}}{2n_{bin}} \cdot n_{bin} \cos 2m\theta_{0,k} \\
&= \frac{m a_{m,k}}{2}(1 + \cos 2m\theta_{0,k}) \qquad (66)
\end{aligned}
$$

$<\sin m\theta>_k$ depends on $\theta_{0,k}$, and with mean value $\frac{m a_{m,k}}{2}$ when $m = \frac{n_{bin}}{2}$.

For a given harmonic m, the bunching factor of all n_p particles is calculated in (67).

$$\begin{aligned}
|b_m|^2 &= \Big|\frac{1}{n_p}\sum_{k=1}^{n_{beamlet}}\sum_{j=1}^{n_{bin}} e^{im(\theta_{j,k}+\delta\theta_{j,k})}\Big|^2, \quad \text{No correlations between beamlets} \\
&= \frac{1}{n_p^2}\sum_{k=1}^{n_{beamlet}}\Big|\sum_{j=1}^{n_{bin}} e^{im(\theta_{j,k}+\delta\theta_{j,k})}\Big|^2 \\
&= \frac{n_{bin}^2}{n_p^2}\sum_{k=1}^{n_{beamlet}}\Big|\frac{1}{n_{bin}}\sum_{j=1}^{n_{bin}} e^{im(\theta_{j,k}+\delta\theta_{j,k})}\Big|^2 \\
&= \frac{1}{n_{beamlet}^2}\sum_{k=1}^{n_{beamlet}}\Bigg[\Big(\frac{1}{n_{bin}}\sum_{j=1}^{n_{bin}}\cos\big(m(\theta_{j,k}+\delta\theta_{j,k})\big)\Big)^2+\Big(\frac{1}{n_{bin}}\sum_{j=1}^{n_{bin}}\sin\big(m(\theta_{j,k}+\delta\theta_{j,k})\big)\Big)^2\Bigg] \\
&= \frac{1}{n_{beamlet}^2}\sum_{k=1}^{n_{beamlet}}\Big(<\cos m\theta>_k^2 + <\sin m\theta>_k^2 \Big) \qquad (67)
\end{aligned}$$

If $m < \frac{n_{bin}}{2}$, we have (68) from previous results.

$$\begin{aligned}
<\cos m\theta>_k &= -\frac{mb_{m,k}}{2} \\
<\sin m\theta>_k &= \frac{ma_{m,k}}{2} \qquad (68)
\end{aligned}$$

Inserting (68) into (67), we have (69).

$$
\begin{aligned}
|b_m|^2 &= \frac{1}{n_{beamlet}^2} \sum_{k=1}^{n_{beamlet}} \Big(< \cos m\theta >_k^2 + < \sin m\theta >_k^2 \Big) \\
&= \frac{1}{n_{beamlet}^2} \sum_{k=1}^{n_{beamlet}} \Big(\frac{m^2 b_{m,k}^2}{4} + \frac{m^2 a_{m,k}^2}{4} \Big) \\
&= \frac{1}{n_{beamlet}^2} \cdot \frac{m^2}{4} \sum_{k=1}^{n_{beamlet}} (b_{m,k}^2 + a_{m,k}^2) \\
&\approx \frac{1}{n_{beamlet}^2} \cdot \frac{m^2}{4} \cdot n_{beamlet} (\sigma_m^2 + \sigma_m^2) \\
&= \frac{1}{n_{beamlet}^2} \cdot \frac{m^2}{4} \cdot n_{beamlet} \cdot \frac{4}{m^2 N_b} \\
&= \frac{1}{n_{beamlet} N_b} \\
&= \frac{1}{N} \qquad (69)
\end{aligned}
$$

If $m = \frac{n_{bin}}{2}$, we have (70) from previous results.

$$
\begin{aligned}
< \cos m\theta >_k &= -\frac{m b_{m,k}}{2} (1 - \cos 2m\theta_{0,k}) \\
< \sin m\theta >_k &= \frac{m a_{m,k}}{2} (1 + \cos 2m\theta_{0,k}) \qquad (70)
\end{aligned}
$$

Inserting (70) into (67), we have (71), and $|b_m|$ depends on $\theta_{0,k}$.

$$
\begin{aligned}
|b_m|^2 &= \frac{1}{n_{beamlet}^2} \sum_{k=1}^{n_{beamlet}} \Big(< \cos m\theta >_k^2 + < \sin m\theta >_k^2 \Big) \qquad (71) \\
&= \frac{1}{n_{beamlet}^2} \sum_{k=1}^{n_{beamlet}} \Big(\frac{m^2 b_{m,k}^2}{4} (1 - \cos 2m\theta_{0,k})^2 + \frac{m^2 a_{m,k}^2}{4} (1 + \cos 2m\theta_{0,k})^2 \Big)
\end{aligned}
$$

From the quiet start section, we know that $\theta_{0,k}$ is uniformly distributed on $(0, \frac{2\pi}{n_{bin}})$, so we can calculate the mean value of $|b_m|^2$ in (72). Note that $b_{m,k}$ and $\theta_{0,k}$ are independent, $a_{m,k}$ and $\theta_{0,k}$ are independent.

$$\begin{aligned}
<|b_m|^2> &= \frac{1}{n_{beamlet}^2}\left\langle\sum_{k=1}^{n_{beamlet}}\left(\frac{m^2 b_{m,k}^2}{4}(1-\cos 2m\theta_{0,k})^2+\frac{m^2 a_{m,k}^2}{4}(1+\cos 2m\theta_{0,k})^2\right)\right\rangle \\
&= \frac{m^2}{4n_{beamlet}^2}\left\langle\sum_{k=1}^{n_{beamlet}}\left(b_{m,k}^2(1-\cos 2m\theta_{0,k})^2+a_{m,k}(1+\cos 2m\theta_{0,k})^2\right)\right\rangle \\
&= \frac{m^2}{4n_{beamlet}^2}n_{beamlet} < b_{m,k}^2(1-\cos 2m\theta_{0,k})^2+a_{m,k}^2(1+\cos 2m\theta_{0,k})^2 > \\
&= \frac{m^2}{4n_{beamlet}}\left(< b_{m,k}^2 >< (1-\cos 2m\theta_{0,k})^2 > + < a_{m,k}^2 >< 1+\cos 2m\theta_{0,k})^2 >\right) \\
&= \frac{m^2}{4n_{beamlet}}\left(\sigma_m^2 < (1-\cos 2m\theta_{0,k})^2 > +\sigma_m^2 < 1+\cos 2m\theta_{0,k})^2 >\right) \\
&= \frac{m^2}{4n_{beamlet}}\sigma_m^2\left(< (1-\cos 2m\theta_{0,k})^2 > + < 1+\cos 2m\theta_{0,k})^2 >\right) \\
&= \frac{m^2}{4n_{beamlet}}\frac{2}{m^2 N_b}\left(< (1-\cos 2m\theta_{0,k})^2 > + < 1+\cos 2m\theta_{0,k})^2 >\right) \\
&= \frac{1}{2n_{beamlet}N_b}\left(< (1-\cos 2m\theta_{0,k})^2 > + < 1+\cos 2m\theta_{0,k})^2 >\right)
\end{aligned} \tag{72}$$

Note that $m = \frac{n_{bin}}{2}$, so the term $< (1-\cos 2m\theta_{0,k})^2 >$ from (72) is calculated in (73).

$$\begin{aligned}
< (1 - \cos 2m\theta_{0,k})^2 > \quad &= \quad < 1 - 2\cos 2m\theta_{0,k} + \cos^2 2m\theta_{0,k} > \\
&= \quad < 1 - 2\cos 2m\theta_{0,k} + \frac{1 + \cos 4m\theta_{0,k}}{2} > \\
&= \quad < \frac{3}{2} - 2\cos 2m\theta_{0,k} + \frac{\cos 4m\theta_{0,k}}{2} > \\
&= \quad \frac{1}{\frac{2\pi}{n_{bin}}} \int_{\theta=0}^{\theta=\frac{2\pi}{n_{bin}}} \left(\frac{3}{2} - 2\cos 2m\theta + \frac{\cos 4m\theta}{2} \right) d\theta \\
&= \quad \frac{3}{2} + \frac{1}{\frac{2\pi}{n_{bin}}} 2 \frac{1}{2m} \sin 2m\theta \Big|_{\theta=0}^{\theta=\frac{2\pi}{n_{bin}}} + \frac{1}{\frac{2\pi}{n_{bin}}} \frac{1}{2} \frac{1}{4m} \sin 4m\theta \Big|_{\theta=0}^{\theta=\frac{2\pi}{n_{bin}}} \\
&= \quad \frac{3}{2} + \frac{n_{bin}}{2m\pi} \sin \frac{4m\pi}{n_{bin}} + \frac{n_{bin}}{16m\pi} \sin \frac{8m\pi}{n_{bin}}, \quad m = \frac{n_{bin}}{2} \\
&= \quad \frac{3}{2} + \frac{1}{\pi} \sin 2\pi + \frac{1}{8\pi} \sin 4\pi \\
&= \quad \frac{3}{2} \qquad (73)
\end{aligned}$$

Similarly, the result of the term $< (1 + \cos 2m\theta_{0,k})^2 >$ from (72) is given in (74).

$$< (1 + \cos 2m\theta_{0,k})^2 > \quad = \quad \frac{3}{2} \qquad (74)$$

Inserting equations (73) and (74) into (72), we have (75).

$$\begin{aligned}
< |b_m|^2 > \quad &= \quad \frac{1}{2n_{beamlet}N_b} \left(< (1 - \cos 2m\theta_{0,k})^2 > + < 1 + \cos 2m\theta_{0,k})^2 > \right) \\
&= \quad \frac{1}{2n_{beamlet}N_b} \left(\frac{3}{2} + \frac{3}{2} \right) \\
&= \quad \frac{3}{2n_{beamlet}N_b} \\
&= \quad \frac{3}{2N} \qquad (75)
\end{aligned}$$

In summary, we have $|b_m| \approx \frac{1}{\sqrt{N}}$ when $m < \frac{n_{bin}}{2}$. And when $m = \frac{n_{bin}}{2}$, $|b_m|$ depends on $\theta_{0,k}$ but with mean value $\sqrt{\frac{3}{2N}}$. To remove the dependence of bunching factor $|b_m|$ on $\theta_{0,k}$, M in equation (55) should satisfy $M < n_{bin}/2$ to make $m < \frac{n_{bin}}{2}$.

There are two ways creating the computational particles for GENESIS simulations, one is generating particles using the built-in routine in GENESIS, given the parameters of the electron beam, another way is reading distributions of electrons from external files. We have used both ways in our start-to-end simulations for coherent electron cooling.

The kicker simulations are similar with the modulator simulations. We read the electron beam distributions from the output of FEL simulations in GENESIS, and put the electrons carrying the amplified modulation signal into the code SPACE for the kicker simulations.

4.2 Simulations Using Internal Electrons

In this section, we present the results of start-to-end simulations using the electrons generated by the internal routine in GENESIS.

As is mentioned above, we use 400 slices in FEL simulations using GENESIS, and the length of each slice is the optical wavelength, which is $1.357e-5$ m typically for the settings of coherent electron cooling. But our modulator simulations only covers a few slices, so we need more particles to fill the remaining slices. We let GENESIS generate particles for the 400 slices, and take 5 slices from the center for our modulator simulations. Again, we need two simulations with identical initial electrons, one without ion and one with ion, to extract the modulation signal by taking difference in final distributions of these two simulations. The resulting modulation is given in figure 124.

We use the final distributions of electrons in modulator section as the input of the FEL simulations using GENESIS. We resolve every real electron in the modulator simulation shown in figure 124, so the shot noise in the bunching factor is in the correct scale during the modulation process. The 5 slices of electrons are replaced back into the center of the 400 slices generated internally by GENESIS. The FEL process amplifies not only the modulation signal, but also noise from the background electrons, and the noise in the background is orders larger than the modulation signal, so we need two simulations for the FEL process, one with the electrons without modulation signal and one with the signal, and take different between the distributions of these two simulations to extract the amplified modulation signal. In FEL process, electron beam passes through a set of magnetics, which bends the

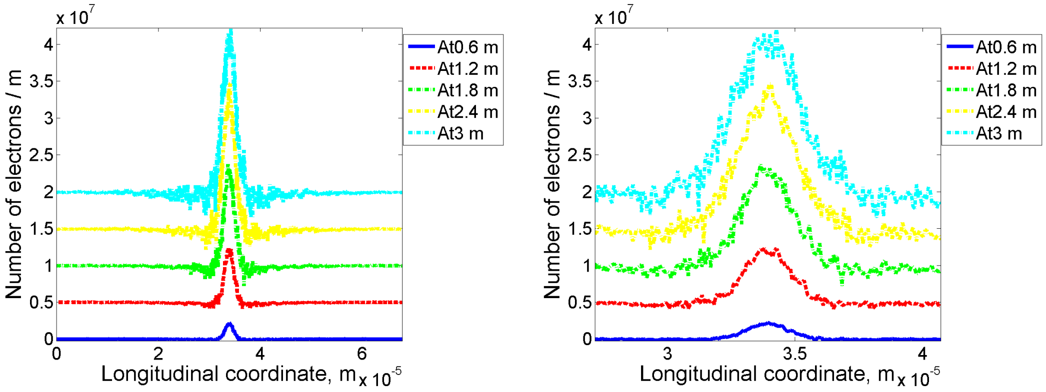

(a) 5 slices (b) 1 slice

Figure 124: Longitudinal density modulation using 5 slices of electrons, with slice width to be optical wavelength ($1.357e-5$ m), visualizations on 5 slices and zoom-in on 1 slice.

trajectory of the electron beam in transverse plane, and these magnetics are called wigglers. In our settings for FEL simulations, the longitudinal length of each wiggler (wiggle period) is 4 cm, the total number of wiggler periods is 188 and the total length of FEL section is 7.5 m in lab frame. The FEL simulation results will be presented in the measurements of bunching factor as this is an important indicator for the FEL process.

The evolutions of the bunching factors due to the modulation signal at various longitudinal location in the FEL process are presented in figure 125. The bunching factors in figure 125 are the differences between the results of two FEL simulations, one as the background and the other carries the modulation signal, so the noise are removed and only the bunching factors due to the modulation signal are extracted. The bunching factor plot in figure 125a shows that all of the 400 slices have zero bunching factor except the center 5 slices, because the 5 slices are taken from the modulator simulations and are affected by the attractions of the single ion. During the FEL process, the modulation signal is increasing dramatically, and becomes wider to cover more slices. The final bunching factor in figure 125i shows that the electron beam has not reached saturation at the end of FEL process.

The maximum bunching factor of all slices at each wiggler period is given in figure 126. The comparison of the maximum bunching factor between the initial stage and final stage of FEL process shows that the original modulation

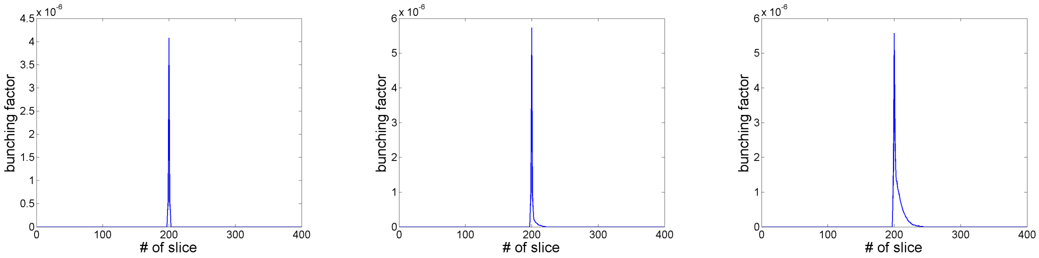

(a) At initial (b) At 25 wiggler period (c) At 50 wiggler period

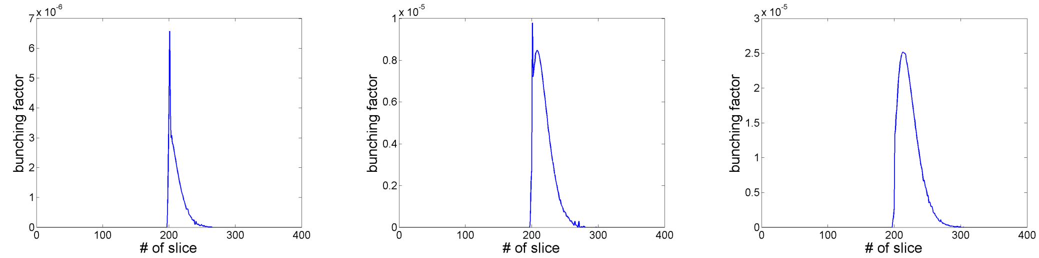

(d) At 75 wiggler period (e) At 100 wiggler period (f) At 125 wiggler period

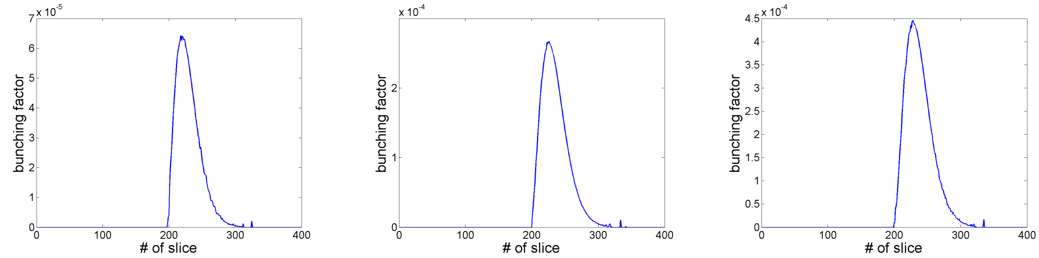

(g) At 150 wiggler period (h) At 175 wiggler period (i) At final

Figure 125: Instantaneous bunching factors of the modulation signal at various locations in the FEL process.

signal is amplified by 2 orders approximately, which is sufficient for the kicker simulations.

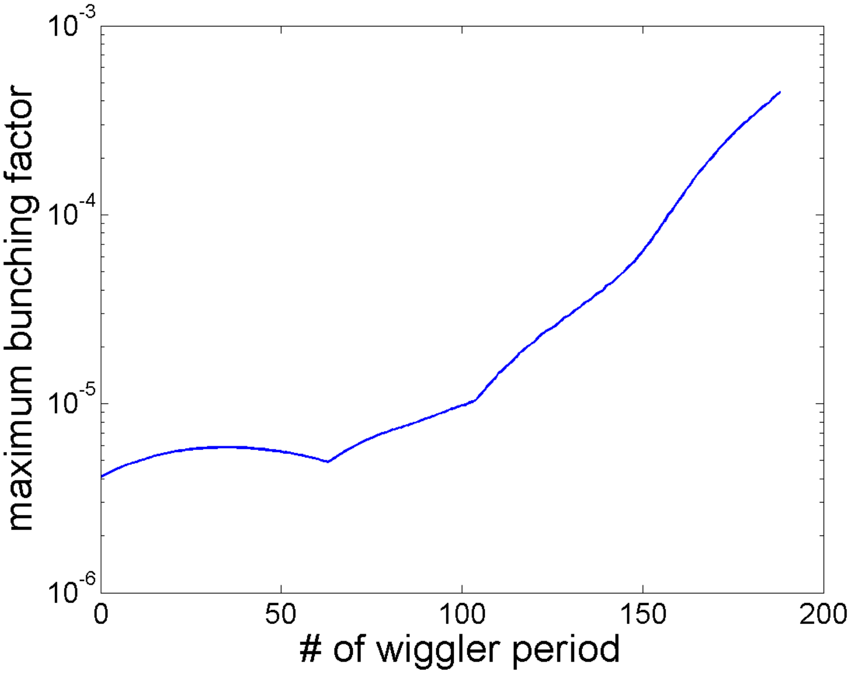

Figure 126: Maximum of bunching factor changes during the FEL process.

The transverse beam sizes of the electron beam in the 200th slice at each wiggler period of the FEL process is presented in figure 127, and it shows that the electron beam's transverse sizes in horizontal and vertical directions are matched well. The matched transverse beam size leads to high gain of the bunching factor in FEL process, and the unmatched beam size may lower the gain of the bunching factor.

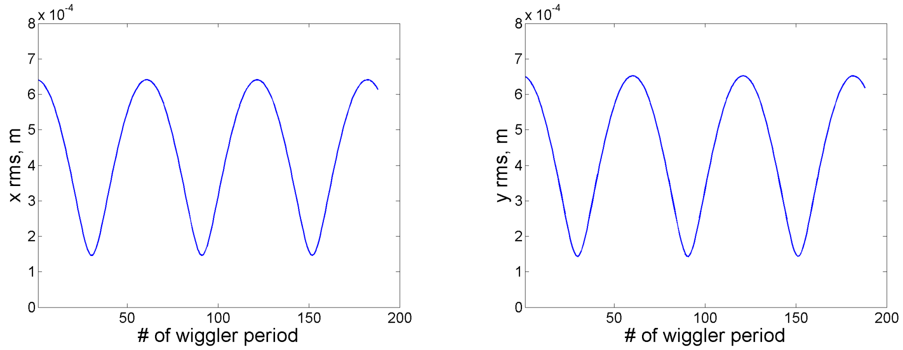

(a) x, horizontal (b) y, vertical

Figure 127: Transverse sizes of the electron beam in the 200th slice (at the center of the computational domain in FEL simulations) at each wiggler period.

We use the distributions of electron from the output of FEL simulations as the input for the kicker simulations. From the 400 slices in FEL simulations, we choose 5 slices with the largest bunching factors at the final stage of FEL section, and read the distributions of the electrons of these 5 slices into code SPACE, and let the electrons propagate through kicker, the third section of coherent electron cooling. We calculate the bunching factors of the 5 slices, at different propagating distances in the kicker section, and give the results in figure 128.

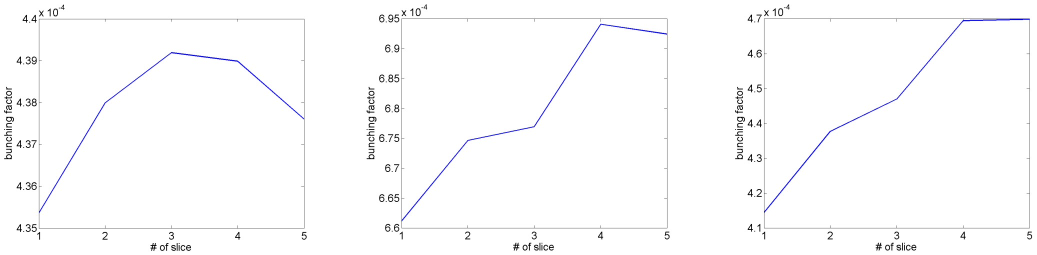

(a) At initial

(b) At 1.2 m

(c) At 2.4 m

Figure 128: Bunching factors of the 5 slices in kicker section, at various propagating distances in lab frame.

In figure 128a, the bunching factors at initial stage of the kicker sections are consistent with the results at the final stage of FEL simulations. There is an increase in bunching factor at propagating distance 1.2 m in kicker, as is shown in figure 128b, followed by a drop in bunching factor at propagating distance 2.4 m, observed in figure 128c. The reason for the behaviors of bunching factor in the kicker section is that, the FEL process amplifies the density and velocity modulation signal. At initial stage of kicker simulations, the velocity modulation makes the electrons continue building the density modulation and increasing the bunching factor. And at a later stage of kicker, the electrons are bunched too much that the bunching reaches the saturation, and the bunching factor drops when the overshooting occurs.

The longitudinal density modulation of the 5 slices in the kicker simulations are given in figure 129. The comparison between figure 124 and figure 129a shows that the original longitudinal density modulation is amplifies by 2 orders, which is the gain from the FEL process. The evolutions of the longitudinal density modulation in figure 129 is similar with the changes of the bunching factor, increase at early stage and decrease at late stage.

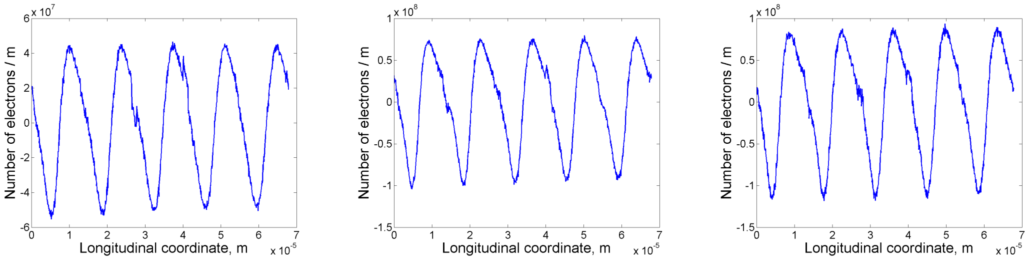

(a) At initial (b) At 0.6 m (c) At 1.2 m

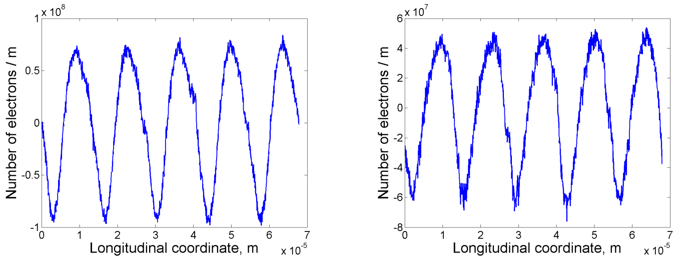

(d) At 1.8 m (e) At 2.4 m

Figure 129: Amplified longitudinal density modulation of the 5 slices in kicker section, at various propagating distances in lab frame.

The longitudinal density modulation in the kicker simulations can be use to calculate the forces on the ions due to the bunched electrons, and estimate the cooling time of the ion beam.

4.3 Simulations Using External Electrons

In this section, we present the results of start-to-end simulations using the electrons from external files.

The electron beams used in previous modulator simulations and start-to-end simulations, with uniform distribution or Gaussian distribution, are generated by code SPACE or GENESIS at the initialization stage when we perform the numerical simulations. Using more realistic electron beam as the input makes the numerical simulation a better tool in support of the coherent electron cooling experiments. There are other simulations performed in RHIC at BNL, starting from the cathode that generates the electrons with low energy, and propagating the electrons through various accelerating components until the entrance of the modulator. We use the external files containing the resulting distributions of electrons from that beam dynamics simulations as our input.

The electron beam in the external file has very large longitudinal size, covering approximately 3000 slices with slice width to be the optical wavelength 1.357e-5 m. The beam parameters varies at different locations of the electron beam. Typical beam parameters are given in figure 130, and we can see that the profile of the beam changes from slice to slice, because of the effects of all the accelerator components from the cathode to the modulator section.

The beam parameters shown in figure 130 contain large noise, because the electron beam in the external file has too few particles, approximately 2e+5 computational electrons distributed in 3000 slices, with each slice containing tens of electrons and some slices are empty, and each computational electron represents 62500 real electrons and makes the poor statistics. The number of computational particles is insufficient for the start-to-end simulations, so we can not use the external file directly. We firstly smooth the beam parameters from slice to slice, and the typical result of longitudinal density distribution after smoothing is given in figure 131, which shows that the large noise in figure 130a is eliminated by the smoothing technique. We apply the same smoothing method to other beam parameters from slice to slice.

We can generate electrons for each slice using the smoothed beam parame-

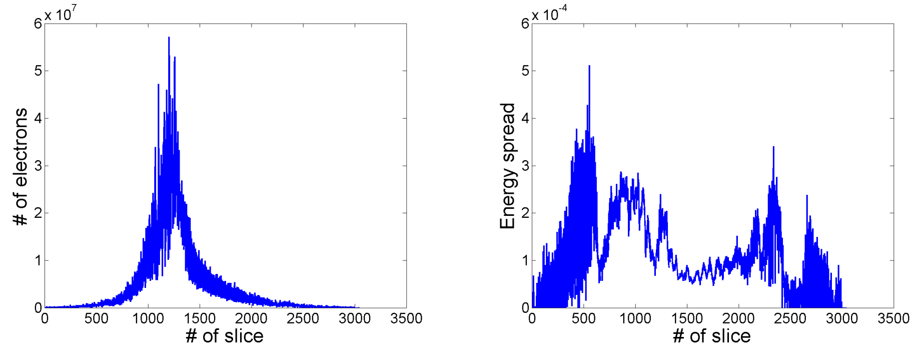

(a) Density (b) Energy spread

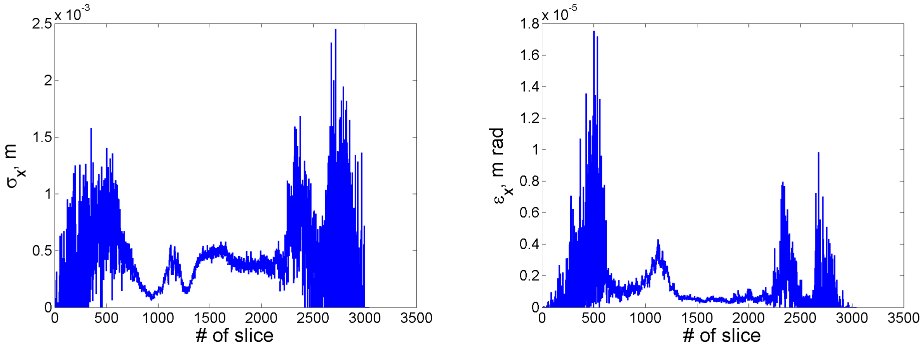

(c) Transverse size (d) Transverse emittance

Figure 130: Beam parameters of the electron beam in the external file from beam dynamics simulations.

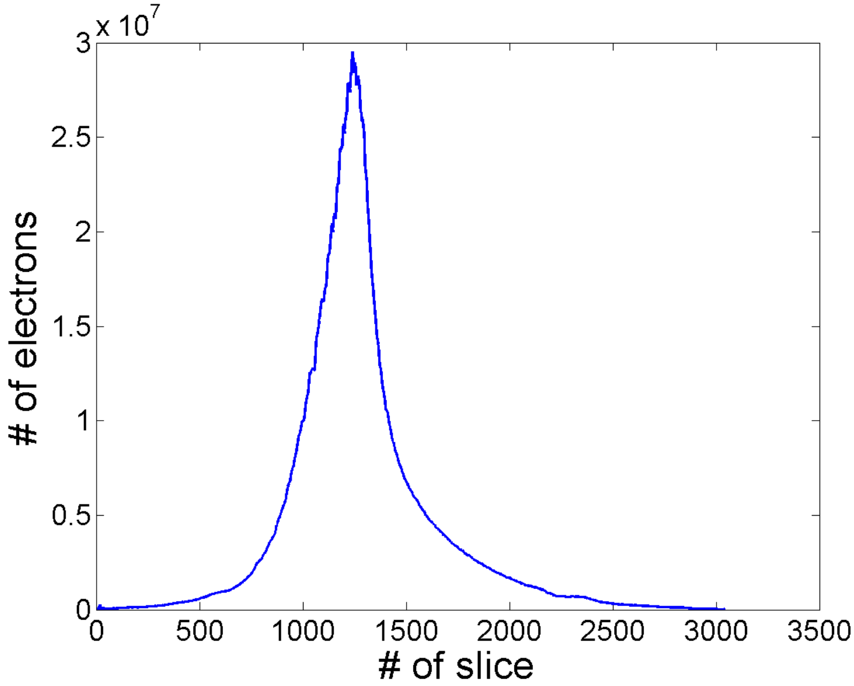

Figure 131: Longitudinal density distribution of the electron beam from the external file after smoothing.

ters of that slice, and the number of computational electrons can be increased by orders compared with the original external file. This up sampling method maintain the global profile of the electron beam. Although GENESIS can generate particles using given parameters, it requires that each slice should have the same number of computational particles and the same beam parameters, which is not applicable for our simulations. So we implement the particle generation routine in code SPACE, and build the electron beam at the initialization of numerical simulations. The algorithm for loading shot noise [23] is included in the implementation, to maintain the correct the shot noise in bunching factors when we use macro computational particles.

The re-built electron beam contains sufficient number of computational electrons for numerical simulations and keep the global profile of the original electron beam from the external file. We use one slice for the modulator simulations, and the results are similar as the modulator section in previous start-to-end simulations using internally generated electrons. Then we take 400 slices from the 3000 slices of the electron beam for the FEL simulations, and the one slice from the modulator simulations is replaced into the center of the 400 slices. To meet the GENESIS's requirement that each slice contains the same number of computational particles, we add electrons with negative energies to each slice, and these electrons will be ignored in the simulations of FEL process in GENESIS.

The bunching factors' evolutions in the FEL process are shown in figures 132 and 133. The initial bunching factor of FEL process, shown in figure 132a is close to the bunching factor in 125a, and indicates that our modulator simulations are consistent when using internally generated electrons and external distributions for the electrons. The effects of the background 400 slices occur at late stages of FEL process. The comparison between figure 132a and figure 132i shows that the modulation signal is increases by one order during the FEL process, and the bunching factor evolutions shown in figure 133 also shows that the gain from the FEL is one order, which is not sufficient for cooling the ion beam in the kicker section.

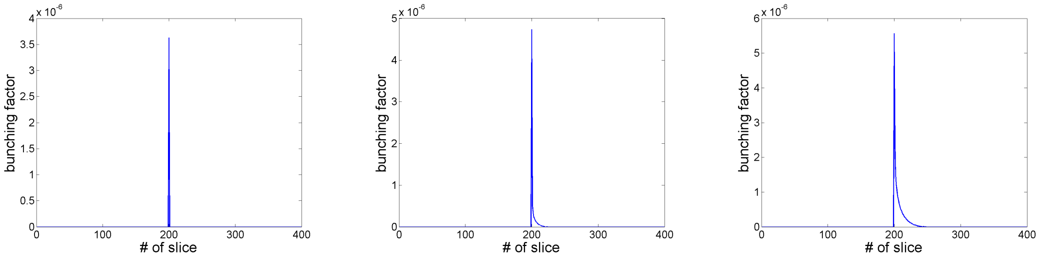

(a) At initial (b) At 25 wiggler period (c) At 50 wiggler period

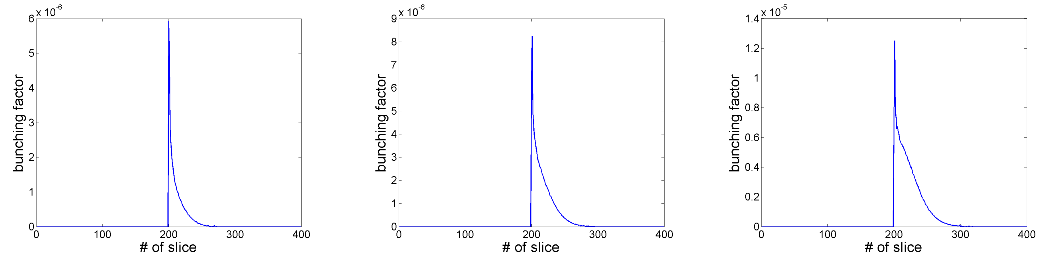

(d) At 75 wiggler period (e) At 100 wiggler period (f) At 125 wiggler period

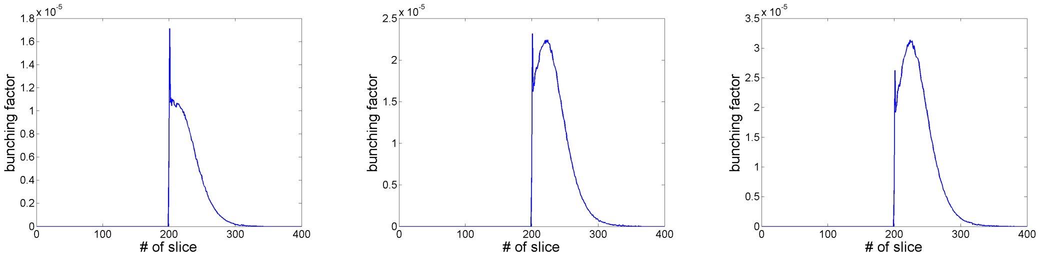

(g) At 150 wiggler period (h) At 175 wiggler period (i) At final

Figure 132: Instantaneous bunching factors of the modulation signal at various locations in the FEL process, using realistic distributions for the background 400 slices.

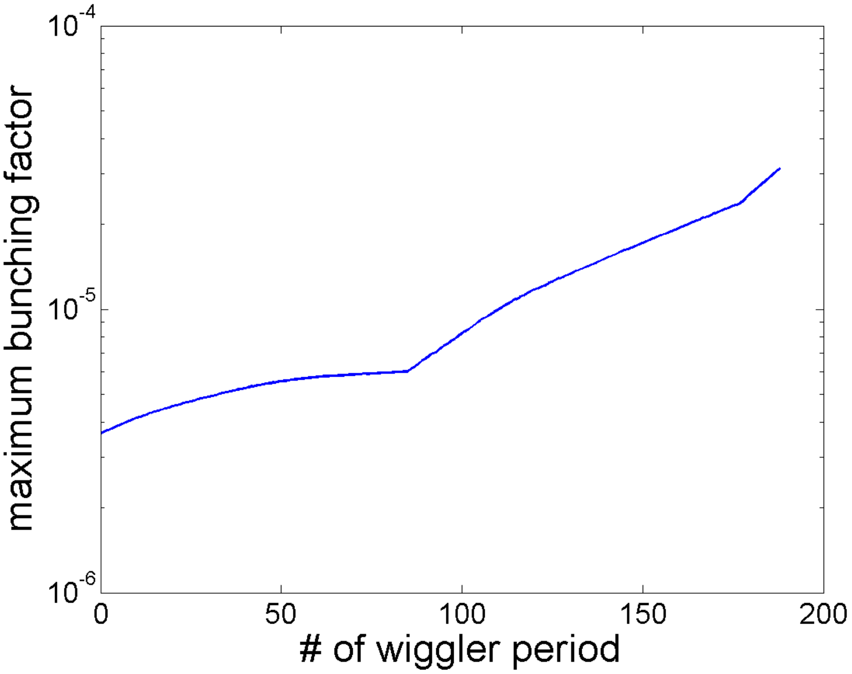

Figure 133: Maximum of bunching factor changes during the FEL process, using realistic distributions for the background 400 slices.

To understand the reasons for the low gain in FEL process when we use external electron beam as the background 400 slices, we track the transverse electron beam size of the 200th slice during the FEL pross, and present the measurements in figure 134. The electron beam size in horizontal and vertical directions are highly unmatched, and this is the reason for the low amplification of the modulation signal during the FEL process.

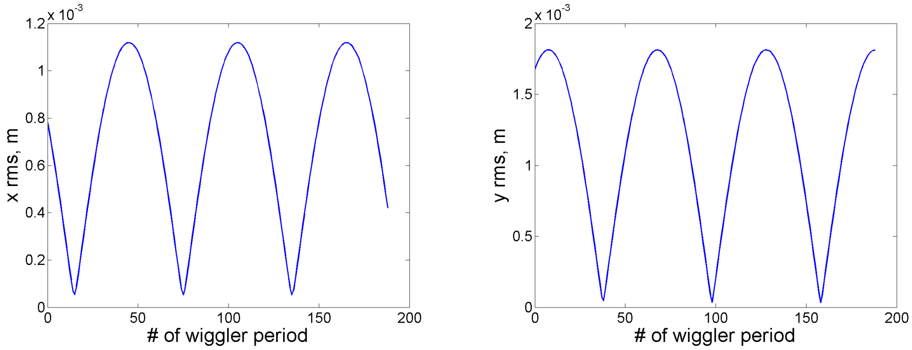

(a) x, horizontal (b) y, vertical

Figure 134: Transverse sizes of the electron beam in the 200th slice (at the center of the computational domain in FEL simulations) at each wiggler period, using realistic distributions for the background 400 slices.

Obtaining the electron beam with matched transverse size at the entrance of FEL section requires more collaborations with scientists conducting the coherent electron cooling experiments. They will tune the accelerator components to provide an electron beam with better profile at the entrance of modulator, and we together will tune the settings of the quadrupoles in modulator section, to make the electron beam's transverse size matched at the entrance of the FEL section.

5 Conclusions

We have presented main results of numerical simulations for the three major components of coherent electron cooling: the modulator, the amplifier and the kicker.

The main tool for our simulations is the code SPACE, a parallel, relativistic, 3D electromagnetic Particle-in-Cell code developed for the simulation of relativistic particle beams, beam-plasma interaction, and plasma chemistry. A module containing electrostatic solver was implemented in code SPACE for simulation studies of coherent electron cooling, as solving the problems of co-propagating electron and ion beams in co-moving frame is electrostatic in nature. Various diagnostic routines have been developed to provide different options of visualizing the simulation results. SPACE resolves local interactions between particles and effects from external fields, and track the motion of every real electron in numerical simulations (each computational particle represents a real particle). We have used SPACE for modulator and kicker simulations to study the local and global dynamics of the electron beam. The open source code GENESIS was used for the simulations of free electron laser (FEL), as the amplifier of coherent electron cooling. The computational domain size is orders larger in FEL section, compared with modulator and kicker section, and computing time of using SPACE in such domain is extremely long, even with the parallel scalability of the code. GENESIS drops local details of beam dynamics with suitable approximations, and solves the bunching of the electron beam in a large scale. Using GENESIS for FEL simulations saves computing time, and keep the major information of electron beam, which are important for coherent electron cooling process.

We have improved the computing efficiency in modulator simulations using single ion, because of the two facts, that ion-ion interactions are negligibly small on length scales relevant to the modulation process and that the relative density modulation of electrons due to ion is orders of magnitudes smaller than unity. Number of electrons used in simulations is reduced because only the electrons affected by the single ion are needed. The range of the ion's electrostatic effect is described by Debye length, which is orders smaller than the longitudinal size of the electron beam. We can repeat the single ion simulations using various locations and velocities for the ion, and use super position principle to get the overall response of electrons due to the whole ion beam.

We have designed the algorithm extracting the modulation signal from the orders larger shot noise. Two simulations with identical initial distributions of electron beam were needed for a given modulation problem. One simulation operated without ion, and another simulation propagated the electron beam with the single ion. With the assumption that the force from an ion only slightly changes the trajectories of the electrons over the modulation process, the influences of the ion can be obtained by taking the difference in the final electron distributions of the two simulations.

We have performed numerical convergence tests for modulator simulations, using different mesh refinements and numbers of computational particles, and showed consistent results of numerical simulations with different resolutions. This test helped us to choose the optical numerical settings for the modulator simulations.

Verification tests have been performed and a good agreement between simulations and theory has been obtained for modulator problem. The analytic solutions to density and velocity modulations only exist for the system containing an infinite electron beam with uniform distribution. In simulations, we used uniformly distributed electrons with realistic thermal velocities, filling the computational domain with periodic boundary condition, to make fair comparisons with theoretical values. The resulting density and velocity modulations due to a stationary ion and a moving ion agree with theory.

Realistic Gaussian electron beam has been used for modulator simulations, with external electric field. The electric field was designed to ideally compensate the beam expansion due to the space charge effect and the thermal velocities. The density and velocity modulations due to the single ion with different locations and velocities have been presented.

Actual quadruples magnetic field used for experiments has been implemented in code SPACE and used for modulator simulations. Modulation process in longitudinal and transverse directions have been predicted for a single ion with center and off-center locations and reference and off-reference velocities with respect to the electron beam. We performed additional phase advance studies to explore the electron beam dynamics in the transverse space with the quadrupole magnetic field, and to explain the behaviors of transverse modulation processes.

The start-to-end process of coherent electron cooling has been studied with simulations by the combination use of code SPACE and GENESIS. We have implemented the routines transferring data between the two codes. A sufficient gain from FEL and a promising cooling result have been obtained when we use Gaussian electron beam. A lower gain from FEL was observed when we use the real distributions of electron beam at the entrance of modulator, caused by unmatched beam size. A suggestion for experiments was provided from numerical simulations, that the quadrupoles in modulator section should be tuned to match the electron beam's transverse size.

While the coherent electron cooling experiments are still in process at Brookhaven National Laboratory, our numerical simulations will continue providing support for the experiments. We will be able to compare our predictions with the physical process when the experiments data are obtained.

Advanced coherent electron cooling (ACEC) will be studied in the future, where the FEL device is replaced by a three-pole wiggler for the amplifier section of the coherent electron cooling.

References

[1] V. N. Litvinenko, Y. S. Derbenev, Free Electron Lasers and High-Energy Electron Cooling, Proceedings of the FEL07(29th International Free Electron Laser Conference) Budker INP, Novosibirsk, Russia, BNL-79509-2007-CP

[2] V. N. Litvinenko, Y. S. Derbenev, Coherent electron cooling[J], Physical Review Letters, 2009, 102(11): 114801.

[3] V. N. Litvinenko, Coherent Electron Cooling, Proceedings of PAC09, Vancouver, BC, Canada, FR1GRI01

[4] K. Yu et al., Proceedings of IPAC 2015, MOPMN012.

[5] L. Arkeryd, On the Boltzmann equation[J], Archive for Rational Mechanics and Analysis, 1972, 45(1): 1-16.

[6] A. A. Vlasov, On Vibration Properties of Electron Gas, J. Exp. Theor. Phys. (in Russian), 1938, 8(3): 291.

[7] X. Wang, R. Samulyak, J. Jiao, K. Yu, Adaptive Particle-in-Cloud method for optimal solutions to Vlasov-Poisson equation, J. Comput. Phys., 316 (2016), 682 - 699.

[8] G. Wang, M. Blaskiewicz, Dynamics of ion shielding in an anisotropic electron plasma, Phys. Rev. E, 78 (2008) 026413.

[9] A. Elizarov, V. Litvinenko, Dynamics of shielding of a moving charged particle in a confined electron plasma, Physical Review Special Topics - Accelerators and Beams, 18 (2015) 044001.

[10] G.I. Bell, I. Pogorelov, B.T. Schwartz, D.L. Bruhwiler, V. Litvinenko, G. Wang, Y. Hao, Modulator simulations for coherent electron cooling using a variable density electron beam, arXiv preprint arXiv:1404.2320, (2014).

[11] J. W. Eastwood and D. R. K. Brownrigg, Remarks on the solution of Poisson's equation for isolated systems, Journal of Computational Physics, 32(1), 1979, 24-38.

[12] J. L. Vay, P. Colella, J. W. Kwan, et al. Application of adaptive mesh refinement to particle-in-cell simulations of plasmas and beams[J]. Physics of Plasmas, 2004, 11(5): 2928-2934.

[13] K. Yu, R. Samulyak, K. Yonehara, B. Freemire, Simulation of beam-induced plasma in gas-filled RF cavities, Phys. Rev. Accel. and Beams, 20 (2017), 032002.

[14] J. Ma et al., Proceedings of IPAC 2015, MOPMN015.

[15] F. F. Rieke, W. Prepejchal, Ionization cross section of gaseos atoms and molecules for high-energy electrons and protons, Phys. Rev. E, 6 (1972), 1507 C 1519.

[16] B. Freemire, High pressure gas-filled RF cavity beam test at the Fermilab MUCOOL test area, Doctoral Thesis, Illinois Institute of Technology, 2013.

[17] B. Freemire, Electron-hydrogen recombination note, 2014, private communication.

[18] G. Wang et al., Proceedings of IPAC 2013, MOPEA083.

[19] G. Bell et al., Proceedings of 2011 Particle Accelerator Conference, New York, NY, USA, MOP067.

[20] Y. Jing, V.N. Litvinenko, Y. Hao, G. Wang, Model Independent Description of Amplification and Saturation Using Green's Function, arXiv preprint arXiv:1505.04735, (2015).

[21] B.D. Muratori, J.K. Jones and A. Wolski, Analytical expressions for fringe fields in multipole magnets, Physical Review Special Topics-Accelerators and Beams, 2015, 18(6): 064001.

[22] S. Reiche, Numerical studies for a single pass high gain free-electron laser, No. DESY-THESIS-2000-012. DESY, 2000.

[23] W. M. Fawley, Algorithm for loading shot noise microbunching in multi-dimensional, free-electron laser simulation codes, physical review special topics - accelerators and beams, volume 5, 070701 (2002)